The University of Sheffield

Thermal and Electromagnetic Analyses of Interior Permanent Magnet Machines Accounting for AC Copper Loss

Yafeng Zhang

A thesis submitted for the degree of Doctor of Philosophy

Department of Electronic and Electrical Engineering
The University of Sheffield

Mapping Building, Sheffield, S1 3JD, UK

October 2020

ABSTRACT

This thesis presents novel methods for AC copper loss calculation and analysis, and investigates the influence of AC copper loss on electromagnetic and thermal performance, with particular emphasis on torque/power-speed characteristics of interior permanent magnet (IPM) machines for low voltage and high-speed operation.

The influences of position and size of both solid and hollow rectangular conductors on the AC copper loss and thermal management capability are firstly investigated by the finite element method. It is shown that the AC copper loss accounts for a major part of the total loss in the IPM machine with solid rectangular conductors. There is a tradeoff between high maximum torque capability and low AC copper loss at high speed. Thus, it is essential to consider AC copper loss in the calculation of torque/power-speed characteristics. With the liquid coolant flows directly inside the hollow conductors, the hollow region should be carefully designed since it affects not only the AC copper loss, but also the thermal management capability. The hollow shape with the best overall performance can be obtained by considering the variable coolant flow rate.

An efficient and accurate hybrid analytical and finite element model has been proposed for calculating the AC copper loss, accounting for the influences of temperature, frequency, current angle, and saturation. Comparing with a pure finite element method, it is much faster to predict the AC copper loss under different frequencies, current levels, and temperatures. By utilizing the proposed method, together with the general lumped thermal parameter model, the torque/power-speed characteristics accounting for AC copper loss can be obtained within a desirable computing time.

Furthermore, a novel lumped thermal parameter network is proposed based on the heat transfer physics. It eliminates the difference in temperature rise between the distributed loss model and the concentrated loss model. Comparing with the existing models, it utilizes full loss and full resistance and maintains the same parallel flux divide ratio comparing with the distribution loss model. The thermal network element with internal heat generation is relatively isolated from other thermal network elements to prevent over-prediction. It has been shown that the proposed method is relatively more accurate than the existing models for the prediction of hot-spot temperature.

All developed analytical and hybrid models, as well as the lumped thermal parameter network, have been validated by the finite element analyses.

ACKNOWLEDGMENTS

I would like to express my deepest gratitude to my supervisor, Prof. Zi-Qiang Zhu, for his illuminating guidance and continuous encouragement during every stage of my PhD study, which have been invaluable in the completion of this thesis.

Special thanks are also due to all my colleagues in the Electrical Machines and Drives Research Group for their kind help and assistance, especially to Dr. Shun Cai, Mr. Srinivas Mallampalli Satsai, Mr. Dawei Liang, Dr. Han Yang, Dr. Shaoshen Xue, Dr. Yue Liu, Dr. Huayang Li, Dr. Jie Ma, Mr. Bo Shao, Mr. Fangrui Wei, and Mr. Xiaoyong Sun.

I also would like to thank Powertrain Electrical Systems, Valeo, France, for their support, help, advice, and supervision, particularly to Dr. Jean-Claude Mipo and Dr. Sophie Personnaz.

Finally, I warmly express my deepest appreciation to my parents for their continuous encouragement and support. I also would like to thank my dear girlfriend, Miss Chenyi Zhang, for her care and understanding during my overseas PhD study, especially when writing this thesis, which I cherish more than the words can express.

CONTENTS

NOMENCLATURES

Variables

Symbol	Meaning	Unit
A	Area	mm^2
AR	Aspect ratio	
B_m	Amplitude of flux density	T
B_{me}	Friction coefficient	$\frac{\mathrm{Nm}}{\mathrm{rad}}$
B_r	Remanence of permanent magnet	T
c_p	Specific heat capacity	$\frac{\mathrm{J}}{\mathrm{kg}\cdot{}^{\circ}\mathrm{C}}$
CA	Conducting area	mm^2
d_0, d_1, d_2, b_1	Insulation thicknesses	mm
D_h	Hydraulic diameter	mm
f	Frequency	Hz
F	Heat flow rate	$\frac{\mathrm{W}}{\mathrm{mm}^2}$
g	Loss generated per unit volume	$\frac{\mathrm{W}}{\mathrm{mm}^3}$

G	Total loss generated	W
h	Thermal convection coefficient	$\frac{\mathrm{W}}{\mathrm{m}^2{}^\circ\mathrm{C}}$
H	Heat flux	W
H_c	Conductor height	mm
H_{ci}	Coercivity of permanent magnet	mm
H_j	Height of hollow channel	mm
H_s	Slot height	mm
H_{st}	Stator height	mm
H_{ttp}	Tooth-tip height	mm
I_d, I_q	D-axis and q-axis currents	A
I_{max}	Maximum phase current	A
I_{layer}	Current per layer in slot	A
I_{rms}	The RMS value of phase current	A
I_{total}	Total current in slot	A
J	Current density	$\frac{\mathrm{A}}{\mathrm{mm}^2}$
k_{h}	Hysteresis loss coefficient	$\frac{\mathrm{W}}{\mathrm{mm}^3}$

k_e	Eddy current loss coefficient	$\frac{\mathrm{W}}{\mathrm{mm}^3}$
l_g	Airgap length	mm
L_a	Axial length	mm
L_d, L_q	D-axis and q-axis inductances	mH
N_{ph}	Phase number	
N_u	Nusselt number	
p	Pole-pair number	
P_{Fe}	Iron loss	W
P_{Fe_Oc}	Open circuit iron loss	W
P_{Fe_Sc}	Short circuit iron loss	W
P_{Fe_d}, P_{Fe_q}	Iron losses in d-axis and q-axis	W
P_{ac}, P_{dc}	AC and DC copper losses	W
P_{cu}	Copper loss	W
P_{me}	Mechanical loss	W
P_r	Prandtl number	
Q	Thermal energy	J

Q_f	Flow rate	$\frac{\mathrm{L}}{\mathrm{min}}$
R_{ac}, R_{dc}	AC and DC resistances	Ω
R_e	Reynolds number	
R_{ph}	Phase resistance	Ω
R_{th}	Thermal resistance	$\frac{°\mathrm{C}}{\mathrm{W}}$
T	Temperature	$°\mathrm{C}$
T_a	Taylor number	
T_{em}	Electromagnetic torque	Nm
T_o	Constant friction load	Nm
V_c	Compensation thermal voltage	V
V_d, V_q	D-axis and q-axis voltages	V
V_{max}	Maximum phase voltage	V
W_c	Conductor width	mm
W_j	Width of hollow channel	mm
W_s	Slot width	mm
W_{so}	Slot opening width	mm

W_t	Tooth width	mm
α_m	Temperature coefficient of remanence	
α_r	Temperature coefficient of resistivity	
β_{ci}	Temperature coefficient of Coercivity	
β_i	Current angle of MTPA	rad
γ	Angle between I_{total} and I_{layer}	rad
δ	Skin depth	mm
ε_{thr}	Emissivity of surface	
λ	Thermal conductivity	$\frac{\mathrm{W}}{\mathrm{m}^\circ\mathrm{C}}$
μ	Fluid kinematic viscosity	$\frac{\mathrm{kg}}{\mathrm{m}\cdot\mathrm{s}}$
μ_m	Magnetic permeability	$\frac{\mathrm{H}}{\mathrm{m}}$
ρ	Density	$\frac{\mathrm{kg}}{\mathrm{m}^3}$
ρ_e	Electrical resistivity	$\Omega\cdot\mathrm{m}$
σ	Electrical conductivity	$\frac{\mathrm{S}}{\mathrm{m}}$
σ_{SB}	Stefan-Boltzmann constant	$\frac{\mathrm{W}}{\mathrm{m}^2\mathrm{K}^4}$
τ_s	Slot pitch	rad

v	Fluid velocity	$\frac{\mathrm{m}}{\mathrm{s}}$
ϕ_{th}	Heat flux	W
Ψ_d, Ψ_q	Flux linkages in d-axis and q-axis	$\mathrm{Wb} \cdot \mathrm{t}$
Ψ_{pm}	Permanent magnet flux-linkage	$\mathrm{Wb} \cdot \mathrm{t}$
ω_e	Electrical angular speed	$\frac{\mathrm{rad}}{\mathrm{s}}$
ω_m	Mechanical angular speed	$\frac{\mathrm{rad}}{\mathrm{s}}$

Abbreviations

2-D	Two-dimensional
3-D	Three-dimensional
AC	Alternating current
CAD	Computer aided design
CFD	Computational fluid dynamics
DC	Direct current
EV	Electric vehicle
FE	Finite element
FEA	Finite element analysis
FEM	Finite element method
FSPM	Fractional-slot permanent magnet
IM	Induction machine
IPM	Interior permanent magnet
LPTM	Lumped parameter thermal model
MFPT	Minimum flux per torque

MMF	Magnetomotive force
MTPA	Maximum torque per Ampere
MTPF	Maximum torque per flux
MTPV	Maximum torque per voltage
PM	Permanent magnet
PMSM	Permanent magnet synchronous machine
PWM	Pulse-width modulation
SFD	Squared-field-derivative
SFPM	Switched flux permanent magnet
SPM	Surface-mounted permanent magnet
SRM	Switched reluctance machine

CHAPTER 1

General Introduction

1.1. Introduction

With the reduction of petroleum resources and the pollution of the atmospheric environment, electric vehicles (EVs) have become an inevitable substitute for traditional vehicles. Since the 1990s, with the development of battery energy storage units, automobile manufacturers began to make attempts in the field of new energy vehicles [Fai96]. For the pure electric vehicles and hybrid electric vehicles, the electrical traction machine is one of the most important components, since it determines the horsepower, the acceleration, and the efficiency. There are several types of electrical machines that can be used as the traction machines for EVs, including induction machines (IM), switched reluctance machines (SRM), and permanent magnet (PM) machines. The PM machines are becoming the most popular ones for EV applications due to high torque/power density, high efficiency, low torque ripples, and low acoustic noise [Zhu07].

Due to the property of the permanent magnet used in this type of machine, the working temperature has a significant influence on the remanence and coercivity [Seb95]. This results in different working points of the magnets and influences the torque capability of the machine [Jah96]. In addition, the temperature will also influence the amount of power loss in electrical machines. Copper loss increases significantly with temperature increasing, although the iron loss is slightly reduced [Liu92] [Xue16]. Thus, the efficiency of the machine is influenced by the operating temperature. While it is well known that the temperature of an object is determined by the ambient temperature and the heat generated inside the object. Thermal analysis is absolutely necessary to predict the working temperature of electrical machines, especially for permanent magnets.

To realize the thermal analysis, all the losses should be calculated first. The losses in the electrical machine include friction loss, windage loss, DC copper loss, AC copper loss, iron loss, and magnet eddy current loss. Due to convenience in the manufacturing process and high packing factor, the companies and suppliers have more interest in large rectangular conductors. It makes the hair-pin winding become more popular for low voltage and high current applications [Rah12] [Jun12] [Par14]. However, AC copper losses of such large conductors may be extremely high. There is a lot of research on the causes of AC copper loss [Kla06] [Pop13] [Sul99a] [Mcc89] [Red08] and most of them are focused on the Litz-wire [Pop13] [Sul99a] [Mcc89] [Red08]. For the electrical machine with hair-pin windings, AC copper loss is usually the majority at high-speed operation.

It should be noted again that the rectangular conductors become more and more popular than Litz-wire in low voltage applications such as Valeo's 48V hybrid vehicle system.

There are several ways to estimate the temperature distributions in electrical machines, for example, the lumped circuit model and the finite element model. The lumped circuit model is not as accurate as the finite element method, but the computing time is much shorter [Bog09]. For all the methods, the transfer coefficients are the most important factors. The authors in [Bog08a] have proposed the method to calculate the critical coefficients by different tests.

In this thesis, AC copper loss is studied in solid rectangular conductors and hollow conductors. A hybrid analytical and finite element model of AC copper loss is proposed considering the temperature effect. The torque-speed characteristics of interior permanent magnet machines are studied accounting for AC copper loss. In addition, a novel analytical thermal model is proposed based on heat transfer physics.

1.2. Permanent Magnet Machines

There are a lot of types of PM machines. They can be generally divided into two groups according to the location of PMs, i.e. stator PM machines and rotor PM machines. The rotor PM machines are more suitable for EV applications due to high torque density. The rotor can also be divided into two types, surface mounted PM machines (SPM) and interior PM machines (IPM).

1.2.1. Surface Mounted Permanent Magnet Machines

The most classic PM machine is surface mounted PM synchronous machine (SPMSM). The rotor lamination is a simple cylinder, and the PMs are glued on the rotor surface. Fig. 1.1 shows two typical SPMSMs with different winding configurations. PM machines with conventional distributed winding is a classic topology. The full pitched stator winding links all the main flux generated by the rotor PMs. Thus, the maximum output torque can be achieved. However, the long end-winding introduces extra copper loss and extends the axial length of the machine. Concentrated windings are usually wound on an individual tooth, and thus, the end winding is short. However, the shot pitch winding may reduce or limit the reluctance torque if there is any. It can be seen that there is no saliency ratio in SPM rotor, the reluctance torque is naturally zero. Thus, the short-pitched concentrated winding is usually employed in SPM machines instead of IPM machines. In addition, i_d does not produce any torque in SPM, when the machine is operating in high speed and field-weakening region, the output torque is low. Furthermore, since PMs are glued on the surface of the rotor laminations, they may disperse from the rotor due to centrifugal force at high speed [Zhu07] [Zhu14] [Ish06].

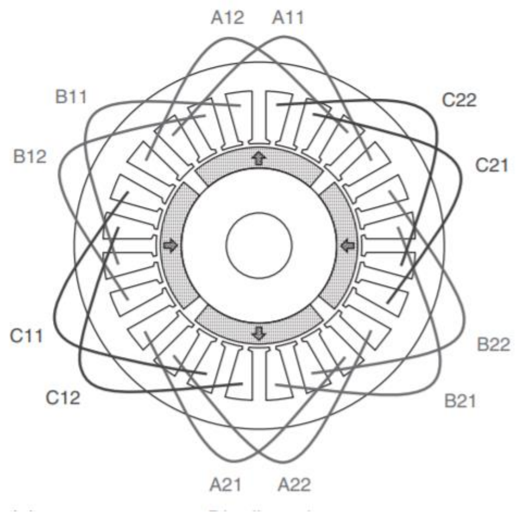

(a) Distributed winding

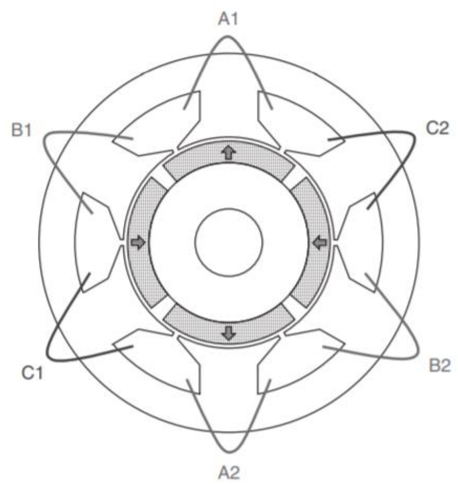

(b) Concentrated winding

Fig. 1.1. Surface mounted PM machine with different winding configurations [Zhu07].

1.2.2. Interior Permanent Magnet Machines

Interior PM synchronous machines (IPMSM) with distributed winding have high torque/power density and high efficiency and are eminently suitable for applications such as electric vehicles. Compared with integer-slot surface-mounted PM (SPM) machines, integer-slot interior PM (IPM) machines exhibit a wider constant power-speed region and a higher demagnetization withstand capability, and are more suitable for traction applications. Other key advantages of IPMSMs include that they can utilize not only the PM torque but also the reluctance torque. In addition, the rotors of IPMSMs can prevent the magnet dispersion from the centrifugal force at high-speed operation under field weakening control, since the magnet is located inside the rotor core [Jah86]. However, the integer-slot IPM machines usually have greater iron losses, especially at high speeds [Azr10] [Sch89] [Zhu02].

Fig. 1.2 shows different rotor topologies, including SPM, I-shaped IPM, V-shaped IPM, and spoked IPM. It can be seen that the PMs in SPM machine are arc and usually difficult to make with good manufacture tolerance [Zhu14]. The rectangular magnet in IPM machines is more desirable.

It can be seen that the air barriers are introduced in I-shaped IPM, as shown in Fig. 1.2(b). They are used to prevent and reduce flux leakage. To achieve higher torque capability, the V-shaped IPM is introduced, two PM pieces are located adjacent with an angle. The fluxes produced by two PM pieces are integrated into one rotor pole, so-called concentrated flux effect or flux focusing effect, as shown in Fig. 1.2(c). In addition, the number of PM layers can be increased to achieve a higher torque capability by a larger saliency ratio, as shown in Fig. 1.2.(d). For a special case of V-shaped IPM, the angle between two adjacent PM pieces is 90 degrees. The rotor can be regarded as a spoke type IPM with circumferentially magnetized magnets, as shown in Fig. 1.2(e). In this topology, the shaft is usually non-magnetic to prevent the short circuit of fluxes. In addition, the air barriers are required and located around the shaft to reduce the leakage.

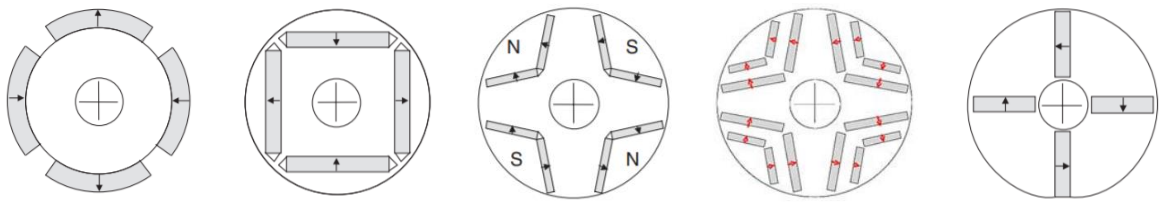

(a) SPM **(b)** IPM-I **(c)** IPM-V **(d)** IPM-V Mutilayer **(e)** IPM-Spoked

Fig. 1.2. Different types of PM rotors [Zhu14].

In [Ge16], the author proposed a novel airspace barrier of spoked type IPMs, as shown in Fig. 1.3. Half of the leakage paths are eliminated. Thus, it can be seen that the leakage fluxes have to pass through the air barrier compared with conventional air barrier design, as shown in Fig. 1.4. In addition, the machine with alternate airspace barriers has higher output torque capability as shown in Fig. 1.5.

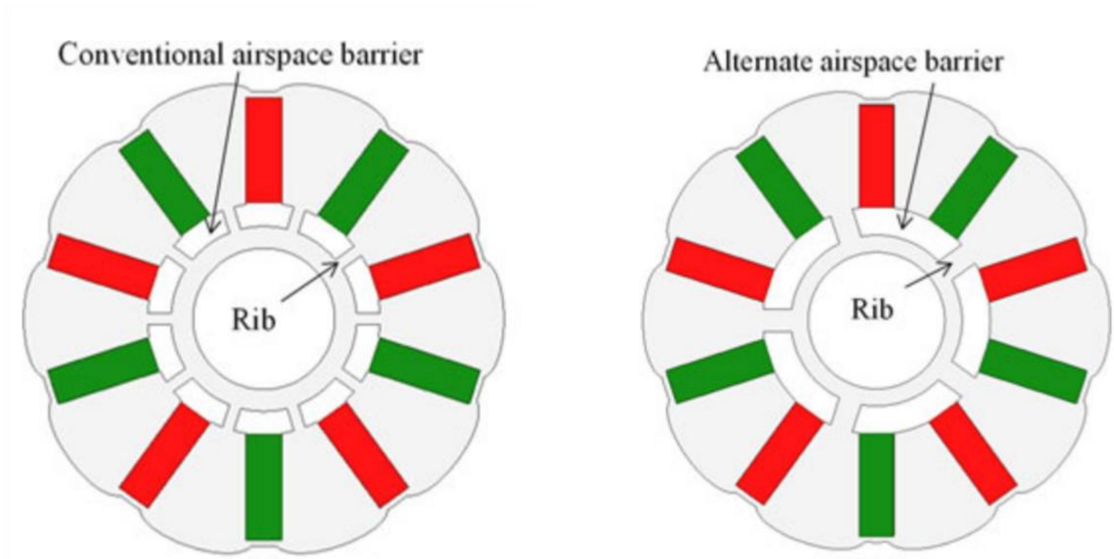

(a) Conventional barriers [DEM13] **(b)** Alternate barriers [Ge16]

Fig. 1.3. Spoke-type IPM rotors with conventional and alternate airspace barriers.

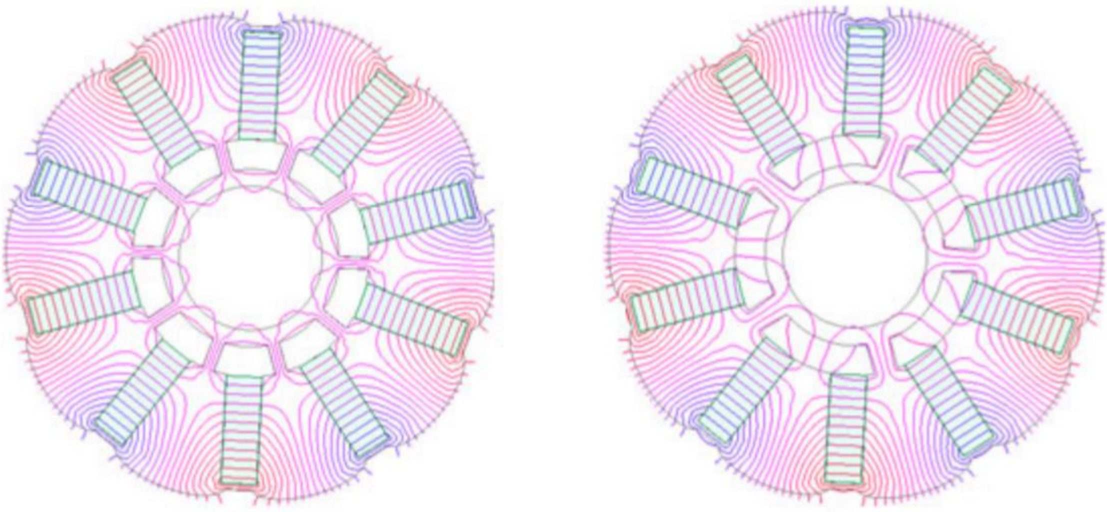

(a) Conventional barriers [DEM13] **(b)** Alternate barriers [Ge16]

Fig. 1.4. Comparison of flux distributions on no load [Ge16].

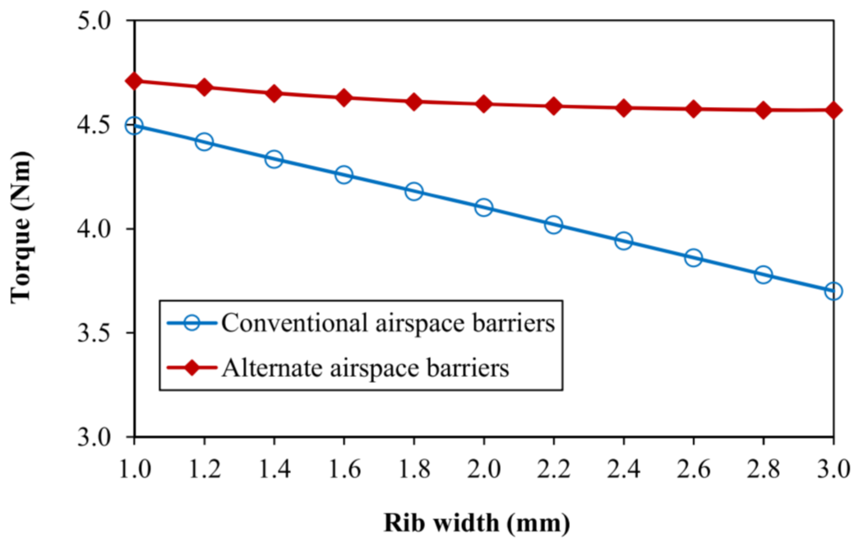

Fig. 1.5. Influence of iron rib width on torque capability [Ge16].

1.2.3. Comparison of SPM and IPM Machines

The advantages and disadvantages of SPM and IPM machines are summarized in Table1.1.

Table 1.1. Comparison of SPM and IPM machines.

	Advantages	Disadvantages
SPM	● Simple rotor geometry ● Less flux leakage ● Short end-winding (concentrated) ● Lower cogging torque	● No reluctance torques ● Poor torque-speed characteristics ● PM dispersion from rotor ● Arc PM shape
IPM	● Wider constant power-speed region ● Better torque-speed characteristics ● Higher demagnetization withstand capability ● Prevent the magnet dispersion ● V-shapsed IPM machines have flux focusing effect ● Rectangular PM shape	● Higher iron losses ● Longer end-winding (distributed) ● Complicated rotor geometry ● Higher flux leakage

1.3. Influence of Temperature on Electromagnetic Performance of Interior Permanent Magnet Machines

1.3.1. Influence of Temperature on PM Materials

For the PM machines, the PMs are the major excitation source for producing the output torque of the machine. However, the ability of PMs to produce the torque is also influenced by the operating temperature since the remanent flux density (B_r) decreases with temperature as shown in Fig. 1.6. The following equations represent the variation of intrinsic remanence and coercivity of PM with temperature [Seb05] [Sun12].

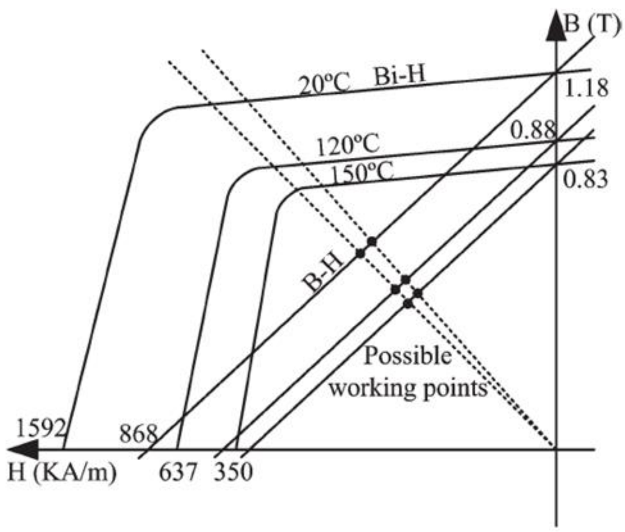

Fig. 1.6. B-H curve of NdFeB magnet material at different temperatures [Sun12].

$$B_r = B_{r0}\left(1 + \alpha_m (T - T_0)\right) \tag{1.1}$$

$$H_{ci} = H_{ci0}\left(1 + \beta_{ci} (T - T_0)\right) \tag{1.2}$$

where B_{r0} and H_{ci0} are the remanence and coercivity of the magnet at temperature T_0, α_m and β_{ci} are the temperature coefficients of the magnet which also depend on the temperature. Most of the NdFeB magnets decreases by 1% of the remanent flux density with the temperature rising by 1°C.

When the temperature beyond 100°C the magnitude of the temperature coefficient becomes higher than the previous value. As Fig. 1.6 shows, the coercivity of the NdFeB magnet has a negative relationship with temperature as well. As temperature increasing, this kind of magnets is more vulnerable to irreversible demagnetization. As for the Ferrite magnets in Table 1.2, the coercivity has a positive relationship with temperature increasing. In other words, this kind of material is safer in high-temperature applications comparing with rare earth materials.

Table 1.2. Temperature influence on different permanent magnet materials [Sun12].

Magnet material	**Grade**	$\boldsymbol{\alpha_m}$**(%/°C) at 20°C**	$\boldsymbol{\beta_{ci}}$**(%/°C) at 20°C**
Bonded NdFeB	MQP-A/ -O	-0.13	-0.40
Bonded NdFeB	MQP-C/ -D	-0.07	-0.40
Casted Alnico	5	-0.02	-0.01
Casted Alnico	8	-0.02	-0.01
Sintered Ferrite	C-5/ -8	-0.20	0.27
Sintered NdFeB	N48M	-0.12	-0.65
Sintered NdFeB	L-38UHT	-0.10	-0.50
Sm_2Co_{17}	27 MGOe	-0.035	-0.20
$SmCo_5$	20 MGOe	-0.04	-0.40

1.3.2. Temperature Effects on IPM Machine Operation

As mentioned previously, the output torque of any PM machine will decrease slightly when the temperature increases, since the torque equation is described by [Qi09].

$$T_{em} = \frac{N_{ph}p}{2}\left(\Psi_{pm}I_q + \left(L_d - L_q\right)I_d I_q\right) \tag{1.3}$$

where T_{em} is the electromagnetic torque, p is the pole-pair number, N_{ph} is the phase number, L_d, L_q, I_d, I_q are the d-axis and q-axis inductances and currents, respectively, and Ψ_{pm} is the PM flux-linkage which is proportional to the remanence of the magnet material at the operating temperature. Therefore, with the temperature increasing, the magnet flux-linkage reduces slightly together with the remanence. On the other hand, the d-axis and q-axis inductances increase slightly when the temperature rises [Che15a]. The resultant constant torque curve of IPM machine (T1 or T2 in Fig. 1.7) will move away from the origin point and rotate counter-clockwise slightly since the machine needs more current to produce the same torque, as illustrated in Fig. 1.8 [Li16]. Consequently, the maximum torque per ampere (MTPA) curves will rotate counter-clockwise slightly since the intersection point between the constant torque curve and the current limit circle changes when the temperature rises. The current angle of MTPA β_i is shown by (1.4).

$$\beta_i = \sin^{-1}\frac{-\Psi_{pm} + \sqrt{{\Psi_{pm}}^2 + 8(L_d - L_q)^2 {I_{max}}^2}}{4(L_d - L_q)I_{ph}} \tag{1.4}$$

where I_{max} is the maximum phase current limited by the control process and the inverter.

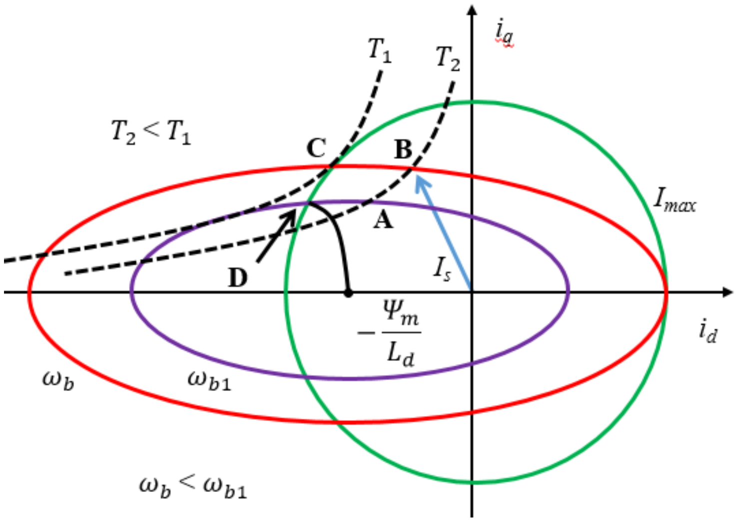

Fig. 1.7. Flux weakening control of IPM.

The following equations describe the voltages in d-axis and q-axis, V_d and V_q. The first terms represent the voltage drops on the resistances, the second terms are due to the transit of the currents and the rest terms come from the cross-coupling between d- and q- axes.

$$V_d = R_{ph} I_d + L_d \frac{dI_d}{dt} - \omega_e L_q I_q \tag{1.5}$$

$$V_q = R_{ph} I_q + L_q \frac{dI_q}{dt} + \omega_e L_d I_d + \omega_e \Psi_{pm} \tag{1.6}$$

where R_{ph} is the phase resistance, ω_e is the electrical angular speed, V_d and V_q are the voltages in d-axis and q-axis, respectively.

In the steady-state condition, the derivation terms disappeared, and the voltage drops on resistances are relatively small comparing with the cross-coupling terms at high operating speed. Thus, the d- and q-axis voltages become

$$V_d{}' = -\omega_e L_q I_q \tag{1.7}$$

$$V_q{}' = \omega_e L_d I_d + \omega_e \Psi_{pm} \tag{1.8}$$

For a fixed DC-bus voltage, the operating voltage should be limited by the maximum voltage V_{max} which depends on the pulse width modulation method.

$$V_d^2 + V_q^2 \leq V_{max}^2 \tag{1.9}$$

Substitute (1.7) and (1.8) into (1.9), the voltage limitation becomes

$$L_q^2 I_q^2 + L_d^2 \left(I_d + \frac{\Psi_{pm}}{L_d}\right)^2 \leq \left(\frac{V_{max}}{\omega_e}\right)^2 \tag{1.10}$$

When the temperature rises, the magnet flux linkage Ψ_{pm} decreases, and the inductances L_d, L_q increase slightly. Consequently, the constant torque curves of IPM machine will shift away from the origin and slightly rotate in a counter-clockwise direction with the increase of the temperature. It is dominated by the PM excited torque varying with temperature. Fig. 1.8(a) shows the variation trend of the constant torque curves of IPM machines at different temperatures.

The maximum torque per ampere (MTPA) is an operating condition, in which the required electromagnetic output torque can be obtained by the minimum input current. It can be achieved by controlling the IPM machines operating on the intersection point between constant torque curves and current limit circles.

The MTPA control of IPM machines is described in equation (1.4). However, the influence of temperature on MTPA curves is not considered in (1.4). However, the variation of MTPA curves can be analysed by the variation of intersection point. It has been discussed previously that the constant torque curves will change when the temperature changes. Thus, it is esay to know that the intersection point between constant current circles and constant torque curves changes will also vary with temperature. Accordingly, the MTPA curve will also be changed. Therefore, the MTPA curves will slightly rotate in a counter-clockwise direction with the increase of temperature. Fig. 1.8(b) shows the variation trend of MTPA curves of IPM machines with the increase of temperature. Under steady-state operation, the centre of voltage limitation ellipses of IPM machines will move towards the origin and the areas coverd by the voltage limitation ellipses will be slightly reduced when the temperature increases, as shown in Fig. 1.8(c).

The maximum torque per voltage (MTPV), maximum torque per flux (MTPF), and minimum flux per torque (MFPT) are the same operating conditions, in which the required electromagnetic torque can be obtained by the minimum voltage or flux. It can be achieved by controlling the IPM machines operating on the intersection point between constant torque curves and voltage limitation ellipses.

When the temperature changes, the MTPV curve will also change due to the variation of the intersection point between curves of constant torque and voltage limitation ellipses. The starting point of MTPV curves will move towards the origin, and the MTPV curves will slightly rotate in a counter-clockwise direction when the temperature increases. The variation trend of the MTPV curves of IPM machines with the increase of temperature is shown in Fig. 1.8(d).

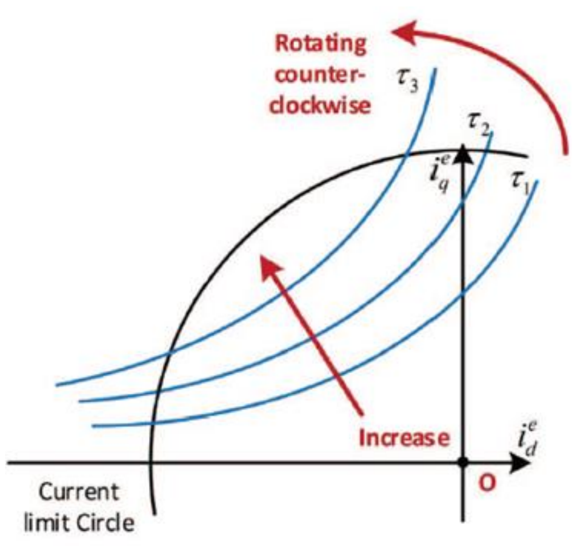

(a) Variation of constant torque curves

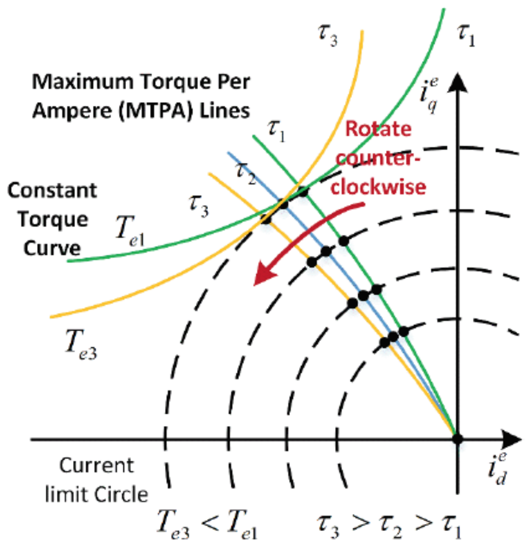

(b) Variation of MTPA curves

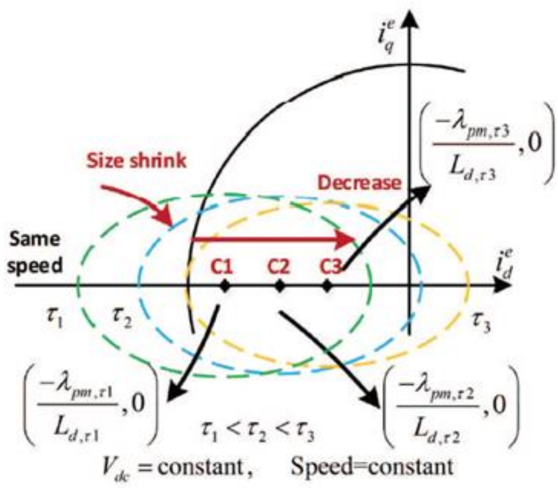

(c) Variation of voltage limit ellipses

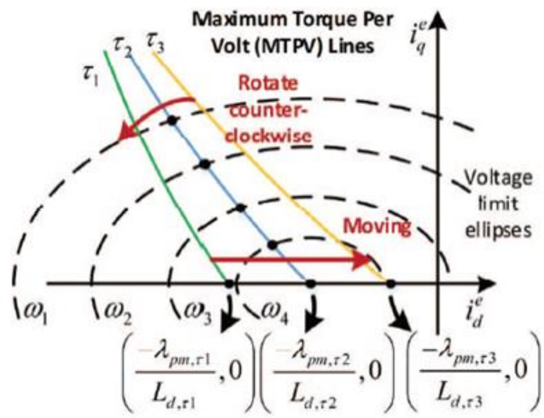

(d) Variation of MTPV curves

Fig. 1.8. Temperature influence on the performance of IPMs [Li16].

1.4. Loss in Electrical Machines

1.4.1. Copper Loss

1.4.1.1. DC Copper Loss

As mentioned previously, the machine losses dominate the machine operating temperature, but both copper loss and iron loss are also influenced by the operating temperature. For a balanced three-phase electrical machine system, the copper loss can be calculated by (1.11), and the phase resistance depends on the wire diameter and the total length used in one phase (1.12).

$$P_{cu} = {I_{rms}}^2 R \tag{1.11}$$

$$R = \rho \frac{L}{A} \tag{1.12}$$

where P_{cu} is the copper loss, I_{rms} is the RMS value of phase current, R is the resistance, ρ is the resistivity, L and A are the length and cross-sectional area of the conductor, respectively.

For the copper loss, the resistivity of the stator winding has a direct relation with its temperature. The resistance of a wire at any temperature can be derived by the resistance at a known temperature as (1.13a) [Liu93a] or (1.13b) [Seb95].

$$R = R_0\big(1 + \alpha_r (T - T_0)\big) \tag{1.13a}$$

$$R = R_0 \frac{234.5 + T}{234.5 + T_0} \tag{1.13b}$$

where α_r is the temperature coefficient of the material, and R_0 is the resistance at the temperature T_0.

1.4.1.2. End-Winding Estimation

In an electrical machine, copper loss is a dominant loss especially when the overlapped winding is employed. Therefore, it is essential to predict the wire length in particular the end-winding. Fig. 1.9 shows the 2D model of the end-winding prediction.

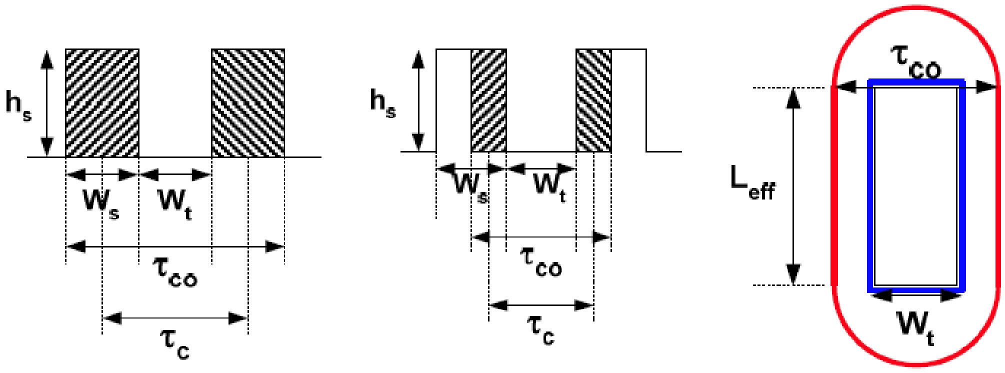

(a) 1 coil-side/slot (b) 2 coils-sides/slot (c) Assumed coil shape

Fig. 1.9. Models of end-windings [Ref06].

Table 1.3. Comparison of different methods to predict the end-winding.

Winding type	Coil pitch	The average length of end-winding in each coil (Half-length)		
Fractional slot (non-overlapped)	1 tooth	Method 1 [Ma16]:	$W_t + \frac{\pi W_s}{2} * k$	(1.14a)
		Method 2 [Ref06]:	$\pi(W_t + W_s * k)/4$	(1.14b)
Integral slot (overlapped)	n-teeth	Method 1 [Ma16]:	$\frac{\pi W_s}{2} * k + (n\tau_s - \gamma) * \left(r_s \pm \frac{H_s}{2}\right) + h_e$	(1.14c)
		Method 2 [Ref06]:	$\frac{\pi}{4} * (n(W_t + W_s) + (k-1)\frac{W_s}{2})$	(1.14d)
Additional equation			$\gamma = \tau_s - \arctan(\frac{W_t}{2}/r_s) * 2$	(1.14f)

where k is a coefficient which depends on single-layer ($k = 1$) or double-layer ($k = 0.5$). The term $r_s \pm \frac{h_s}{2}$ depends on the internal rotor or external rotor. For the internal rotor, r_s is the stator inner radius and the sign is positive, while for the external rotor, r_s is the stator outer radius and the sign is negative. h_e is the extra length for the overlapped parts.

It should be noted that the methods to estimate the end-winding length cited in Table 1.3 are only suitable for conventional strand windings.

1.4.1.3. AC Copper Loss

Skin effect

There is an effect on the copper loss at high speed which is named the skin effect in the time-varying electromagnetic field. The induced eddy currents are focused on the surface which reduces the material conducting area and increases the resultant resistance. The depth is related to the material conductivity, the permeability, and the electrical frequency, (1.15). For a conductor with a radius 'a' carrying current $I\cos\omega t$, shown in Fig. 1.10, the relationship between the resultant resistance and DC resistance is shown by (1.16). Mellor [Mel11] developed an expression to calculate AC copper loss considering the frequency and the temperature effects, and in (1.17), f_{2ac} is the frequency at which AC resistance is twice of DC resistance. The skin depth is roughly equal to the conductor radius at this frequency, and this expression uses this frequency to represent DC resistance [Mel11].

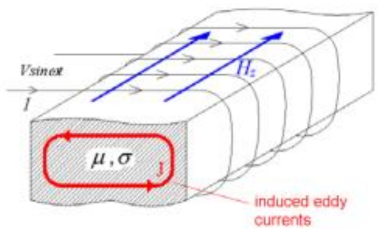

(a) Eddy current model

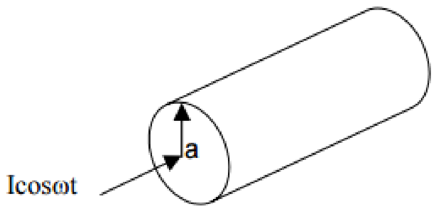

(b) Model of AC resistance

Fig. 1.10. Models in the time-varying field.

$$\delta = \sqrt{\frac{2}{\omega\sigma\mu_m}} \tag{1.15}$$

$$\frac{R_{ac}}{R_{dc}} \approx \frac{a}{2\delta} \tag{1.16}$$

$$P_{ac} = {I_{rms}}^2 R_{dc}\left[\frac{f/f_{2ac}}{\sqrt{\left(1+\alpha_r(T-T_0)\right)}}\right] + \left(1+\alpha_r(T-T_0)\right) \tag{1.17}$$

where δ is the skin depth at speed ω, σ is the electrical conductivity, μ_m is the magnetic permeability, and α_r is the temperature efficiency of the resistance, R_{ac} and R_{dc} are AC resistance and DC resistance, respectively.

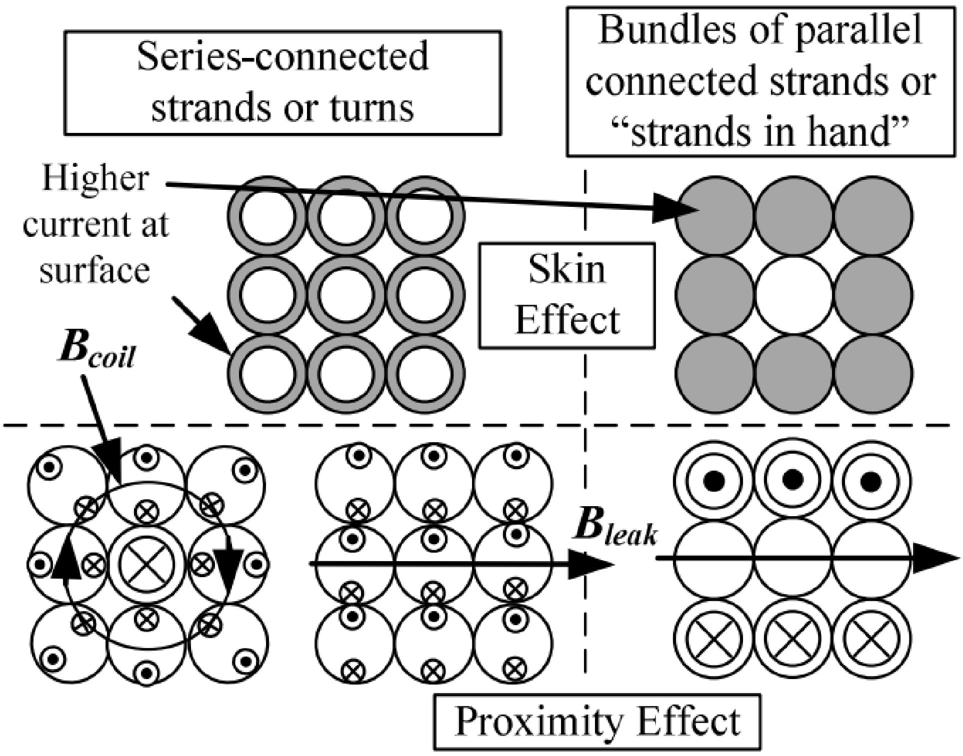

Fig. 1.11. Skin and proximity effects on coils [Pop13].

Proximity effect

Furthermore, when the parallel paths of coil conductors are located in different positions of the slot they will be affected by the circulating current between conductors and also the eddy currents in individual conductors. It is due to the alternative flux linkage between the conductors introduced by the rotor magnets, armature leakage, and mutual coupling. This is called proximity effect and should be distinguished from skin effect in windings as illustrated in [Kla06]. The differences between proximity effect and skin effect are also discussed in [Sul99a] and [Mcc89]. The difference and the similarity of the skin effect of individual conductors and the proximity effect of bundles of parallel conductors are illustrated in Fig. 1.11. In [Pop13], it has been shown that the skin effect can be eliminated with thin wire. However, the proximity effect will still exist. It was illustrated in [Kla06] that the total conductors in a slot can be separated into bundles of parallel wires. Higher losses will be generated when the end winding is tight and the strands do not change position between coil sides.

There is much literature that discusses the losses in machine windings, including the analytical calculation, finite element analysis (FEA), and their hybrid method. In [Tho09], a 1-D analytical model to accurately estimate the proximity losses in switched flux PM machines (SFPM) has been developed. Wojda presented the analytical optimization of solid-round-wire inductor windings to achieve the minimum AC resistance [Woj13]. Phung presented two complementary numerical approaches to predict proximity losses in rectangular conductors [Phu07]. Nan in [Nan03] and [Nan04] improved the accuracy of prediction on proximity effect loss presented in [Dow66] and [Fer94], as shown by Fig. 1.12(a). The idea is to simulate a single wire with symmetrical boundary conditions and find out its behaviour in a winding. Sullivan introduced the squared-field-derivative (SFD) method which allows calculating losses of each winding in multi-winding transformers. It considers the two-dimensional (2-D) and three-dimensional (3-D) field effects and is suitable for arbitrary waveforms. The predicted AC resistance by SFD comparing with the measured value is shown by Fig. 1.12(b) [Sul01] [Sul99b]. In [Wro10a] and [Wro12], an investigation into proximity losses in end-winding informed from the 3-D FEA is presented. Iwasaki firstly took account of the influence of the pulse-width modulation (PWM) and stated that significant proximity loss exists due to high-frequency current ripples induced by the pulse-width modulation (PWM) [Iwa09]. Reddy analysed the proximity losses in high-speed PM machines, surface mounted PM machines (SPM) with concentrated windings, and fractional-slot PM machines (FSPM) in [Red08] [Red10] [Red11]. In [Sim18], the author presents a shaped slot winding profile which can reduce AC copper loss based on the time-harmonic finite element model.

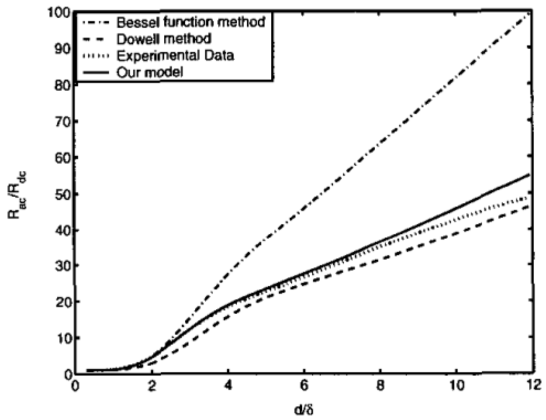

(a) Comparison of experimental data for AC resistance with different models [Nan03]

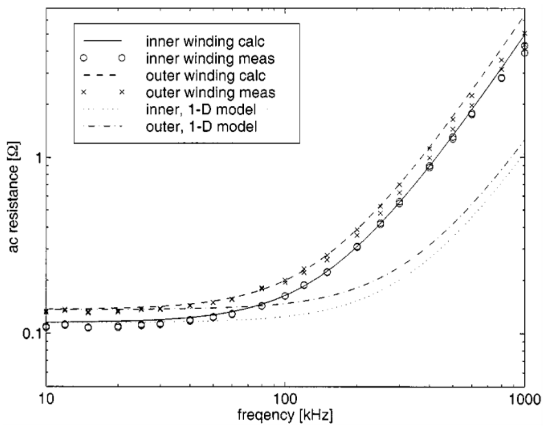

(b) Measured AC resistance compared to AC resistance predicted by the SFD method and 1-D model [Sul01]

Fig. 1.12. Prediction of AC resistance by different methods.

Mellor stated that the distribution of the magnetic flux causes eddy current in the axial direction for radial field machines, and the largest eddy currents are induced close to the slot opening, resulting in non-uniform current distribution in each conduction, shown in Fig. 1.13 [Mel06].

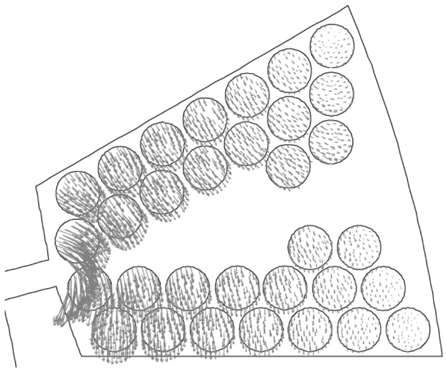

(a) Flux line distribution in slot

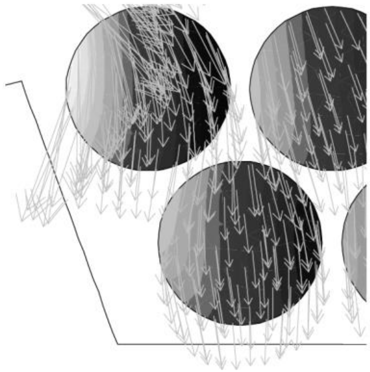

(b) Resultant non-uniform current distribution

Fig. 1.13. Flux variation in stator winding [Mel06].

Mellor demonstrated several winding methods in half-slot and compared the ratio of AC to DC loss. It can be seen that the losses are the lowest when the conductors are located near the slot bottom (see Figs.1.14c and e) and when the conductor height is minimum in the radial direction, Fig. 1.14(f). The author further investigated two winding topologies (g) and (h) which use 2-strand and 3-strand bar conductors to reduce the conductor height in the radial direction and improve the packing factor [Mel06].

Table 1.4. Comparison of different winding models [Mel06].

Winding model	(a)	(b)	(c)	(d)	(e)	(f)	(g)	(h)
Packing factor	50%	50%	50%	50%	50%	50%	32%	45%
P_{ac}/P_{dc} at 400Hz	7.62	4.10	2.94	6.97	5.90	2.66	1.50	2.00

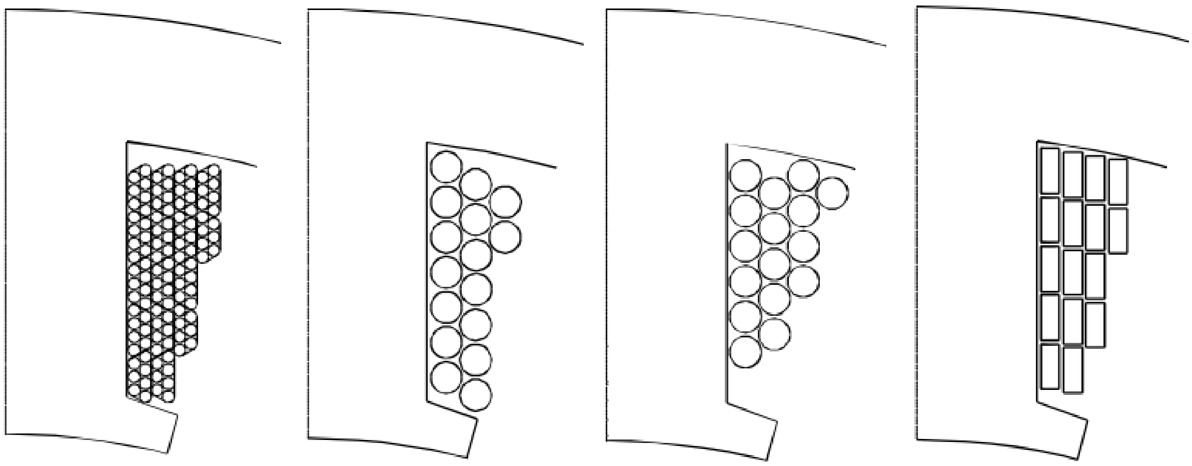

(a) Baseline, 7-strands of parallel conductors wound uniformly around the tooth

(b) Single round conductor

(c) Single round conductor concentrated at bottom of slot

(d) Bar conductor

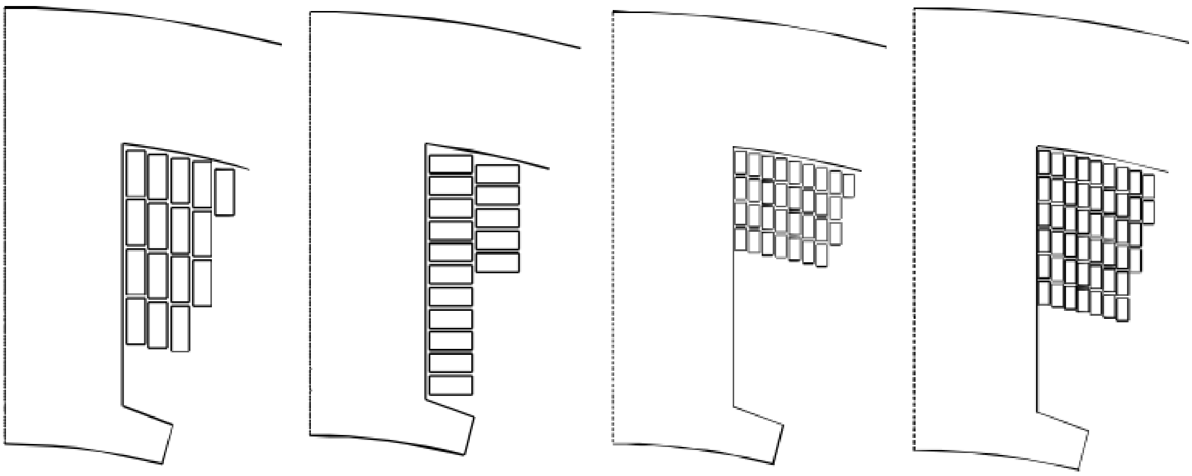

(e) Bar conductor concentrated at bottom of slot

(f) Bar conductor with a different orientation

(g) 2-strands of parallel conductors

(h) 3-strands of parallel conductors

Fig. 1.14. Different winding models in a half slot [Mel06].

In [Mel06], the authors also analyse the rectangular conductors, as shown in Fig. 1.14. There is a lot of literature that focuses on rectangular conductors as well. In [Li18] and [Vol18], the author provides the analytical method, finite element method, and a hybrid method to model AC copper loss. However, the temperature effect and current effect are not studied. In [Aoy18], the author studies the influence of parallel path on DC copper loss and eddy current loss. In [Bar18], the author presents that introducing a space between the conductors and tooth tips can reduce AC copper loss. In [Bol02], the author presents an analytical method to predict AC copper loss of rectangular conductors. The model is shown in Fig. 1.15.

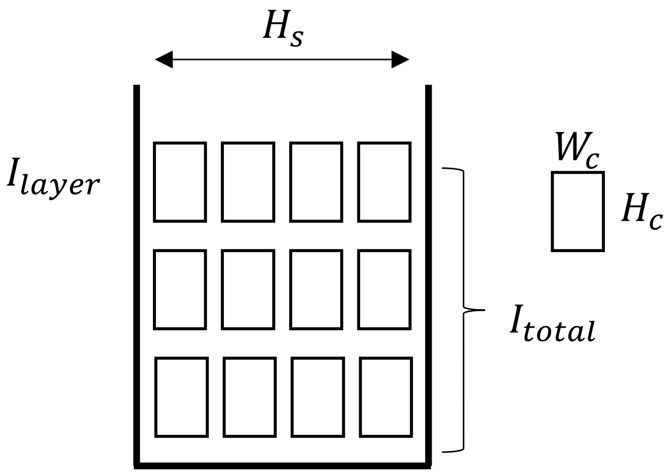

Fig. 1.15. Multiple rectangular conductors in a parallel slot [Bl02].

AC to DC resistance coefficients for the pth layer (K_{RP}) in the slot shown in Fig. 1.15 can be obtained by the following equations:

$$K_{RP} = \varphi(\xi) + \frac{I_{total}\left(I_{total}\cos\gamma + I_{layer}\right)}{I_{layer}^2}\psi(\xi) \tag{1.18}$$

$$\varphi(\xi) = \xi\frac{\sinh 2\xi + \sin 2\xi}{\cosh 2\xi - \cos 2\xi} \tag{1.19}$$

$$\psi(\xi) = 2\xi\frac{\sinh\xi - \sin\xi}{\cosh\xi + \cos\xi} \tag{1.20}$$

$$\xi = H_c\sqrt{\frac{\omega\mu_m\sigma}{2}\frac{n_c W_c}{H_s}} \tag{1.21}$$

where I_{total} is the total current in the slot, I_{layer} is the current per layer in the slot, γ is the angle between I_{total} and I_{layer}, n_c is the number of conductors in each layer, H_c, W_c, W_s are the conductor and slot dimensions shown in Fig. 1.15.

The average value of K_{RP} for m layers can be calculated by (1.22) and (1.23) for the case $\gamma = 0°$ and $\gamma \neq 0°$ respectively.

$$K_{Rm} = \frac{1}{m}\sum_{1}^{m} K_{RP}\,(p) = \varphi(\xi) + \frac{m^2 - 1}{3}\psi(\xi) \tag{1.22}$$

$$K_{Rm} = \varphi(\xi) + \left(\frac{m^2(5 + 3\cos\gamma)}{24} - \frac{1}{3}\right)\psi(\xi) \tag{1.23}$$

1.4.2. Iron Loss

Iron loss is another major loss in electrical machines, especially at high-speed operation. Since iron loss affects the efficiency of electrical machines, temperature distribution, cooling requirements, and PM demagnetisation, etc., its accurate prediction is essential to evaluate the performance of electrical machines. However, iron loss is one of the most difficult losses to predict accurately in electrical machines. Starting from the first expression by Steinmetz (1.24a) [Ste92], several models were developed based on Steinmetz's model. These models improve the accuracy of the estimated iron losses in laminations [Xue16].

$$P_{Fe} = k_{\mathrm{h}} f {B_m}^{1.6} + k_e f^2 {B_m}^2 \qquad \text{Steinmetz} \qquad (1.24a)$$

$$P_{Fe} = k_{\mathrm{h}} f B_m + k_{\mathrm{ex}} f^{1.5} {B_m}^{1.5} + k_c f^2 {B_m}^2 \qquad \text{Bertotti} \qquad (1.24b)$$

$$P_{Fe} = k_{\mathrm{h}} f {B_m}^{\alpha} + \frac{k_{\mathrm{c}}}{T}\int_0^T B(t)^2 dt + 8.67 k_{\mathrm{ex}} f^{1.5} {B_m}^{1.5} \qquad \text{Atallah} \qquad (1.24c)$$

$$P_{Fe} = k_{\mathrm{h}}(f, B_m) f {B_m}^{\alpha(f,B_m)} + k_e(f, B_m) f^2 {B_m}^2 \qquad \text{Ionel} \qquad (1.24d)$$

$$P_{Fe} = k_{\mathrm{h}} f {B_m}^2 + k_e f^2 {B_m}^2 \qquad \text{Boglietti} \qquad (1.24e)$$

where P_{Fe} is the iron loss, k_{h} and α are the hysteresis loss coefficients, k_e is the eddy current loss coefficient, k_c is the classical loss coefficient, k_{ex} is the excess loss coefficient, f is the frequency, B_m is the amplitude of flux density.

Bertotti improved the expression into three items including hysteresis loss, classic eddy current loss, and extra loss [Ber85]. Atallah investigated the coefficients in Bertotti's model and then improved the accuracy [Ata92]. Since the B-H curves of soft magnetic materials vary with applied field strength, Ionel improved the coefficients related to the frequency and flux density [Ion07]. The three-term expression is difficult to verify in reality, a new two-term approach is developed in [Bog03a], where the classical loss and excess loss in Bertotti's three-term model are combined into a global eddy current loss. However, the previous expressions do not consider the temperature influence on the iron loss, Equation (1.25c) considered the eddy current loss influenced by the iron resistance that is proportional to the temperature [Che15b]. Xue developed a model (1.25d), in which the coefficients of eddy current loss and hysteresis loss accounting the temperature are variables. It can estimate the total iron loss more accurately varying with temperature [Xue16]. As Fig. 1.16 shows, the iron loss prediction with variable coefficients is the most accurate model.

$P_{Fe} = k_{\mathrm{h}} f {B_m}^2 + k_e f^2 {B_m}^2$	Constant coefficients	(1.25a)
$P_{Fe} = k_{\mathrm{h}}(f, B_m) f {B_m}^2 + k_e(f, B_m) f^2 {B_m}^2$	Coefficients vary with frequency and flux density	(1.25b)
$P_{Fe,T} = k_{\mathrm{h}} f {B_m}^2 + \dfrac{k_e}{1+\alpha(T-T_0)} f^2 {B_m}^2$	Temperature influence on the resistance of iron introduced	(1.25c)
$P_{Fe} = k_{\mathrm{h}}(f, B_m, T) f {B_m}^2 + k_e(f, B_m, T) f^2 {B_m}^2$	Coefficients vary with frequency, flux density, and temperature	(1.25d)

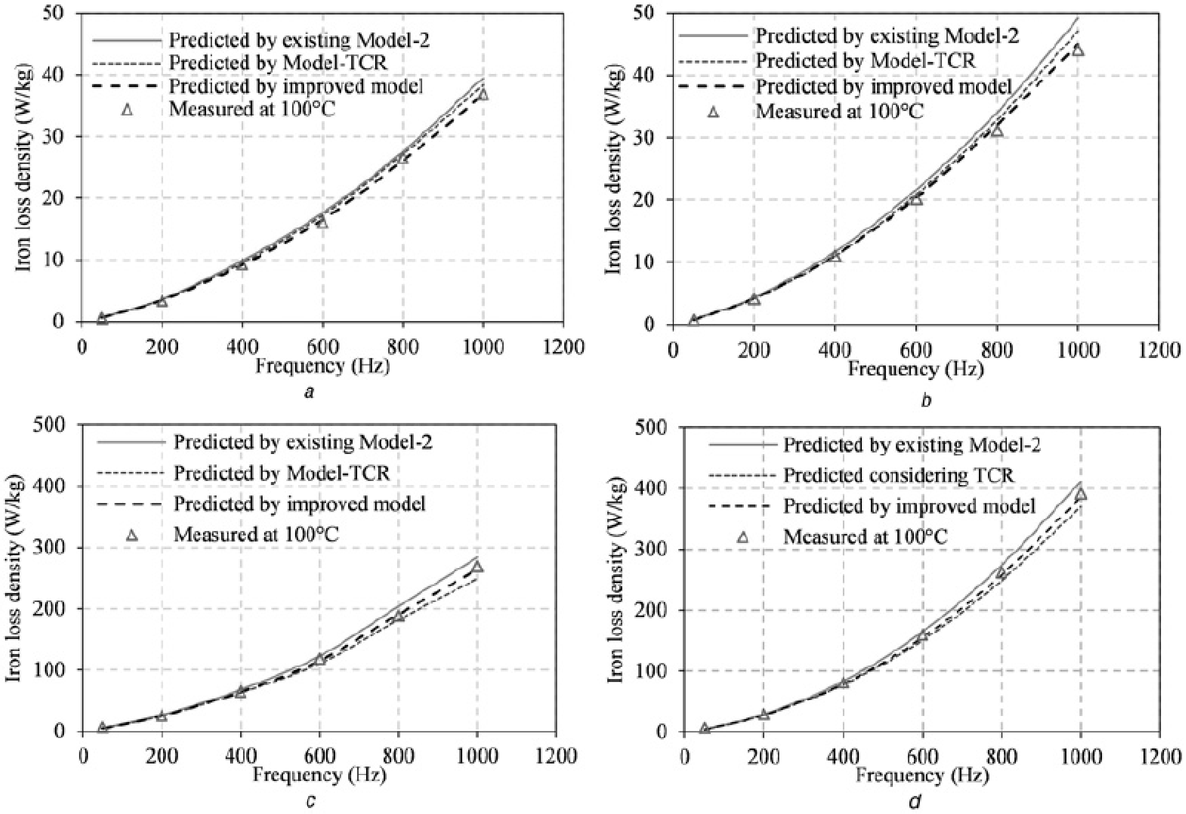

Fig. 1.16. Iron losses vary with frequency at 100°C, Model 2 (1.23b), Model-TCR (1.23c), Improved model (1.25d) [Xue16].

Chen developed a model of iron loss in d- & q- axes which can be used in the simulation of machine drive systems. The open circuit and the short circuit losses can be predicted by employing the previous models at corresponding conditions [Che15c].

$$P_{Fe\_d} = \frac{\Psi_q^2}{\Psi_d^2 + \Psi_q^2} P_{Fe\_Oc} + P_{Fe\_Sc}$$

$$P_{Fe\_q} = \frac{\Psi_d^2}{\Psi_d^2 + \Psi_q^2} P_{Fe\_Oc} \tag{1.26}$$

where P_{Fe_d}, P_{Fe_q}, Ψ_d and Ψ_q are the iron losses and flux linkages in d-axis and q-axis, respectively. P_{Fe_Oc} and P_{Fe_Sc} are the iron losses in open-circuit and short-circuit respectively.

Han investigated the effects of rotor and stator magnetomotive force (MMF) harmonics on iron losses [Han07a] [Han07b] [Han08]. It has been proved that there are specific orders influence the iron loss greatly, where it can be limited by the machine geometries and the winding topologies [Han10]. Some of the results are shown in Fig1.17. By introducing the two-layer rotor the total iron loss can be reduced even if non-optimised. The reason is due to the rotor slot harmonic number changes when the rotor topology changes.

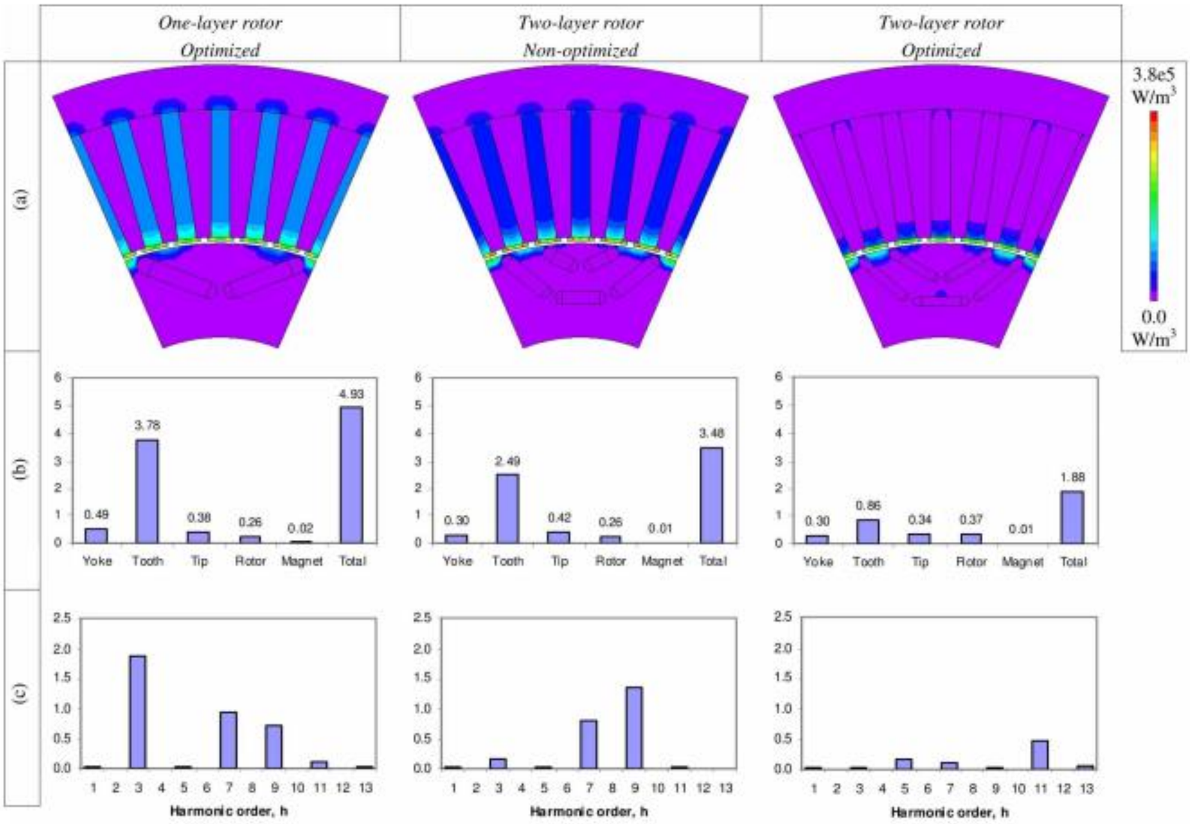

Fig. 1.17. FE-calculated total iron losses under short-circuit conditions at 8224 r/min. (a) Total (hysteresis plus eddy current) core loss density distribution. (b) Breakdown of the total core losses into five major parts of the machine [kW]. (c) Spectra of the total core losses in the stator teeth [kW] [Han10].

In conclusion, the development of the iron loss models is improving the accuracy and considering more effects, such as frequency, flux density, and temperature. From the Boglietti's two-term model, the eddy current loss is defined proportional to frequency square, the hysteresis loss is proportional to frequency and both of them are proportional to flux density square.

1.4.3. Magnet Loss

Although many authors developed the expressions to estimate the eddy current losses of PMs. It is still difficult to estimate them since the equations are extremely complicated in the SPMs. When applied to the IPMs, the expressions should be modified by different rotor topologies, the magnet position, and the flux barriers. Therefore, it is more difficult to calculate the PM loss in IPMs. However, according to the literature, the eddy current loss can be reduced by segment the PMs in circumferential and axial [Ata00] [Tod04] [Wan10] [Kaw09].

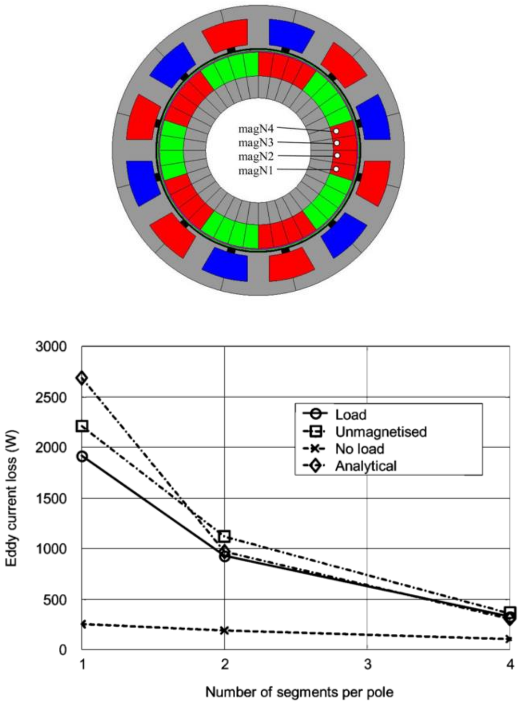

(a) Circumferential segment [Tod04]

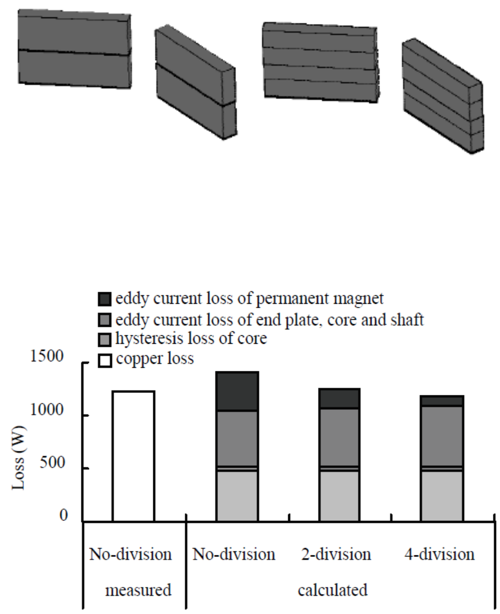

(b) Axial segment [Kaw09]

Fig. 1.18. Magnet segment in different directions to reduce eddy current loss.

1.4.4. Mechanical Loss

The final component of the machine loss is mechanical loss. It is the sum of the bearing friction loss and the windage loss [Yah14].

$$P_{me} = B_{me}\omega_{me}^2 + T_o\omega_{me} \tag{1.27}$$

Equation (1.27) represents the analytical model of mechanical loss, where B_m is the friction coefficient, T_o is the constant friction load, and ω_m is the operating mechanical speed. The two coefficients can be calculated by the no-load testing. However, the rotating rotor magnetic field can generate the induced current in the stator winding and the cogging torque due to the interaction between the rotor field and the stator slot opening [Zhu00]. The more accurate method is employing a dummy rotor machine with un-magnetized magnets.

1.5. Heat Transfer

1.5.1. Heat Transfer Physics in Electrical Machines

In general, the heat flux is always transferring from a high-temperature region to a lower temperature region. As long as the temperature difference exists between two objects or two parts of the same object without any thermal-protective coating between them, the thermal transfer will not stop unless the temperature is the same. There are three basic forms of thermal transfer, i.e. conduction, convection, and radiation. The conduction transfers energy by the movement and/or vibration of a molecule, an atom, or an electron. The conduction between fluids is similar to the momentum transfer between molecules. The convection transfers heat by the macroscopic movement of the fluid micelles. Therefore, the convection can only exist in fluids and accompany with momentum transfer. The radiation removes heat by electromagnetic waves and does not need material as a medium [Bil67] [Mca54].

In reality and also in electrical machines, the heat transfer process is complicated since the conduction, convection, and radiation exist at the same time generally. As mentioned previously, in the analysis of the electrical machines, a strong interaction between electromagnetic and thermal designs should be considered. It is very difficult to predict one accurately without the other, i.e., the copper loss and iron loss are seriously related with the temperature and vice versa [Bog09].

1.5.1.1. Thermal Conduction

Thermal conduction is one of the heat transfer phenomena when there is no macroscopic movement in the medium. It can happen between any two objects with different temperatures no matter whether they are solid, liquid, or gas. However, only the heat transfer inside solids is pure conduction strictly. For fluids, the natural convection happens due to the density difference caused by temperature gradient even in stationary states. Therefore, the conduction occurs with the convection at the same time in fluids [Yun11].

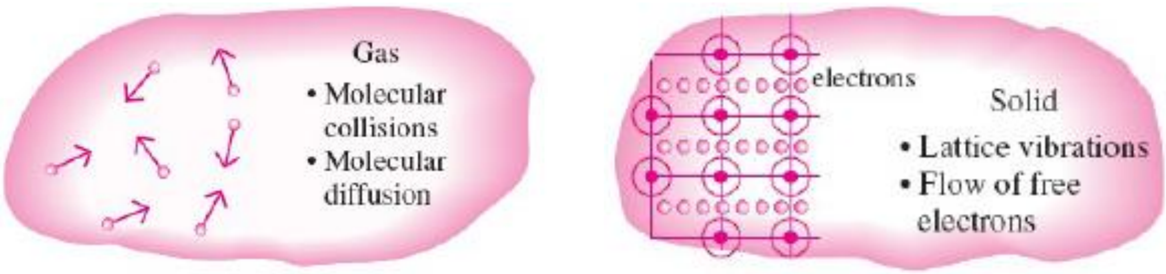

Fig. 1.19. The difference in physical properties between solid and gas [Yun11].

The theory of heat conduction is published by J. Fourier in 1822 [Fou22]. The rate of heat conduction through a medium in a specified direction is expressed by Fourier's law of one-dimensional heat conduction as:

$$\frac{dQ}{dt} = -\lambda A_s \frac{dT}{dx} \tag{1.28}$$

where Q is the thermal energy transferred in Joules, t is the time, λ is the thermal conductivity, A_s is the cross-sectional area of the heat flow, T is the temperature, x is the distance.

The negative sign in (1.28) represents that the heat flux is flowing in the direction of decreasing temperature. In other words, the gradience of temperature is negative when heat flux is flowing in a positive direction. In addition, the rate of the heat changing is proportional to the product of the area of flow and the temperature gradient. The constant λ is the thermal conductivity which is a material property [Sim88].

It should be noted that thermal conduction is the most common heat transfer process in electrical machines, i.e. the heat transferring in the conductor in the axial direction, and the heat transferring in the laminations [Mel91].

1.5.1.2. Thermal Resistance

The heat transfers through a solid material resulting in the temperature difference can be treated as a current source generated current flowing through a resistance and the resulted voltage difference. In the thermal circuit, the temperature is similar to the voltage in the electrical circuit, the power loss (W) is regarded as current and the rest term can be viewed as a thermal resistance [Yun11].

$$\frac{dQ}{dt} = \dot{Q} = -\lambda A_s \frac{dT}{dx} \tag{1.29}$$

$$\dot{Q} = -\lambda A_s \frac{T_2 - T_1}{L} \tag{1.30}$$

$$\Delta T = \frac{L}{\lambda A_s} \dot{Q} \tag{1.31}$$

$$R_{th} = \frac{L}{\lambda A_s} \tag{1.32}$$

where L is the length in heat flow, A_s is the cross-sectional area of the heat flow, λ is the heat conductivity, R_{th} is the thermal resistance.

1.5.1.3. Interface and Conductor Coefficients

The heat transfer is usually occurring through complex structures made of different materials, joined by a thin interface. Fig. 1.20 illustrates the case of steady conduction across an interface and a discontinues temperature occurs and a fictitious temperature drop (ΔT) can be found. With the steady heat flux, the equation (1.31) is set up, and the unit interface conductance is shown by equation (1.34) [Cro77].

$$Q = -\lambda_A \frac{dT}{dx}\bigg|_A = -\lambda_B \frac{dT}{dx}\bigg|_B \tag{1.33}$$

$$h_i = \frac{Q}{\Delta T} \tag{1.34}$$

where h_i is the interface conductance.

There are two requirements which the boundary conditions at an interface should be based on. Firstly, two bodies in contact must have the same temperature at the contact face. Secondly, there is no energy that can be stored in an interface, and thus the heat flux on the two sides of an interface must be the same.

The prediction accuracy of machine thermal performance is dependent upon the estimation of many thermal contact resistances within the machine such as the contact resistance between the stator lamination and housing, and the contact resistance between the slot-liner to lamination, etc. Thermal contact resistance is caused by the imperfections in the contacting surfaces. It is a complex function of smoothness of the surfaces, material hardness, air pressure, and interface pressure. In a design process, the easiest way to calculate the thermal contact resistance is to base the thermal resistance on an average interference air gap [Sta05]. Table 1.5 summarised several typical effective interface gaps and the conductance of different materials.

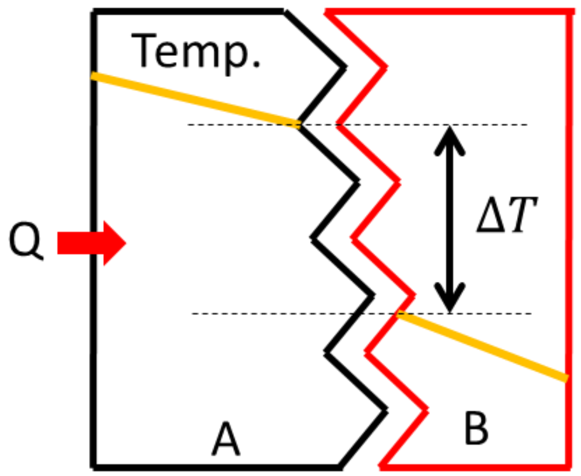

Fig. 1.20. The general model of the interface between the two materials.

Table 1.5. Effective interface gap and the conductance of different materials [Sta05].

	Interfacial conductance $[\frac{W}{m^2C}]$	Effective interface gap [mm]
Ceramic-Ceramic	500- 3000	0.0087- 0.0052
Ceramic-Metal	1500- 8500	0.0031- 0.0173
Graphite-Metal	3000- 6000	0.0043- 0.0087
Stainless-Stainless	1700- 3700	0.0070- 0.0153
Aluminium-Aluminium	2200- 12000	0.0022- 0.0012
Stainless-Aluminium	3000- 4500	0.0058- 0.0087
Iron-Aluminium	4000- 40000	0.0006- 0.0060
Copper-Copper	10000- 25000	0.0010- 0.0026

1.5.1.4. Newton's Cooling Law

Convection-cooling is sometimes called "Newton's law of cooling". For a solid heat source, when the temperature difference between the surrounding medium and the source is not large (less than 50°C), the transferred heat from the source is proportional to the temperature difference. The empirical formula is Newton's cooling law.

$$\frac{dQ}{dt} = hA_s(T_s - T_0) \qquad (1.35)$$

where Q is the thermal energy transferred in Joules, A_s is the surface area, $(T_s - T_0)$ is the temperature difference between the surface and the surrounding medium and h is the heat transfer coefficient. Newton's cooling law states that the rate of heat loss of a heat body is proportional to the temperature difference between the body and its surroundings [Bou97] [Joo11] [Ner08].

1.5.1.5. Thermal Convection

For the successful design of many engineering systems, the ability to predict the rate of heat transfer between a fluid medium and a solid boundary is essential. Thermal convection can happen if one of the objects is fluid and a relative motion occurs at the surface. Convections are usually divided into two categories, namely forced convection and natural convection. When the fluid motion is produced by the applied pressure or viscous forces on the fluid boundary the process is termed as forced convection. In natural convection, the fluid motion is due to the buoyancy forces induced by temperature gradients or concentration gradients [Lew96].

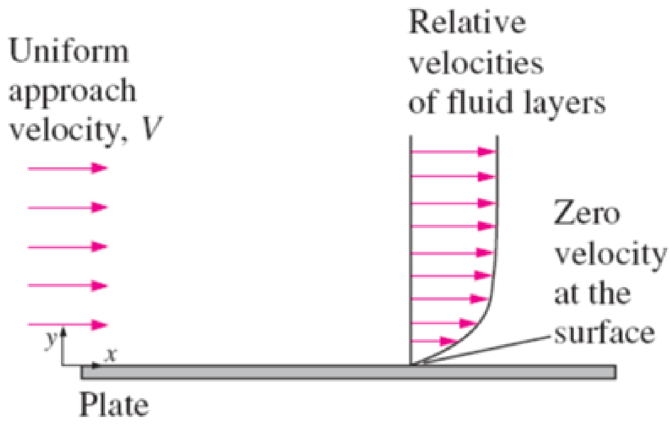

Fig. 1.21. Model of thermal convection [Yun11].

The heat transfer rate through a fluid by convection is much higher than by conduction. Heat transferred from the solid surface to the fluid layer adjacent to that surface can be regarded as pure conduction since there is no relative speed. Therefore,

$$\dot{Q}_{conv} = \dot{Q}_{cond} = -\lambda A \frac{dT}{dy}\bigg|_{y=0} \tag{1.36}$$

It is similar to the thermal conduction, the heat transferred by convection can be regarded as a current source flowing through a resistor, and the thermal resistance of convection is:

$$R_{th} = \frac{1}{hA_s} \tag{1.37}$$

where h is the convection heat transfer coefficient.

Convection heat transfer is strongly dependent on the fluid properties, such as the dynamic viscosity, the thermal conductivity, the fluid density, and the specific heat, as well as the fluid velocity. It is also depending on the roughness and the geometry of the solid surface. In addition, the fluid flow type such as streamlined flow or turbulent flow is also a considerable effect. The convection coefficient h is not an inherent property of the fluid material. It is a parameter determined by the experiment. The value of the convection coefficient is depending on several influences such as the surface geometry, the nature of fluid motion, the material properties of the fluid, and the bulk fluid velocity. There are several numbers that can describe the efficiency of convection, and thus affecting the heat transfer coefficient.

Nusselt number:

$$N_u = \frac{\dot{Q}_{conv}}{\dot{Q}_{cond}} = \frac{hL}{\lambda} \tag{1.38a}$$

Reynolds number:

$$R_e = \frac{\text{Inertial forces}}{\text{Viscous forces}} = \frac{\rho v L}{\mu} \tag{1.38b}$$

Prandtl number:

$$P_r = \frac{\text{Molecular diffusivity of momentum}}{\text{Molecular diffusivity of heat}} = \frac{c_p \mu}{\lambda} \tag{1.38c}$$

Taylor number:

$$T_a = \frac{\rho^2 \omega^2 r_{ml} \delta^3}{\mu^2} \tag{1.38d}$$

where L is the characteristic length, ρ is the fluid density, v is the fluid velocity, μ is the fluid kinematic viscosity, c_p is the specific heat capacity, δ is the airgap length, r_{ml} is the mean logarithmic radius.

The first one is the Nusselt number which is a dimensionless coefficient that describes the goodness of convection heat transfer. The Nusselt number represents the enhancement of heat transfer. It can be regarded as a ratio between the heat convection and heat conduction through the same fluid layer. Thus, the larger the Nusselt number, the more effective the heat dissipation by convection.

The second one is called the Reynolds number. The Reynolds number can be regarded as the ratio between inertial forces and viscous forces acting on a fluid object. The value of the Reynolds number determines the laminar flow or turbulent flow.

The Prandtl number is also a dimensionless parameter. It describes the relative thickness of the velocity and the thermal boundary layers. For gases, the Prandtl numbers are around 1, which demonstrates that the momentum dissipates through the fluid at about a similar rate to heat. When P_r << 1, thermal diffusivity is very high, and when P_r >> 1, thermal diffusivity is very low relative to momentum.

The last one is the Taylor number which is proportional to the speed cube. This number is highly related to the forced convection cooling [Bog08a] [Bog09].

The heat convection coefficients are the most difficult parameters to be determined in electrical machines. They are usually obtained by the properties of the material if the surface is smooth, such as the water channel. For the complicated geometries, it is usually obtained by tests [Bog09].

1.5.1.6. Thermal Radiation

The thermal radiation is electromagnetic radiation which carries energy away from the emitting object. It is produced by the thermal motion of charged atoms in substances. When the temperature of an object is greater than absolute zero, the collisions between atoms change the kinetic energy of the atoms or molecules. This results in the particle quantum transition which produces electromagnetic radiation.

The rate of thermal dissipation through radiation depends on the position and the temperature difference between the surfaces where the heat-exchanging happening. The larger the temperature difference between the surfaces, the higher the rate of heat dissipation from the high-temperature surface to the low-temperature surface.

$$\dot{Q}_{radi} = \frac{\phi_{th}}{S} = \varepsilon_{thr}\sigma_{SB}(T_1^4 - T_2^4) \tag{1.39}$$

$$R_{radi} = \frac{1}{h_{radi}S} \tag{1.40}$$

$$h_{radi} = \varepsilon_{thr}\sigma_{SB}\frac{(T_1^4 - T_2^4)}{T_1 - T_2} \tag{1.41}$$

where $\dot{Q}_{radi}$ is the net radiation heat exchange, ϕ_{th} is the total heat flux, S is the area, ε_{thr} is the emissivity of the surface, σ_{SB} is the Stefan-Boltzmann constant, R_{radi} is the thermal resistance of radiation, and h_{radi} is the radiation coefficient.

As mentioned previously, the radiation can be modelled as thermal resistance and this coefficient is mainly depending on the temperature difference. The following values are test results at 27.8℃ housing temperature [Bog06].

$h_{radi} = 8.5\ \mathrm{W/m^2/°C}$	between stator copper and iron core
$h_{radi} = 6.9\ \mathrm{W/m^2/°C}$	between end winding and external cage
$h_{radi} = 5.7\ \mathrm{W/m^2/°C}$	between external cage–ambient

Comparing with thermal convection and thermal conduction, the thermal radiation inside electrical machines is not a significant heat transfer method due to the relatively low gradience of temperature. In electrical machines, heat transfer through radiation usually occurs within the inner components, such as, between the end windings and the end-caps, and between the housing surface and the ambient medium.

The radiation heat transfer inside the electrical machines can be identified by the following assumptions. Firstly, the surface heat exchange properties should be assumed as constant at all wavelengths. Secondly, the irradiation is regarded as the blackbody emission at the respective temperature [Bog08a] [Bog09] [Joo11].

1.5.2. Temperature Influence on Thermal Conductivities

The heat transfer coefficients vary with temperature because of the lattice vibration in solid or molecular diffusion in gas.

Liu [Liu93b] stated that the surface heat transfer coefficients are highly dependent on the temperature of the surface. Therefore, the equivalent thermal resistance of the surface is non-linear and results in a non-linear thermal network. The computed equivalent conductance for the cylindrical frame of the test machine, plotted as a function of its surface temperature, is shown in Fig. 1.22. Table 1.6 shows the variation of thermal conduction coefficients of copper and aluminum with temperature [Liu93b].

Table 1.6. Conductivities at different temperatures [Liu93b].

Temperature (K)	The conductivity of materials (W/m*K)	
	Copper	Aluminium
100	482	302
200	413	237
300	401	237
400	393	240
600	379	231
800	366	218

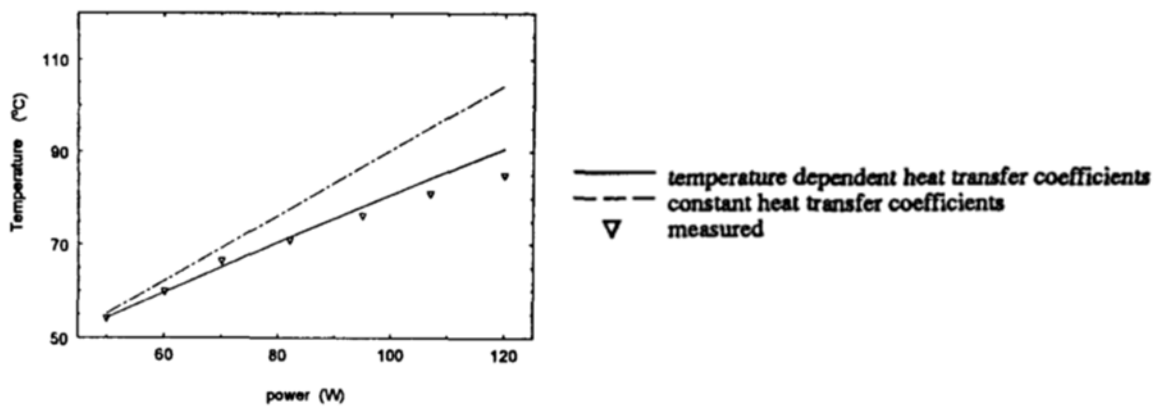

Fig. 1.22. Variation of temperature with input power of copper winding [Liu93b].

1.5.3. Thermal Analysis Methods

In [Bog09], the author compared several methods for the thermal calculation of electrical machines, and the advantages and the disadvantages are summarized in Table 1.7. The lumped circuit models and the Motor-CAD can quickly calculate the temperature at different positions in electrical machines, and the rest two methods can be used to verify the results. For lumped circuit models, the losses in different parts should be calculated by finite element methods as well as the thermal resistances based on machine geometry. For the Motor-CAD, when the motor geometry and materials are set, the program can run thermal tests related to the results from electromagnetic tests or the inputs from users [Bog09].

Table 1.7. Comparison of different methods of thermal analysis.

	Advantages	Disadvantages
LPTN (user built)	Simple, easy to link with other calculations	Less accuracy
Analytical (Motor-CAD)	Only need to input details geometry, winding, and materials used	Geometry is based on a fixed set of topologies
FEM	Can model solid component conduction more accurately than the thermal network	Long model setup and computation times
CFD	Improving the accuracy calculation when fulid is account, usually use CFD to predict convection coefficient	Long model setup and computation times

The most common methods for thermal analysis of electrical machines are lumped parameter thermal model (LPTM) [Mel91] and finite element (FE) model [Bog09]. The LPTM is less accurate than the finite element method, but the computing time is much shorter [Bog09]. Indeed, for both LPTM and finite element method, the thermal transfer coefficients are required. The authors in [Bog08a] focus on the determination of critical thermal parameters which are important in thermal models and have proposed the method to calculate them by different tests. There are a lot of existing LPTMs built by different authors for different types of machines including PM machines [Lee12] [Liu93] [Ref04] [Joo11], induction machines [Mel91] [Mel88] [Bog08a] [Bog09] [Bou97] [Bog03] [Sta05] [Sta06], switched reluctance machines [Li11] and switched flux machines [Li12].

1.5.4. Lumped Parameter Thermal Model

The lumped parameter thermal model (LPTM) is the most widely used thermal analysis method in the literature. Fig. 1.23 shows 4 typical lumped models for different types of electrical machines. There are three types of components in lumped circuit models, i.e. thermal resistance, thermal capacitance, and power loss source. The first one, Fig. 1.23(a), is for the induction machines, there are 17 nodes in this model the outer cage is modelled as a single resistor. The second one, Fig. 1.23(b), is for the switch reluctance machine. The author separated the natural convection and forced convection into two resistors and the total 5 current sources to represent the iron loss in stator back iron (behind slot and tooth), stator tooth, rotor tooth, and rotor back iron. The third network, Fig. 1.23(c), is for the switched flux machine. The geometry of this machine is similar to the switched reluctance machine, the only difference is a piece of PM is employed inside the stator tooth. Therefore, compared with the third and the second models, there is a third vertical branch to model the PM, while for the switched reluctance machine only two branches to represent the slot and tooth regions. The fourth model, Fig. 1.23(d), is for the IPM machine with I shaped PM. This model is more complicated than the first three models, since the end-winding influence is considered, and also the geometry is more complicated than other machines. The rotor has the magnets and also the flux barriers, the two resistances in parallel between the magnet and the flux barrier represent the heat flow through the magnet to the barrier in both positive and negation circumferential directions. The end-winding can only dissipate heats through the end-cup air by convection and radiation.

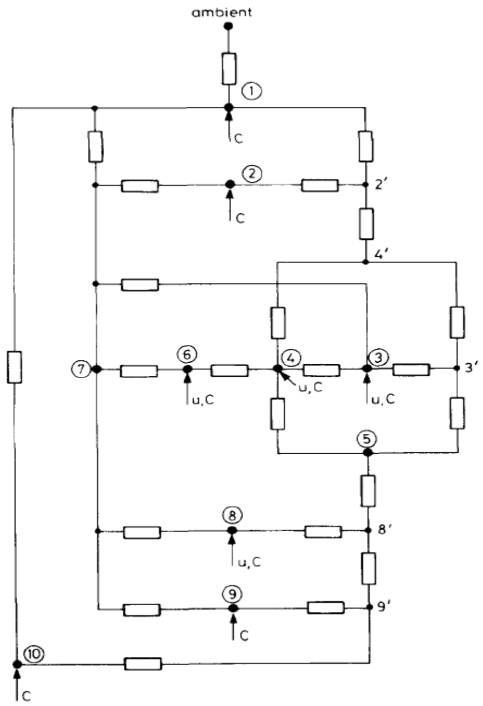

(a) Induction machine [Mel91]

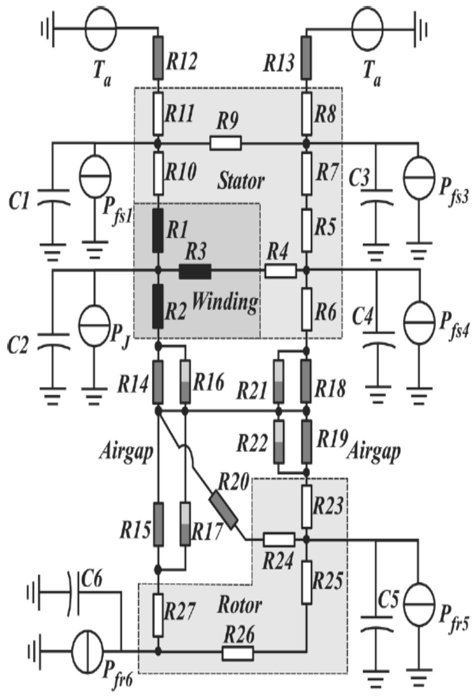

(b) Switch reluctance machine [Li11]

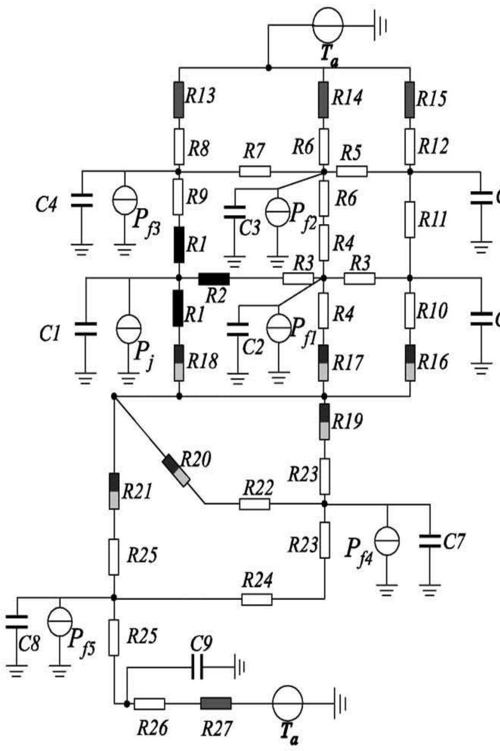

(c) Switched flux machine [Li12]

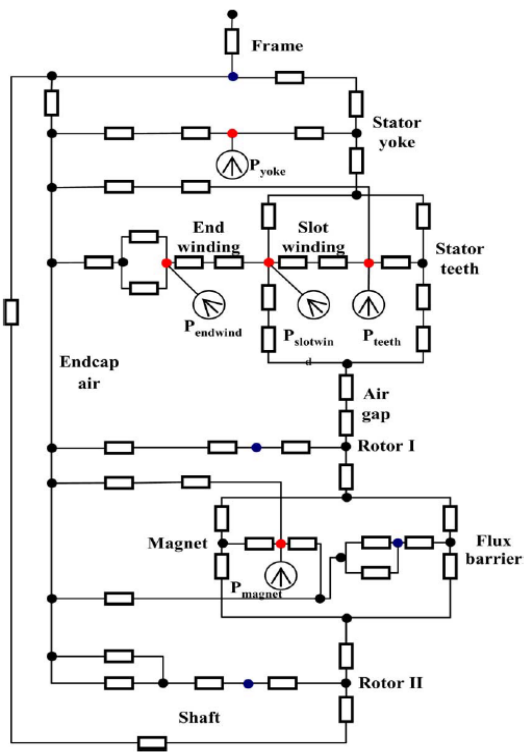

(d) Interior PM machine [Lee12]

Fig. 1.23. Lumped circuit model for different types of machines.

It can be seen that the lumped circuit models compared in Fig. 1.23 are complicated. This is due to the fact that the author in [Mel91] focused on the average temperature of each component in electrical machines. Fig. 1.24 shows a general 3-D cylindrical component which has inner radius R_i, outer radius R_o, and axial length L. The thermal resistance in the radial direction of this component is derived by Mellor in [Mel91] as shown in (1.44). Since they are complicated equations, several authors derived the simplified equations to model the cylindrical equations. However, by applying with the same input values, the results of initial equations are roughly two times of the simplified results. The difference between the two models and equations will be studied and discussed in this thesis.

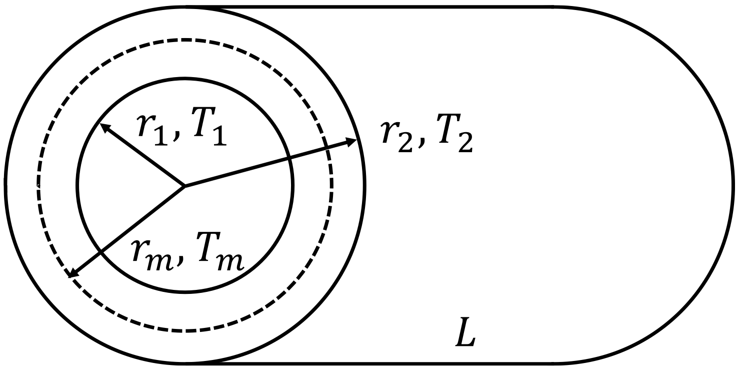

Fig. 1.24. General cylindrical component.

The one-dimensional heat conduction equation in the radial direction of a cylindrical ring, Fig. 1.24, can be described as,

$$\frac{\partial^2 T_r}{\partial r^2} + \frac{1}{r}\frac{\partial T_r}{\partial r} + \frac{g}{\lambda} = 0 \tag{1.42}$$

where T_r is the radial temperature, r is the radius, g is the loss generated per unit volume (W/m^3), and λ is the thermal conductivity.

The general solution of (1.42) gives the temperature profile radially,

$$T_r = a \ln r - \frac{gr^2}{4\lambda} + b \tag{1.43}$$

where a and b are constants.

By introducing the boundary conditions $T_r = T_1 |_{r=r_1}$ and $T_r = T_2 |_{r=r_2}$ into (1.43), the constants a and b can be determined. Thus, the radial temperature profile and the mean temperature can be obtained as,

$$T_r(r) = \frac{g}{4\lambda}\left[\frac{\ln {}^{r}/_{r_1}}{\ln {}^{r_2}/_{r_1}}(r_2^2 - r_1^2) + (r_1^2 - r^2)\right] + \frac{\ln {}^{r}/_{r_1}}{\ln {}^{r_2}/_{r_1}}(T_2 - T_1) + T_1 \tag{1.44}$$

$$T_m = \left(\frac{T_2 r_2^2}{r_2^2 - r_1^2} - \frac{T_2}{2\ln\frac{r_2}{r_1}}\right) + \left(\frac{T_1}{2\ln\frac{r_2}{r_1}} - \frac{T_1 r_1^2}{r_2^2 - r_1^2}\right) + \frac{g}{8\lambda}\,(r_2^2 + r_1^2) - \frac{g(r_2^2 - r_1^2)}{8\lambda\ln\frac{r_2}{r_1}} \tag{1.45}$$

For the case without internal heat generation, the temperature distribution inside the element is due to the temperature difference between the inner surface and the outer surface. The expressions to represent the thermal resistance in the radial direction are summarized in (1.44) [Mel91].

$$
\begin{cases}
R_{1a} = \dfrac{1}{4\pi\lambda L}\left[\dfrac{2r_2^2 \ln\left({r_2}/{r_1}\right)}{r_2^2 - r_1^2} - 1\right] \\[2em]
R_{1b} = \dfrac{1}{4\pi\lambda L}\left[1 - \dfrac{2r_1^2 \ln\left({r_2}/{r_1}\right)}{r_2^2 - r_1^2}\right] \\[1em]
R_{1m} = -\dfrac{\left[(r_2^2 + r_1^2) - \dfrac{4r_2^2 r_1^2 \ln\left({r_2}/{r_1}\right)}{(r_2^2 - r_1^2)}\right]}{8\pi\lambda L(r_2^2 - r_1^2)}
\end{cases}
\tag{1.44}
$$

$$
\begin{cases}
R_{2a} = \dfrac{1}{2\pi\lambda L}\ln\left({r_m}/{r_1}\right) \\[1em]
R_{2b} = \dfrac{1}{2\pi\lambda L}\ln\left({r_2}/{r_m}\right)
\end{cases}
\tag{1.45}
$$

The thermal model is presented in Fig. 1.25(a). It can be seen that there are three resistances, the resistance R_{1m} is negative and used to correct the output temperature. It should be noted that in this method, the element is not separated at a visible radius but an ideal location with the mean temperature.

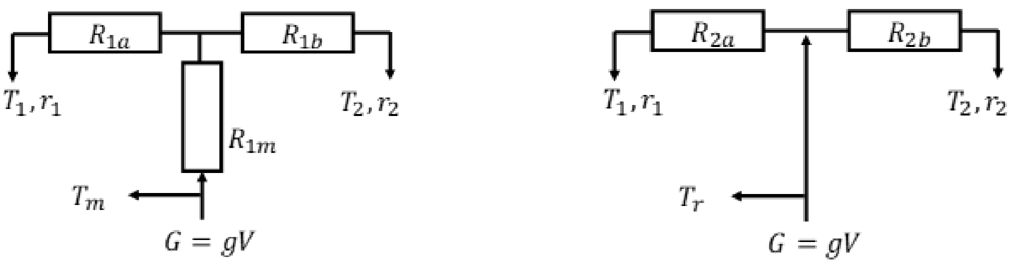

(a) Mellor's model **(b)** Simplified model

Fig. 1.25. Lumped circuit thermal models of the general cylindrical component.

Another method is based on the simplified LPTMs. The main idea is to separate the element at the mean radius and treat the two small rings as zero loss generation [Bog03b] [Ref04] [Joo11] [Bog08b] [Yu10] [Bim18] [Zhu15]. All the losses are assumed to be generated at a surface inside the element, e.g. the surface of constant radius r_m in Fig. 1.24, which separates the original ring into two parts. Thus, a simpler expression can be employed. The expressions and the model are presented in (1.45) and Fig. 1.25(b), respectively. In [Ger06a], Gerling gave several methods to correct the calculation with concentrated loss, including modifying the loss to half value and adding two voltage sources on the main branch. The model investigated in [Ger06a] is presented in Fig. 1.26. The two voltage sources are used to correct the output temperature, the details will be presented in Chapter 6.

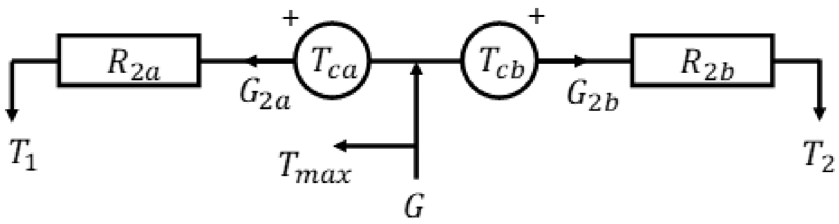

Fig. 1.26. Lumped circuit model investigated in [Ger06a].

1.6. Scope and Contributions of Thesis

1.6.1. Aims and objectives

The aim of this thesis is to investigate AC copper loss in electrical machines and to link it with thermal analysis of electrical machines. This thesis is organized in 7 chapters as follows.

Chapter 1 is the current chapter with a brief introduction about the background of this thesis, the scope of the thesis, and the scientific contributions.

Chapter 2 investigates the influence of design parameters on AC copper loss and torque/power-speed characteristics of IPM machines with rectangular conductors. In this chapter, several basic parameters are selected to analyse their influence on AC copper loss. Three typical models are compared in torque-speed characteristics and efficiency maps.

Chapter 3 investigates the influence of design parameters on AC copper loss and torque/power-speed characteristics of IPM machines with hollow conductors. In this chapter, the thermal dissipation capability and the generated AC copper loss are both analysed.

Chapter 4 analyses the electromagnetic performance of the prototype IPM machine considering AC copper loss. In this chapter, a hybrid analytical and finite element model of AC copper loss with considering the temperature effects are proposed. The results are validated by the finite element method.

Chapter 5 analyses the thermal dispassion performance of the prototype IPM machine considering AC copper loss.

Chapter 6 proposed a novel lumped parameter model of general elements and compared with existing models. The proposed model is derived by analytical equations and has the highest accuracy comparing with other models.

Chapter 7 provides a summary of the main results and the conclusions of this thesis and gives proposals for future studies.

1.6.2. Contributions

The contributions of this thesis are summarised as follows:

- AC copper losses of solid and hollow conductors in the slot are analysed. It shows how the design parameters affect AC copper loss.
- A hybrid analytical and finite element model of AC copper loss is developed. It considers the temperature effect and the saturation effect. It has shorter computing time with desirable accuracy.
- The influence of AC copper loss on the torque/power-speed characteristic is considered. It helps the simulation more accurately, especially for the machines equipped with solid conductors.
- A novel analytical thermal model is developed. It eliminates the error introduced by the concentrated loss model and the distributed loss model. It has good accuracy comparing with existing models and FE models.

1.6.3. Publications

- Yafeng Zhang, Z. Q. Zhu, Shun Cai, Dawei Liang, Srinivas Mallampalli, J.C. Mipo, and S. Personnaz, "One-dimensional lumped parameter thermal model of electrical machines," Proc. IET Science, Measurement & Technology. Under revision.
- Dawei Liang, Z. Q. Zhu, Yafeng Zhang, J.H. Feng, S.Y. Guo, Y.F. Li, J.Q. Wu, and A.F. Zhao, "A hybrid lumped-parameter and 2-d analytical thermal model for electrical machines," IEEE Trans. on Industry Applications. Accepted.
- Y. F. Zhang, Z. Q. Zhu, J.C. Mipo, S. Personnaz, "Influence of slot and rectangular conductor design parameters on AC copper loss and torque /power-speed characteristics of IPM machines with rectangular conductors," drafted and to be submitted.
- Y. F. Zhang, Z. Q. Zhu, J.C. Mipo, S. Personnaz, "Influence of design parameters of hollow conductors on AC copper loss and thermal dissipation capability in permanent magnet synchronous machines," drafted and to be submitted.

CHAPTER 2

Influence of Slot and Rectangular Conductor Design Parameters on AC Copper Loss and Torque/Power-Speed Characteristics of IPM Machines with Rectangular Conductors

In this chapter, the influence of slot and rectangular conductor design parameters on AC copper loss and torque/power-speed characteristics of interior permanent magnet (IPM) machines is investigated. It is shown that the relative ratios between the slot dimensions and the conductor size have a strong impact on AC copper loss. However, the lower AC copper loss occurs only when the slot width or depth is extremely large, which is hard to realize in a real machine due to space limitation. In addition, the position of the conductors determines the maximum improvement of the height and width ratios between slot and conductor. The slot aspect ratio is also studied with different packing factors and two type orientations of the conductors. It is shown that the tendency of AC copper loss against the slot aspect ratio is opposite for the conductors in different orientations. In addition, the overall AC copper loss of two types of conductors decreases with a lower packing factor. It is shown that the conductor aspect ratio is the most dominant parameter. The torque/ power-speed characteristics are also investigated since it is important to study the balance between high torque and low AC copper loss. It is shown that with a wider and shorter conductor, the high-speed performance can be improved significantly. However, the low-speed torque is sacrificed due to the limited space for the stator tooth.

2.1. Introduction

The large rectangular conductors, including hairpin winding, become more popular due to the convenience in the manufacturing process and high packing factor for the low voltage and high current applications [Rah12] [Jun12] [Par14]. The machines employed with rectangular wire windings have high torque /power density. In addition, a good heat dissipation capability is also shown between the conductors and the slot due to a high packing factor [Mom19] [Pop18] [Ish15]. However, these rectangular conductors usually have large cross-section area, which results in significant skin and proximity effects at high speed. In addition, AC copper loss of such large conductors may be extremely high. Recently, there is a lot of research focusing on the reduction of AC copper losses in rectangular conductors [Sim18] [Bar18] [Vol19]. It has been shown that AC copper loss is related to the conducting area, i.e. the height and width of the conductor, the distance between the slot opening and the conductor, and the slot opening. Furthermore, some novel methods to reduce AC copper loss are summarized in [Zha19], including different conductor phase arrangement, twisting criterion [Vet15], and hybrid conductors [Fan18]. In [Mel06], it has been shown that the minimum AC copper loss occurs when the conductors are located at the slot bottom, especially when the long side of the conductor is parallel to the slot bottom. However, it is hard to achieve this due to the space limitation in a multi-phase machine with larger slot numbers.

In this chapter, the influence of fundamental design parameters on AC copper loss is studied accounting for airspaces between the conductors and the slot. The parametric study is based on a simplified model in Cartesian coordinate to investigate the relationship between the design parameters and AC copper loss. The influence on torque-speed characteristic is also studied based on a baseline IPM machine. It will be shown that with a wider and shorter conductor, the low-speed torque is decreased due to the limited space for the stator tooth. However, high-speed performance improves significantly, especially maximum output power and efficiency.

2.2. Torque-Speed Curve with and without AC Copper Loss

In the conventional calculation of torque-speed and power-speed curves, AC copper losses are usually not considered, while for the rectangular conductors, AC copper losses cannot be neglected. Fig. 2.1 shows the torque/power-speed characteristics with and without consideration of AC copper loss for the baseline IPM machine. It should be noted that the baseline machine is designed for hybrid vehicle and operating under the 48V system. It is employed with the hair-pin windings and the conductor size is 5mm*2mm. It can be seen that AC copper loss (or AC resistance) limits the torque and output power in the flux-weakening region. Thus, in order to maintain the machine output performance, it is important to minimize AC copper loss by choosing appropriate design parameters. It should be noted that the machine speccifications and ratings can be found in Appendix.

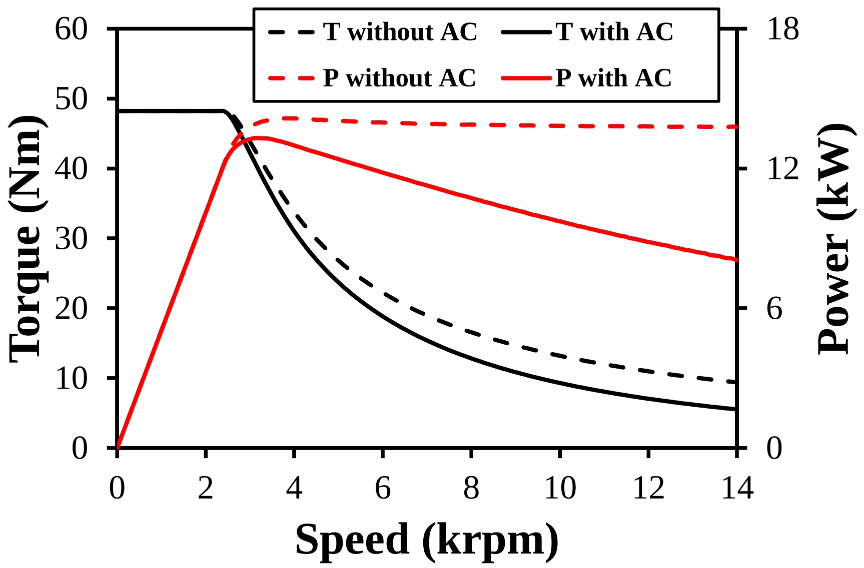

Fig. 2.1. Torque/power-speed envelops with/without accounting for AC copper loss.

2.3. Influence of Slot Aspect Ratios on AC Copper Loss with Constant DC Copper Loss

In order to study the influence of slot parameters on AC copper loss, a linear model of a parallel slot without tooth tips (the influence of tooth-tips will be investigated later) is shown in Fig. 2.2, where the stator height H_{st} and stator width W_{st} are not limited. H_s, W_s, H_c, W_c, are the height and width of the slot and the conductor, respectively. d_1 and b_1 represent the slot liner and other insulation material at the slot bottom and slot side, respectively. d_0 represents the distance between the conductor and the slot opening and d_2 represents the relative position between two conductors.

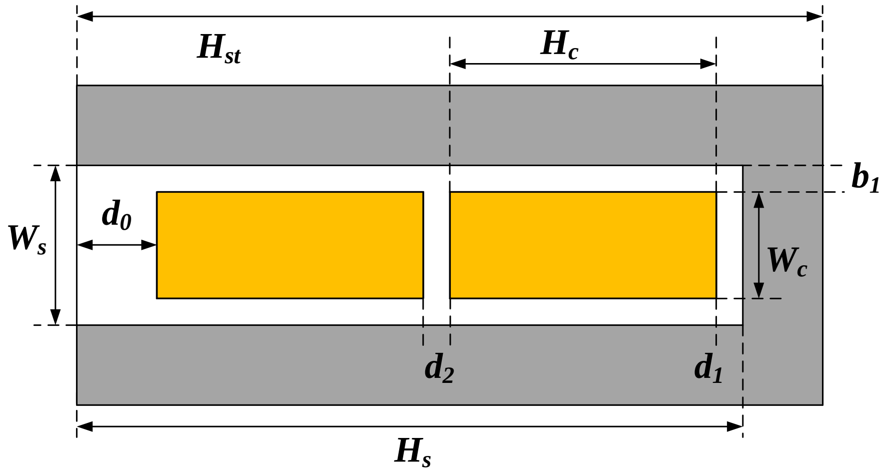

Fig. 2.2. The simplified model of a parallel slot without tooth tip.

2.3.1. Slot Width

Firstly, AC copper loss against the slot width is shown in Fig. 2.3(a). The x-axis R_w represents the ratio of slot width and the conductor width. It should be noted that only the slot width is varying, and other parameters are not changed. In addition, three horizontal conductor positions are compared in Fig. 2.3, where 'middle' represents the conductors located at the middle of the slot, 'side1' represents the conductors touch the same slot side, and 'side2' represents the conductors touch the different sides, as shown in Fig. 2.4(a) to (c) respectively. It can be seen that AC to DC ratio (AC copper loss) decreases with slot width increasing. In addition, the conductors located in the middle of the slot has the lowest AC copper loss. It should be noted that the frequency focused in this chapter is 1000Hz which is half of the maximum operating speed. The skin depth of copper at 1000Hz is about 2mm.

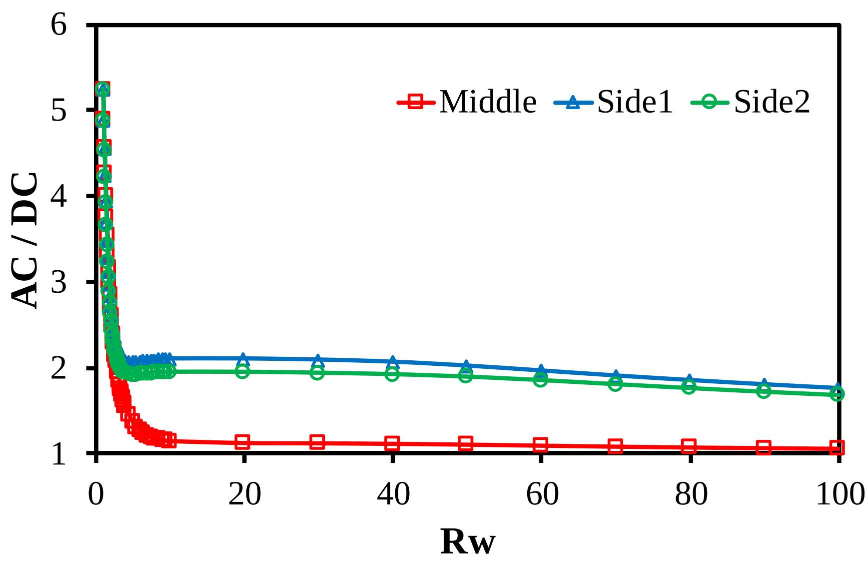

Fig. 2.3. AC copper loss against slot width with horizontal conductors at 1000Hz.

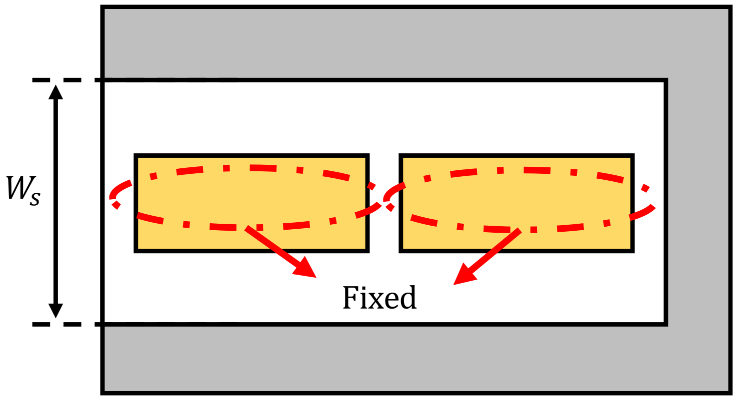

(a) Middle

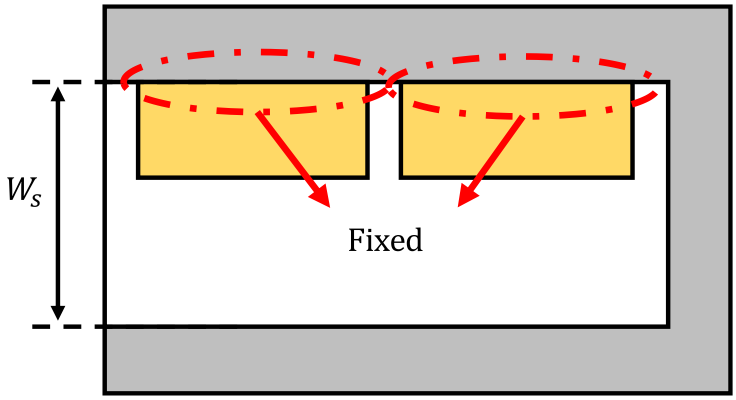

(b) Side 1

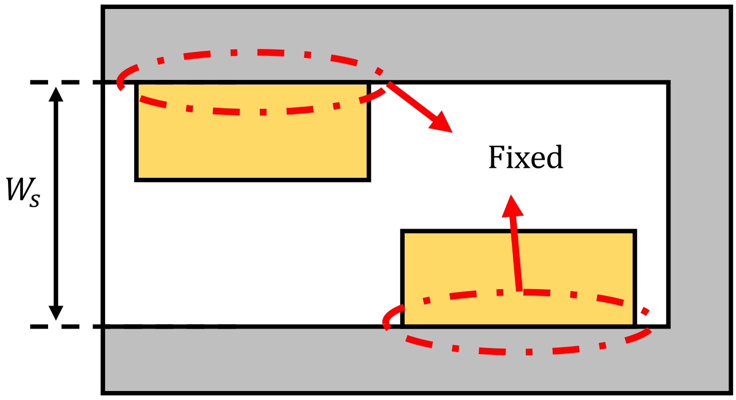

(c) Side 2

Fig. 2.4. Different positions of the conductors when varying the slot width $\boldsymbol{W_s}$.

2.3.2. Slot Depth

The second parameter to study is the slot depth. Three conductor positions are compared, at the slot opening, at the middle of the slot, and at the slot bottom, as shown in Fig. 2.6 (a) to (c) respectively. It can be seen in Fig. 2.5, when the conductors are located at the slot opening, increasing the slot depth does not help that much. For the conductors located at the middle and bottom of the slot, it has more significant effects. It should be noted that R_h represents the ratio between the slot depth and the conductor height. In addition, when the slot depth tends to infinite, the conductor located in the middle of the slot has slightly lower AC copper loss than the conductors located at slot bottom. It should be noted that the improvements by increasing slot width and slot depth are saturated around 10 times.

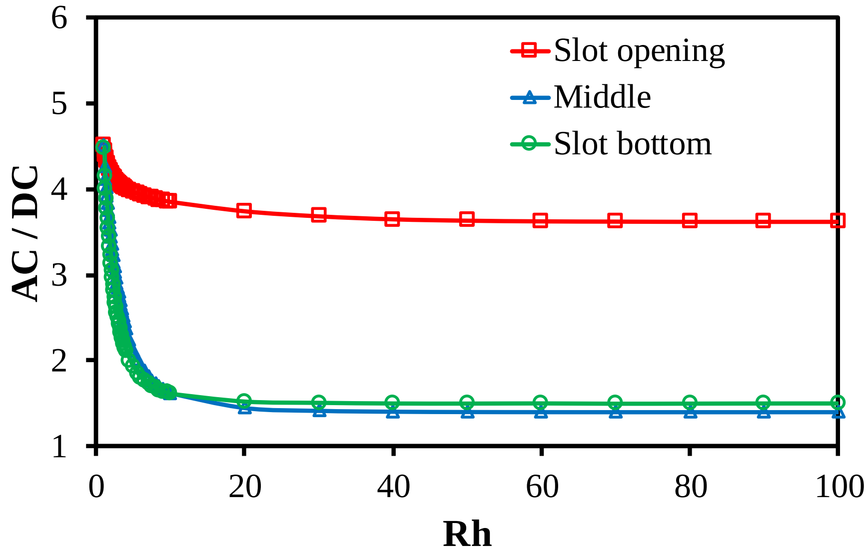

Fig. 2.5. AC copper loss against slot depth with horizontal conductors at 1000Hz.

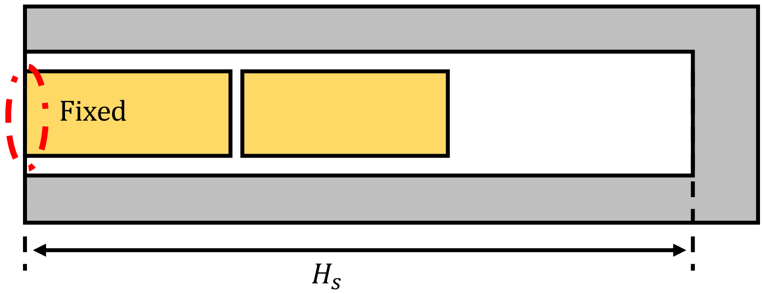

(a) Slot opening

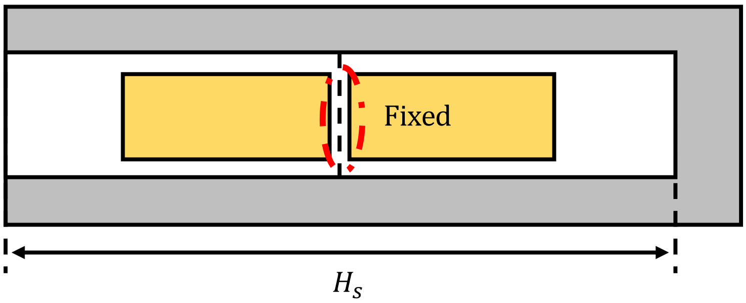

(b) Middle

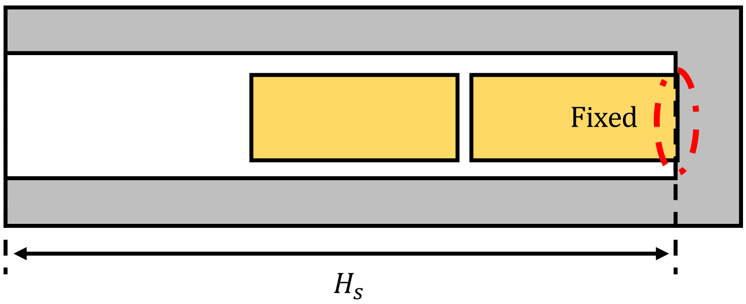

(c) Slot bottom

Fig. 2.6. Different positions of the conductors when varying the slot depth $\boldsymbol{H_s}$.

2.3.3. Slot Aspect Ratio

The above analysis shows that AC copper loss can be minimized if the slot width and slot depth are extremely large. However, this is only in theory. It is impossible to have such a large slot in a real electrical machine with a fixed outer diameter. Thus, the slot aspect ratio should be studied with a fixed slot area where the packing factor is selected as 0.7, 0.5, 0.3 and the conductor cross-section area maintains the same. It should be noted that the aspect ratio is defined as W_s/H_s. Two conductor arrangements shown in Fig. 2.7 are analyzed, and the maximum and minimum aspect ratios are limited by the packing factor and the conductor sizes. For the horizontal conductors, the aspect ratios are smaller due to the minimum slot depth should accommodate two conductor heights. While for the vertical conductors, the slot width is larger and results in a larger aspect ratio. When the conductor arrangement is in different directions, the relationship between AC copper loss and the aspect ratio is opposite as shown in Fig. 2.8, where the y-axis is in logarithmic scale with a base of 2.

The general tendency of AC copper loss for different conductor orientation can be explained by the direction of the leakage fluxes, as sketched in Fig. 2.9. When the aspect ratio is small, the vertical leakage fluxes are dominating and perpendicular to the long side of the horizontal conductors. Thus, for the horizontal conductor, AC copper loss is high at a small aspect ratio. For the same reason, the vertical conductor has high AC copper loss at a large aspect ratio.

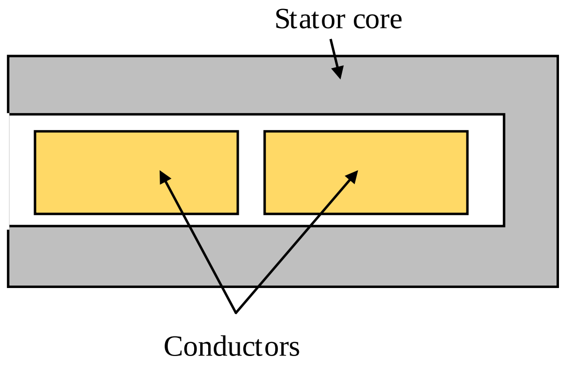

(a) Horizontal conductors (smaller aspect ratio)

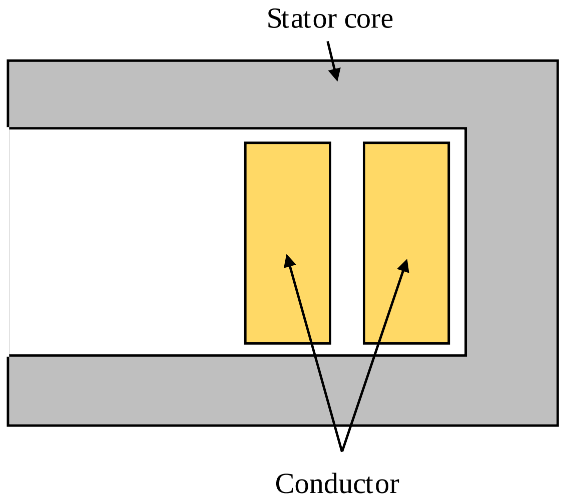

(b) Vertical conductors (larger aspect ratio)

Fig. 2.7. Orientations of conductors in the slot.

For the horizontal conductors, AC copper loss increases initially with the slot aspect ratio increasing, and after reaching the maximum point, it decreases. While for the vertical conductors, AC copper loss decreases initially, and then increases after the minimum point. The initial increase and decrease can be explained by the flux-line and current density distributions, as shown in Fig. 2.10. Since the relationship between AC copper loss and the slot aspect ratio is opposite for the conductors in different orientations, it is worth to study the conductor aspect ratio as well.

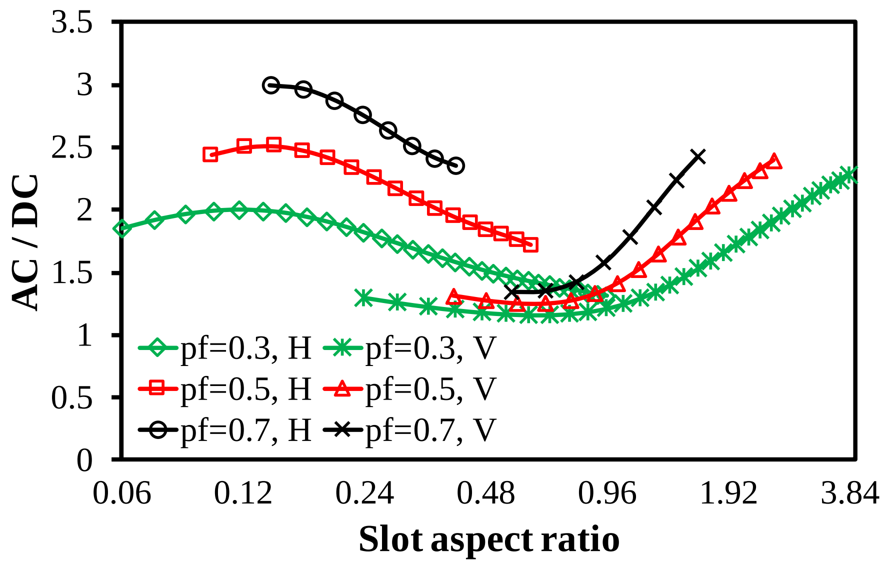

Fig. 2.8. AC copper loss against aspect ratio at 1000Hz.

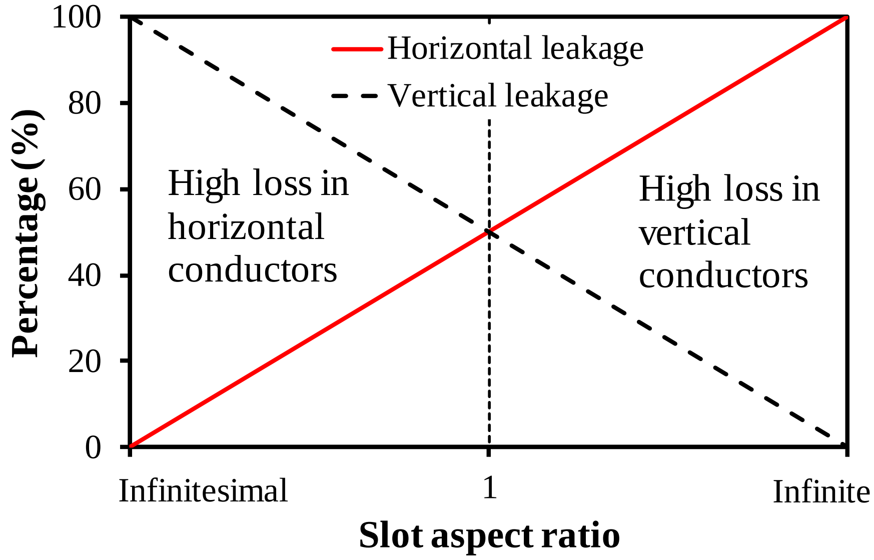

Fig. 2.9. Sketched diagram of leakage fluxes.

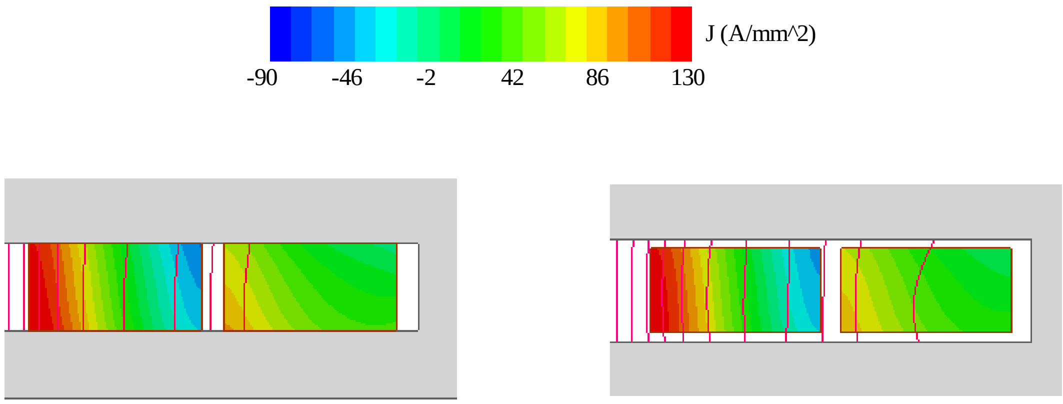

(a) Horizontal conductors,
aspect ratio=0.1

(b) Horizontal conductors,
aspect ratio=0.144

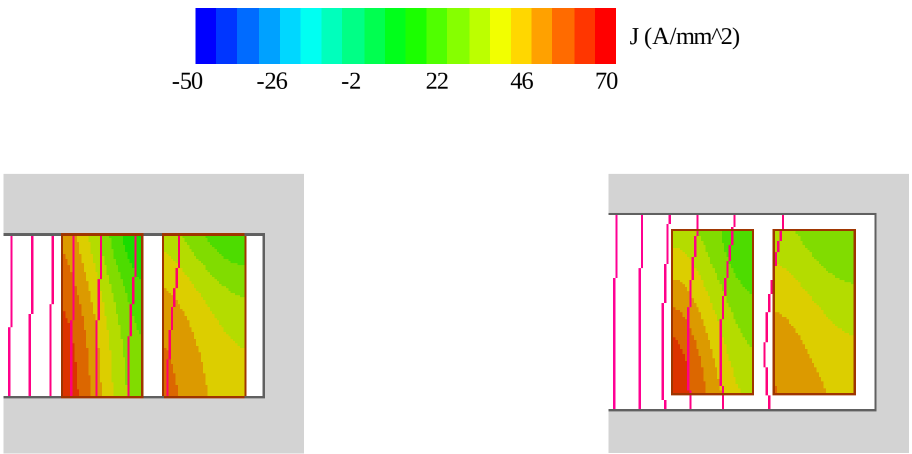

(c) Vertical conductors,
aspect ratio=0.4

(d) Vertical conductors,
aspect ratio=0.576

Fig. 2.10. Leakage flux lines and current density distributions at 1000Hz $(\boldsymbol{\omega t = \pi/2})$.

2.4. Influences of Tooth Tip and Slot Opening on AC Copper Loss

In the previous section, the linear model of a parallel slot without tooth tips has been utilized to study the influence of the slot aspect ratio on AC copper loss. However, most electrical machines employ tooth-tips with a reduced slot opening. Thus, it is worth to study the influence of tooth tips, i.e. slot opening. Fig. 2.11 shows the model of a slot with tooth-tips, where W_{so} and H_{ttp} are the slot opening width and the tooth tip height, respectively. d_0 represents the distance between the conductor and the slot opening. The full load AC copper loss varies with tooth tip height and slot opening width as summarized in Fig. 2.12. It can be seen that the lowest AC copper loss occurs when the slot opening is zero and the tooth-tip has a certain height. It can be explained that when the tooth-tip height is too thin, the lamination material is in the saturation region, the magnetic property behaviors like air. When the conductors are located in the closed slot with a thick tooth tip, the majority of the flux lines flow through the lamination materials. Thus, the introduced AC copper loss is minimized. More importantly, it can be seen that when the slot opening ratio is larger than 0.2, AC copper loss does not vary greatly with both tooth-tip height and slot opening width. It should be noted the slot opening ratio in Fig. 2.12 is defined as the slot opening width (W_{so}) divided by slot width (W_s).

In addition, when the input current is zero, AC copper loss induced by PM only is presented in Fig. 2.13. It can be seen that when the maximum AC copper loss generated by PM occurs at large slot opening width and thin tooth-tip. While it becomes flat when the slot opening ratio is smaller than 0.5. However, this loss is usually relatively small and negligible comparing with rated DC copper loss in low voltage high current system. For example, the rated current of the baseline machine is 230Arms and DC copper loss is around 900W. Thus, it can be concluded that AC copper loss can be minimized by closing the slot with a certain thickness, while the flux leakages between teeth will reduce the output torque. In the most electrical machines with tooth-tips, the smaller slot opening the lower AC copper loss. However, the limitation usually depends on the material property and manufacturing process.

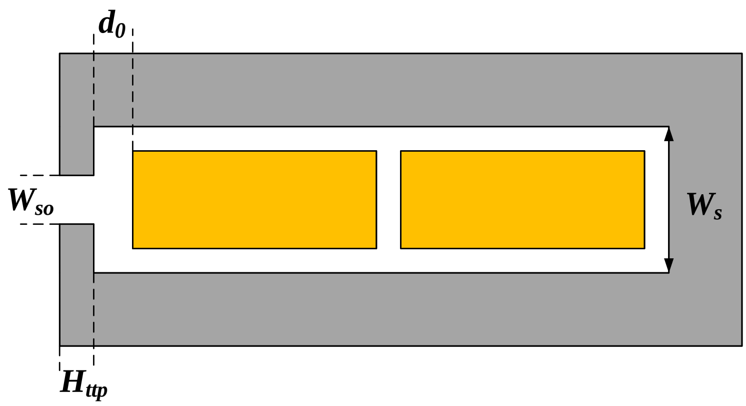

Fig. 2.11. The simplified model of a parallel slot with tooth-tips**.**

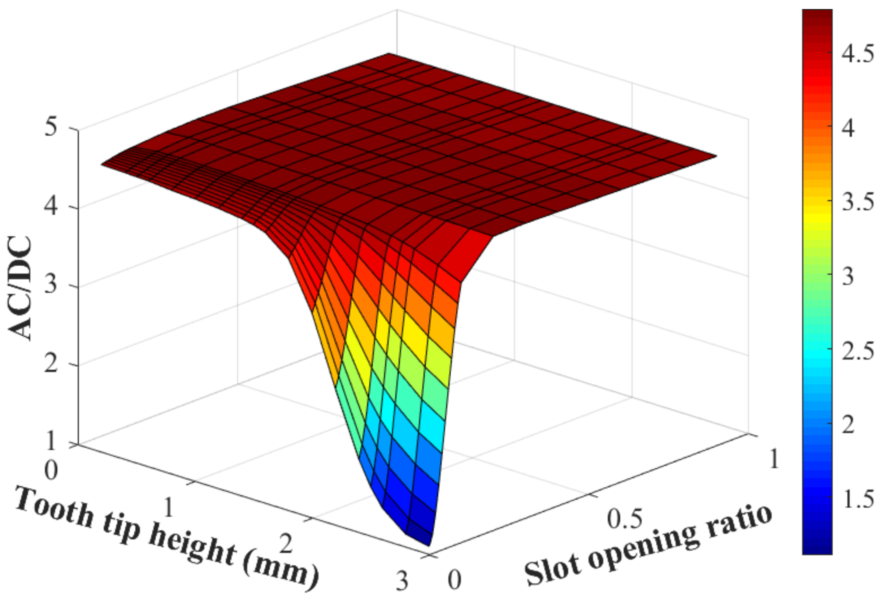

Fig. 2.12. AC loss to DC loss ratio against tooth-tip height and slot opening ratio at 1000Hz.

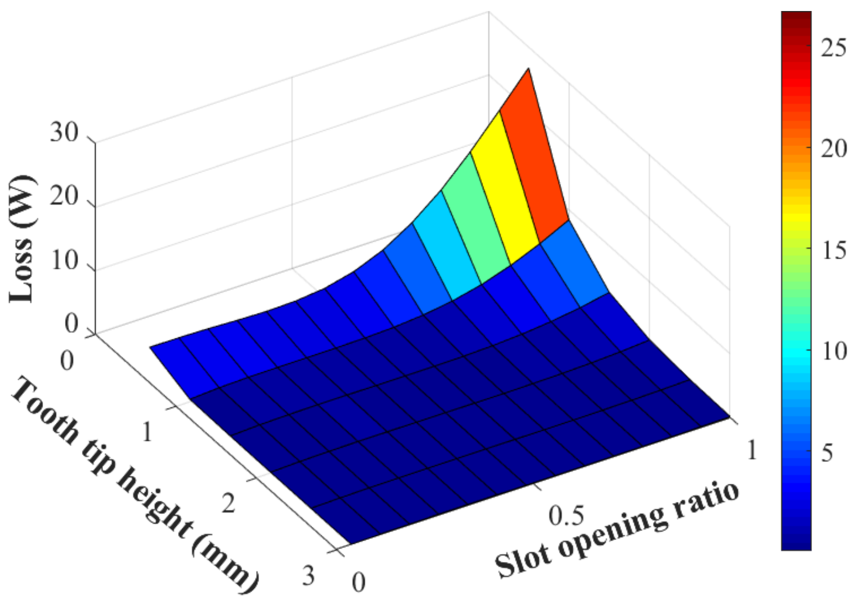

Fig. 2.13. AC loss against tooth-tip height and slot opening ratio at 1000Hz (PM only).

2.5. Influence of Conductor Aspect Ratio on AC Copper Loss

In the previous section, the influences of tooth-tips and slot opening are studied. In order to eliminate these influences, the focus of the investigation will be on the conductor aspect ratio in this section. The conductors are located in the slot with fixed tooth-tip height and slot opening width.

In section III, it has been shown that when the conductors are located in the slot without tooth tips, AC copper losses are different when the conductors are in different orientations. The different orientation of the conductor can also be regarded as the reciprocal aspect ratio value of the conductor. Generally, when the aspect ratios of the conductor are reciprocal, the conductors are identical if their surround boundaries are uniform, i.e. surrounded by uniform material. As can be seen in Fig. 2.14, if there is only one conductor in the air, AC to DC copper loss ratios are identical for the conductors with reciprocal aspect ratio, i.e. A and B with aspect ratios 0.4 and 2.5 respectively. It can be seen that when the conductor C has the aspect ratio equal to 1, AC copper loss is the highest. However, for the conductors located in the slot with semi-open slot opening, the previous phenomenon disappeared due to non-uniform material around the conductor. The copper loss densities and the flux lines for each case are shown in Fig. 2.15. It can be seen that the flux lines are closed inside the conductors in Figs. 2.15(a)-(c), while the flux lines flow through the conductor in Figs. 2.15(d)-(f). It should be noted that the slot-opening and the isolation thickness between the conductor and the slot remain unchanged.

For the square conductor in the air (aspect ratio = 1), more flux lines are enclosed inside the conductor comparing with rectangular conductors (aspect ratio $\neq$ 1). Although there are two high loss density regions in the rectangular conductor, the square conductor has more area generating losses, as shown in Figs. 2.15(a)-(c). In Fig. 2.15(e), the conductor is only affected by the flux at the slot opening region, the flux lines do not across the whole conductor. Thus, this case has the lowest AC copper loss.

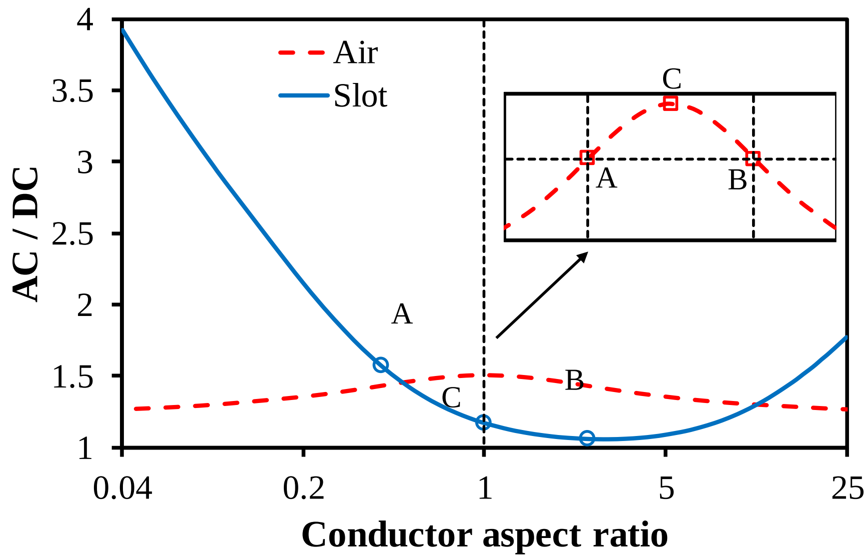

Fig. 2.14. AC copper loss against the conductor aspect ratio at 1000Hz.

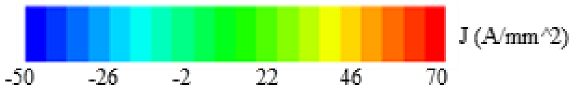

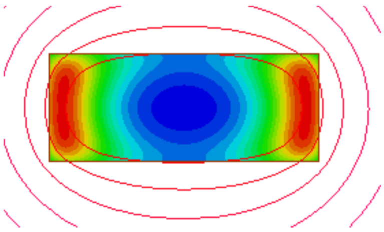

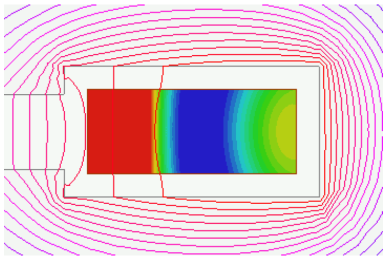

(a) Conductor A in the air

(d) Conductor A in the slot

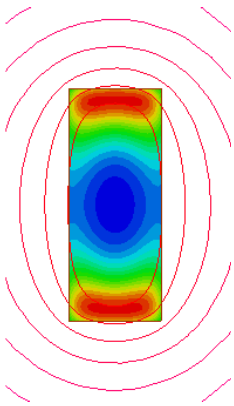

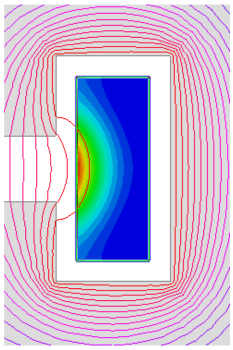

(b) Conductor B in the air

(e) Conductor B in the slot

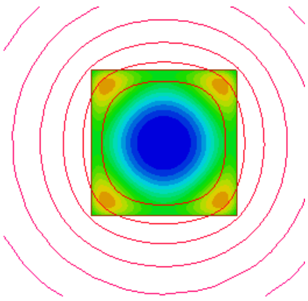

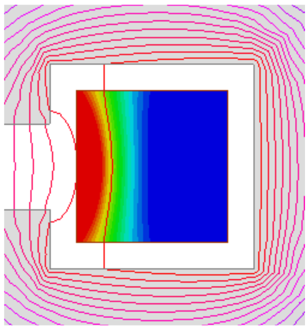

(c) Conductor C in the air

(f) Conductor C in the slot

Fig. 2.15. Leakage flux lines and loss density distributions ($\boldsymbol{\omega t = \pi/2}$).

The above analysis agrees with the conclusion in [Mel06] to a certain extent. However, for machines with a large number of slots, it is hard to achieve the high aspect ratio of the conductor due to space limitation, i.e. Fig.2.15(e). In the previous analysis, AC copper loss can be reduced by increasing the gap thickness (b_1) between the conductor and the stator teeth or increasing the conductor aspect ratio. A higher aspect ratio of the conductor represents wider conductor width (W_c). Including with the gap thickness (b_1), they share the limited space with the tooth width. Thus, it is worth showing which one is more beneficial to AC copper loss reduction in a real machine. It should be noted that the y-axis in Fig. 2.16 is the tooth width to the slot width ratio. It has the smallest limitation value of 0, which means the tooth width is completely removed. In addition, it also has the largest limitation value which represents the slot width equal to the conductor width. The black dashed line in Fig. 2.16 represents the modified slot width only, the conductor shape remains unchanged. The red solid line represents that the conductor width also varies with the slot width by keeping the same gap thickness, and the conductor height decreases to maintain the same area. It can be seen that when the conductor shape and the slot shape vary together, AC copper loss reduces significantly. It can be explained by two combined beneficial features of conductor shape and slot shape. In Fig. 2.15(b), two features are speared and show the improvement of AC copper loss reduction. It is easy to see that the influence of conductor shape is dominated. More importantly, the highest improvement on AC copper loss reduction occurs at a low tooth-slot width ratio. The output torque will be affected since the magnetic flux path is changed.

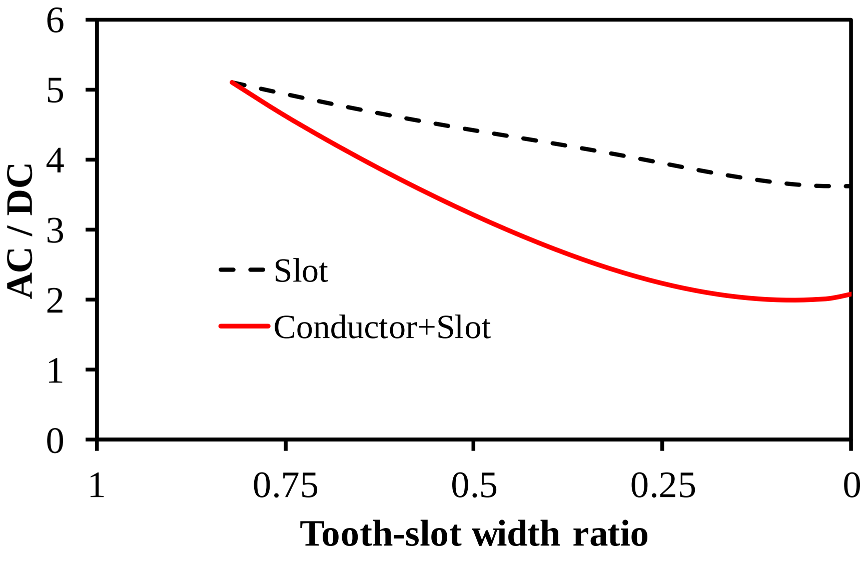

(a) AC to DC copper loss ratio

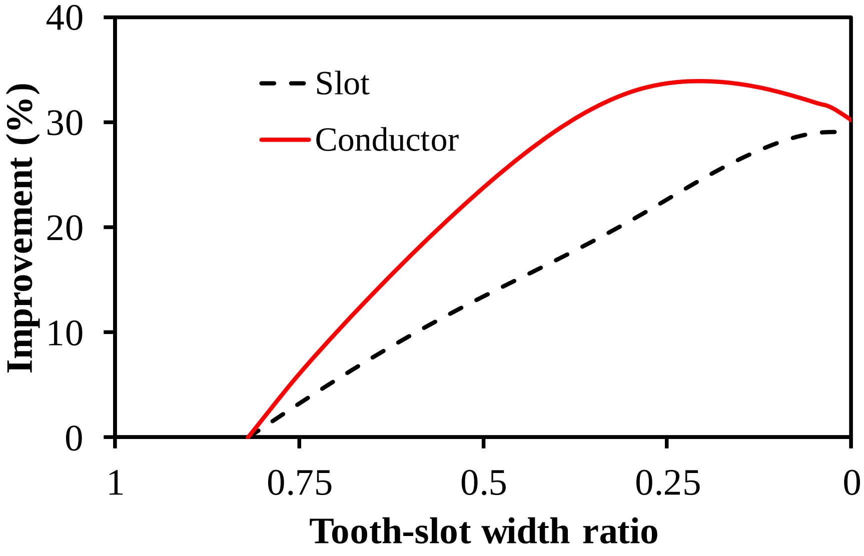

(b) Improvement on AC copper loss reduction

Fig. 2.16. Influences of slot and conductor shapes on AC copper loss.

2.6. Influence of Slot Aspect Ratio on Torque-Speed Characteristic of Electrical Machines

In the previous analysis, it can be seen that AC copper loss decreases with lower packing factor generally. However, as mentioned previously, one of the purposes to use rectangular conductors is to realize a high packing factor and high thermal dissipation capability. In addition, the size of the slot will be limited by other dimensions, such as tooth width and back-iron thickness in normal electrical machines. These parameters are related with the paths of the magnetic fluxes, and affect the output torques. Thus, it is important to calculate the torque-speed curves for different slot aspect ratio and conductor aspect ratio combinations. By way of example, the torque/power-speed characteristics of the baseline machine with/without considering AC copper loss are shown in Fig. 2.1. It clearly shows the significant influence of AC loss on the power capability of the machine, particularly at high speed. It should be noted that the cross-sectional area of the conductor maintains the same to ensure the same current density and the same DC copper loss. Since it has been shown that the conductor shape influences more on AC copper loss than the slot shape. The conductor shape is focused in this case, and the slot shape is dependent on the conductor shape to accommodate the conductors.

Three typical models of slot and conductor shapes are summarized in Fig. 2.17 based on the baseline machine. Fig. 2.17(a) shows the slot and conductor shapes of the baseline machine. Fig. 2.17(b) shows the slot shape with a wider and shorter conductor and the tooth-tip always remains the same with the baseline machine. Fig. 2.17(c) shows the machine with the same conductor in Fig. 2.17(b), while the tooth-tip height varies to keep close to the conductors. The objective of the variable tooth-tip is to achieve the widest critical tooth width. The torque-speed and power-speed characteristics are shown in Fig. 2.18. It should be noted that the conductor aspect ratio of the baseline machine is 0.4.

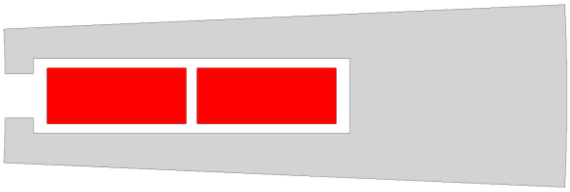

(a) Baseline

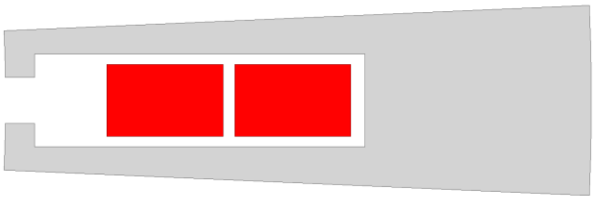

(b) Fixed tooth-tip

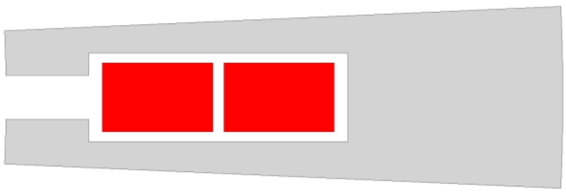

(c) Variable tooth-tip

Fig. 2.17. Different models of slot and conductor shapes.

It can be seen that the baseline machine has the highest torque at low speed in Fig. 2.18(a) since the machine has the widest tooth width. However, due to its high AC resistance, the low-speed torque is limited by the voltage. It is more clear to see the power-speed curves, the output power of the baseline machines drops to 80% of the maximum power at 10000rpm and 50% at 20000rpm. By employing the wider and shorter conductors, the high-speed performance is improved significantly. The output powers at 20000rpm are above 70% of the maximum output power for both two cases. It is mainly due to the low AC copper loss, as shown in Fig. 2.18(c). In addition, the high-speed performance of the machine with a fixed tooth-tip is better than the machine with variable tooth-tip. It can be seen that the machine with a fixed tooth-tip and a wider conductor has the largest operation area enclosed by the power-speed envelope. However, the maximum torque of the fixed tooth-tip in the constant torque region is slightly lower than the variable tooth-tip. It is due to that the tooth width is slightly wider in the machine with variable tooth-tip. However, since the objective is to gain more torque and less loss at high-speed operation, the peak torque at low speed could be sacrificed slightly. Fig. 2.19 shows the reduction of the low-speed torque against the conductor shapes. Since it is unacceptable to see the maximum torque drops greatly, the 90% point is chosen as an example. Thus, two typical efficiency maps of the baseline machine and the machine with a wider conductor and a fixed tooth-tip are compared in Fig. 2.20. It can be seen that the high-efficiency area is expanded when a different conductor is employed. The possible highest efficiency is about 65% in the baseline machine at 10000rpm. In the modified machine, the possible highest efficiency is 75% at the same operation speed. However, it must be noted that the maximum torque is reduced about 10% to improve the high-speed performance and keep the same dc resistance.

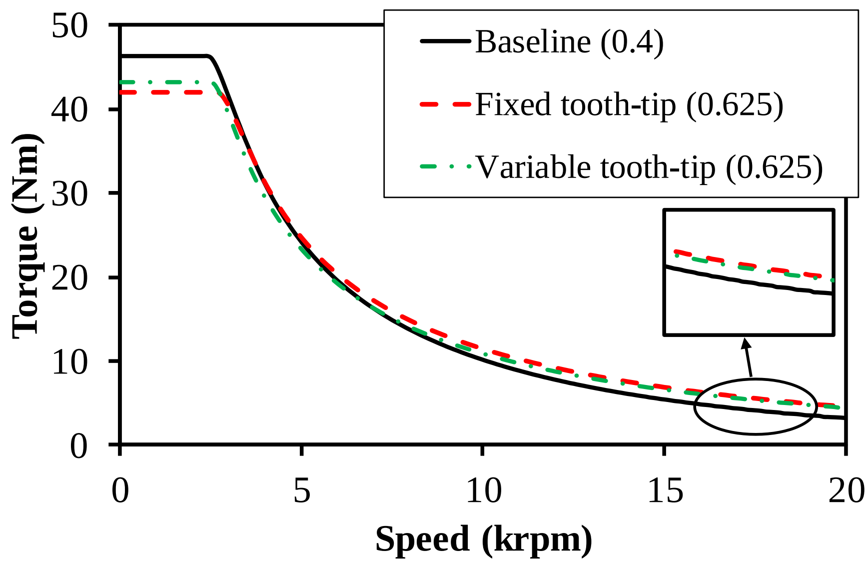

(a) Torque

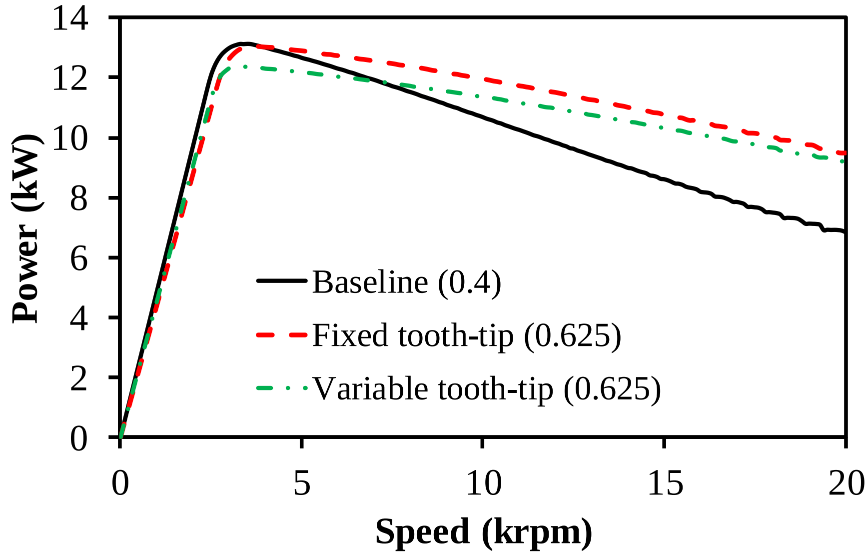

(b) Power

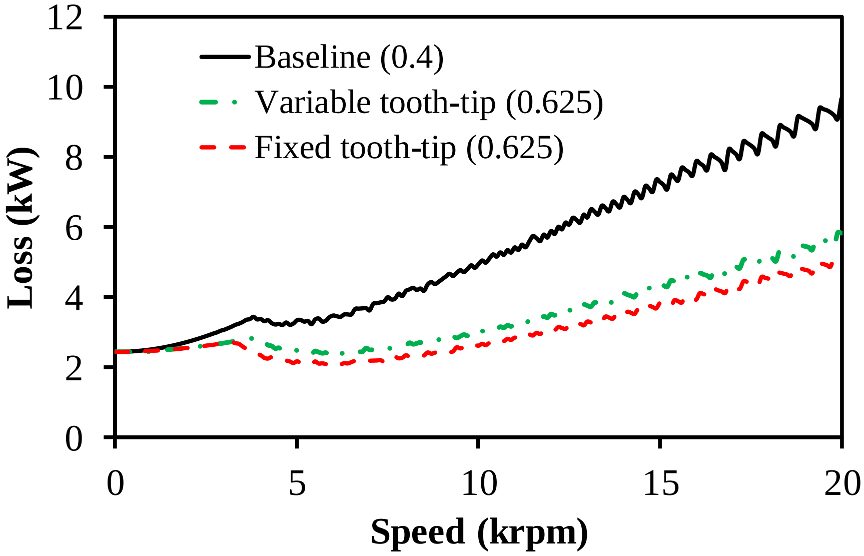

(c) Copper loss

Fig. 2.18. Torque/power-speed characteristics and AC copper losses.

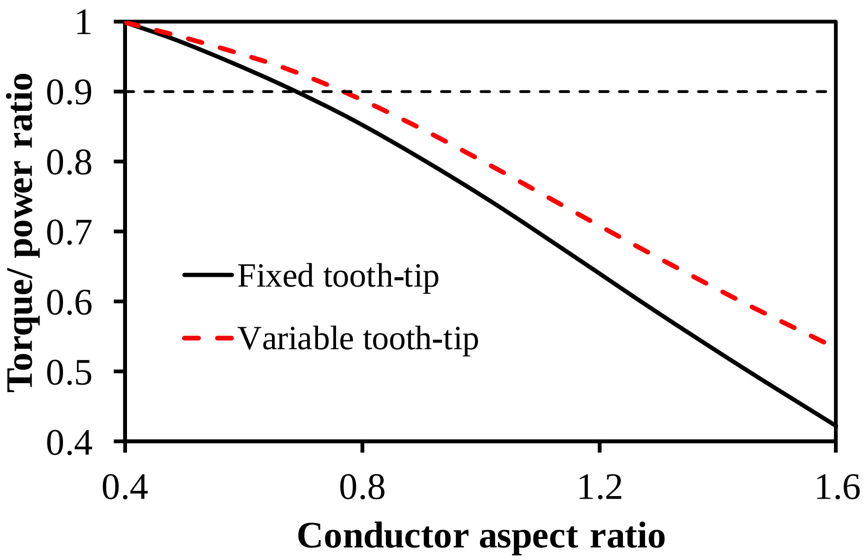

Fig. 2.19. Low-speed torque vs. conductor aspect ratio.

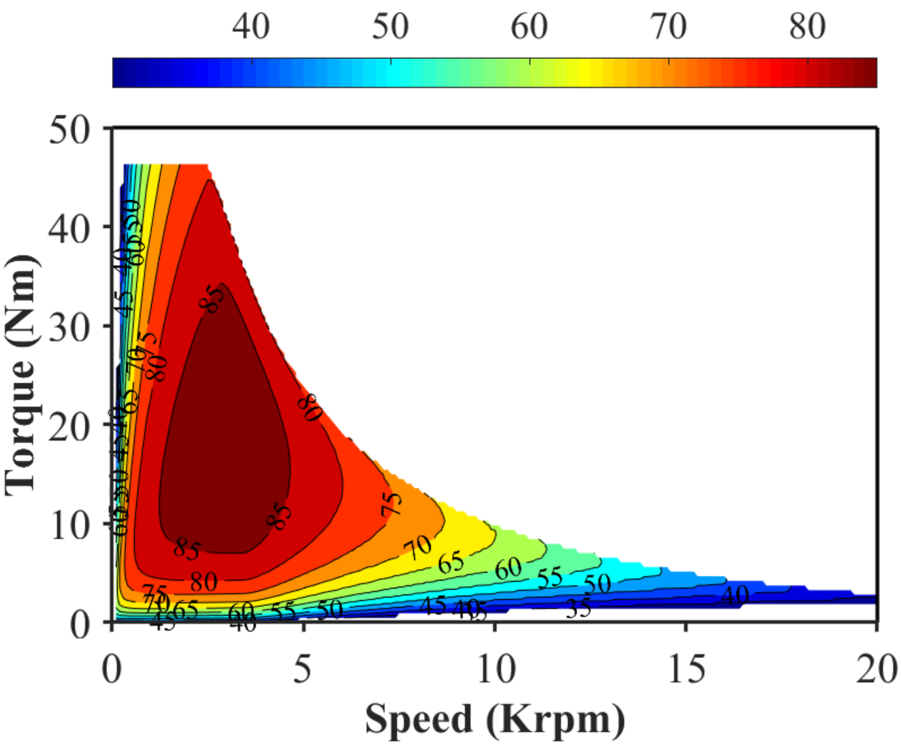

(a) Baseline

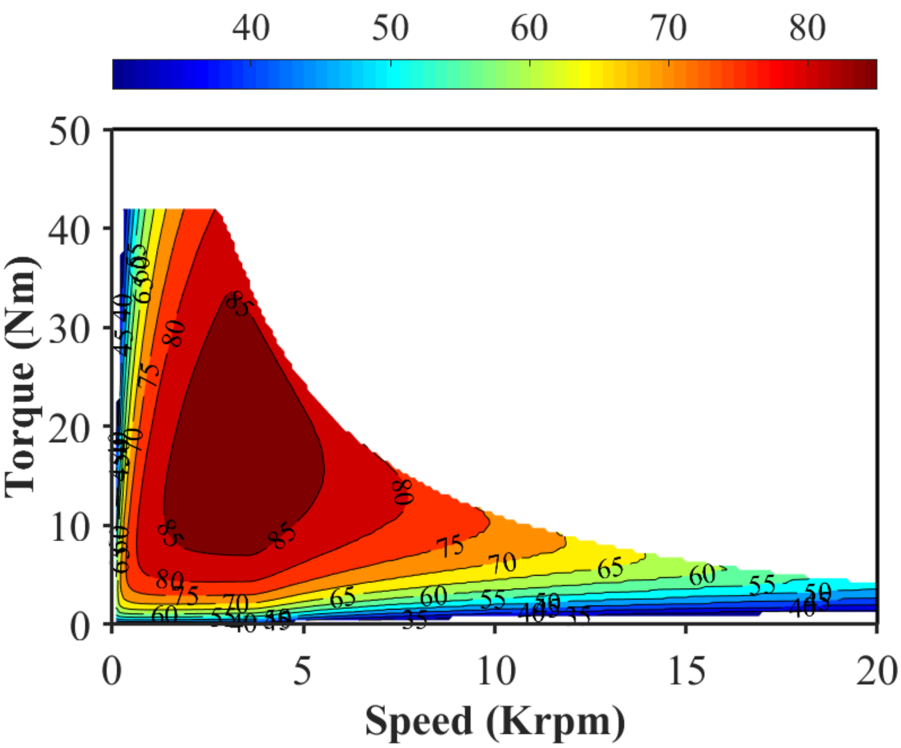

(b) Fixed tooth-tip with wider conductor

Fig. 2.20. Efficiency maps.

2.7. Conclusion

In this chapter, the influences of design parameters of the slot and conductors on AC copper loss and torque-speed characteristics of hair-pin windings are studied. It is shown that the relative ratios between the slot size and the conductor size impact AC copper loss strongly. In addition, the positions of the conductor determine the maximum improvement of width ratio and height ratio between slot and conductor. When the slot width and slot depth are considered together as the aspect ratio, it is shown that the tendency of AC copper loss is opposite between different orientations of conductors in the slot. This is related with the dominating leakage flux in horizontal and vertical directions. The overall AC copper loss decreases with a lower packing factor. However, the lower packing factor results in lower thermal dissipation capability. Besides, it shows that the conductor aspect ratio also has dominated AC copper loss. Furthermore, due to the space limitation in the electrical machine with a fixed outer diameter, more space for the slot means that less space lamination materials such as stator teeth. The lamination material determines the flux paths and the output torque. Thus, it is necessary to calculate the torque/power-speed characteristics and the corresponding temperatures for different design parameters. It has been shown that by varying the conductor shape and keeping the conductor cross-sectional area, the low-speed torque decreases due to the thinner stator tooth. However, the machine performance at high-speed improves significantly, especially maximum output power and efficiency. It is worth noting that for the machine with a large number of conductors, there will be some difference. However, the overall tendencies are similar.

CHAPTER 3

Influence of Design Parameters of Hollow Conductors on AC Copper Loss and Thermal Dissipation Capability in Permanent Magnet Synchronous Machines

In this chapter, the influences of design parameters of hollow conductors on AC copper loss and thermal dissipation capability in permanent magnet synchronous machines are studied by the finite element method. It has been shown that it is better to locate the coolant channel in the conductor towards the bottom of the slot, both in cases of single conductor and two conductors. In addition, it has been shown that the transposition in conventional hair-pin winding may cause additional loss. Furthermore, the influences of coolant channel shapes on the thermal dissipation capability and the AC copper loss are discussed. It has been shown that for the temperature rise the thermal dissipation capability is more dominant than the AC copper loss in different kinds of conductors. More importantly, it has been shown that by considering the flow rate as a variable, the better overall performance can be obtained.

3.1. Introduction

In conventional electrical machines with liquid cooling, the water jacket is located in the housing and removes the heat from the stator core to the ambient [Kra08]. However, the majority of heat is generated in the slot, especially for the rectangular conductors with high AC copper loss [Bar18]. Thus, this part of heat has to flow through several components before dissipating to coolant [Sug70]. These components including wire insulation, impregnation, slot liner, and interface gap between the stator and the housing, which have poor thermal conductivities. The direct cooling system of an electrical machine with hollow conductors has been proposed in [Che19] and [Tan15]. In this cooling system, the dissipating path of the heat generated in the slot is shorter. The author in [Che19] presented a complete thermal network of the hollow conductor. The authors in [Sta06] summarized several useful expressions of round ducts and rectangular ducts, including laminar flow and turbulent flow.

In this chapter, both the AC copper loss and the thermal dissipation capability of hollow conductors are discussed. The relative positions between the coolant channel, the conductor, and the slot are studied firstly. It will be shown that the lowest AC copper loss occurs when the conductor is located at the slot bottom and the coolant channel is located at the conductor towards the bottom of the slot. In the conventional hair-pin winding, there is a transposition at the end-winding. This transposition will influence the AC copper loss when the hollow conductor is employed. It will be shown that the minimum AC copper loss occurs when there is no transposition. Furthermore, the influences of the coolant channel shape on AC copper loss and the thermal dissipation capability are analyzed by the finite element method. It will be shown that the minimum AC copper loss occurs when the conductor is the shortest. However, this kind of conductor has poor thermal dissipation capability since the coolant channel area is usually small. More importantly, the coolant flow rate is usually set as constant in literature. It will be shown that the flow rate can be considered as a variable with a limitation so that it can obtain better overall performance with a lower flow rate.

3.2. Influence of Conductor Relative Positions on AC Copper Loss

The model of a single hollow conductor located in a fixed parallel slot without slot tips is shown in Fig. 3.1, with the stator height H_{st}, the slot depth H_s, and the slot width W_s being fixed. d_1 and b_1 represent the slot liner and other insulation material at the slot bottom and slot side, respectively. Thus, the maximum size of the conductor width W_c is limited. H_c is the height of the conductor, H_j is the height of the coolant channel, d_0 represents the distance between the conductor and the slot opening, and d_c represents the relative position between the coolant channel and the conductor. It is well known that the AC copper loss can be minimized by adjusting the conductor location close to the slot bottom, e.g. moving the conductor in Fig. 3.2(a) to Fig. 3.2(c). When the hollow conductors are employed, the location of the coolant channel should also be considered. By introducing two variables, R_1 and R_2, which represent the position of the conductor and the water channel, are defined in (3.1) and (3.2).

It should be noted that in this section the dimensions of the conductor are set as constants, i.e. H_c=5mm, W_c=2mm, H_j=2mm, W_j=1.6mm. Fig.3(a) shows the 3-D plot of AC to DC copper loss ratio against R_1 and R_2. It can be seen that the minimum AC to DC copper loss ratio occurs when R_1 and R_2 approach to 1, e.g. Fig. 3.2(d).

To study the influence of R_1 on AC copper loss, two normal solid conductors are introduced as references in Fig. 3.3(b). NC1 represents the conductor with the same outer dimensions of the hollow conductor (5mm×2mm), while NC2 has the same conducting area (3.4mm×2mm). It can be seen that the conductor NC1 has the highest AC to DC copper loss ratio, since it has a larger conducting area and results in heavy skin effect. It is easy to know that NC2 has the lowest AC to DC copper loss ratio since it is shorter than other conductors. In addition, when R_1 approaches 0.2, the AC to DC copper loss ratio becomes stable, as shown in Fig. 3.3(b). It can be explained that as the conductor moves away from the slot-opening region, the flux lines across the conductors are more vertically, as shown in Fig. 3.4. Thus, for the objective of minimization of the AC copper loss, it is not necessary to locate the conductor at the slot bottom, including the normal conductors. As the coolant channel moving from towards slot opening (Fig. 3.2a) to towards slot bottom (Fig. 3.2c), the AC to DC copper loss ratio increases firstly. After reaching a maximum point, around R_2=0.2, it decreases. In addition, the AC to DC copper loss ratio of the hollow conductor R_2=1 is similar to NC2. This can also be explained by current density distributions, as shown in Fig. 3.4. It should be noted that both R_1 and R_2 cannot be selected as 1. The available deepest position of the conductor should keep the space of the slot liner d_1. It should be noted that if R_2=1, the coolant channel will be open, as shown in Fig. 3.4(c) and Fig. 3.4(d). Thus, the available value of R_2 should consider the critical thickness of the copper wall.

$$R_1 = \frac{d_0}{H_s - H_c} \tag{3.1}$$

$$R_2 = \frac{d_c}{H_c - H_j} \tag{3.2}$$

where d_0 is the distance between the conductor and the slot opening, d_c is the distance between the conductor and the hollow region, H_s is the height of the slot, H_c is the height of the conductor and H_j is the height of the hollow region.

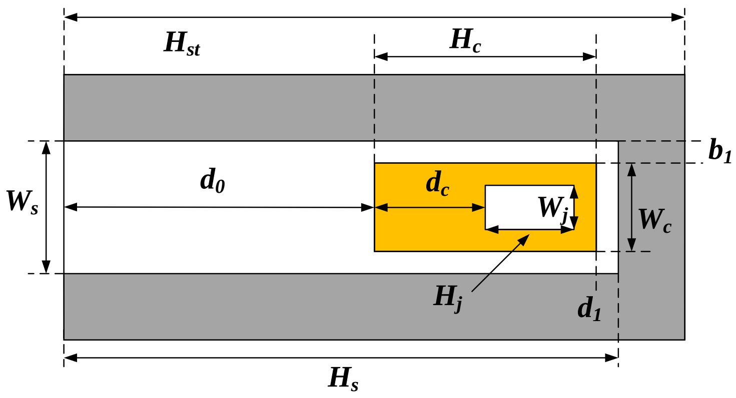

Fig. 3.1. Model of hollow conductor located in the parallel slot without slot tips.

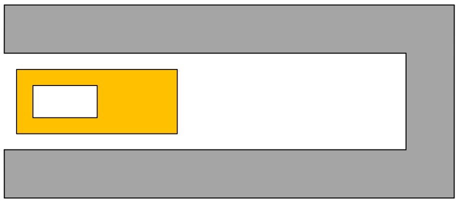

(a) Hollow conductor located at slot opening with coolant channel towards slot opening (Cond1)

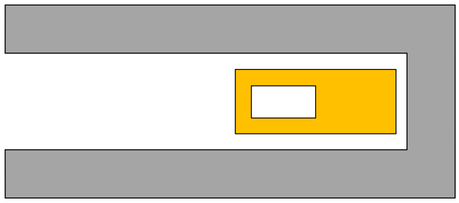

(b) Hollow conductor located at slot bottom with coolant channel towards slot opening (Cond2)

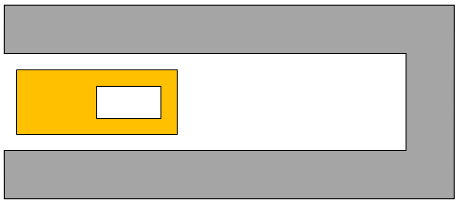

(c) Hollow conductor located at slot bottom with coolant channel towards slot bottom (Cond3)

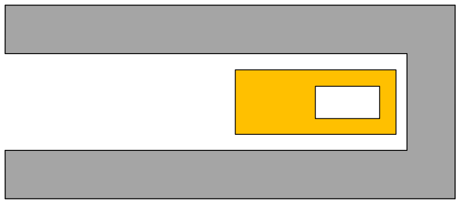

(d) Hollow conductor located at slot bottom with coolant channel towards slot bottom (Cond4)

Fig. 3.2. Different configurations of hollow conductors located in the slot.

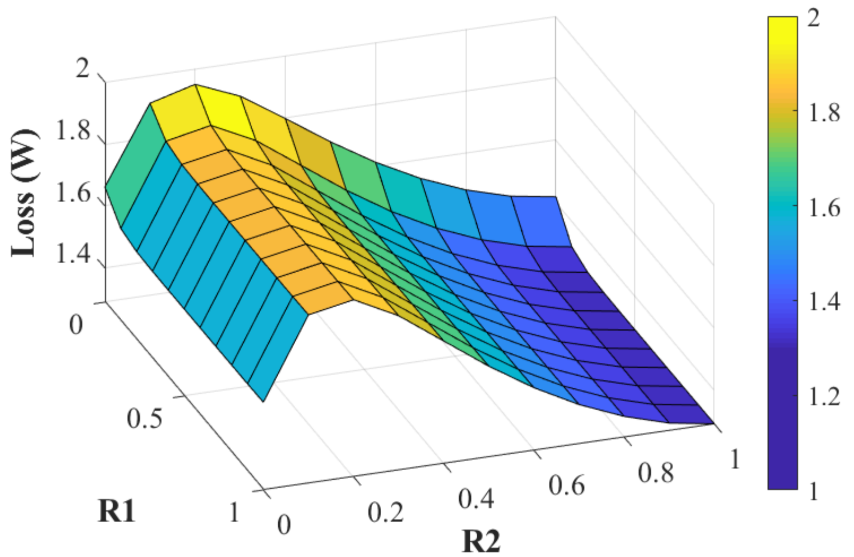

(a) AC to DC copper loss ratio against R_1 and R_2

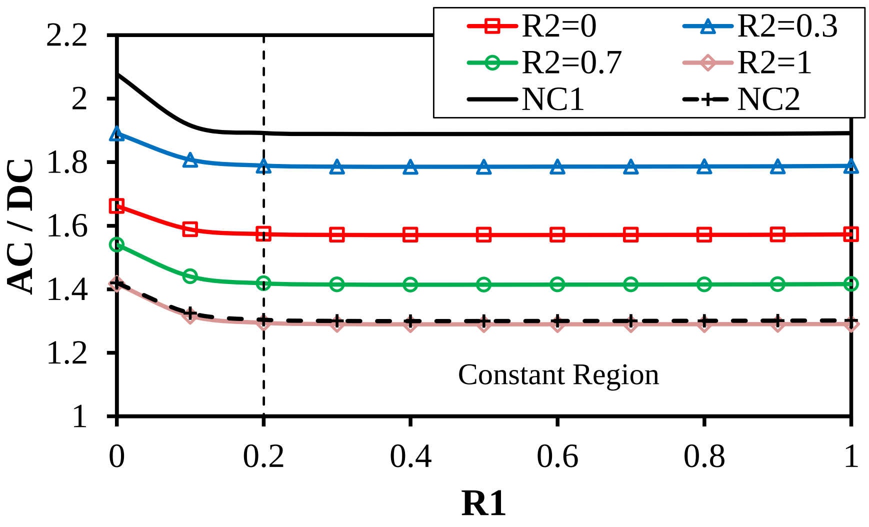

(b) AC to DC copper loss ratio against R_1

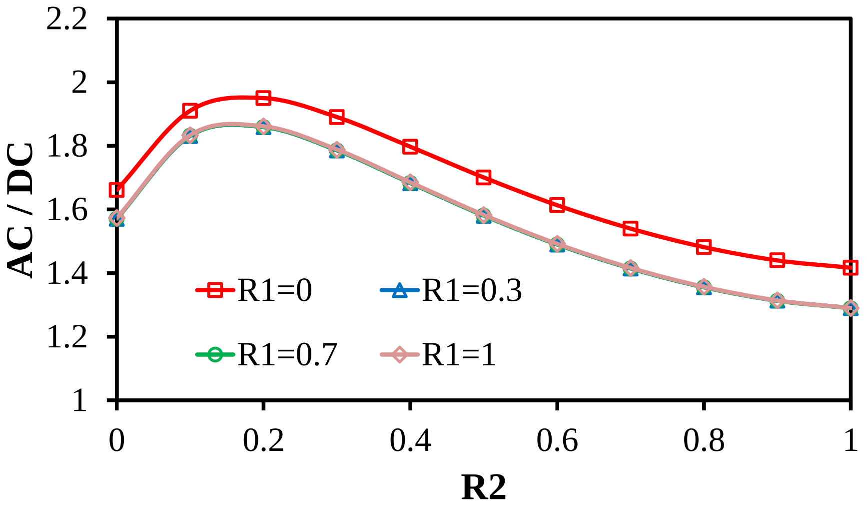

(c) AC to DC copper loss ratio against R_2

Fig. 3.3. Influence of relative positions between conductor, hollow region, and slot on AC to DC copper loss ratios at 1000Hz.

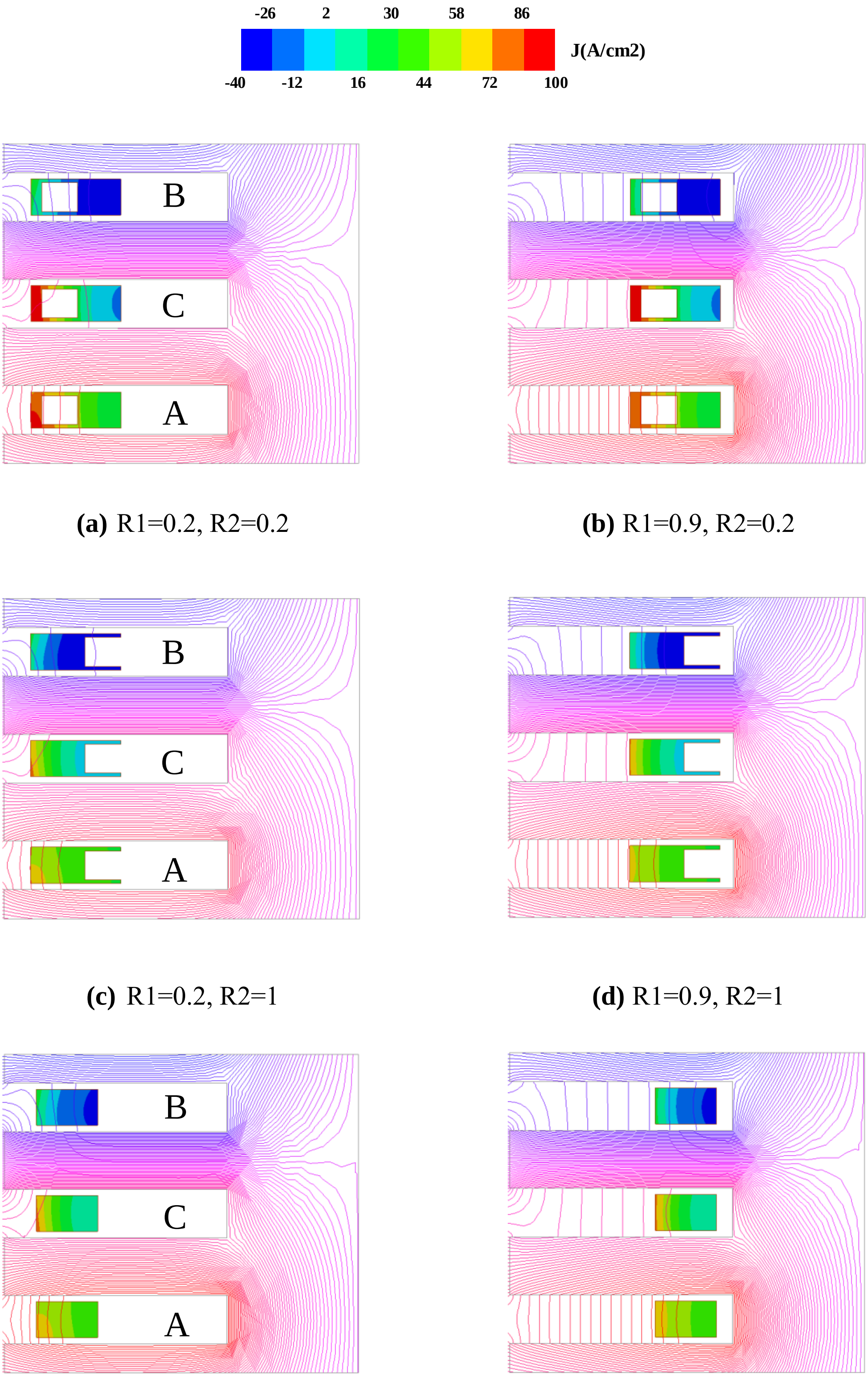

(a) R1=0.2, R2=0.2 **(b)** R1=0.9, R2=0.2

(c) R1=0.2, R2=1 **(d)** R1=0.9, R2=1

(e) NC2 0.2 **(f)** NC2 0.9

Fig. 3.4. Current density and flux lines of different conductors in slot at 1000Hz ($\boldsymbol{\omega t = \pi/2}$).

3.3. Influence of Conductor Arrangement on AC Copper Loss

In the conventional hair-pin winding, usually there is more than one conductor in one slot, and exists a transposition at the ending end-winding region as shown in Fig. 3.5. The side A close to the slot bottom becomes the side A’ close to the slot opening after the transposition. For the conventional solid conductor and symmetrical hollow conductor, AC copper loss is the same with and without the transposition. However, when the conductor is asymmetric, with and without the transposition will be different in the generated AC copper loss. The models of two conductors located in the slot with and without transposition are shown in Fig. 3.6.

In the previous analysis, it has been shown that the minimum AC copper loss occurs when the hollow region of the conductor is located towards the bottom of the slot no matter whether the conductor is at the slot opening or the slot bottom, as shown in Fig. 3.2(c) and Fig. 3.2(d). However, the analysis is given for a single conductor in the slot. It is worth analyzing the AC copper loss generated by each individual conductor when there is more than one conductor in the slot, as shown in Fig. 3.6 and Fig. 3.7(a). It is easy to see that Cond 1 (Fig. 3.2a) and Cond 3 (Fig. 3.2c) have higher AC copper loss. This is due to the fact that these two conductors are located close to the slot opening region as grouped as Group 1 in Fig. 3.7(a). In addition, there is less active conducting material towards the slot opening in Cond1. The skin effect near the slot opening part in Cond1 is more severe than that in Cond3 and thus Cond1 generates more AC copper loss. For the same reason, the AC copper loss generated by Cond2 (Fig. 3.2b) is higher than that of Cond4 (Fig.3. 2d), although these two conductors are located at the slot bottom (Group 2). Fig. 3.7(b) shows the total AC to DC copper loss ratio generated by different winding layouts shown in Fig. 3.6. The winding layout with the lowest AC copper loss is Cond3 in series with Cond4. These two conductors both generate the lowest AC copper loss in each group. It can be seen that the locations of the hollow region in these two conductors are the same. Thus, the minimum AC copper loss requires each conductor to generate the lowest AC copper loss and it is usually without the transposition at the end-winding. However, if the conductors are arranged in the wrong orientation, it could generate the highest AC copper loss when there is no transposition, e.g. Cond1+Cond2 in Fig. 3.7(b).

It should be noted that the AC to DC copper loss ratio in Fig. 3.7(a) is much higher than in Fig. 3.7(b). It is because that the total AC to DC copper loss ratio can be regarded as the average of two series conductors.

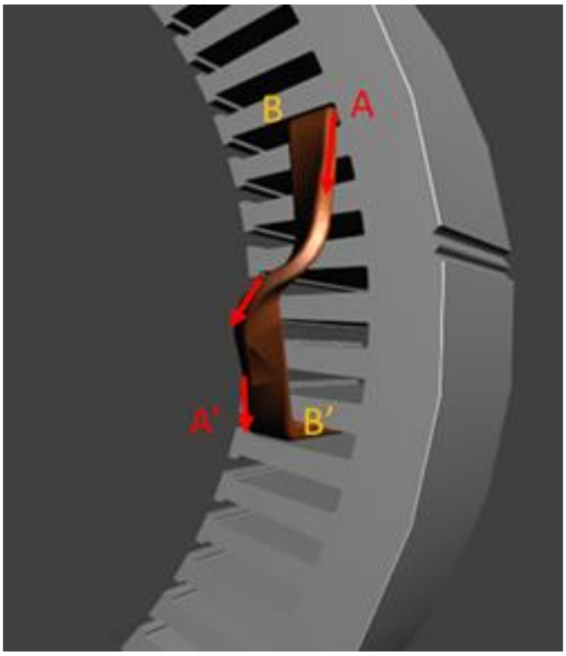

Fig. 3.5. Model of conventional hair-pin winding with transposition at end-winding.

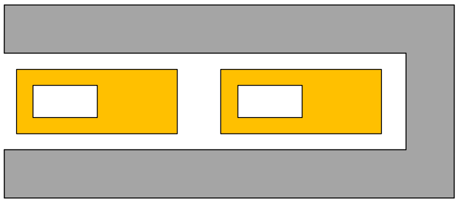

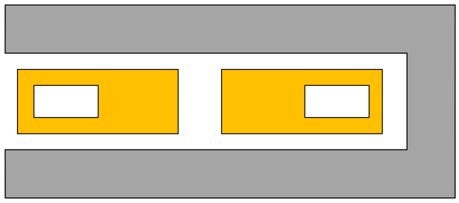

(a) Cond1 and Cond2 without transposition **(b)** Cond1 and Cond 4 with transposition

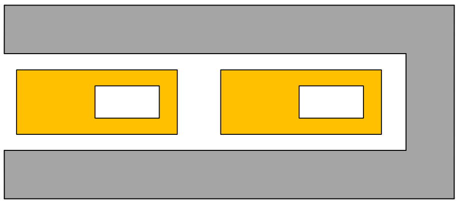

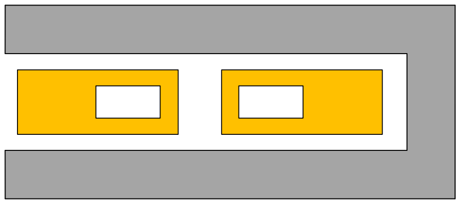

(c) Cond3 and Cond4 without transposition **(d)** Cond3 and Cond2 with transposition

Fig. 3.6. Different types of winding layout with and without transposition.

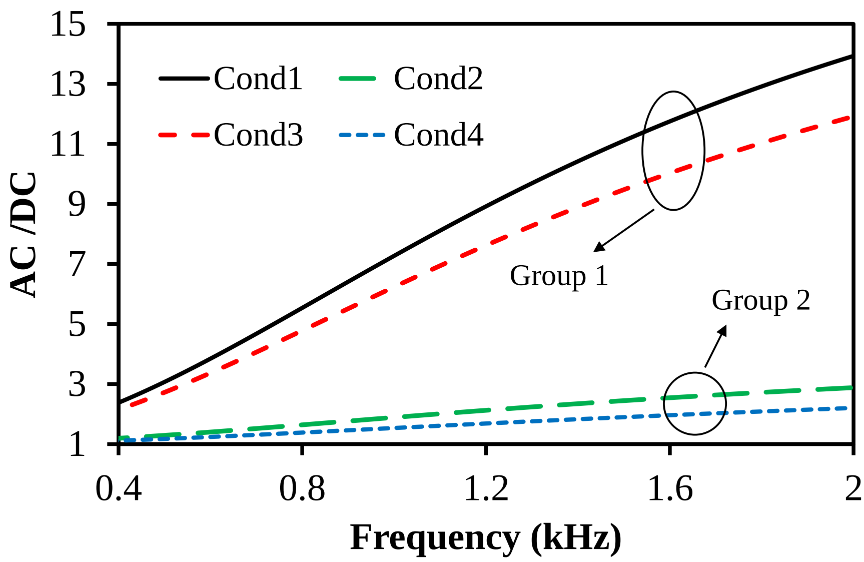

(a) AC to DC copper loss ratio generated by individual conductors when there are two conductors in one slot

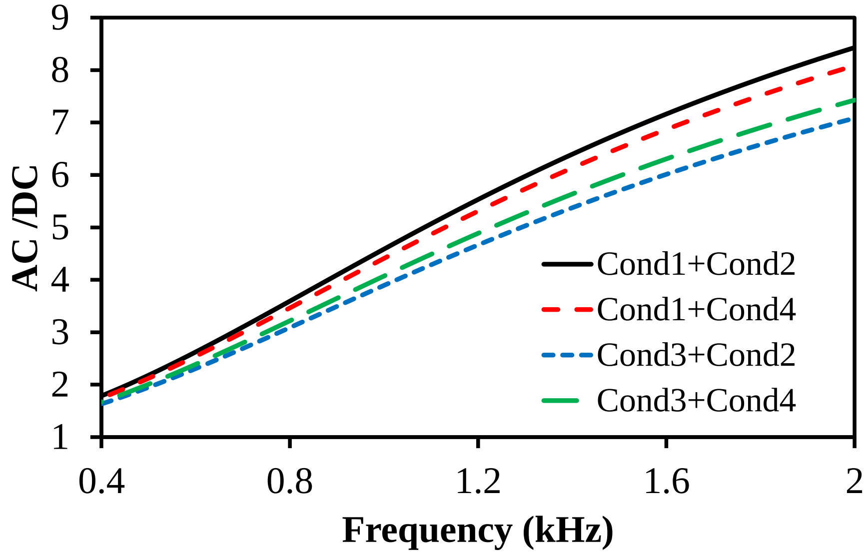

(b) Total AC to DC copper loss ratio generated by different winding layouts

Fig. 3.7. AC to DC copper loss ratio of individual conductors when there are two conductors in one slot and total winding layouts.

3.4. Influence of Conductor Aspect Ratio on AC Copper Loss

As previously analysed, R_1 is not necessarily approaching to 1. However, the larger gap between the conductor and the slot bottom influences the heat dissipation capability, although in this type of conductor, the coolant channel is the major path of the heat flux [Che19]. It is still better to locate the conductor at the slot bottom ($R_1 \approx 1$) when the heat dissipation capability is considered. As the optimum locations of conductor and coolant channel are studied with the fixed coolant channel shape. It is necessary to study the influence of the shape of the coolant channel on loss generation and heat dissipation capability. By introducing another set of two variables R_3 and R_4 defined in (3.3) and (3.4). The outer height of the conductor H_c can be written as a function of two variables (3.5),

$$R_3 = \frac{W_j}{W_c} \tag{3.3}$$

$$R_4 = \frac{H_j}{H_c} \tag{3.4}$$

$$H_c = \frac{CA}{W_c - R_3 R_4 W_c} \tag{3.5}$$

where CA is the conducting area,W_j, H_j, W_c,and H_c are the widths and heights of the hollow channel and the conductor, respectively. W_c is the fixed outer width. The outer height H_c is shown in Fig. 3.8(a).

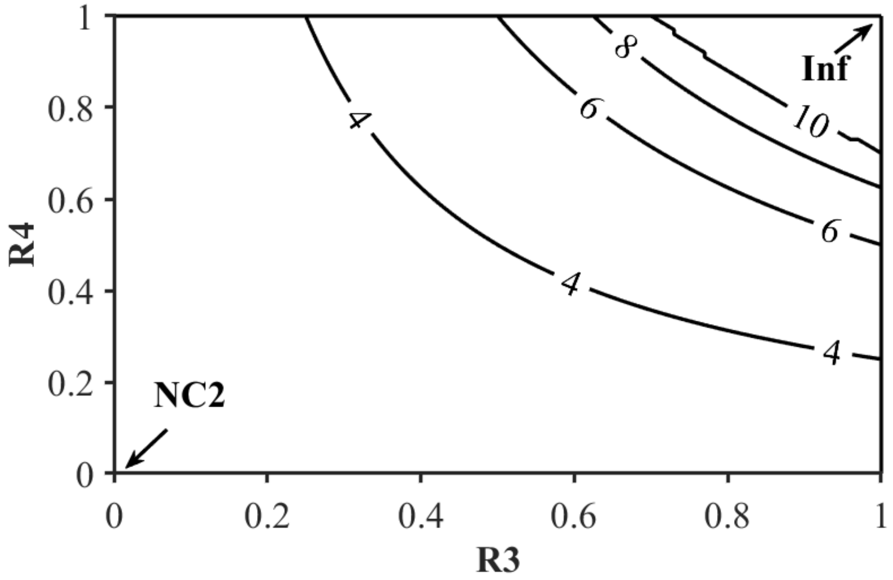

(a) Conductor height

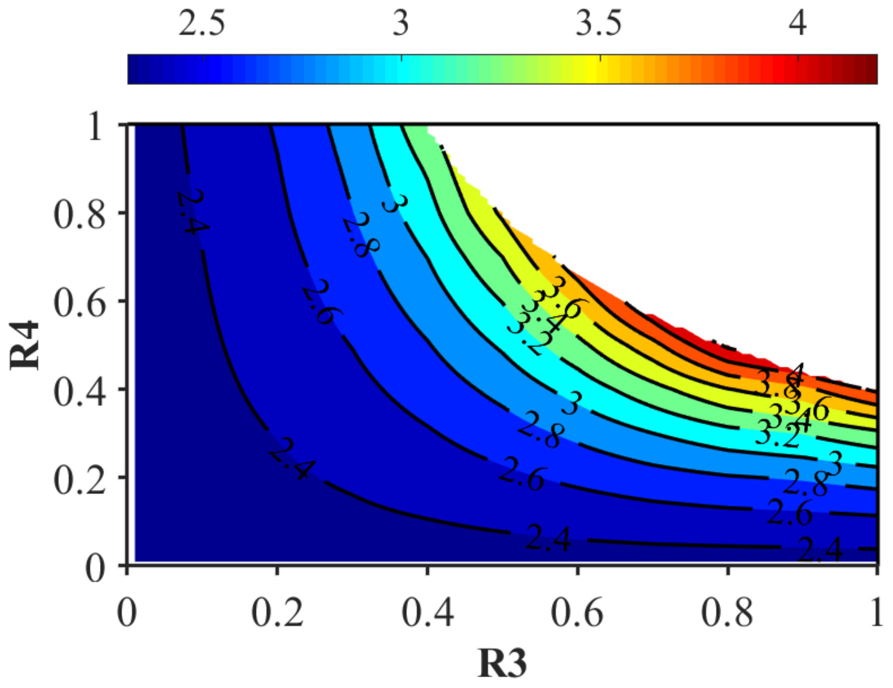

(b) AC copper loss (kW)

Fig. 3.8. Variation of conductor height and AC copper loss with R_3 and R_4 of the conductor.

It should be noted that in this case, the conducting area maintains constant to ensure the same DC copper loss. It can be seen that as R_3 and R_4 increases, H_c will approach to infinite which is unrealistic. Thus, it should be limited according to the slot depth. The variations of AC copper loss with R_3 and R_4 of the conductors are shown in Fig. 3.8(b). It is easy to see that the AC copper loss increases with the conductor outer dimensions significantly. In addition, the AC copper loss increases more significantly with R_4 than R_3. This is due to the fact that when R_4 increases, there is less material for the conductor towards the slot opening for conducting the eddy current. Thus, the current density in this region is further increased. Fig. 3.9 shows the current density and the flux lines for different types of hollow conductors.

It can be seen that the flux lines in each figure of Fig. 3.9 are similar, especially for two figures in the same row. For example, Version A and Version B in Fig. 3.9(a) and 9(b) have the same outer dimensions, it is easy to obtain by (5). The flux lines across the conductors are the same in the two figures due to the fact that the relative relationship between the magnetic source and the slot is almost the same. However, the current density shows that the conductor with lower R_3 and higher R_4 has less area to conduct the eddy current in the conductor towards the slot opening. This results in higher AC copper loss as shown in Fig. 3.10. The AC copper loss generated by Version A is higher than that of Version B, and the AC copper loss generated by Version C is higher than that of Version D.

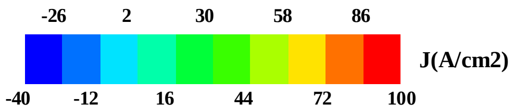

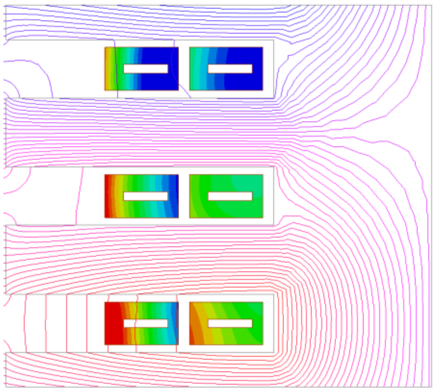

(a) Version A, R_3=0.2, R_4=0.6

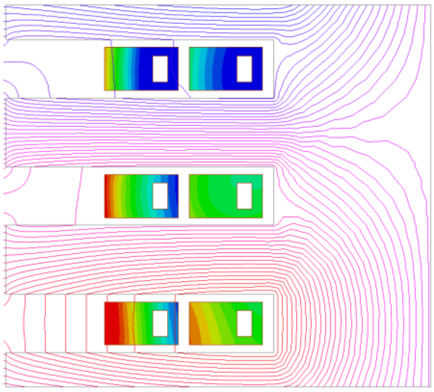

(b) Version B, R_3=0.6, R_4=0.2

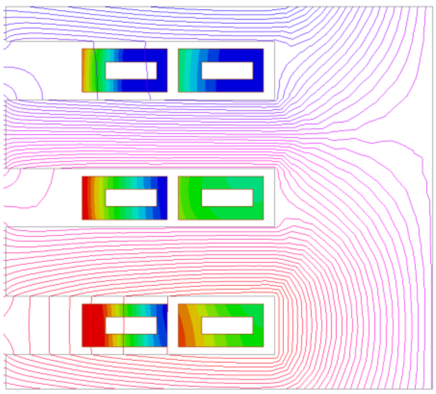

(c) Version C, R_3=0.4, R_4=0.6

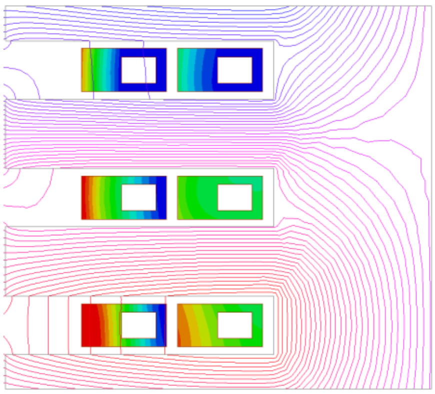

(d) Version D, R_3=0.6, R_4=0.4

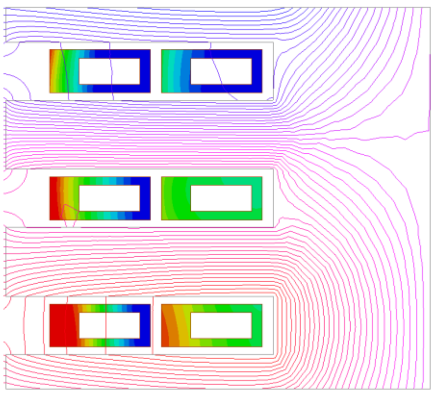

(e) Version E, R_3=0.6, R_4=0.6

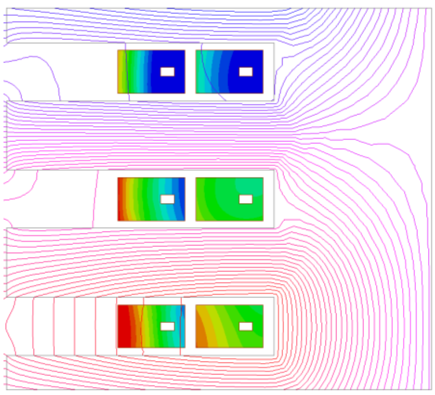

(f) Version F, R_3=0.2, R_4=0.2

Fig. 3.9. Current density and flux lines of different conductors in the slot at 1000Hz ($\boldsymbol{\omega t = \pi/2}$).

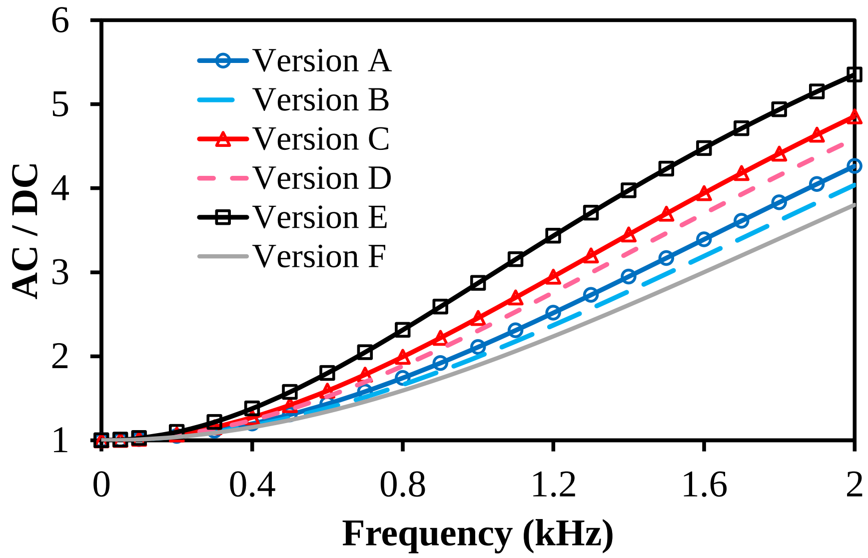

Fig. 3.10. AC to DC copper loss ratio against frequency for different versions of conductors.

3.5. Influence of Conductor Shape on Thermal Dissipation Capability

In the previous section, the influence of the hollow channel shape on the AC copper loss is presented. The main propose of equipping with hollow conductors is to decrease the winding temperature. The hollow region can be used as the coolant channel. The shape of the coolant channel determines the capability of thermal dissipation when the flow rate and fluid speed are set as constants. It should be noted that since the coolant flows directly inside the conductor, the coolant must not conduct electrically. In this case, the thermal oil XcelTherm 500 is selected as an example, its thermal and fluidic properties being summarized in Table 3.1. Fig. 3.11 shows the convection coefficient (h) and the equivalent thermal resistance against with the aspect ratio of the coolant channel with the same cross-sectional area. It can be seen that the thermal dissipation capability is the worst when the aspect ratio is equal to 1, i.e. the square shape. The aspect ratio is defined by (3.6). It should be noted that the convection coefficient h and the simplified thermal resistance R_j can be calculated by (3.7) to (3.13) [Tan15] [Sta06] [Wib66].

Table 3.1. General properties of XcelTherm 500.

Thermal conductivity (λ)	0.134 $\frac{W}{m°C}$
Density (ρ)	761.7 $\frac{kg}{m^3}$
Specific heat capacity (C_p)	2354 $\frac{J}{kg°C}$
Dynamic viscosity (μ)	0.002744 $\frac{kg}{ms}$

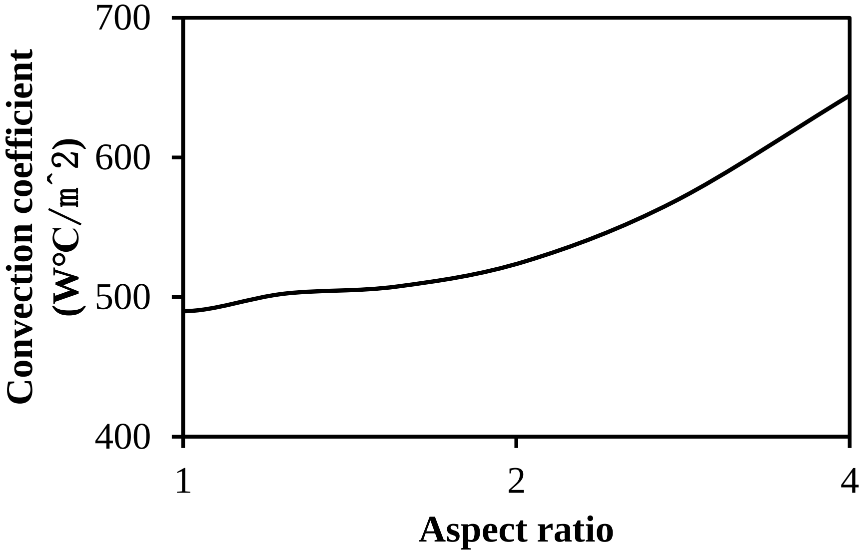

(a) Convection coefficient

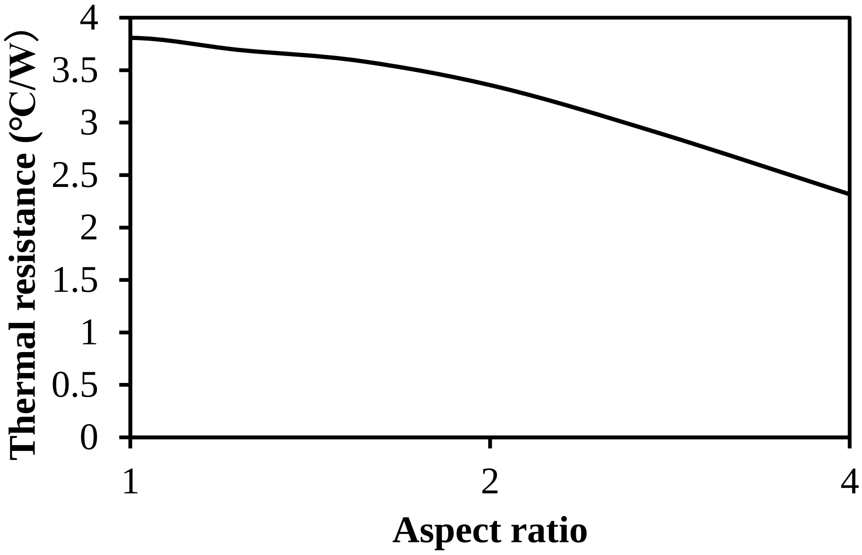

(b) Thermal resistance

Fig. 3.11. Convection coefficient and equivalent thermal resistance against with aspect ratio of coolant channel with the same cross-sectional area.

$$AR = \max(\frac{W_j}{H_j}, \frac{H_j}{W_j}) \tag{3.6}$$

$$D_h = 2\frac{W_j H_j}{H_j + W_j} \tag{3.7}$$

$$P_r = \frac{\mu C_p}{\lambda} \tag{3.8}$$

$$R_e = \frac{\rho D_h v}{\mu} \tag{3.9}$$

$$v = \frac{Q_f}{W_j H_j} \tag{3.10}$$

$$N_u = 7.49 - 17.02\,AR + 22.43(AR)^2 - 9.94(AR)^3 + \frac{0.065\left({}^{D_h}/_{L_a}\right)R_e P_r}{1 + 0.04\left({}^{D_h}/_{L_a}\,R_e P_r\right)^{2/3}} \tag{3.11}$$

$$h = \frac{\lambda N_u}{D_h} \tag{3.12}$$

$$R_j = \frac{1}{2hL_a(H_j + W_j)} \tag{3.13}$$

where AR is the aspect ratio, D_h is the hydraulic diameter, P_r is the Prandtl number, R_e is the Reynolds number, N_u is the Nusselt number, μ is the dynamic viscosity, C_p is the specific heat capacity, λ is the thermal conductivity, v is the mean velocity of coolant, Q_f is the mean flow rate of coolant.

It is worth mentioning again the convection coefficient and the thermal resistance presented in Fig. 3.11 are obtained with a constant flow rate, a constant coolant velocity, and a constant cross-sectional area. While the cross-sectional area could be variable as analysed in Section IV. According to (3.10), the flow rate is the product of the cross-sectional area and the coolant velocity. This is usually considered as a constant value since it is related with the coolant pump.

Continuing the analysis in Section 3.4, the available conductor size without considering the coolant has been calculated. In this case, the coolant flow rate in each channel is set as 0.04 L/min to ensure the total flow rate is under 6 L/min (144 channels). It should be noted that the combinations of R_3 and R_4 will be flited out when the Reynolds number (R_e) is larger than 200 to ensure the coolant is laminar flow [Nel09]. The thermal resistance is shown in Fig. 3.12, where the right-top corner region is filtered out due to the oversized conductor height, the left part is flited out to ensure the laminar flow. It can be seen that the lowest thermal resistance occurs when R_4 is large and R_3 is small. This is the opposite condition for lower AC copper loss. Thus, the resultant temperature is necessary to be calculated. It should be noted that the authors in [Che19] have presented that more than 90% of the loss is dissipated to the liquid coolant. Thus, in this case, all the heat generated in the conductor is assumed to flow into the coolant. The resultant temperature difference is shown in Fig. 3.13. It can be seen that the thermal dissipation capability is more dominant in the left-top region and the loss is dominant in the right-bottom region. It should be noted that when R_4 or R_3 equals to 1, the conductor hollow channel will be open, no coolant can flow in the conductor. Thus, there must leave a margin for a certain wall thickness when selecting the conductors.

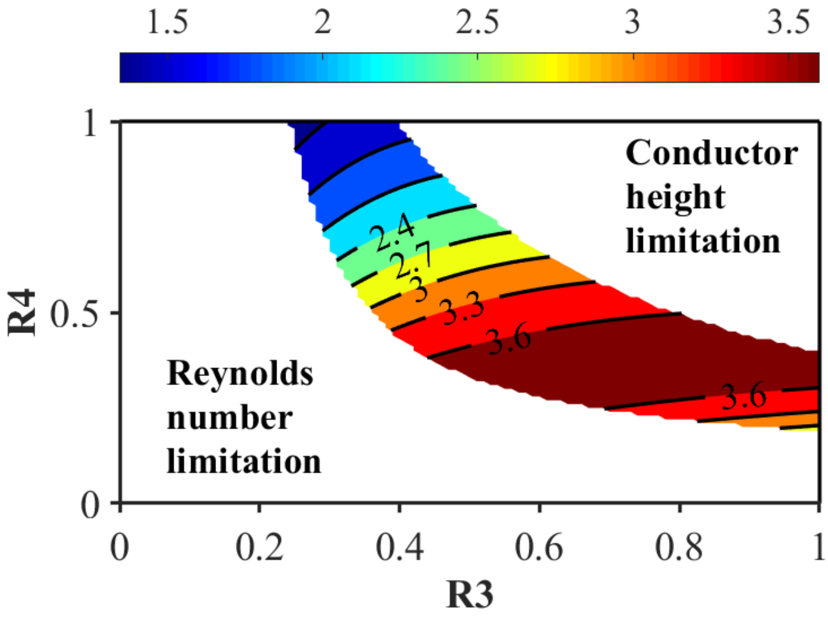

Fig. 3.12. Thermal resistance map with different channel shapes in conductors (Q=6L/min).

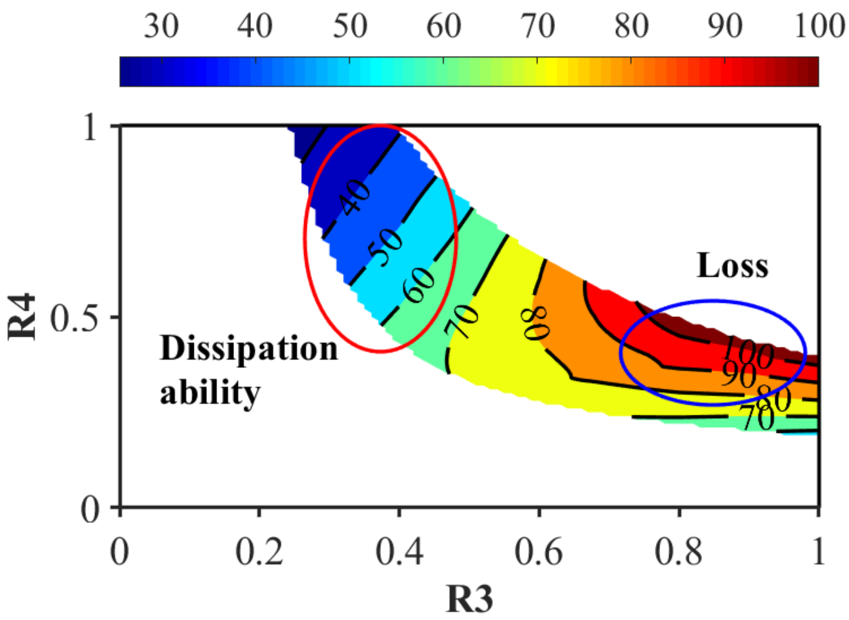

Fig. 3.13. The temperature difference between the conductor and the coolant for different channel shapes (Q=6L/min).

There are six examples in Section 3.4 and only Version C, Version D, and Version E are available under the flow rate equals to 6 L/min. The AC copper loss and the thermal dissipation capability of these conductors are compared in Table 3.2. It should be noted that the flow rate is adjusted to ensure the Reynolds number is 200.

Table 3.2. Comparison of loss and temperature.

Name	Loss (kW)	Q(L/min)	R_j (℃/W)	T (℃)
Version A	2.6	5	0.0144	39
Version B	2.5	5.5	0.0252	62
Version C	3.0	6	0.0195	60
Version D	2.8	6	0.0256	73
Version E	3.5	6	0.022	78
Version F	2.3	1.4	0.1729	408

It can be seen in Table 3.II, the conductor generating the lowest AC copper loss has the worse thermal dissipation capability than Version F. By adjusting the flow rate, the conductor Version A gives the best overall performance. It is worth showing the available flow rate map against $R_4$and R_3, as shown in Fig. 3.14. It is worth noting again, the flow rate shown in Fig. 3.14(a) is calculated by (3.9) and (3.10) and the Reynolds number is set equal to 200. The maximum flow rate is set as 6L/min, and it can be seen that the region flow rate equal to 6 L/min in Fig. 3.14(a) is the same as that in Fig. 3.12. The thermal resistance is shown in Fig. 3.14(b). By considering the variable flow rate, the map of available thermal resistance is extended comparing with Fig. 3.12. In addition, the conductors in the extended region can achieve better thermal dissipation capability with a lower flow rate. However, these conductors will be flited out if the flow rate is set to large. Finally, the temperature is shown in Fig. 3.14(c). This is calculated by the product of Fig. 3.8 and Fig. 3.14(b). It can be seen that there are two hot regions, one of them is due to the high loss and another one is due to the worse thermal dissipation capability. By changing the flow rate from a constant to a variable, the overall temperature can be reduced by about 20 degrees.

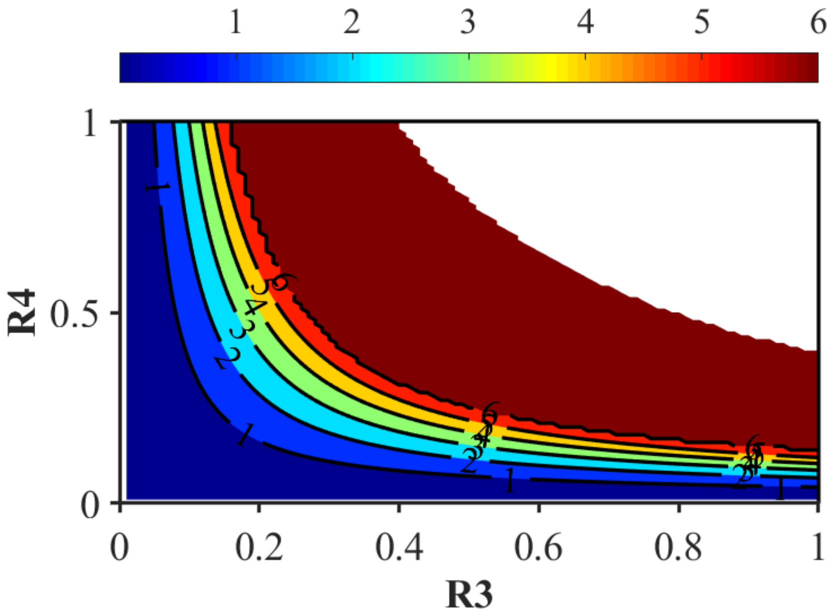

(a) Flow rate

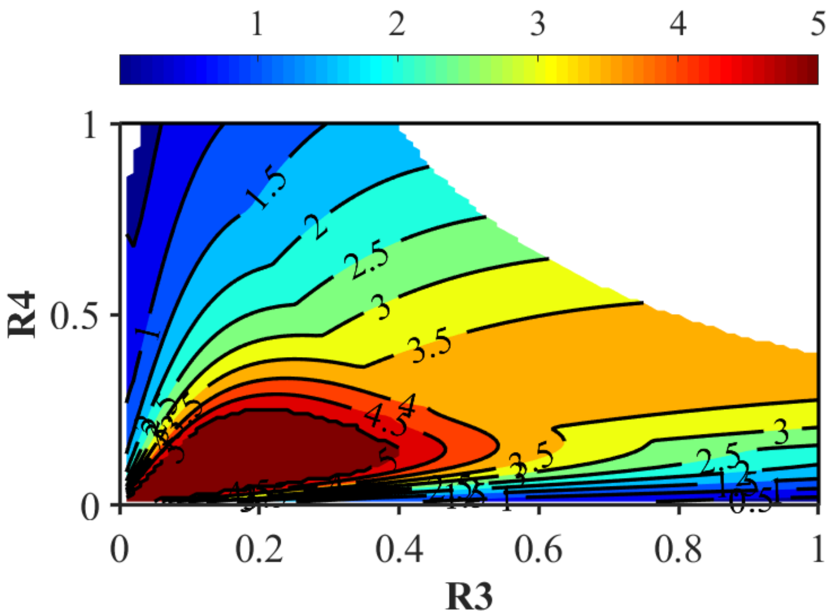

(b) Thermal resistance

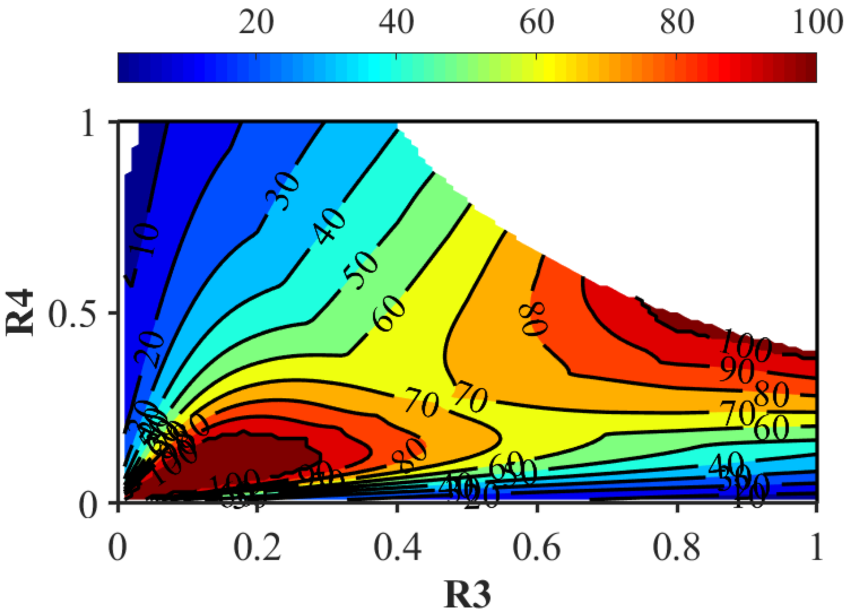

(c) Temperature rise (Loss calculated at 1000Hz)

Fig. 3.14. Flow rate, thermal resistance, and temperature rise against R_3 and R_4.

3.6. Conclusion

In this chapter, the influences of design parameters of the hollow conductors on the AC copper loss and thermal dissipation capability are studied. It is shown that the relative positions between the hollow region, the conductor, and the slot impact the AC copper loss strongly. In addition, four versions of winding connections are analyzed with and without the transposition at the end-winding region. It has been shown that the minimum AC copper loss occurs when the hollow regions are located at the conductors towards the slot bottom and without transposition. Furthermore, the influences of the hollow shape on AC copper loss and the thermal dissipation capability are analyzed. It should be noted that the conducting area maintains the same to keep the same DC copper loss. It has been shown that the AC copper loss generated by the case $R_4 < R_3$ is lower than the case $R_4 > R_3$. The minimum AC copper loss occurs when the conductor is the shortest. However, these conductors generating lower AC copper loss could have worse thermal dissipation capability since the hollow region is very small. In the conventional analysis of the convection coefficient, the flow rate is usually set as constant. However, it has been shown that better overall performance can be obtained by considering the variable flow rate.

CHAPTER 4

Electromagnetic Performance of PM Machines Accounting for AC Copper Losses

In this chapter, a hybrid analytical and finite element model of AC copper loss is proposed. It has been shown that with consideration of the AC copper losses it results in a 6 kW reduction in the maximum output power estimation. Compared with the finite element method, the developed model is efficient and accurate to predict the actual loss in the windings. In addition, by utilizing the proposed method, the torque/power-speed characteristics and efficiency maps considering AC copper loss can be obtained within a desirable computing time.

4.1. Introduction

Interior permanent magnet synchronous machines (IPMSMs) with distributed windings have been used for many applications including hybrid and electric vehicles. It has high torque density and high efficiency, and can utilize not only the permanent magnet (PM) torque but also the reluctance torque. The interior PM typed rotor can prevent the magnet dispersion from the centrifugal force at high-speed operation, since the magnet is located inside the rotor core [Jah86]. In addition, it has a good flux weakening capability, a wide constant power region, and a high demagnetization withstand capability. However, the IPM machines usually have a higher iron loss due to significant armature reaction as a result of a small effective air gap, especially at high speeds [Aza10] [Sch89] [Zhu02].

Due to the convenience in the manufacture and high packing factor, the large rectangle conductors become more popular for low voltage and high current applications [Rah12] [Jun12] [Par14]. However, AC copper losses of such large conductors may be extremely high at high speed operation. There is a lot of research on the causes of AC copper loss [Kla06] [Pop13] [Sul99a] [Mcc89] [Red08] but rare of them is focus on rectangular conductors . The AC copper loss is caused by the eddy-current effects in the winding which include skin effect and proximity effect. The skin effect is the non-uniform current density distribution in a single conductor. The high-frequency current tends to flow towards the surface rather than the whole conductor [Sul99]. Different from the skin effect [Kla06], the proximity effect is the current distribution due to the magnetic fields generated by the nearby conductors [Pop13] [Sul99a] [Mcc89]. Even with thin wire to eliminate the skin effect, the proximity effects still exist [Pop13]. Many authors work on the analytical prediction of AC copper losses 31-48[Tho09] [Woj13] [Phu07] [Nan03] [Nan04] [Dow66] [Fer94] [Sul01] [Sul99b] [Wro10a] [Wro12] [Iwa09] [Red10] [Red11] [Mel06] [Wro10b] [Ger04] [Bol02]. In [Tho09], a 1-D analytical model to accurately estimate the proximity losses in flux switching PM machines (FSPM) has been developed. The author of [Woj13] presented the analytical optimization of solid-round-wire inductor windings to achieve the minimum AC resistance. The author of [Phu07] presents two complementary numerical approaches to predict proximity losses in rectangular conductors. The authors in [Nan03] and [Nan04] improve the accuracy of prediction on proximity effect loss presented by [Dow66] and [Fer94], and the idea is to simulate a single wire with symmetrical boundary conditions to find its behavior in a conductor. In [Mel06] [Wro10b] [Ger04] [Bol02], the authors also consider the temperature effects on the AC copper loss. However, it is hard to consider the slot geometry and magnetic saturation effect by the analytical method.

Recently, there are several papers focusing on the reduction of AC copper losses. In [Sim18], the author presents a shaped slot winding profile which can reduce the AC copper loss based on the time-harmonic finite element model. In [Li18] and [Vol18], the author provides the analytical method and finite element method, and a hybrid method to model the AC copper loss. However, the temperature effect and current effect are not studied. In [Aoy18], the author studies the influence of parallel path on DC copper loss and eddy current loss. However, due to the manufacture consideration, the number of parallel paths is not suitable to be too large. In [Bar18], the author presents that introducing a space between the conductors and tooth tips can reduce the AC copper loss. However, the temperature influence on the AC copper loss and the overall winding temperature are not studied.

In this chapter, a hybrid analytical and finite element method to predict the AC copper loss is proposed. It has higher accuracy than the existing analytical model since the geometry effect (i.e. the slot tips and slot opening) and saturation effect (i.e. current amplitude and current angle) can be considered. In addition, it is more efficient than FE method, since the temperature effect can be separated to reduce computing time in FE, and considered individually in the analytical model.

4.2. Variation of AC Copper Loss with Temperature

As mentioned previously, the AC copper loss in the prototype machine is very high due to the large conductors used in the machine. It should be noted that the length of end-winding per phase is equal to the active length per phase for this particular machine. The machine geometry and parameters are summarized in Appendix 1. Fig. 4.1 shows the variation of the AC copper loss and DC copper loss with the operation speed. In order to simulate the machine in 2D instead of 3D, the following assumptions are made:

- The R_{ac} to R_{dc} ratio of the end-winding part is equal to 1 [28].

- The current influence on the AC resistance is not considered in this section and will be presented in the next section.

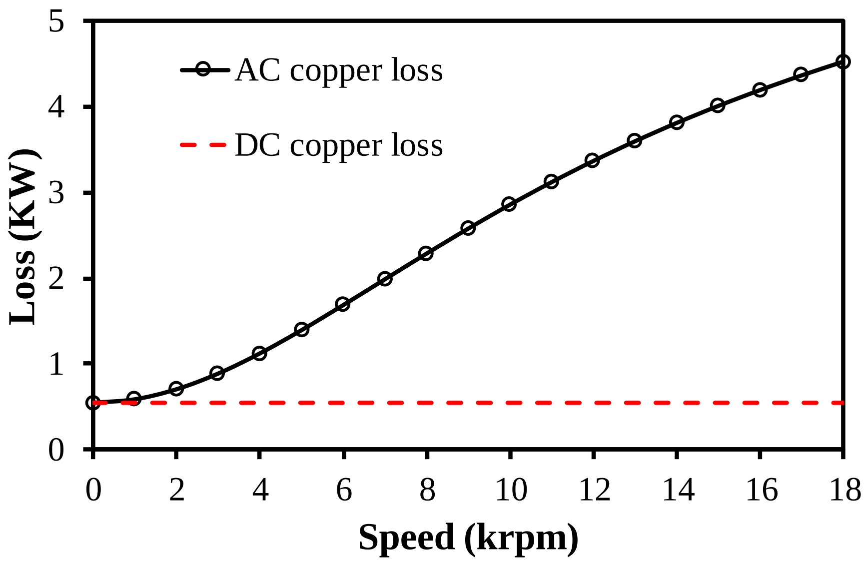

Fig. 4.1. AC and DC copper losses at 20 °C.

Since the skin effect is one of the major reasons resulting in high copper loss, the skin depth is given in (4.1). Assuming the relative permeability maintains the same as temperature increases, the resistivity will also affect the skin depth and the conducting area. The phase resistance can be written as a function of temperature and frequency (speed) as given in (4.2).

$$\delta = \sqrt{\frac{2\rho}{\omega\mu_m}} \tag{4.1.}$$

$$R_{ph}(T,f) = \rho(T)\frac{L}{A(T,f)} \tag{4.2}$$

$$\frac{R_{ph}(T,f)}{R_{ph}(T_0,f)} = \frac{\rho(T_1)\frac{L}{A(T,f)}}{\rho(T_0)\frac{L}{A(T_0,f)}} = \frac{\rho(T)}{\rho(T_0)}\frac{A(T_0,f)}{A(T_1,f)} \tag{4.3}$$

where δ is the skin depth, ρ is the resistivity, μ_m is the permeability, f is the frequency, R_{ph} is the phase resistance, A is the conducting area, T is the temperature of the conductor and T_0 is the reference temperature.

Fig. 4.2 shows the variation of AC copper loss with speed at different temperatures when the input current is set as I_q = 60A and I_d = -250A for q- and d-axis currents. Fig. 4.3 shows the variations of R_{ac} to R_{dc} ratio. It can be seen that although the R_{ac} to R_{dc} ratio decreases with temperature increasing, the absolute value of total copper loss does not change significantly, shown in Fig. 4.2. It can be explained by the fact that the resistivity increases with temperature, the DC resistance is higher while the skin depth is also larger at high temperature. At high speed and low-speed regions, the loss at higher temperature is slightly higher than that at low temperature, while in the middle-speed range, the difference between AC copper losses with different temperatures is minor.

The copper loss at 20 °C in Fig. 4.2 is chosen as reference, the ratio of equivalent phase resistance between the higher temperature and the reference (20 °C) is presented in Fig. 4.4. For example, the green line (60 °C /20 °C) in Fig. 4.4 represents that the resistance at 60 °C divided by the resistance at 20 °C. At zero speed, the resistance ratio is equal to the resistivity ratio since the conductors have the same conducting areas. As the speed increases, the resistance ratio initially decreases greatly and then increases slightly after the critical point. It is worth noting that the resistance ratio between high temperature and low temperature could be smaller than 1 at a certain speed which means at one speed the conductor with higher temperature has lower resistance than the conductor with lower temperature. This phenomenon is a combined result between the resistivity and the equivalent conducting area of the conductor as shown in (4.3). Since the resistivity is only related with the temperature by a fixed coefficient, the conducting area is the only factor of the resistance which varies with the speed. Fig. 4.5 shows the variation of conducting area of the winding at different temperatures with speed. The area is calculated based on the AC copper loss shown in Fig. 4.2 and the Ohm's law. The ratio of the conducting area between the high temperature and the reference temperature (20 °C) is presented in Fig. 4.6, together with the resistivity ratio in dashed lines. It can be seen that at a certain speed, the area ratio is higher than the resistivity ratio.

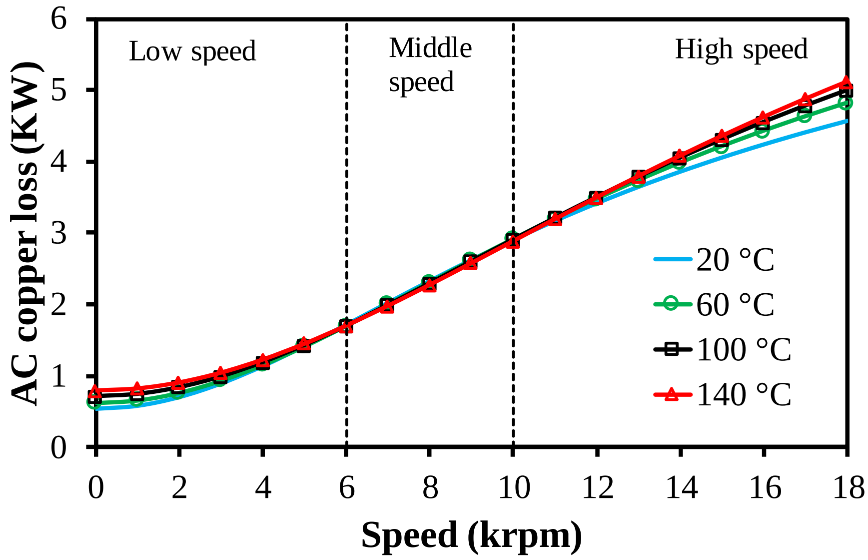

Fig. 4.2. Variation of AC copper loss with speed at different temperatures.

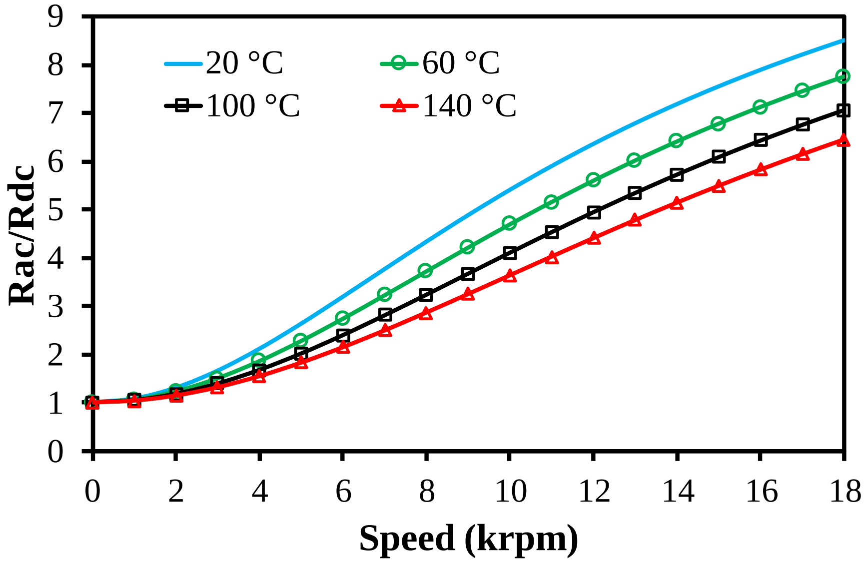

Fig.4.3. AC resistance to DC resistance ratio at different temperatures.

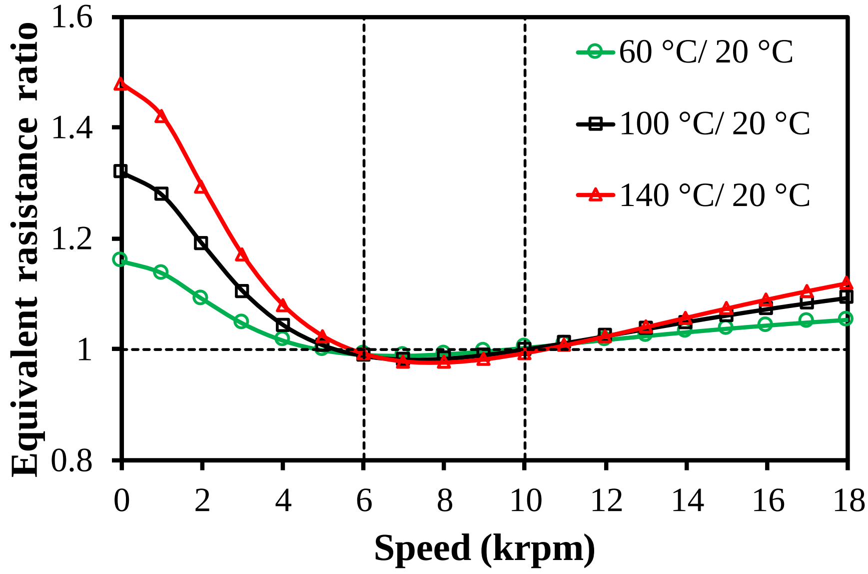

Fig. 4.4. Variation of equivalent phase resistance ratios between high temperatures and 20 °C with speed.

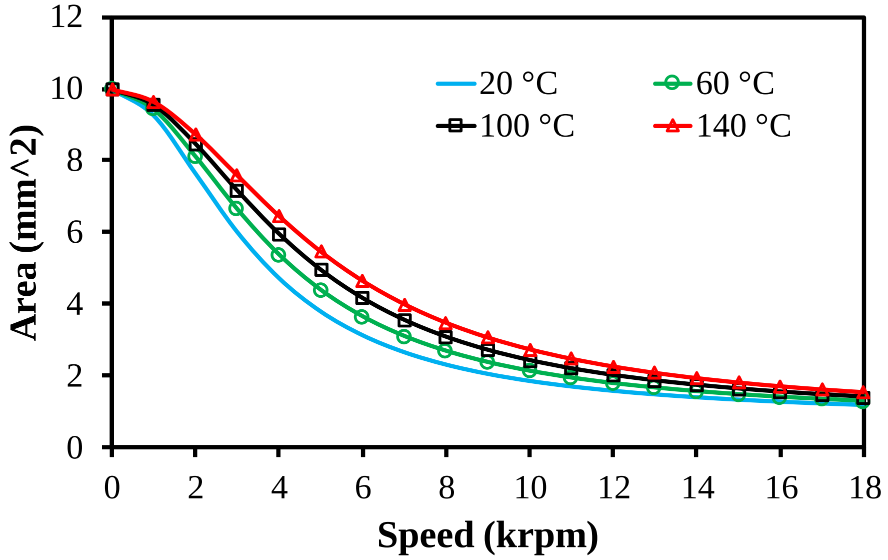

Fig. 4.5. Conducting area variation with speed.

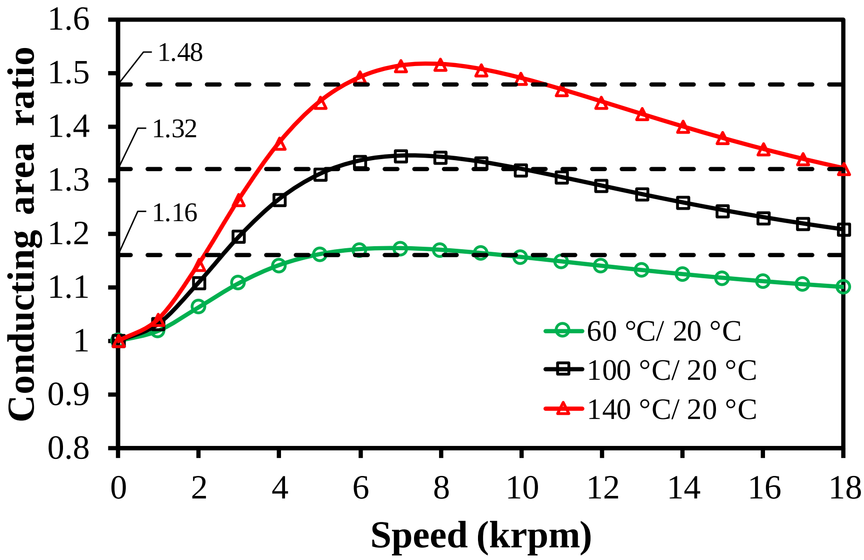

Fig. 4.6. Variation of conducting area ratio with speed at different temperature ratios.

4.3. Improved Analytical Method for Calculating AC Copper Loss and AC Resistance

It takes a long time by the FE method to compute the variation of AC copper loss with operating speed especially when coupled with the thermal analysis and torque-speed characteristic calculation. Thus, it is worth calculating the AC copper loss by a reliable analytical model. It has been proposed in [27], the analytical model which is suitable for the rectangular conductors in parallel slots. The AC to DC resistance coefficient for the p^{th} layer (K_{RP}) in the slot shown in Fig. 4.7 can be obtained by the following equations:

$$K_{RP} = \varphi(\xi) + \frac{I_{total}\left(I_{total}\cos\gamma + I_{layer}\right)}{I_{layer}^2}\psi(\xi) \tag{4.4}$$

$$\varphi(\xi) = \xi\frac{\sinh 2\xi + \sin 2\xi}{\cosh 2\xi - \cos 2\xi} \tag{4.5}$$

$$\psi(\xi) = 2\xi\frac{\sinh\xi - \sin\xi}{\cosh\xi + \cos\xi} \tag{4.6}$$

$$\xi = H_c\sqrt{\frac{\omega\mu_m\sigma}{2}\frac{n_c W_c}{H_s}} \tag{4.7}$$

where I_{total} is the total current in the slot, I_{layer} is the current per layer in the slot, γ is the angle between I_{total} and I_{layer}, n_c is the number of conductors in each layer, H_c, W_c, W_s are the conductor and slot dimensions shown in Fig. 4.7.

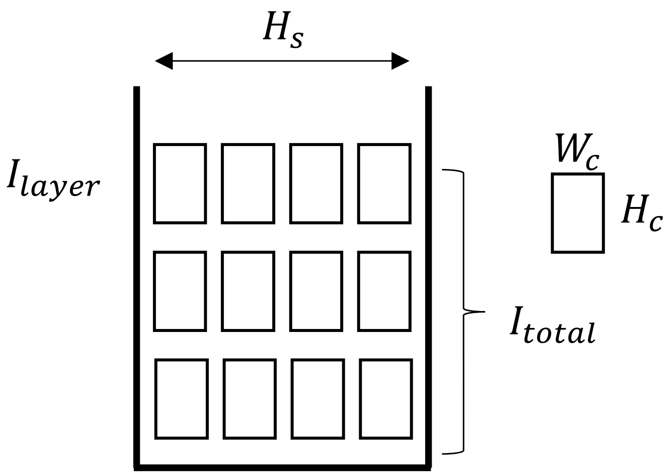

Fig. 4.7. Multiple rectangular conductors in a parallel slot.

The average value of K_{RP} for m layers can be calculated by (4.8) and (4.9) for the case $\gamma = 0°$ and $\gamma \neq 0°$ respectively.

$$K_{Rm} = \frac{1}{m}\sum_{1}^{m} K_{RP}\,(p) = \varphi(\xi) + \frac{m^2 - 1}{3}\psi(\xi) \tag{4.8}$$

$$K_{Rm} = \varphi(\xi) + \left(\frac{m^2(5 + 3\cos\gamma)}{24} - \frac{1}{3}\right)\psi(\xi) \tag{4.9}$$

Fig. 4.8 compares the R_{ac} to R_{dc} coefficients by the FE method and the analytical method. It shows that in the low-speed region, the analytical results match well with the FE results. However, in the high-speed region, it deviates from the FE results. Thus, it could be over predicted in AC copper loss when the analytical method is employed directly. The difference between the analytical and FE results is because the analytical model does not consider the lamination geometry effect, i.e. the slot tips and slot opening, and magnetic saturation effect due to different current angles. In addition, these two effects can be neglected at low frequency, whereas they become more obvious at high frequency. It should be noted that these two effects can be considered together in the terms of flux density variation (B) in (4.10).

Furthermore, the flux density variation (B) is not related with the temperature (T). Thus, they cannot be considered individually. Fig.4.9 compares the variation of the resistance ratio with speed at different temperature ratios. Due to the fact that the temperature is an individual factor and is not related with the flux density. It can be seen that the resistance ratio at different temperature ratios has a better agreement than the R_{ac} to R_{dc} coefficient. Thus, it is better to predict the R_{ac} to R_{dc} coefficient by the temperature ratio.

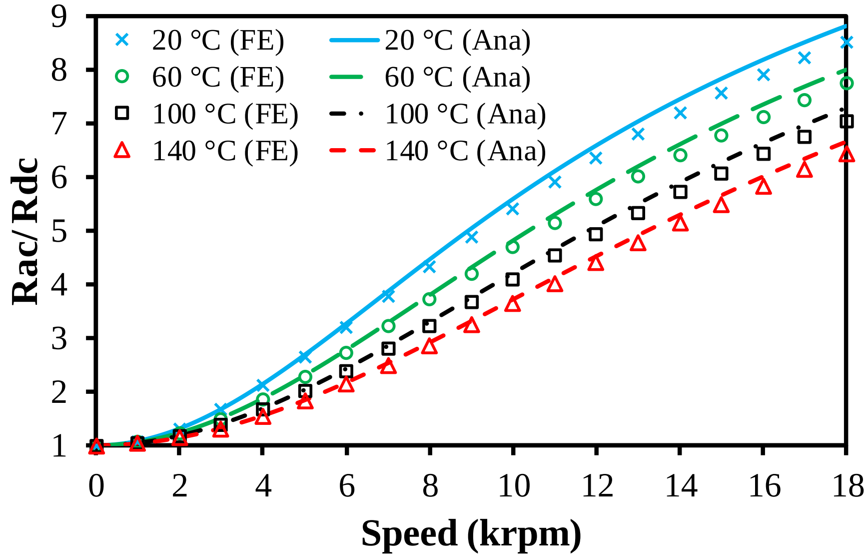

Fig. 4.8. Comparison of AC resistance to DC resistance ratio between analytical and FE at different temperatures, at I_q=60A and I_d=-250A.

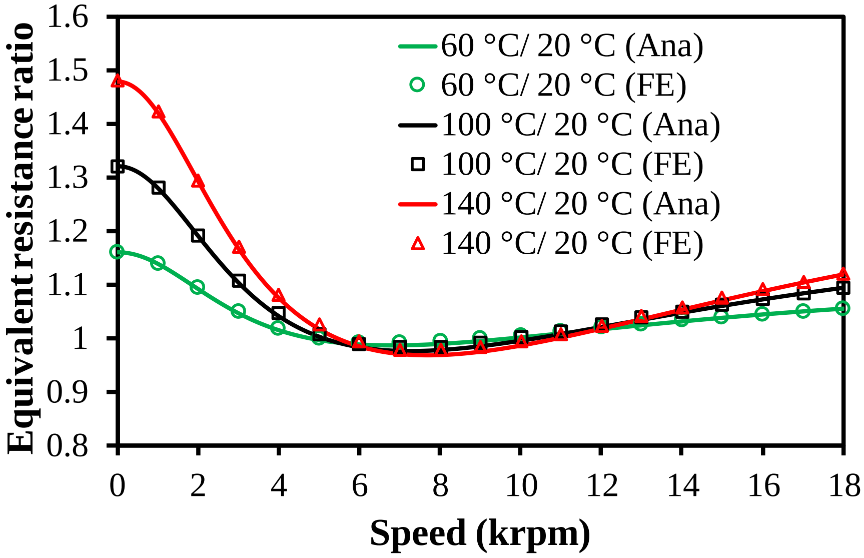

Fig. 4.9. Comparison of equivalent resistance ratio between analytical and FE results, at I_q=60A and I_d=-250A.

The proposed hybrid analytical and FE model to predict the AC copper loss is based on separating the temperature and flux density effects. The new R_{ac} to R_{dc} coefficient can be calculated as:

$$\frac{R_{ac}}{R_{dc}}(T,f,B) = \frac{K_{Rm}(T.f)}{K_{Rm}(T_0,f)} * \left[\frac{R_{ac}}{R_{dc}}(f,B)|_{T_0}\right] \tag{4.10}$$

$$\text{Ana} + \text{FE}(T,f,B) = \text{Ana}.(T,f,T_0) * \text{FE}(f,B)|_{T_0} \tag{4.11}$$

where $\frac{R_{ac}}{R_{dc}}(f,B)|_{T_0}$ is the reference value which can be calculated from FE or test.

With the help of FE method to calculate at the reference temperature (20 °C), the AC copper loss or R_{ac} to R_{dc} ratio at any temperature can be obtained more accurately than the original analytical method.

The FE results shown in Fig.4.10 as marks are the same as those shown in Fig.4.10, and the dashed lines are the analytical results. Fig. 4.11 compares the R_{ac} to R_{dc} ratio with the temperature at 10 krpm and 18 krpm. It can be seen that the difference between FE and analytical results can be significantly reduced by the new method (4.10) and (4.11) which are shown as solid lines in Figs. 4.10 and 4.11. This proposed method utilizes the temperature ratio for prediction.

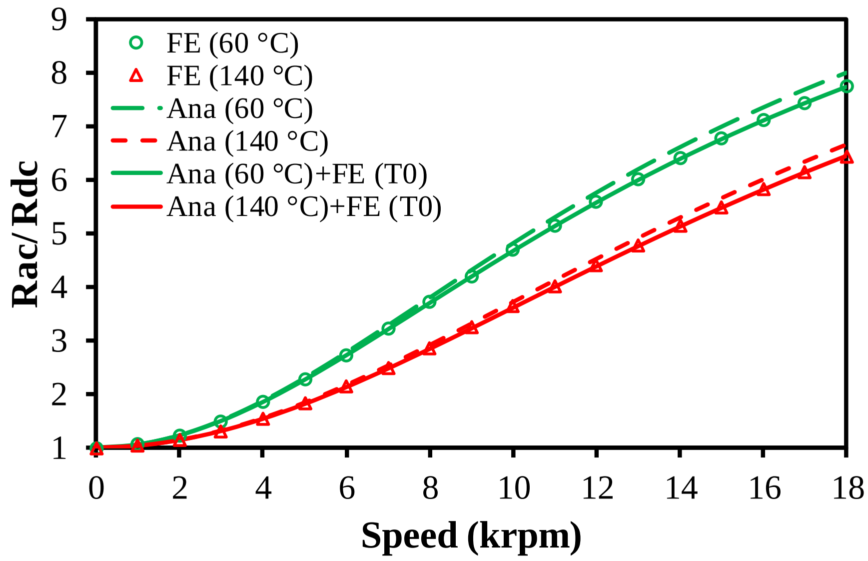

Fig. 4.10. Comparison of AC resistance to DC resistance ratio against speed, at I_q=60A and I_d=-250A ($\boldsymbol{T_0}$= 20 °C).

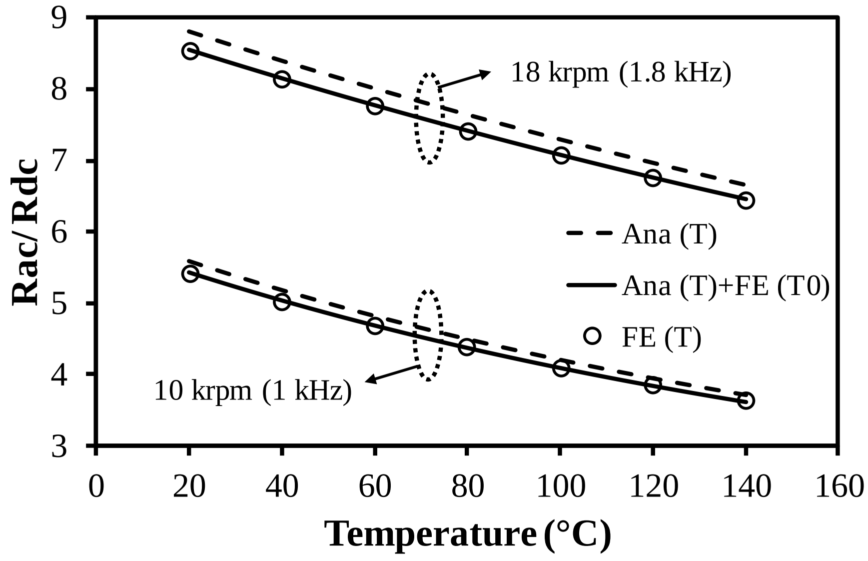

Fig. 4.11. Comparison of AC resistance to DC resistance ratio against temperature, at I_q=60A and I_d=-250A ($\boldsymbol{T_0}$= 20 °C).

It should be noted that the current and current angle will also affect the ratio of R_{ac} to R_{dc} due to the flux density distribution in the conductors. However, these effects are not considered in the existing analytical model. The comparisons are shown in Figs.4.12 and 4.13.

During the thermal analysis, the above method is efficient and accurate to predict the AC copper loss in the slot. The temperature of the conductor, the flux density, and the operating speed of the machine are the three major factors that affect the AC copper loss. For the most accurate method (FE), all three factors should be considered. Thus, the result is a three-dimensional matrix. However, they can be separated by using the above method. The influence of the frequency and flux density (current) are considered and included in the term of $\frac{R_{ac}}{R_{dc}}(f,B)|_{T_0}$ obtained from FE or test. The temperature is considered in the external analytical function. In addition, if the input is a test result, the reference temperature does not have to be constant at different speeds.

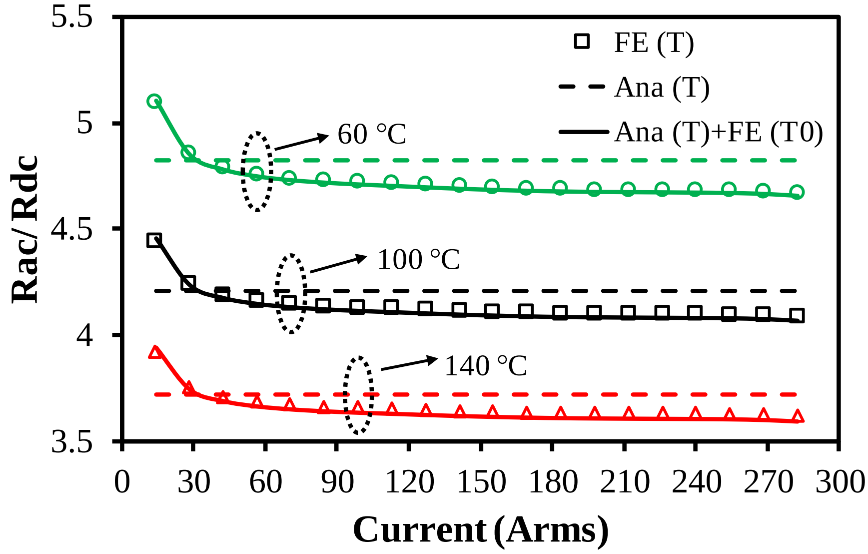

Fig. 4.12. Comparison of AC resistance to DC resistance ratio against the current at 10 krpm and I_q=60A, I_d=-250A ($\boldsymbol{T_0}$= 20 °C).

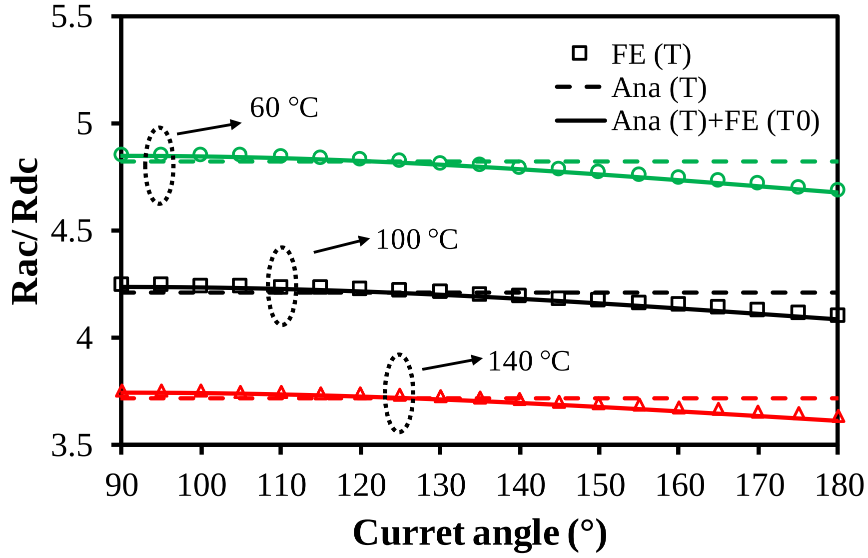

Fig. 4.13. Comparison of AC resistance to DC resistance ratio against current angle at 10 krpm and 30 Arms ($\boldsymbol{T_0}$= 20 °C).

In conclusion, the proposed hybrid analytical and FE model (Ana + FE) can predict the AC copper loss with high accuracy compared with the existing model. With the helping of FE, the proposed model can also consider the geometry effect and saturation effect which are not considered in the existing model. It should be noted that the FE is still the most accurate method. However, it takes a long time to calculate the AC copper loss especially when considering the temperature effect. By utilizing the proposed method, the temperature effect can be separated from the FE, considered individually, and linked with the LTPM model. It is more accurate compared with the existing analytical model and more efficient than the direct FE calculation. The following investigation will be conducted based on the proposed method.

4.4. Influence of AC Copper Loss on Torque-Speed Characteristics

The torque-speed characteristic is one of the most important performance to evaluate the electrical machines. However, it is usually calculated without considering AC copper loss. In the prototype machine, the performance has a significant difference with and without considering AC copper loss, as shown in Fig. 2.1. The current density distributions under low-speed and high-speed operating conditions on the torque-speed envelops are shown in Fig. 4.14. It can be seen that when AC effect is not considered, the current densities are uniformly distributed inside the conductors, as shown in Fig. 4.14(a) and 4.14(c). At low operation speed, the current density accounting for AC effect is slightly different from that without considering it, as shown in Fig. 4.14(a) and 4.14(b). As the operation speed increasing, the current density is more un-uniformly distributed inside the conductors.

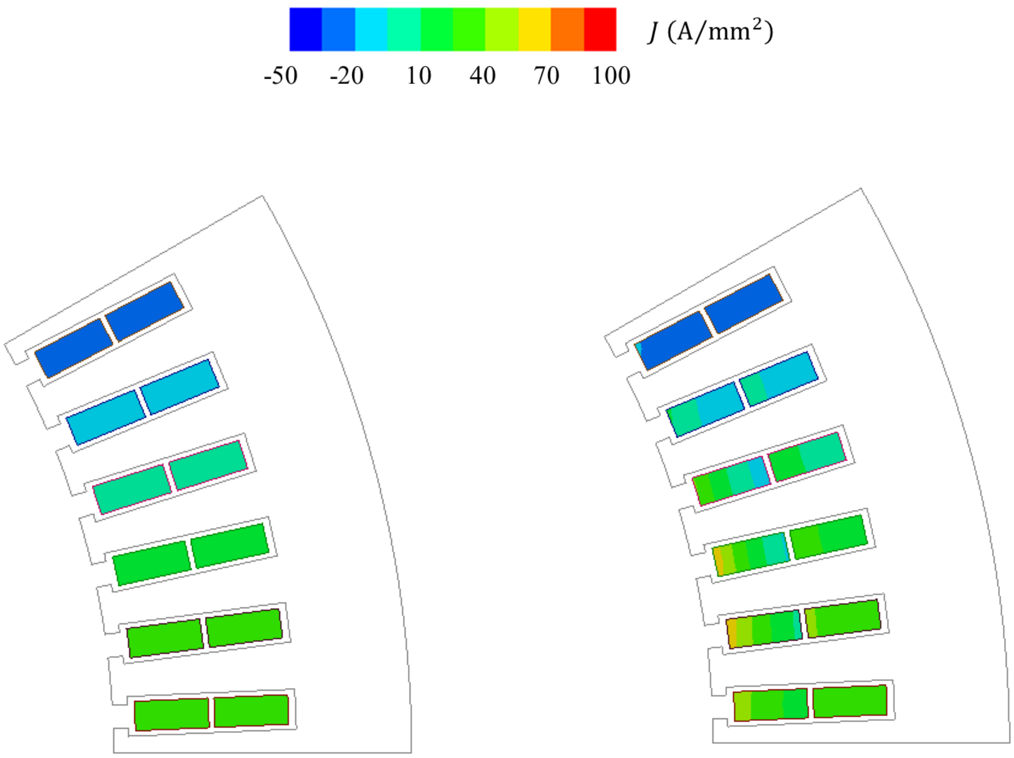

(a) 2krpm without AC effect

(b) 2krpm with AC effect

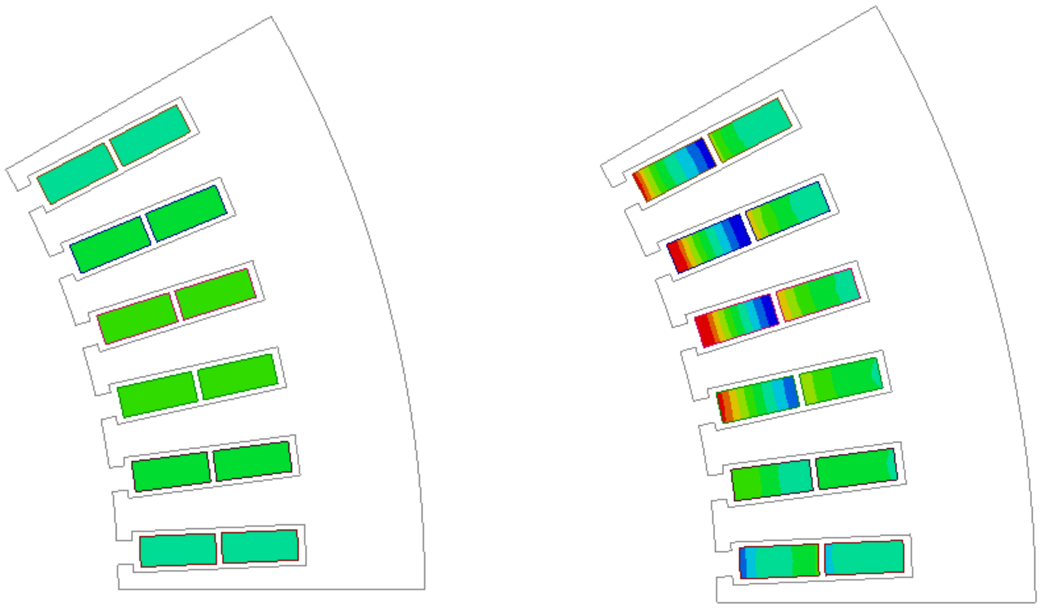

(c) 10krpm without AC effect

(d) 10krpm with AC effect

Fig. 4.14. Current density distribution with and without AC effect at different speeds ($\boldsymbol{\omega t} = \boldsymbol{\pi/2}$).

It can be seen that the high-speed torque reduces when AC copper loss is considered under the same voltage limitation. It can be simply explained that the equivalent resistance is increased, and more voltage drops on the resistor when AC copper loss is considered. Fig. 4.15 and 4.16 shows equivalent phase resistance with and without considering AC effects. The phase resistance remains a constant value at a different frequency when the AC effect is not considered. While when AC effects are considered, the equivalent phase resistance is generally increasing with frequency and speed.

Fig. 4.17 and 4.18 show the copper loss with and without considering AC effect, respectively. It can be seen that when AC effect is considered, the copper is significantly increased comparing with the copper loss without AC effects, especially at the high-speed operation region.

More importantly, the efficiency maps with and without considering AC copper loss is shown in Fig. 4.19 and 4.20. It can be seen that the high-efficiency operation region significantly shrinks to the low-speed operation regions. The performance of the electrical machine can be overestimated without considering AC effects.

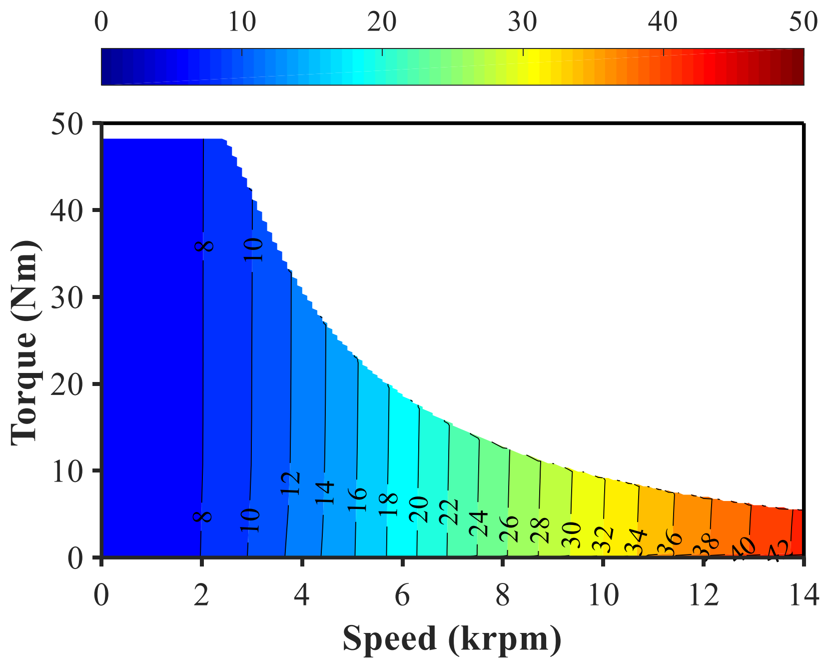

Fig. 4.15. Phase resistance with considering AC effects (mOhm).

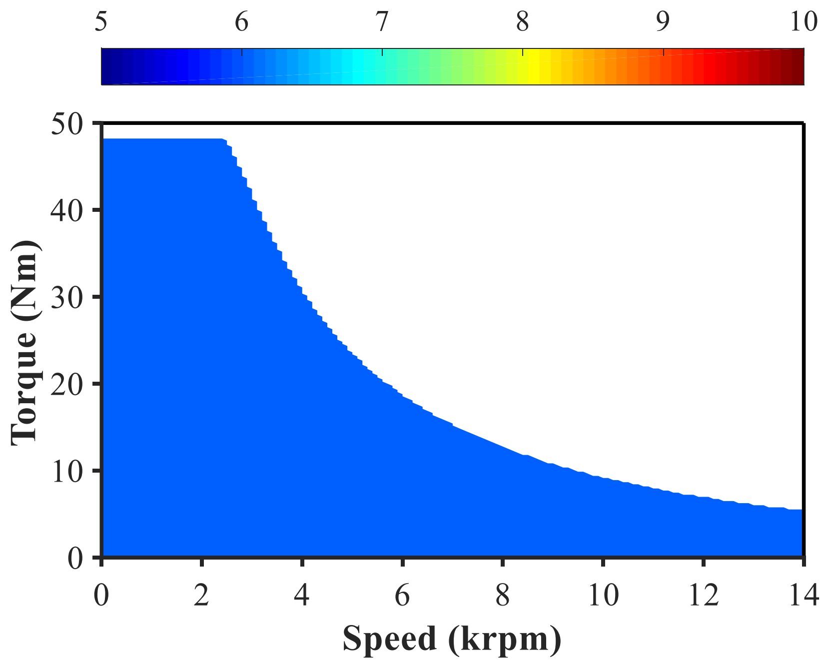

Fig. 4.16. Phase resistance without considering AC effects (mOhm).

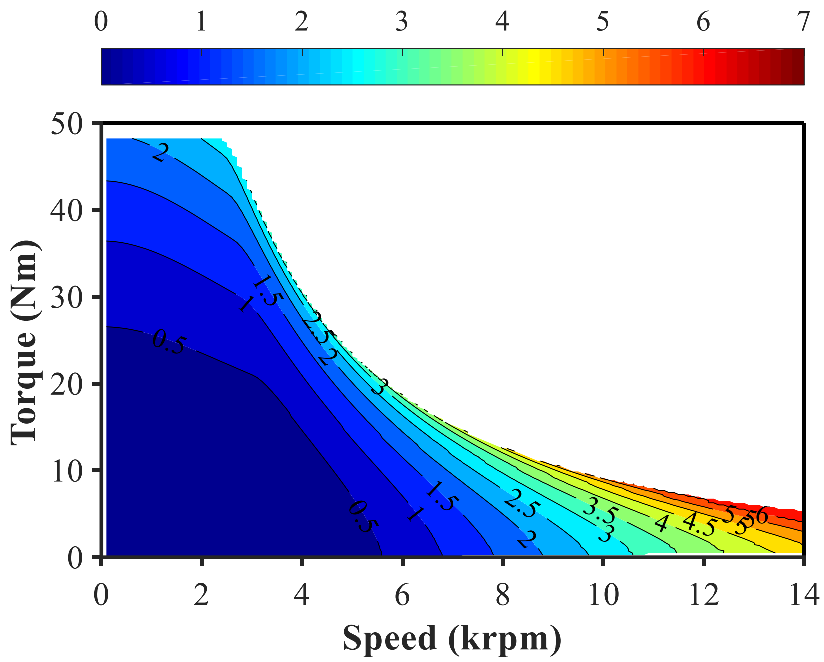

Fig. 4.17. Copper loss with considering AC effects (kW).

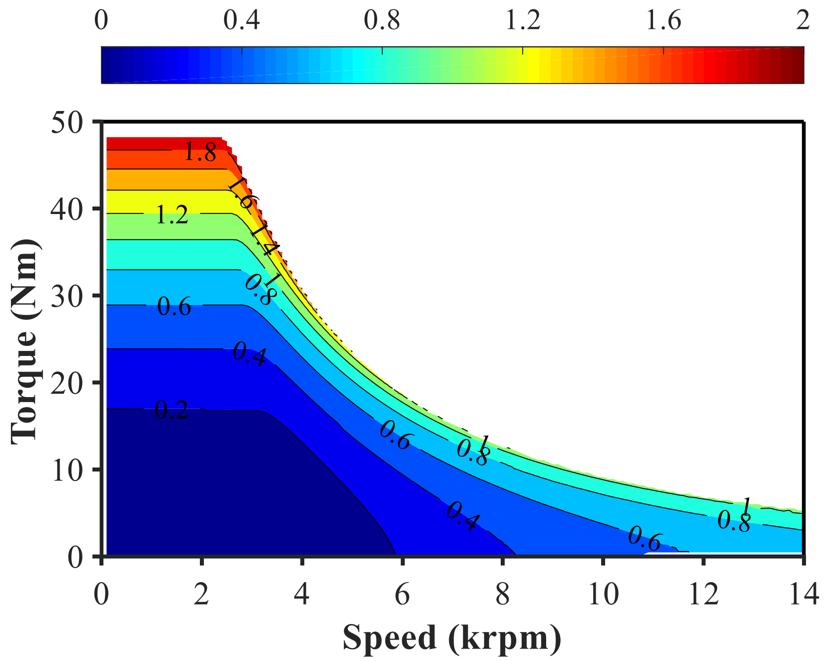

Fig. 4.18. The copper loss without considering AC effects (kW).

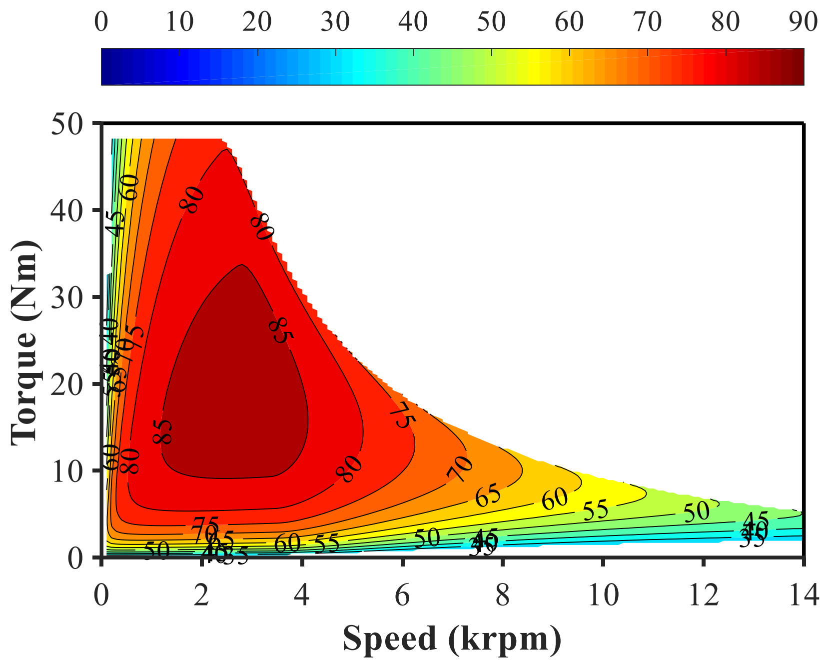

Fig. 4.19. The efficiency with considering AC effects (%).

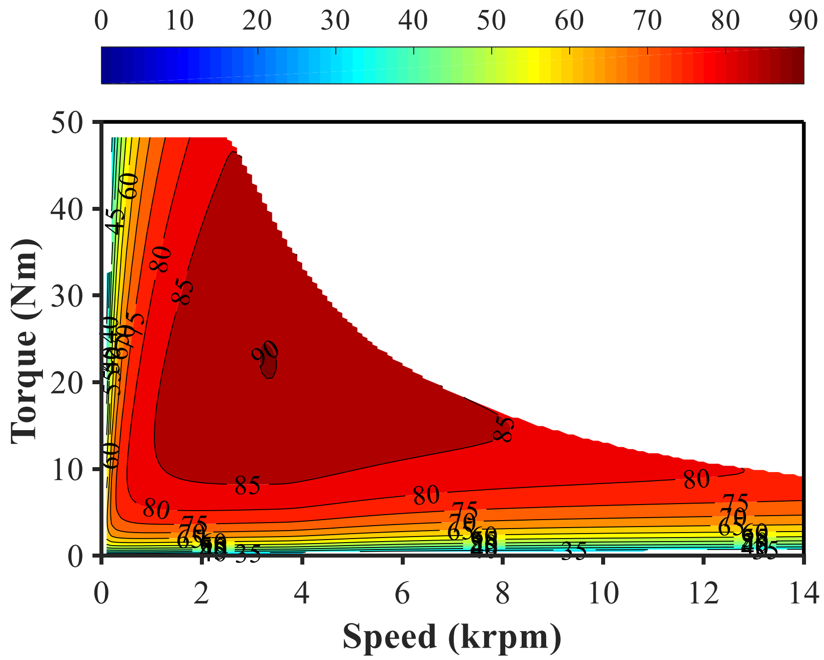

Fig. 4.20. The efficiency without considering AC effects (%).

4.5. Conclusion

The AC copper loss could be one of the major losses in the electrical machines especially with the large solid conductors and at high-speed operation. Generally, it is simply considered during the machine design process. However, a large amount of AC copper loss and high equivalent resistance limits the machine output power. An efficient and accurate hybrid method is proposed to predict the ac copper loss of the rectangular conductors at different temperatures. It is a faster method comparing with the pure FE method, and it can also consider the effects which are not considered in the existing analytical model. With the help of FE method, the saturation effect due to different d- and q-axis currents and geometry effect (i.e. slot tips and slot opening) can be considered. In addition, it is more convenient to couple with the thermal model to consider the temperature effect compared with FE.

By utilizing the proposed method, the torque/power-speed characteristics and efficiency maps can be obtained within a desirable computing time. It has been shown that the machine performance has a significant difference between with and without considering AC copper loss. When AC effect is ignored, the machine performance could be overestimated, especially in the high-speed operation region.

CHAPTER 5

Thermal Performance of PM Machines Accounting for AC Copper Losses

In this chapter, a simple lumped parameter thermal model is developed accounting for AC copper loss which is critical in the thermal analysis. It has been shown that with and without considering AC copper losses it results in an 80 °C difference in the winding temperature and 6 kW reduction in the maximum output power estimation. Compared with the finite element method, the developed model is effective and accurate to predict the actual loss and temperature in the windings. In addition, to reduce AC copper loss and limit the winding temperature, smaller conductors located at the bottom of the slot could be employed.

5.1. Introduction

There are several ways to estimate the temperature distributions at different positions in electrical machines, for example, by employing the lumped parameter thermal model (LPTM) [MEL91] and the finite element (FE) model [Bog08]. The LTPM is less accurate than the finite element method, but the computing time is much shorter [Bog09]. Indeed, for both LTPM and finite element method, the thermal transfer coefficients are required. The authors in [BOG08] focus on the determination of critical thermal parameters which are important in thermal models and have proposed the method to calculate them by different tests. There are a lot of existing LTPMs built by different authors for different types of machines including PM machines [Lee12] [Liu93] [Ref04] [Joo11], induction machines [Mel91] [Bog08] [Bog09] [Mel88] [Bou97] [Bog03] [Sta05] [Sta06], and switched reluctance machines [Li11]. Most of LTPMs are built based on the most classic paper on the thermal modelling of electrical machines [Mel91]. Both [Lee12] and [Ref04] present the LTPM of IPM machines. The authors in [Lee12] use the original equation presented in [Mel91] and also consider the heat transfer in the axial direction, while the authors in [Ref04] utilize the simplified equations and simplified internal convections with a lower number of nodes based on [Kyl95]. However, both of the models do not consider AC copper loss at high speed which is quite important for the machines employing the large rectangular conductors.

In this chapter, a simple lumped parameter model is developed with accounting for AC copper loss. It has been shown that AC copper loss is a major part of total losses in electrical machines, especially at high-speed operation. Thus, it is necessary to predict the temperature accounting for AC copper loss.

A method to balance the equivalent phase resistance at different low and high speeds is presented which maintains the same conductor per slot in the same stator. It has shown that by appropriately decreasing the conductor size the average temperature of the winding at high speed can be decreased significantly, albeit with sacrificed low-speed resistance and temperature. The optimum conductor size is selected based on the overall performance.

5.2. Lumped Parameter Thermal Model of Prototype IPM Machine

Fig. 5.1 shows the lumped parameter thermal network including the heat transferring in three directions based on [Ref04] [Bog03]. This model is intended to compute the temperature distribution in the prototype IPM machine in a steady-state condition. For this reason, thermal capacitances have been neglected. The two voltage sources represent the ambient temperature and the water temperature in the water jacket. There are 4 major losses are considered in this model which are the stator and rotor iron losses (P_{Fe_s} and P_{Fe_r}), copper loss in active length (P_{Cu_a}) and copper loss in end winding (P_{Cu_e}). Since this model is built for the spoked IPM machines, the magnet is not totally covered by rotor laminations and can directly contact the air in the air gap. Thus, there are a totally 4 convection resistors in the air gap ($R_{11} - R_{13}$, R_{15}). The geometry and parameters of the prototype machine are summarized in the Appendix.

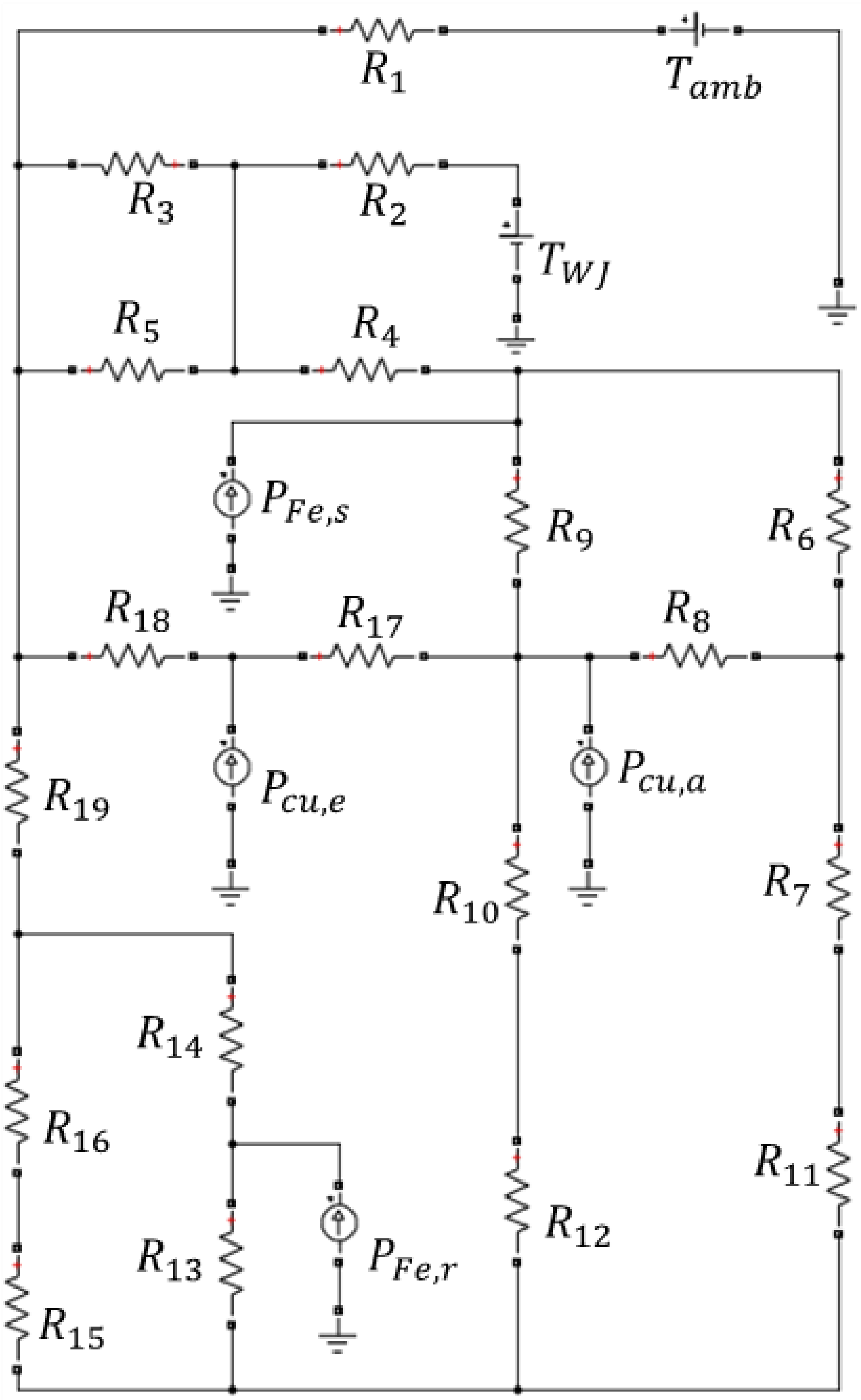

Fig. 5.1. The simplified LPTM of IPM machine.

5.2.1. External Convection Resistances (R_1 and R_2)

The resistor R_1 represents the combination of natural convection and radiation between the external housing and the nearby ambient air. For a self-coolant machine, this resistor is the most important factor since it determines the capability of heat dissipation. As [Bog08] [Sim88] [Sta05] mentioned, this resistor can be determined by a DC current test. During the test, the rotor is locked to ensure only DC copper loss in the stator winding. Thus, the thermal resistance can be computed by the following equation:

$$R_1 = \frac{T_{housing} - T_{amb}}{P_{dc}} \tag{5.1}$$

where $T_{housing}$ is the external frame temperature during DC test, T_{air} is the ambient temperature during the DC test, and P_{dc} is the power loss during the DC test.

$$\begin{aligned} N_{u,WJ} = {} & 7.49 - 17.02\frac{H}{W} + 22.43\left(\frac{H}{W}\right)^2 - 9.94\left(\frac{H}{W}\right)^3 \\ & + \frac{0.065\left({D_h}/{L_a}\right) R_e P_r}{1 + 0.04\left({D_h}/{L_a}\, R_e P_r\right)^{2/3}} \end{aligned} \tag{5.2}$$

$$D_h = \frac{4 * W * H}{4 * (W + H)} \tag{5.3}$$

$$h_{WJ} = \frac{N_{u,WJ} * \lambda}{L_c} \tag{5.4}$$

$$R_2 = \frac{1}{h_{WJ} A_{WJ}} \tag{5.5}$$

where H is the height of the channel, W is the width of the channel D_h is the hydraulic diameter, L_a is the active length of the water jacket, R_e and P_r are the Reynolds number and the Prandtl number, L_c is the characteristic length and equal to the hydraulic diameter in this case, and A_{WJ} is the outer surface area of the water jacket.

5.2.2. Conduction in Housing ($R_3 - R_5$)

R_3 represents the radial conduction resistor between the outer surface and the water jacket which is a region from R_{wout} to R_{hout} shown in Fig. 5.2.

$$R_3 = \frac{1}{2\pi\lambda_{hou}L_h}\ln\left({R_{hout}}/{R_{wout}}\right) \tag{5.6}$$

where R_{hout} is the outer radius of the housing, R_{wout} is the inner water jacket radius, L_h is the housing stack length, and λ_{hou} is the thermal conduction coefficient of the housing.

R_4 represents the combined radial conduction resistor from the stator back-iron to the water jacket. In this case, R_4 can be regarded as three resistors in series. R_{bi_out} and $R_{housing\_in}$ represents the radial conduction resistor of the outer part of the back-iron and the inner part of the housing, respectively. Due to the machine manufacture and assembly tolerances, there has a small gap between the housing and the lamination. R_{ig} represents the thermal resistor of the thin gap, and the equation (5.9) is a different form from the other two equations. It is due to that the gap length is extremely small comparing with the width, and the circular ring can be treated as a long and thin rectangle.

$$R_4 = R_{bi\_out} + R_{ig} + R_{houing\_in} \tag{5.7}$$

$$R_{bi\_out} = \frac{1}{2\pi\lambda_{lam}L_s}\ln\left({R_{sout}}/{R_{sm}}\right) \tag{5.8}$$

$$R_{ig} = \frac{l_{ig}}{2\pi R_{sout}\lambda_{air}L_s} \tag{5.9}$$

$$R_{housing\_in} = \frac{1}{2\pi\lambda_{hou}L_h}\ln\left({R_{win}}/{R_{sout}}\right) \tag{5.10}$$

where R_{win} is the inner radius of the water jacket, R_{sout} is the outer radius of the stator lamination, R_{sm} is the average radius of the stator back-iron, l_{ig} is the length of the interface gap between the housing and the lamination, L_s is the stack length of stator lamination, λ_{lam} and λ_{air} are the thermal conduction coefficients of lamination material and air, respectively.

Besides the radial thermal transfer, the heat is also transferring in the axial direction in the housing. R_5 represents the axial thermal resistor from the center of the housing to the end-plates.

$$R_5 = \frac{L_h}{4\pi\lambda_{hou}(R_{hout}^2 - R_{sout}^2)} \tag{5.11}$$

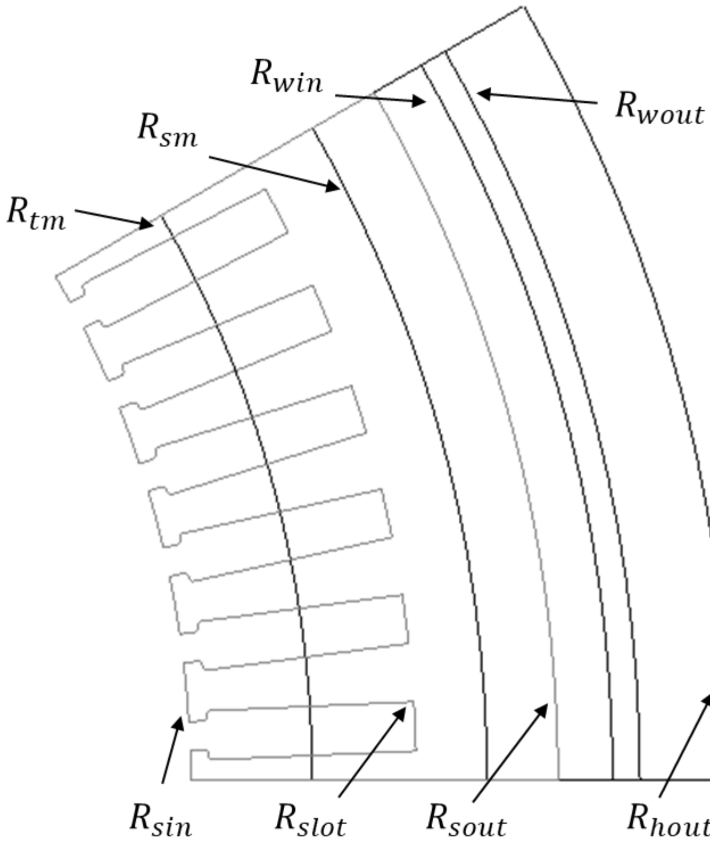

Fig. 1.2. Main radii of stator and housing.

5.2.3. Conduction in Stator ($R_6 - R_{10}$)

R_6 represents the inner stator back-iron behind the teeth and the top half of stator teeth. Although this thermal resistor is a combined one like R_4, it can be calculated directly because of the same material and the same stack length. Different from other radial thermal resistance, the stator teeth are separated by slots. Thus, a ratio of tooth arc to slot pitch is introduced as follows,

$$R_6 = \frac{\theta_{tp}/\theta_{ta}}{2\pi\lambda_{lam}L_s}\ln\left({}^{R_{sm}}/_{R_{tm}}\right) \tag{5.12}$$

where R_{sm} is the mean radius of the stator back-iron, R_{tm} is the mean radius of the stator teeth, θ_{ta} is the tooth arc, θ_{tp} is the tooth/slot pitch.

Similarly, the bottom part of the stator teeth can be calculated by the same equations with different radius. In this case, the slot tips are ignored and the slot is a rectangular shape.

$$R_7 = \frac{\theta_{tp}/\theta_{ta}}{2\pi\lambda_{lam}L_s}\ln\left({}^{R_{tm}}/_{R_{sin}}\right) \tag{5.13}$$

where R_{tm} is the mean radius of the stator teeth, R_{sin} is the inner radius of the stator core.

R_8 and R_9 are the thermal resistors between the slot windings and the stator core in circumferential and radial directions, respectively. R_8 can be calculated by

$$R_8 = \frac{l_{eqs}}{N_s\lambda_{eq}L_s d_{slot}} \tag{5.14}$$

$$l_{eqs} = \frac{S_{slot} - S_{cond}}{l_{peri}} \tag{5.15}$$

where l_{eqs} is the equivalent length of air and insulations in the slots, λ_{eq} is the equivalent thermal coefficient of air and insulations in the slots, d_{slot} is the depth of the slot, S_{slot} is the area of one slot, S_{cond} is the total area of the conductors in one slot, and l_{peri} is the perimeter of the stator slot, N_s is the number of slots.

While R_9 is a combined thermal resistor including the inner half of the stator back-iron behind the slots. This resistor R_{bi_in} can be calculated based on R_6. There is a ratio of θ_{tp}/θ_{ta} in R_6 representing the stator back-iron behind the teeth. Thus, a ratio of (1-θ_{tp}/θ_{ta}) should be introduced in R_{bi_in} to maintain the sum equal to 1.

$$R_9 = R_{bi\_in} + R_{slot\_bi} \tag{5.16}$$

$$R_{bi\_in} = \frac{1 - \theta_{tp}/\theta_{ta}}{2\pi\lambda_{hou}L_s} \ln\left({}^{R_{sm}}/_{R_{tm}}\right) \tag{5.17}$$

$$R_{slot\_bi} = \frac{2l_{eqs}}{N_s\lambda_{eq}L_s w_{slot}} \tag{5.18}$$

R_{10} represents the thermal resistor in the bottom half of the slot. It can be calculated as the same equation of R_{slot_bi}. The equivalent thermal coefficient of air and insulations can be determined by DC test [Bog03].

$$R_{10} = R_{slot\_bi} = \frac{2l_{eqs}}{N_s\lambda_{eq}L_s w_{slot}} \tag{5.19}$$

5.2.4. Axial Transferring of Winding (R_{17} and R_{18})

The heat generated in the winding is not only transferring to the stator core but also transferring from the end-winding regions to the end-plates. Since this transferring is in the axial direction, the thermal resistor can be calculated by the definition equation (5.20). The nominator in equation (5.20) is $L_s/2$ representing the heat transferring from the center of the object to one of the end. However, the heat must transfer in parallel from the center to both two ends. Thus, the axial thermal resistor of winding can be calculated by

$$R_{17} = \frac{L_s/2}{\lambda_{cu} S_{cu}}/2 \tag{5.20}$$

where S_{cu} is the total area of the copper in all slots, λ_{cu} is the thermal conduction coefficient of copper.

For the same reason, the convection resistors are also in parallel from two end-windings to the two end-plates. The convection coefficient from the end-windings to the end-plates can be estimated according to [Mel88] and [Bog03]. Thus, R_{18} can be calculated by

$$R_{18} = \frac{1}{2h_{ew}(R_{slot}^2 - R_{sin}^2)\pi} \tag{5.21}$$

$$h_{ew} = 15.5\,(0.15 R_{rout}\omega_r + 1) \tag{5.22}$$

where h_{ew} is the convection coefficient from the end-windings to the end-plates, R_{slot} is the radius of the bottom of the slot, R_{sin} is the inner radius of the stator, $(R_{slot}^2 - R_{sin}^2)\pi$ represents the cross-sectional area of the end-winding of one side, R_{rout} is the outer radius of the rotor and ω_r is the rotor mechanical speed.

5.2.5. Conduction in Rotor ($\boldsymbol{R_{14}}, \boldsymbol{R_{16}}, \boldsymbol{R_{19}}$)

The designed rotor has a complicated geometry for optimizing the electro-magnetic performance. To simplified the thermal modelling, the rotor can be treated as shown in Fig. 5.3.

R_{14} represents the heat conduction of the rotor pole in the radial direction behind the position of rotor iron loss generated. Assuming the iron loss is generated at $R_{fe,r}$, the resistor R_{14} actually means the heat transfer from R_{r1} to R_{rin}. Similar to the stator teeth and slots, there is a ratio of rotor arc to rotor pole pitch introduced to correct the actual surface area of rotor lamination.

$$R_{14} = \frac{\theta_{rp}/\theta_{fe,r}}{2\pi\lambda_{lam}L_s} \ln\left({}^{R_{fe,r}}\!\big/_{R_{rin}} \right) \tag{5.23}$$

where $R_{fe,r}$ is the assumed position of iron loss generation, R_{rin} is the radius of the bottom of the rotor magnet slot, θ_{rp} is the rotor pole pitch, and $\theta_{fe,r}$ is the rotor pole arc at $R_{fe,r}$.

R_{16} is a combined resistor including the thermal conduction of PMs in the radial direction and the equivalent conduction between PMs and rotor poles. In addition, the PM can be divided into two parts e.g. a rectangular top component and a trapezoidal bottom component. It should be noted that the total area is used for calculation which is the cross-sectional area of one PM times the number of poles. The equation of trapezoidal components is modified according to [Liu93]. The equivalent conduction between PMs and rotor poles can be calculated as the same method of stator slot to the stator core.

$$R_{16} = R_{PM,top} + R_{PM,bot} + R_{PM,rot} \tag{5.24}$$

$$R_{PM,top} = \frac{H_{mt}}{N_p\lambda_{pm}L_sW_{mt}} \tag{5.25}$$

$$R_{PM,bot} = \frac{H_{mb} \ln \left({W_{mt}}/{W_{mb}} \right)}{N_p \lambda_{pm} L_s (W_{mt} - W_{mb})} \tag{5.26}$$

$$R_{PM,rot} = \frac{\frac{S_{slot,pm} - S_{pm}}{l_{peri,pm}}}{N_p \lambda_{air} L_s l_{peri,pm}} \tag{5.27}$$

where H_{mt}, W_{mt}, H_{mb}, W_{mb} are the height and width of the top and bottom parts of PMs, respectively, λ_{pm} is the thermal conduction coefficient of PM, N_p is the number of the pole, $S_{slot,pm}$ is the area of rotor magnet slot, S_{pm} is the area of PM, and $l_{peri,pm}$ is the perimeter of PM.

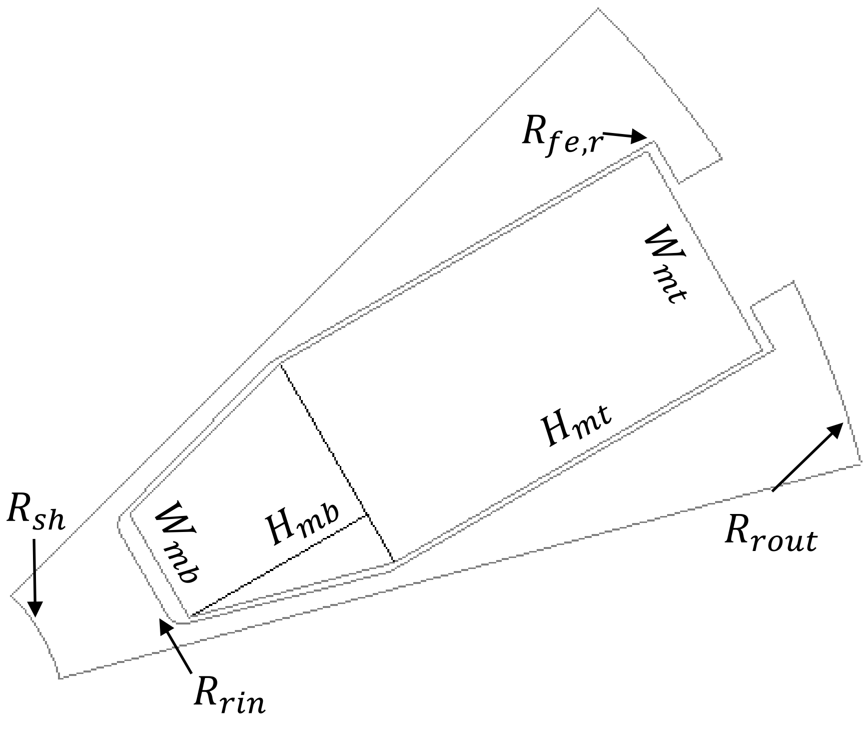

Fig.5.3. Simplified geometry of the rotor.

5.2.6. Convection in Air-gap ($\boldsymbol{R_{11}-R_{13}},\ \boldsymbol{R_{15}}$)

There are four resistors related to the convection in the air-gap. R_{11} is the convection resistor at the surface of stator teeth, R_{12} is the convection resistor at the slot region, R_{13} represents the convection resistor at the surface of rotor poles and the radial conduction of the top of the rotor pole, and R_{15} expresses the convection resistor at the surface of the PMs.

$$R_{11}=\frac{\theta_{tp}/\theta_{tta}}{2\pi h_{ag}L_s R_{sin}} \tag{5.28}$$

$$R_{12}=\frac{1-\theta_{tp}/\theta_{tta}}{2\pi h_{ag}L_s R_{sin}} \tag{5.29}$$

$$R_{13}=\frac{\theta_{rp}/\theta_{ra}}{2\pi h_{ag}L_s R_{rout}}+\frac{\theta_{rp}/\theta_{ra}}{2\pi\lambda_{lam}L_s}\ln\left({R_{rout}}/{R_{fe,r}}\right) \tag{5.30}$$

$$R_{15}=\frac{1-\theta_{rp}/\theta_{ra}}{2\pi h_{ag}L_s R_{rout}} \tag{5.31}$$

where θ_{tp} is the stator tooth pitch, θ_{tta} is the surface arc of the stator tooth tip, θ_{rp} is the rotor pole pitch, θ_{ra} is the outer surface arc of the rotor pole, h_{ag} is the forced air convection in the air-gap which can be computed as (5.32). Since the air-gap is a narrow ring with $R \gg l$, the characteristic length is twice the air-gap length.

$$h_{ag}=\frac{N_u\lambda_{air}}{2l_g} \tag{5.32}$$

where λ_{air} is the air conduction coefficient, l_g is the air-gap length, and N_u is the Nusselt number.

There are two methods to compute the Nusselt number. The first one is related with the Reynolds number and the Prandtl number. Firstly, the critical Reynolds number should be calculated as a reference,

$$R_{e,cr} = 100\sqrt{R_{sin} l_g} \tag{5.33}$$

The Reynolds number of different fluid speeds in the air-gap can be calculated as equation (5.34). The Nusselt number can be calculated by the following relationships [Bog03],

$$\begin{cases} N_u = 2, & R_e < R_{e,cr} \\ N_u = 0.386 \dfrac{1}{\sqrt{R_{sin} l_g}} P_r^{0.27}, & R_e > R_{e,cr} \end{cases} \tag{5.34}$$

where R_e and P_r are the Reynolds number and the Prandtl number of fluid speed, respectively.

The second method to determine the Nusselt number is according to the Taylor number [Tri06] [Bec62].

$$\begin{cases} N_u = 2, & T_a < 1078 \\ N_u = 0.128 {T_a}^{0.367}, & 1800 < T_a < 12000 \\ N_u = 0.409 {T_a}^{0.241}, & 12000 < T_a < 4 \cdot 10^6 \end{cases} \tag{5.35}$$

where T_a is the Taylor number of fluid speed.

5.3. DC Test for Critical Parameters

As mentioned previously, a DC test is taken to determine the critical coefficients. This test is taken in the chamber with fixed air temperature equal to 90°C to simulate the engine temperature. The inlet liquid temperature of the stator water jacket is 65°C . The flow rate of the liquid is 6L/min in the channel with 2.35mm height and 62mm width. The computed coefficients of the water jacket are shown in Table 5.1. The tested IPM prototype machine has 72 slots and 12 poles and dual-three phase windings with a 30° difference to achieve the maximum winding factor. During the DC test, the current increases from 20A to 120A to avoid demagnetization. Figs.5.4 and 5.5 compare the temperatures in windings and stator back-iron measured and predicted by the proposed thermal model together with Motor-CAD. The largest difference between the measurement and the prediction occurs in the winding at 20A, and the difference is 1.2°C. The critical parameters obtained by the DC current tests and material thermal coefficients are listed in Table 5.2.

Table 5.1. Parameters of Cooling Liquid and Coolant Channel

Parameter	Value (Unit)
Channel height	2.35mm
Channel width	62mm
Specific heat capacity of the liquid	3436 J/(Kg·°C)
Density of the liquid	1053 Kg/m^3
Thermal conductivity of the liquid	0.3927 W/(m·°C)
Flowing rate	6 L/min
Water jacket convection coefficient	1133 W/(m^2·°C)
Reynold number	2319
Prandtl number	12.35

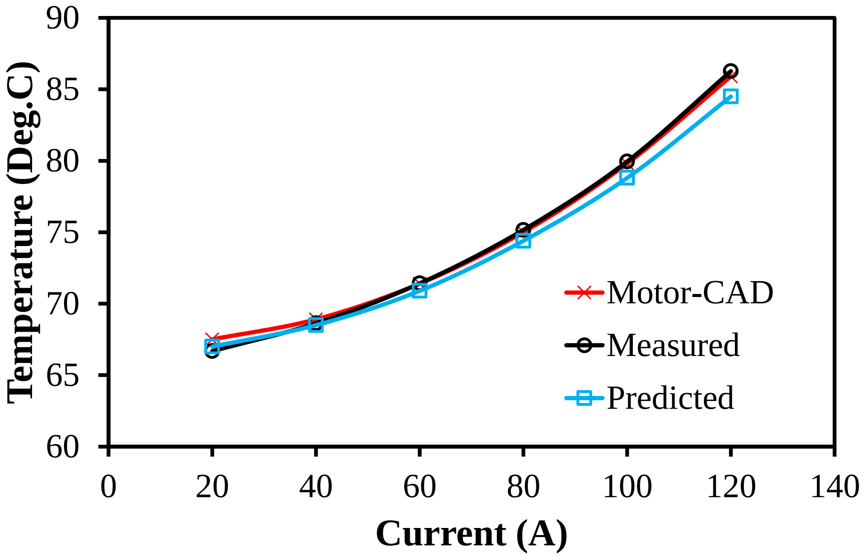

Fig. 5.4. Measured and predicted winding temperatures in DC tests.

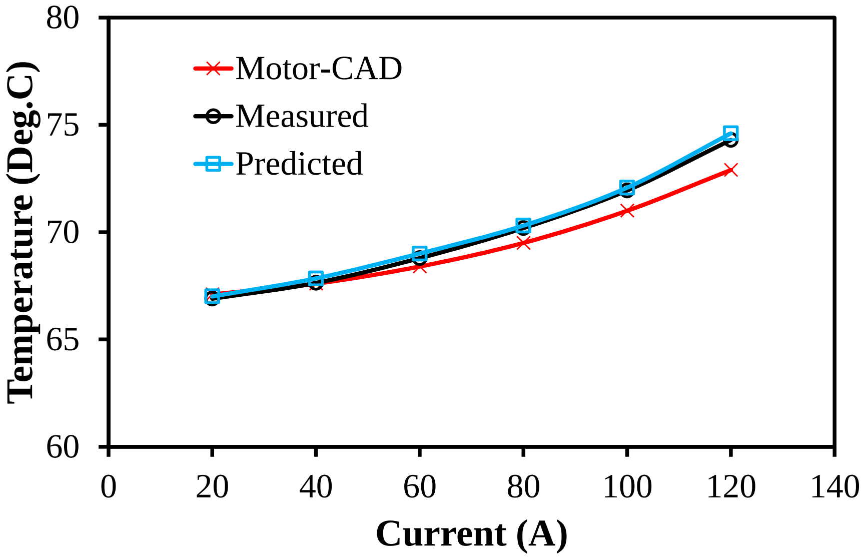

Fig. 5.5. Measured and predicted back-iron temperatures in DC tests.

TABLE 5.2. Parameters of Thermal Model

Parameter	Value (Unit)
External convection resistor	2.1 W/°C
Interface gap	0.015 mm
End-winding convection to end-plates	6.1 W/(m^2·°C)
Slot conduction coefficient	0.15 W/(m·°C)
Copper conduction coefficient	401 W/(m·°C)
Lamination conduction coefficient	30 W/(m·°C)
PM conduction coefficient	2.9 W/(m·°C)
Housing conduction coefficient (Al)	168 W/(m·°C)

5.4. Influence of Conductor Size on Temperature and AC Copper Loss

It is shown in Fig. 4.1 that the high-speed AC copper loss is much higher than the DC copper loss for the prototype machine. The temperature of the conductor should be also higher when AC copper loss is considered. It is presented in [Aoy18] and [Bar18] that the AC copper loss can be reduced by utilizing the smaller conductors, increasing the parallel paths, or introducing a space at the slot opening. However, due to the manufacture consideration, it is more convenient to employ a smaller number of parallel paths. The purposed method in this chapter is to balance the equivalent phase resistance of all speeds, high and low speeds, by varying the conductor size. Thus, it is worth comparing the machine performance with different conductor sizes. It should be noted that the conductors are always located at the bottom of the same slot shown in Fig. 5.6. The insulation thicknesses d_1 and d_2 keep the same when varying the conductor height H_c.

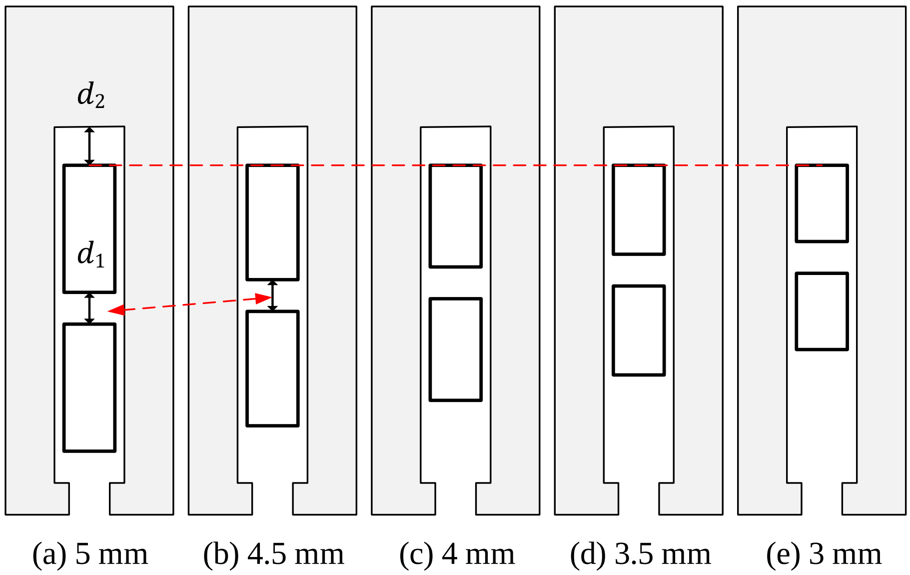

Fig. 5.6. The same slot with different conductor height.

Figs. 5.7 and 5.8 show the phase resistance and the ratio of R_{ac} to R_{dc} at 20 °C for different conductor sizes. Although the DC resistance is higher for the smaller conductors due to the smaller conducting area, the high-speed AC copper loss is much smaller. In addition, since the slot dimensions and the number of the conductor per slot are kept the same, the thermal network is shown in Fig. 5.1 does not change except the resistance value. The smaller conductors result in the increased thermal resistance in the same slot. It can be simply explained as the packing factor decreased and more insulation material is used in the slot. It can be seen that the most significant component is the outer conductor close to the slot opening, due to the small conductors located at the bottom of a slot. However, this resistance is not on the main path of the heat-dissipating. The major heat in the slot flows into the stator teeth and back-iron and finally sunken by the water jacket in the housing. These components do not have a great change since the stator and the location of the inner conductor keep the same. The only changed resistance is the conductor to teeth due to the conducting area reduced for smaller conductors. Another part of the heat transfers in the axial direction to the end-winding and convents to the housing. The resistance representing for the axial transferring in conductors increases with reducing conductor size due to the smaller conducting area. However, the resistance representing for end-winding convection does not have a great change since it is mainly related to the speed, and the convection area does not reduce greatly. Thus, due to the big difference of the copper loss and relatively minor difference of the thermal resistance, the temperature of the conductor is mainly influenced by the loss generated in the slot.

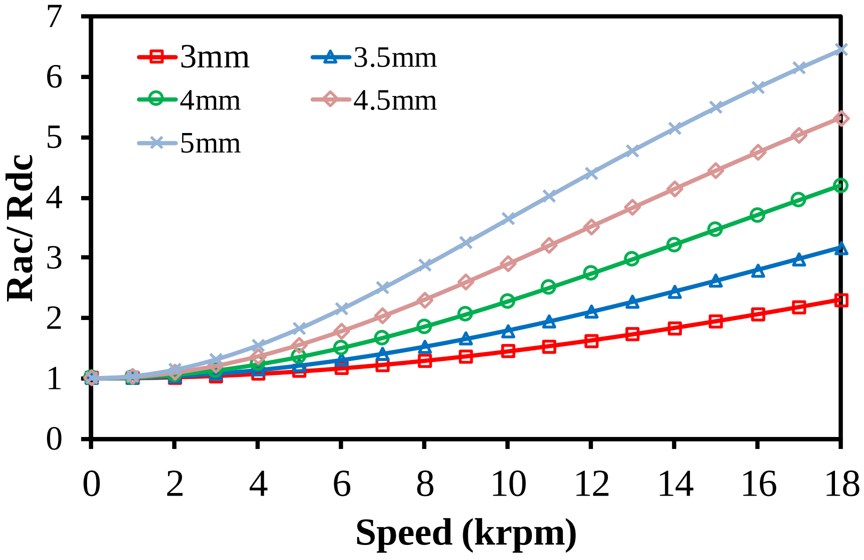

Fig. 5.7. AC to DC resistance ratio of different conductor sizes.

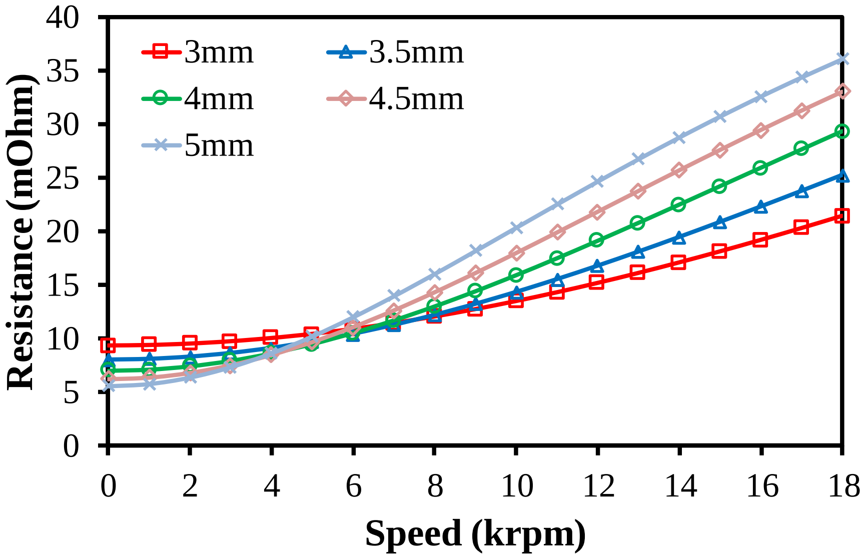

Fig. 5.8. Total phase resistance of different conductor sizes.

5.4.1. Full Load Transient Performance

Fig. 5.9 shows the full-load (230Arms) and transient (20s) machine performance with different conductor sizes considering AC copper loss and temperature. Fig. 5.9(a) compares the torque-speed characteristic between different conductor sizes. It can be seen that the maximum torque can be maintained and the high-speed torque can be improved with smaller conductors. However, the corner speed is slightly reduced due to higher resistance for smaller conductors in low-speed region. It is much clearer to see in the power-speed curves in Fig. 5.9(b) that with the larger conductors, the maximum power at the corner is the highest. However, the output power cannot be maintained and reduced with speed significantly. With a smaller conductor, the power-speed curve is flatter because of the less AC copper loss generated than the larger conductors shown in Fig. 5.9(b). Fig. 5.9(e) compares the variation of average conductor temperature between different conductor sizes with speed on the torque-speed curves. For the above torque-speed characteristic, the thermal network calculates the transient temperature of the conductors within 20 seconds for each speed. In this case, the ambient temperature is set at 25 °C, and the water jacket setting is the same as shown in Table 5.1. In the low-speed region, using smaller conductors resulting in the temperature increased by 20 degrees. However, it improves by a maximum of 60 degrees in the high-speed region. If the limited temperature of the conductor is 180 °C, the 5 mm and 4.5 mm conductors are not suitable for this application. It should be noted that the temperature of PM is not influenced during 20 seconds transient calculation.

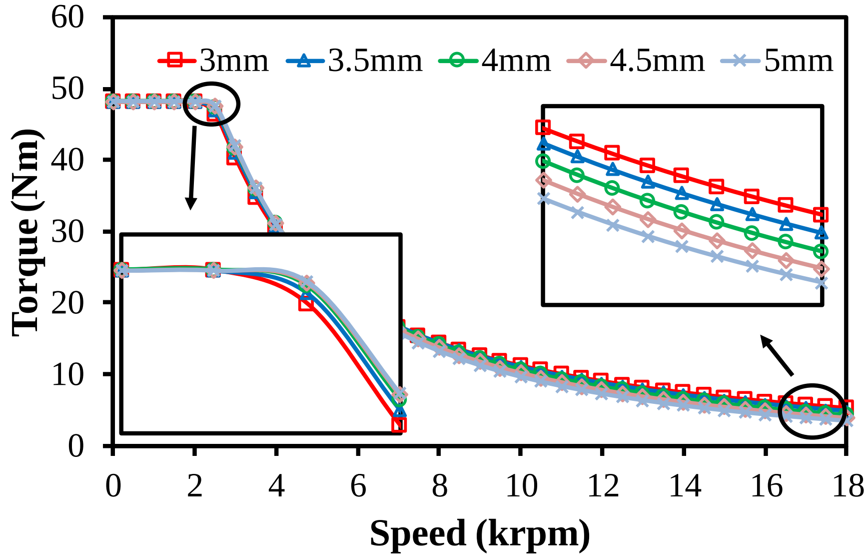

(a) Torque-speed curves

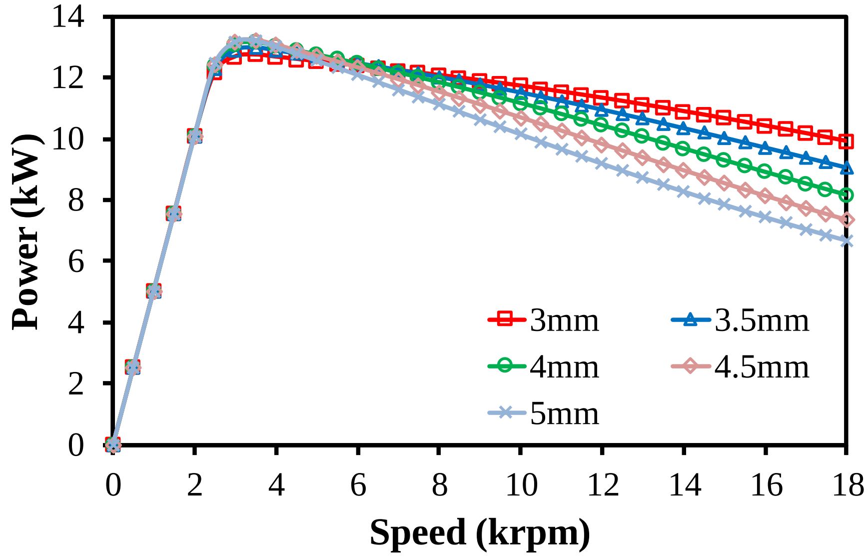

(b) Power-speed curves

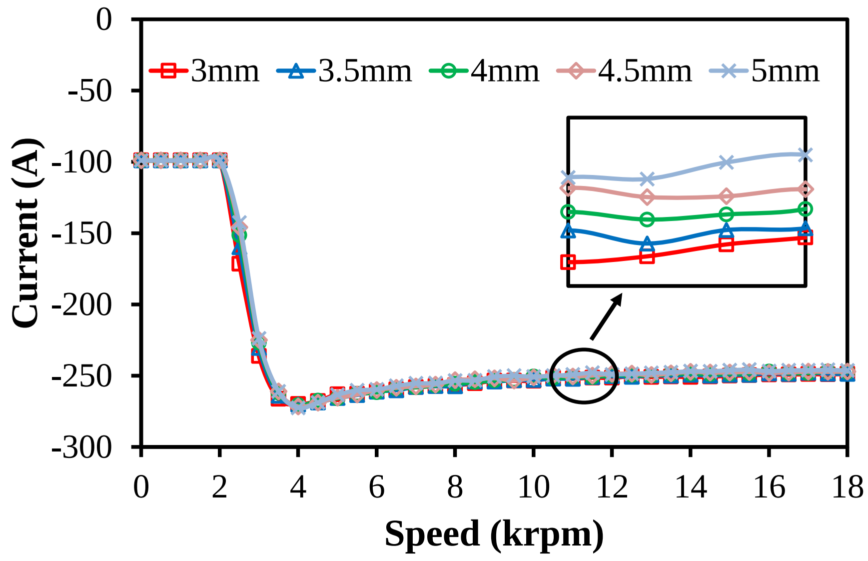

(c) D-axis currents

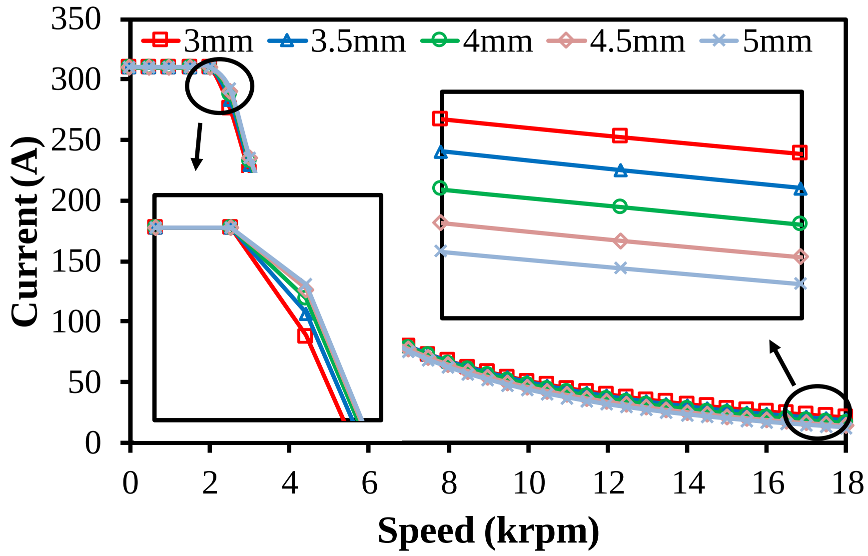

(d) Q-axis currents

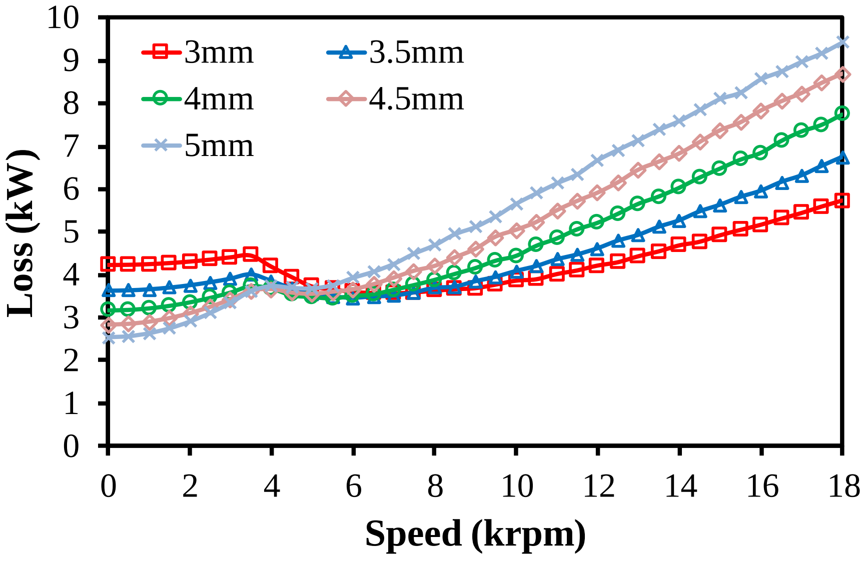

(e) Copper loss

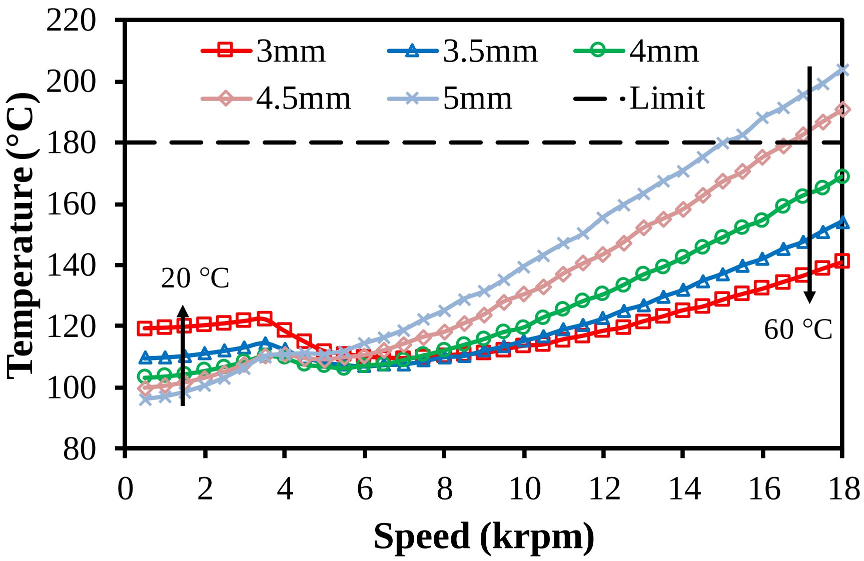

(f) The average temperature of the conductors in 20s

Fig. 5.9. Full load machine performance (transient) with different conductor sizes.

5.4.2. Half Load Steady-State Performance

The steady-state temperatures of the winding and the PM should also be considered. The steady-state temperatures are calculated with the half-load (120Arms) current from 0 rpm to 11 krpm, since the reduced current limits the maximum speed at 11 krpm. Although the copper loss is much lower in the continuous operation mode shown in Fig. 5.10(a). The temperatures are higher than the transient mode, as shown in Fig. 5.10 (b). For the same limited temperature of the winding, only 3.5 mm and 3 mm conductors can be employed. It is important that the temperature of the PM varies greatly as well, as shown in Fig. 5.10(c). From 0 rpm to 8 krpm, the PM temperature is lower with the 3.5mm conductor, and from 8 krpm to 11 krpm the 3mm conductor is better. The speed range of lower PM temperature with the 3.5 mm conductor is larger than the 3 mm conductor shown in Fig.5.10(d). In this case, the 3.5mm conductor is selected as the optimum choice.

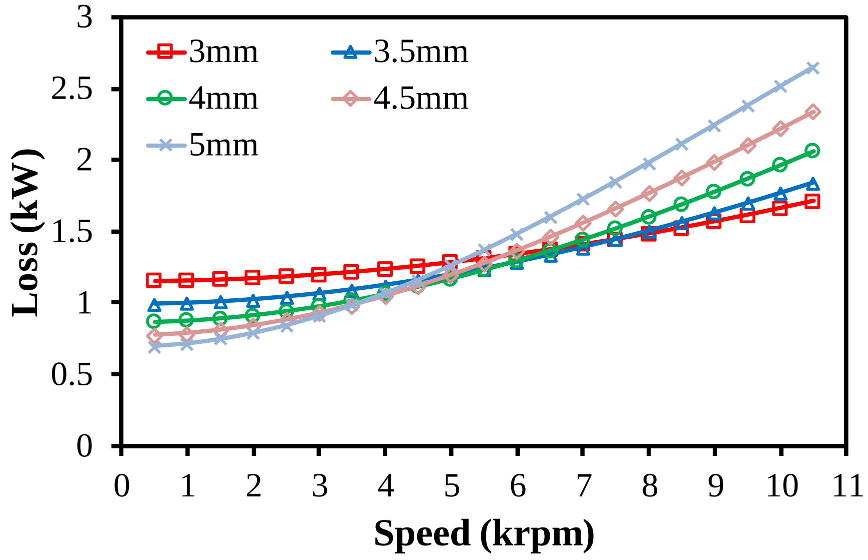

(a) Copper loss

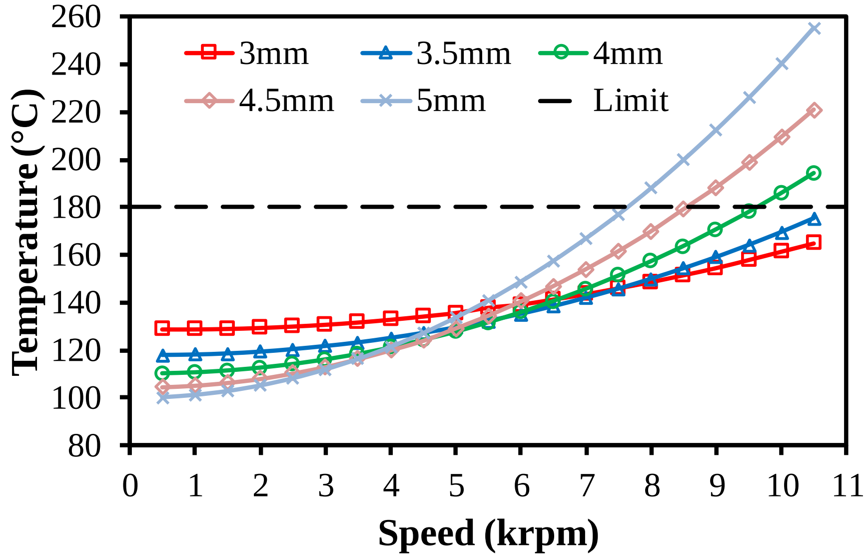

(b) The average temperature of the conductors

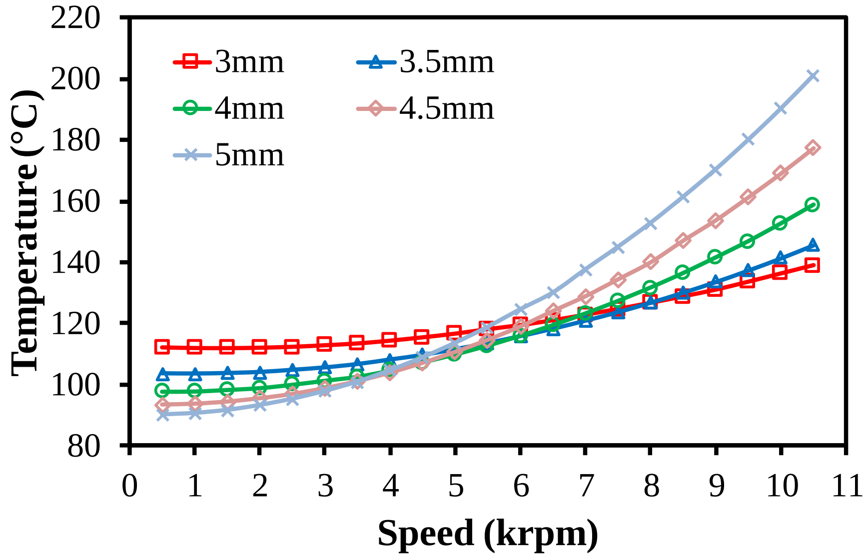

(c) The average temperature of the PMs with all conductors

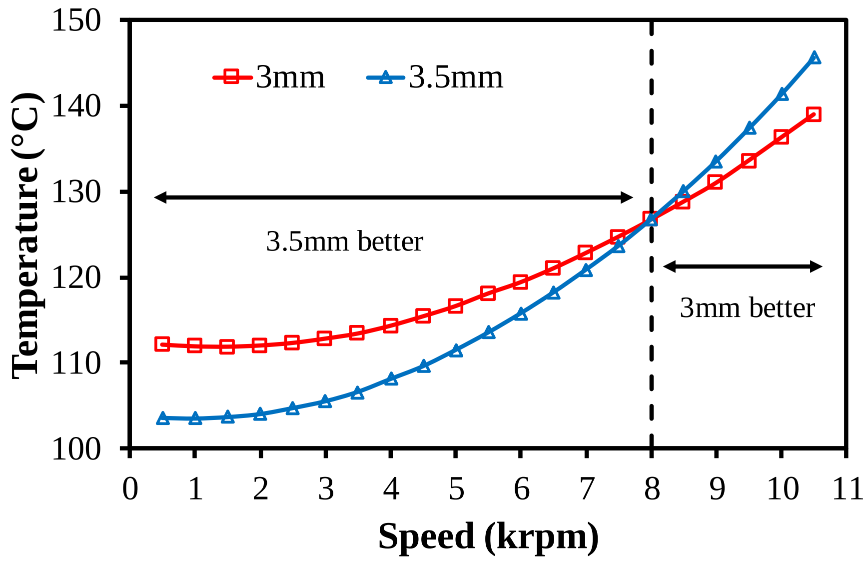

(d) The average temperature of the PMs with 3 mm and 3.5 mm conductors

Fig. 5.10. Steady-state temperatures with half-load current (120Arms).

5.5. Conclusion

AC copper loss could be one of the major losses in the electrical machines especially with the large solid conductors and at high-speed operation. It has been shown that the copper loss at high speed can be reduced by employing smaller conductors. However, the lower speed copper loss will be increased.

The optimal conductor size is found according to the overall loss and temperature. For smaller conductors, although DC resistance is increased, AC resistance can be limited significantly. Thus, not only the temperature but the field-weakening performance can also be improved. However, due to the higher DC resistance, the maximum power capability and corner speed could be affected and slightly reduced.

CHAPTER 6

One-Dimensional Lumped Parameter Thermal Model of Electrical Machines

In this chapter, a simple one-dimensional lumped parameter thermal model is developed. Comparing with the existing thermal models, the novel lumped parameter thermal model has fewer nodes with adequate accuracy. The proposed thermal model is built on the basis of the concentrated loss model, in which all losses are concentrated at one node. However, when the concentrated loss model is employed, it will lead to an excessive temperature rise, which results in an inaccuracy prediction. This chapter improves the accuracy of the concentrated loss model analytically by utilizing a compensation thermal voltage. It shows that the developed concentrated loss model has a simpler structure of the thermal resistance network and desirable accuracy comparing with existing lumped parameter models and finite element models.

6.1. Introduction

Permanent magnet machines are now widely used due to high power density and high efficiency. In consideration of the permanent magnets and winding insulation that are sensitive to the increase in temperatures, the operating temperature influences the performance of electrical machines [Zhu02] [Seb95]. In addition, the interaction between the temperature and the power loss should also be considered during the thermal analysis [Liu93a] [Xue16]. Thus, it is necessary to detect or accurately predict the temperatures of PMs and copper windings.

There are several ways to perform the thermal analysis of electrical machines, such as finite element method (FEM), computational fluid dynamics (CFD), and lumped parameter thermal model (LPTM) [Bog09]. The first two methods can model and analyze complicated device geometry while the computation time is very long. Due to the convenience of the network analysis, the LPTM is still the preferred method. When the LPTM is employed, the concentrated loss model is used to replace the distributed loss model in FEM. Nevertheless, the hot spot temperature is different between the concentrated loss model and the distributed loss model [Ger06a] [Ger06b]. The distributed loss model is defined as that with the loss generated uniformly inside the element, i.e. the material has a fixed loss density (g). The concentrated loss model means that the total loss of the element is generated at a surface of constant radius r inside the element and usually this radius is the mean radius in a cylindrical machine. The difference of temperature rises between the two loss models is caused by the unequable heat fluxes flow through the material, as will be discussed and analyzed in this chapter.

The lumped circuit thermal model of a cylindrical ring is presented in Fig. 6.1(a), the analyzed object is treated as an intact element (hollow cylinder) [Sim75]. The LPTM is shown in Fig. 6.1(b), where R_r is the thermal resistance between the inner radius r_1 and the outer radius r_2, T_1 and T_2 are the boundary temperatures at r_1 and r_2 respectively. However, in practice, it is desirable that the temperature inside the element should be detected or calculated. Thus, at least one node should be introduced and the object is divided into two parts, as shown in Fig. 6.1(c). There are generally two existing methods to divide the object into two elements according to the definition of the detected temperature, T' in Fig. 6.1(c). It should be noted that the thermal resistance R_r is divided into R_a and R_b.

In [Mel91], Mellor firstly investigated the average temperatures of the elements instead of the hot spot temperature. When the element generates an internal loss, an extra resistor is added to correct the error between the concentrated loss model and the distributed loss model. It should be noted that in Mellor's method, the element is not separated at a visible radius but an ideal location with the mean temperature. Some of the researchers followed Mellor's method and their LPTMs are generally complicated [Rob86] [Lee12] [Liu93b] [Mel88] [Li11] [Bou97].

Another method is based on the simplified LPTMs. The main idea is to separate the element at the mean radius, and treat the two small rings as zero loss generation [Sim14] [Bog03] [Zhu15] [Ref04] [Joo11] [Bog08] [Yu10] [Bim18]. All the losses are assumed to be generated at a surface inside the element, e.g. the surface of constant radius r_m in Fig. 6.1(a), which separates the original ring into two parts. Thus, a simpler expression can be employed. In [Ger06a], Gerling gave several methods to correct the calculation with concentrated loss, including modifying the loss to half value and adding two thermal voltage sources on the main branch. However, the investigation is only focused on the Cartesian coordinate, e.g. the heat transfers in the axial direction of the electrical machines.

This chapter further investigates this issue in the radial direction. A new LPTM with one compensation thermal voltage source on the sub-branch is proposed. The proposed model gives an accurate prediction of the hot spot temperature by a simple network. The temperature difference between the distributed loss model and the concentrated loss model is eliminated by the compensation thermal voltage, which is relatively isolated from the element with internal loss and other elements. It will be shown in this chapter that modifying the loss, modifying the conductivity, and compensation thermal voltage on the main branch are equivalent in an intact element with internal loss. However, in more complicated cases, their accuracy is decreased, while the proposed method can still give an accurate prediction.

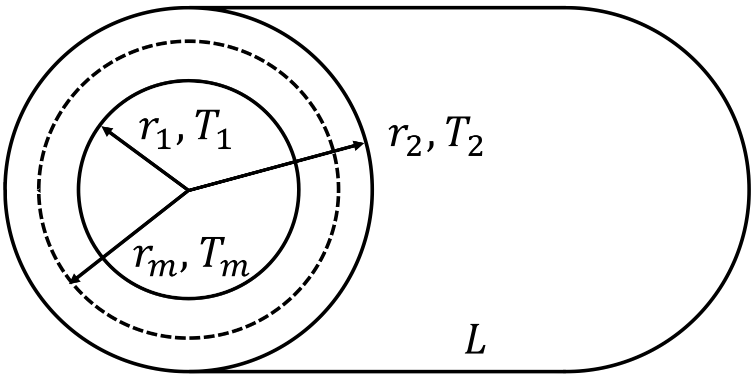

(a) Geometry

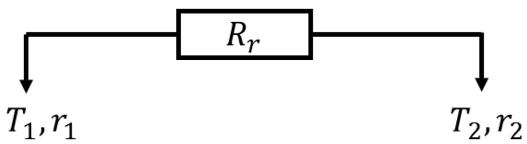

(b) LPTM without the center node

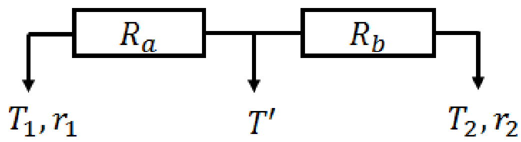

(c) LPTM with the center node

Fig. 6.1. Cylindrical ring and thermal networks.

6.2. Heat Transfer Equation and Conventional LPTMs

The one-dimensional heat conduction equation in the radial direction of a cylindrical ring, Fig. 6.1(a), can be described as,

$$\frac{\partial^2 T_r}{\partial r^2}+\frac{1}{r}\frac{\partial T_r}{\partial r}+\frac{g}{\lambda}=0 \tag{6.1}$$

where T_r is the radial temperature, r is the radius, g is the heat generated per unit volume (W/m^3), and k is the thermal conductivity.

The general solution of (6.1) gives the temperature profile radially,

$$T_r=a\ln r-\frac{gr^2}{4\lambda}+b \tag{6.2}$$

where a and b are constants.

By introducing the boundary conditions $T_r=T_1\,|_{r=r_1}$ and $T_r=T_2\,|_{r=r_2}$ into (6.2), the constants a and b can be determined. Thus, the radial temperature profile and the mean temperature can be obtained as,

$$T_r(r)=\frac{g}{4\lambda}\left[\frac{\ln {}^{r}/_{r_1}}{\ln {}^{r_2}/_{r_1}}(r_2^2-r_1^2)+(r_1^2-r^2)\right]+\frac{\ln {}^{r}/_{r_1}}{\ln {}^{r_2}/_{r_1}}(T_2-T_1)+T_1 \tag{6.3}$$

$$T_m=\left(\frac{T_2r_2^2}{r_2^2-r_1^2}-\frac{T_2}{2\ln\frac{r_2}{r_1}}\right)+\left(\frac{T_1}{2\ln\frac{r_2}{r_1}}-\frac{T_1r_1^2}{r_2^2-r_1^2}\right)+\frac{g}{8\lambda}\,(r_2^2+r_1^2)-\frac{g(r_2^2-r_1^2)}{8\lambda\ln\frac{r_2}{r_1}} \tag{6.4}$$

6.2.1. LPTMs of Cylindrical Ring without Internal Loss Generation

The heat transfer model in the radial direction can be analyzed in a cylindrical ring, as shown in Fig. 6.1(a). For the case without internal heat generation, the temperature distribution inside the element is due to the temperature difference between the inner surface and the outer surface. There are two sets of expressions to represent the thermal resistance in the radial direction, (6.5) and (6.6) [Ger06a] [Li11]. It should be noted that the size of the ring element is as follows [Xue16].

Set 1:

$$\begin{cases} R_{1a} = \dfrac{1}{4\pi\lambda L}\left[\dfrac{2r_2^2 \ln\left({}^{r_2}/_{r_1}\right)}{r_2^2 - r_1^2} - 1\right] \\ R_{1b} = \dfrac{1}{4\pi\lambda L}\left[1 - \dfrac{2r_1^2 \ln\left({}^{r_2}/_{r_1}\right)}{r_2^2 - r_1^2}\right] \\ R_{1m} = -\dfrac{\left[(r_2^2 + r_1^2) - \dfrac{4r_2^2 r_1^2 \ln\left({}^{r_2}/_{r_1}\right)}{(r_2^2 - r_1^2)}\right]}{8\pi\lambda L(r_2^2 - r_1^2)} \end{cases} \tag{6.5}$$

Set 2:

$$\begin{cases} R_{2a} = \dfrac{1}{2\pi\lambda L}\ln\left({}^{r_m}/_{r_1}\right) \\ R_{2b} = \dfrac{1}{2\pi\lambda L}\ln\left({}^{r_2}/_{r_m}\right) \end{cases} \tag{6.6}$$

where λ is the thermal conductivity of the material, L is the length of the cylindrical ring, r_1 and r_2 are the inner and outer radii, r_m can be any radius between r_1 and r_2, and generally, r_m is the mean radius.

The main difference between the two sets of equations is the definition of T' in Fig. 6.1(c). With the thermal resistance R_{1a} and R_{1b}, the temperature T' is the mean temperature of the whole element. With the thermal resistance R_{2a} and R_{2b}, T' represents the temperature at the selected radius r_m. By varying the value of r_m, the radial temperature profile can be obtained. With the same element size and the same boundary conditions, the temperature distribution is calculated by FEM and shown in Fig. 6.2. The radial temperature profile and the mean temperature are compared with the FEM results from point A to point B, as shown in Fig. 6.3. It can be seen that the temperature profile obtained by Set 2 is the same as FEM. While due to the different purposes, Set 1 expression can only give the mean temperature of the element.

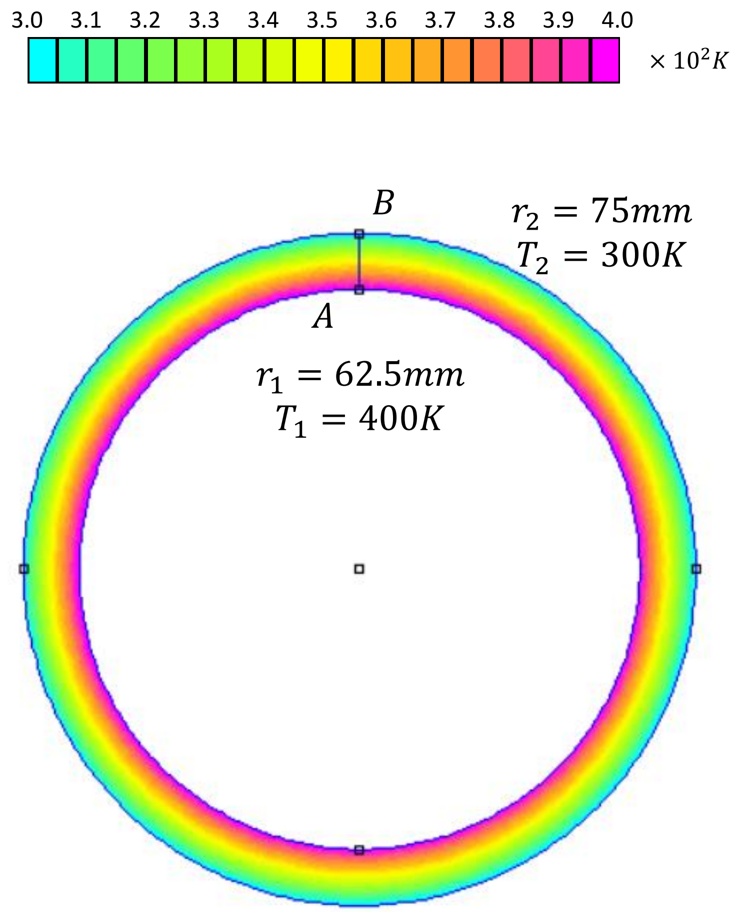

Fig. 6.2. Temperature distribution in FEM**.**

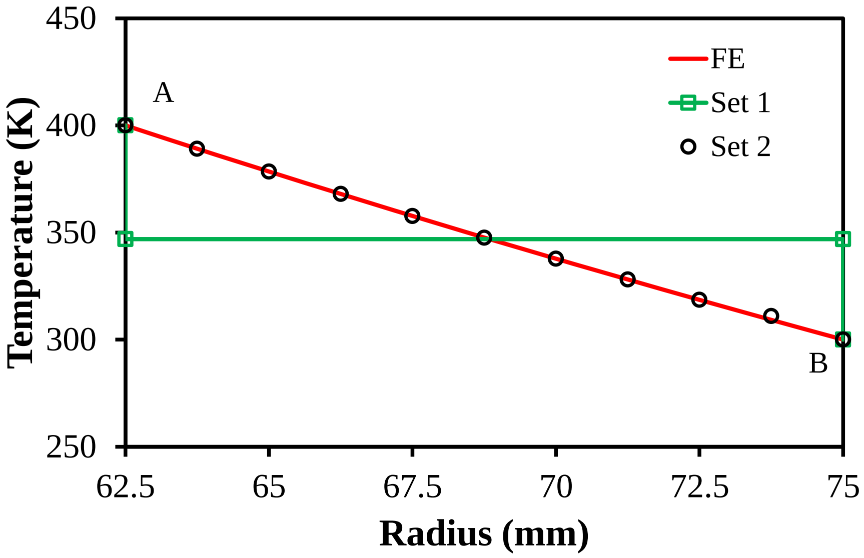

Fig. 6.3. Comparison of radial temperature profiles without heat generation between different methods.

6.2.2. LPTMs of Cylindrical Ring with Internal Loss Generation

For an element with an internal heat source, it is usually assumed that the heat density distribution is uniform inside the element. However, when the LPTM is used to analyze the thermal behavior, the heat source (G) is assumed to be concentrated at one face at either the geometry center or the mean radius for the Mellor's model and the simplified model, respectively, as shown in Fig. 6.4, where R_{1a}, R_{1b}, R_{1m}, R_{2a}, R_{2b} are the thermal resistances which can be found in (6.5) and (6.6), g is the loss density, V is the element volume and G is the total loss.

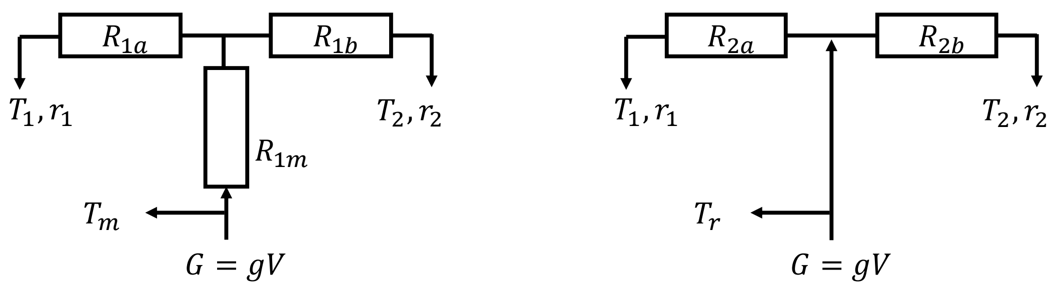

(a) Mellor's model (Set 1) **(b)** Simplified model (Set 2)

Fig. 6.4. LPTM models.

The difference between the real case (distributed loss) and the LPTM model (concentrated loss) can be demonstrated by the FEM analysis. Fig. 6.5 shows the cross-sectional temperature distributions with a distributed loss model and concentrated loss model. In the distribution loss model, the material between r_1 and r_2 is set with uniform loss density g. While in the concentrated loss model, the equivalent loss is applied to the mean radius r_m and the material loss density is 0. It should be noted that for simple analysis, the boundary temperatures at inner and outer radii are set as the same, i.e. $T_1 = T_2 = T_0 = 300K$. The radial temperature profile is compared in Fig. 6.6. It can be seen that with the concentrated loss model, the temperature profile is linearly increasing from both sides to the center of an element. However, the temperature profile is a second-order function when the distributed loss model is employed. In addition, both temperature profiles are not symmetrical since in the cylindrical ring the two surfaces are not the same. More importantly, the maximum temperature with concentrated loss is higher than the distributed loss. In Mellor's model, an additional resistance R_{1m} is added to the central node to eliminate the temperature difference between the different loss generation models, Fig. 6.4(a). This resistance is obtained from the circuit diagram and based on the correct temperature calculated by the analytical equation [Sim75]. However, an extra resistor and an extra node are generated. More importantly, the Mellor's model can give the average temperature accurately, while the hot spot temperature is more important to prevent the electrical machines from overheating. The following study is based on the simplified models.

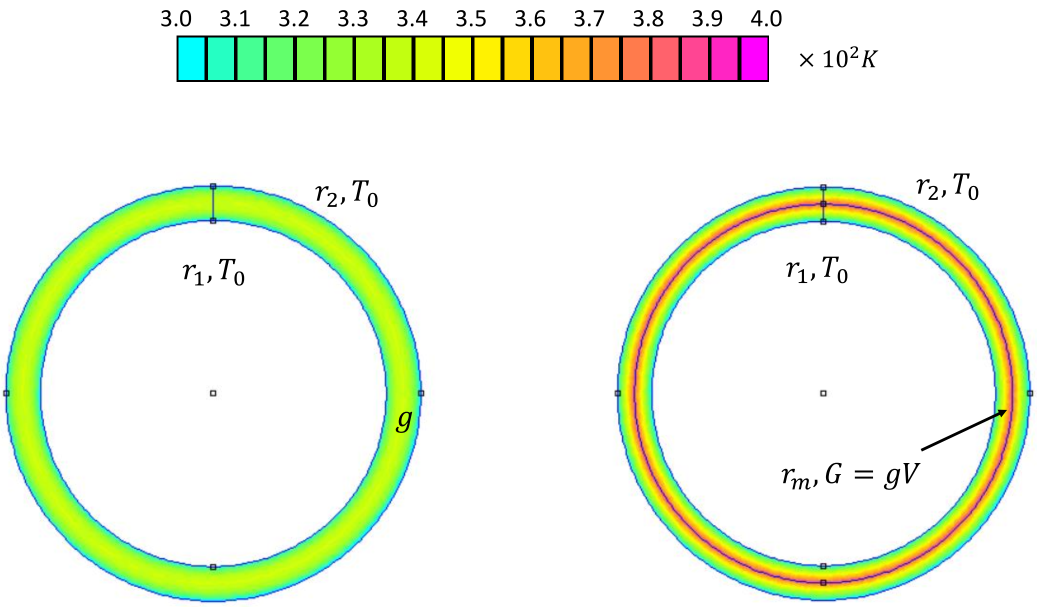

(a) Distributed loss model **(b)** Concentrated loss model

Fig. 6.5. Comparison of distribution loss model and concentrated loss model with the same loss in FEM.

The temperature difference between the distributed loss model and the concentrated loss model can be explained from the heat flux flowing rate and the flowed heat flux, as shown in Fig. 6.7 and Fig. 6.8, respectively. It should be noted that the heat flux H is calculated as the product of the heat flow rate F and the corresponding surface area. For the distributed loss model with uniform heat density, there is no heat at the geometry center with infinitesimal width and volume. By moving the radius to left or right, the generated heat increases with the radius difference from the geometry center and the covered volume. It should be noted that in the Cartesian coordinate, the heat flow rate F and the heat flux H is linear with the distance x, while in the cylindrical coordinate, the heat flow rate F and the heat flux H should be obtained from the heat transfer equations as,

$$F(r) = -\lambda \frac{dT_r(r)}{dr} \tag{6.7}$$

$$H(r) = (2\pi r L)F(r) \tag{6.8}$$

By substituting (6.3) into (6.7) and (6.8),

$$F(r) = \frac{g}{4}\left[2r - \frac{(r_2^2 - r_1^2)}{\ln {}^{r_2}/_{r_1}}\frac{1}{r}\right] \tag{6.9}$$

$$H(r) = \pi L \frac{g}{2}\left[2r^2 - \frac{(r_2^2 - r_1^2)}{\ln {}^{r_2}/_{r_1}}\right] \tag{6.10}$$

$$H(r) = \frac{G}{2(r_2^2 - r_1^2)}\left[2r^2 - \frac{(r_2^2 - r_1^2)}{\ln {}^{r_2}/_{r_1}}\right] \tag{6.11}$$

where G is the total heat which can be written as the product of the volume V and the heat density g.

As mentioned earlier, the generated heat is zero at r_s, where is the center of the distributed loss model in the ring. It is easy to obtain since H is a quadratic function. By applying the condition (6.12) to (6.11), the distributed loss center can be found in (6.13). In addition, since all the heat fluxes flow to the boundaries, the sum of the heat fluxes at r_1 and r_2 is equal to the total heat generated in the element, (6.14).

$$H(r_s) = 0 \tag{6.12}$$

$$r_s = \sqrt{\frac{(r_2^2 - r_1^2)}{2\ln {}^{r_2}/_{r_1}}} \tag{6.13}$$

$$H(r_2) - H(r_1) = G \tag{6.14}$$

The resultant temperature rise inside the element can be regarded as the sum of the product of the element thermal resistance and the heat flux. For the infinitesimal elements, the total heat received can be considered as the area under the heat flux curves shown in Fig. 6.8. Thus, the temperature rise can be calculated by the radial integration of H , as given by,

$$\Delta R_e = \frac{1}{2\pi\lambda L r} \tag{6.15}$$

$$\Delta T(r) = \Delta R_e H(r) \tag{6.16}$$

$$\Delta T_d = \int_{r_s}^{r_1} \Delta R_e H(r)\, dr \tag{6.17}$$

$$\Delta T_d = \frac{G}{4\pi\lambda L}\left[\frac{2\ln\left(\frac{\sqrt{\frac{(r_2^2 - r_1^2)}{2\ln {}^{r_2}/_{r_1}}}}{r_1}\right) - 1}{2\ln {}^{r_2}/_{r_1}} + \frac{r_1^2}{(r_2^2 - r_1^2)}\right] \tag{6.18}$$

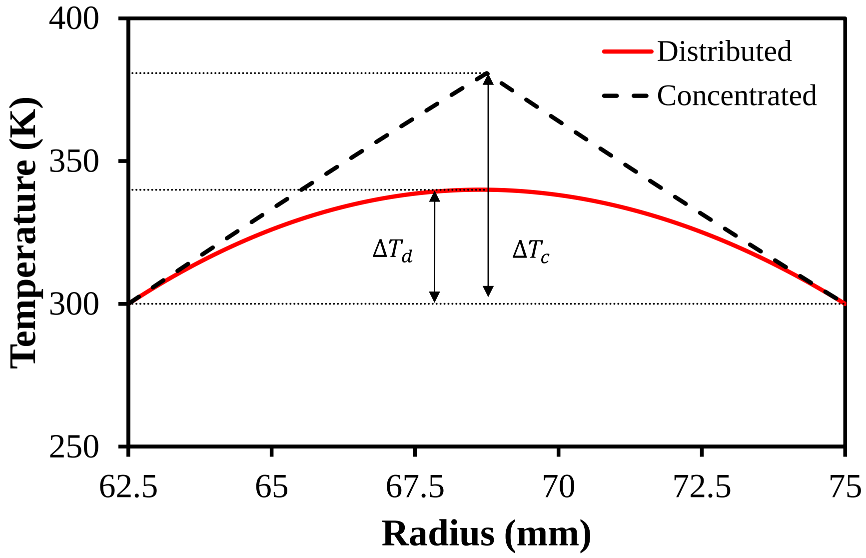

Fig. 6.6. Comparison of radial temperature profile between the distributed loss model and concentrated loss model.

When the concentrated loss is employed, the internal heat flux density is zero. However, the same amount of loss $G = gV$ is applied at the radial surface $r = r_m$. Thus, this amount of heat will flow to the inner surface and outer surface in parallel. Due to the area difference, the heat flow rate decreases with the radius for the outer half of the ring, i.e. 68.75mm to 75mm, while it increases in another half as shown in Fig. 6.7. In addition, more heat flows to the outer surface and less heat flows to the inner surface, as shown in Fig. 6.8. The temperature difference, ΔT_c, between the hot spot and the inner boundary is shown in (6.19) and (6.20).

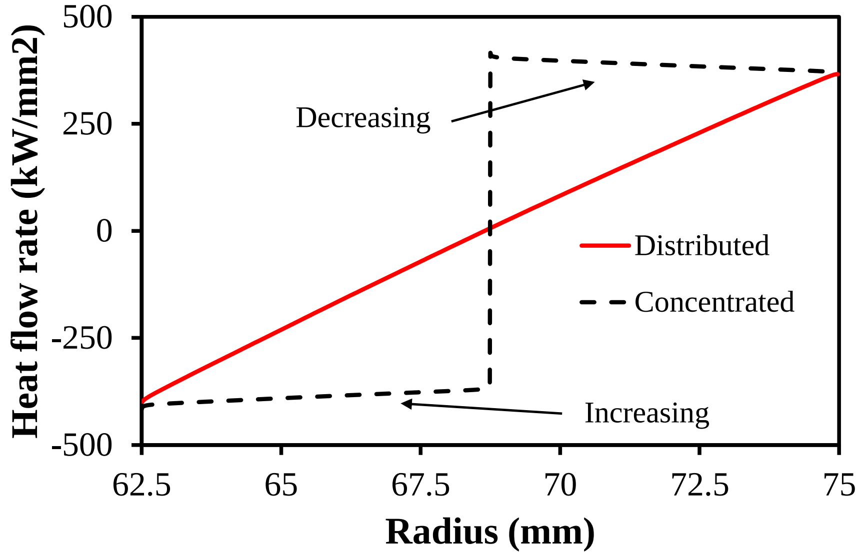

Fig. 6.7. Ccomparison of radial heat flow rate (F) profiles between the distributed loss model and the concentrated loss model.

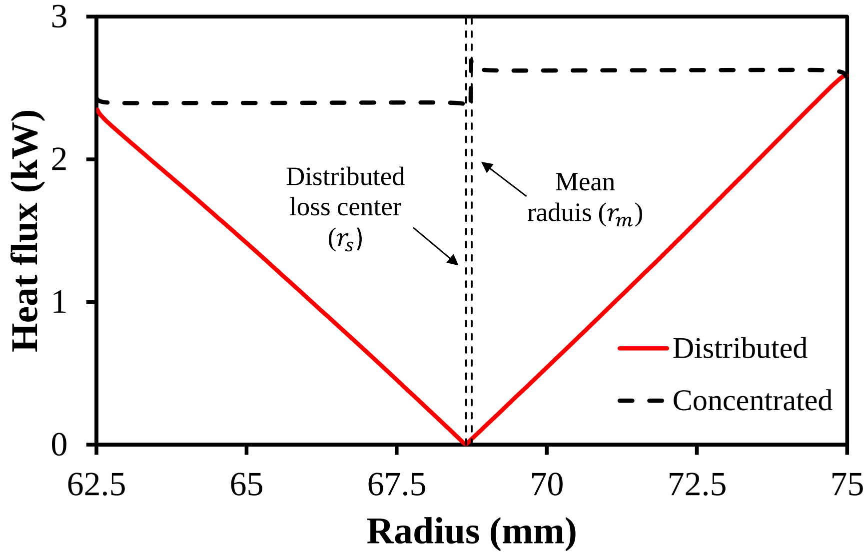

Fig. 6.8. Comparison of radial heat flux (H) profiles between the distributed loss model and the concentrated loss model.

$$\Delta T_c = \int_{r_1}^{r_m} \Delta R_e G_2 \, dr \tag{6.19}$$

$$\Delta T_c = \frac{G}{2\pi\lambda L} \frac{\ln\frac{r_m}{r_1}\ln\frac{r_2}{r_m}}{\ln\frac{r_2}{r_1}} \tag{6.20}$$

where G_2=$\ln\frac{r_2}{r_m} / \ln\frac{r_2}{r_1}$ is the heat flux flows to the outer surface.

It is worth noting that the distributed loss center is not at the mean radius. It is actually r_s shown in (6.13). The difference between the distributed loss center and the mean radius is related to the outer and inner radii of the ring element. By introducing a new variable, $t = \frac{r_2 - r_1}{r_1}$, when t approaches 0, the difference also approaches 0, or vice versa.

To study the relationship of the distribution loss model and the concentrated loss model, the ratio of increased temperature with the same amount of loss can be calculated by (6.21). By substituting $t = \frac{r_2 - r_1}{r_1}$, and limiting t to 0, the ratio is equal to $\frac{1}{2}$. Thus, for the same amount of the loss, the highest temperature difference of concentrated loss model (ΔT_c) is twice higher than the distributed loss model (ΔT_d), as shown in Fig. 6.6. Except for the Mellor's method with an extra negative resistance to correct the center temperature, modifying the loss value to half in the concentrated loss model can also give the correct center temperature value, as shown in Fig. 6.9.

$$f_{\Delta T} = \frac{\Delta T_d}{\Delta T_c} = \frac{\left[\frac{2\ln\left(\frac{\sqrt{\frac{(r_2^2 - r_1^2)}{2\ln {r_2}/{r_1}}}}{r_1}\right) - 1}{2\ln {r_2}/{r_1}} + \frac{r_1^2}{(r_2^2 - r_1^2)}\right]}{2\frac{\ln\frac{r_m}{r_1}\ln\frac{r_2}{r_m}}{\ln\frac{r_2}{r_1}}} \tag{6.21}$$

$$\lim_{t\to 0} f_{\Delta T} = \frac{1}{2} \tag{6.22}$$

$$\lim_{t\to 0} \frac{H(r_2)}{G_2} = 1 \tag{6.23}$$

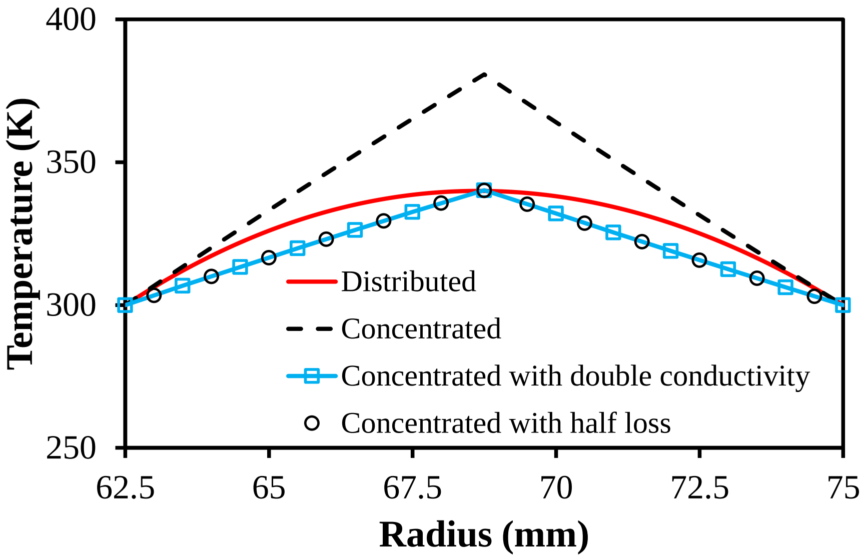

Fig. 6.9. Comparison of the radial temperature profile of the element with internal heat generation between different models.

A similar phenomenon exists in the Cartesian coordinate as well, as presented by [Ger06a]. The authors also give the solution with a reduced power loss model. In addition, since the heat transfer in the Cartesian coordinate is symmetrical, the distributed loss center and the geometry center are the same. It should be noted that the temperature difference between the outer surface and the internal hot spot is the product of thermal resistance and the loss. Thus, reducing the value of power loss is equivalent to increase the thermal conductivity of the material, as shown in Fig. 6.9. It should be noted that the authors in [Ger06a] presented another model, which introduces two compensated thermal voltage sources. All of three models are shown in Fig. 6.10, where T_{max} is the maximum temperature at the hot spot, G_{2a} and G_{2b} are the heat fluxes flow through R_{2a} and R_{2b} respectively, and $T_{ca} = \frac{G_{2a}R_{2a}}{2}$, $T_{cb} = \frac{G_{2b}R_{2b}}{2}$ are the compensated thermal voltage sources. These models give the same result in a single element since the hot spot temperature expressions, (6.24), are the same, while they have different effects when two or more elements connected in series, will be discussed in Section 6.4.

$$\left.\begin{array}{ll} \text{Half loss:} & T_{max} = \dfrac{G_{2b}}{2} R_{2b} + T_2 \\[2ex] \text{Double conductivity:} & T_{max} = G_{2b} \dfrac{R_{2b}}{2} + T_2 \\[2ex] \text{Gerling's:} & T_{max} = G_{2b}R_{2b} - \dfrac{G_{2b}R_{2b}}{2} + T_2 \end{array}\right\} \tag{6.24}$$

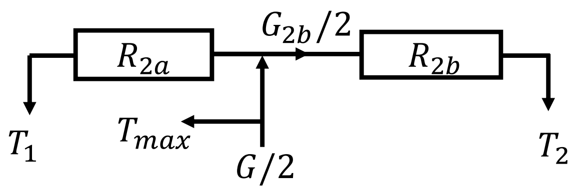

(a) Half loss model

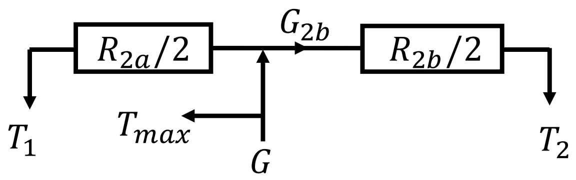

(b) Double conductivity model

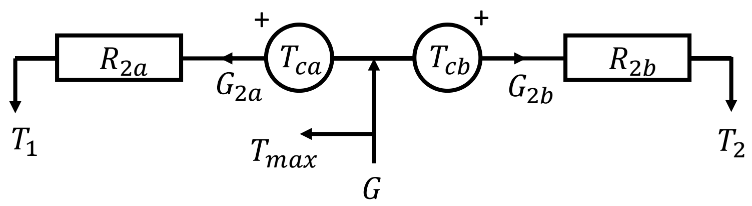

(c) Compensation thermal voltage model (Gerling's)

Fig. 6.10. LPTM models of a single element with internal loss.

6.3. Proposed Methods

The proposed model uses the original concentrated loss model with a compensated thermal voltage between the centre node and the detected node shown in Fig. 6.11(a), where G_a and G_b are the heat fluxes flow through R_a and R_b respectively. The hot spot temperature is relatively isolated from the heat fluxes and other elements. The compensated thermal voltage V_c is calculated by the parallel path ratio, which gives the location of the hot spot in the distributed loss model. This method utilized the conclusion that the parallel path ratio in the distributed loss model and the original concentrated loss model is the same. In addition, the main difference between the proposed model and the existing models is that the existing models are built based on the ratio $\frac{\Delta T_d}{\Delta T_c}$. The proposed model is proposed according to the subtraction $\Delta T_c - \Delta T_d$.

In order to explain the model clearly, a more general sandwich model in the Cartesian coordinate is built and analysed, as shown in Fig. 6.12. It is worth noting that the heat is generated in the element $ABB'A'$, and surrounded by non-heating elements $PBB'P'$, and $AQQ'A'$,. The corresponding LPTM is presented in Fig. 6.11(b), where R_{PB}, R_{BC}, R_{AC} and R_{AQ} represent the thermal resistances of the corresponding region marked in Fig. 6.12. It can be seen that due to the unbalanced load at two sides, the hot spot of the distributed loss model is not at the centre. While in the concentrated loss model, which is used in LPTMs, the loss is assumed generated at the centre. The horizontal temperature profiles and the heat flux profiles are compared in Fig. 6.13 and 6.14 respectively. It should be noted that the temperature rise of the distributed loss model (ΔT_d) is equal to the integration of the product of the heat flux and thermal resistance from point D to point O. It can be regarded as the area of the triangle DAO. The temperature rise of the concentrated loss model (ΔT_c) should be equal to the integration from point D to point I, which is the area of the rectangle $DACI$. Thus, the temperature difference between the distributed loss model and the concentrated loss model can be regarded as $S_{DACI} - S_{DAO}$. Since points *A, C, D, I* are defined clearly according to the geometry, the critical part is to find point O.

It is mentioned that the location of point O, i.e. the hot spot in the distributed loss model, can be found according to the flux deviation ratio. Since in one element, the thermal conductivity maintains the same, the slope of $\overline{OD}$ and the slope $\overline{FO}$ are opposite. Thus, the right triangle $\varDelta EBO$ is similar to $\varDelta DAO$, and the distance $\overline{OA}$ can be distributed as $\frac{\overline{AD}\,\overline{BA}}{\overline{AD}+\overline{BE}}$. By substituting the physical meaning, the compensation thermal voltage V_c can be derived as shown below:

$$R_{AO} = R_{AB}\frac{G_b}{G} \tag{6.25}$$

$$\Delta T_c = R_{AC}G_b \tag{6.26}$$

$$\Delta T_d = \frac{R_{AO}G_b}{2} \tag{6.27}$$

$$V_c = \Delta T_c - \Delta T_d = G_b R_{AC}\left(1 - \frac{R_{AC} + R_{BC}}{2R_{AC}}\frac{G_b}{G}\right) \tag{6.28}$$

It should be noted that V_c is calculated by focusing on the right side of the above derivation. It is also feasible to derive it from the left side i.e. $S_{EJCB} - S_{EBO}$.

More importantly, when there is more than one heat source and connected in series, at most one hot spot exists in one of the elements. The maximum temperatures of other elements are located at the interface. When two elements with the same dimension, the same material, and the same loss are located adjacently, the hot spot occurs at the interface. The case of two elements located adjacently and both with internal heat source is presented in Fig. 6.15. The corresponding LPTM is presented in Fig. 6.11(c), the subscription 1 and 2 distinguish two elements and $T_{if.}$ is the temperature at the interface between the two elements. The positive directions of the heat fluxes G_{a1}, G_{b1}, G_{a2}, G_{b2} are defined as the directions of the corresponding arrows shown in Fig. 6.11(c). The total flux flows to the boundary T_1 is equal to $G_{a1}+G_{a2}$, while the total flux flows to the boundary T_2 is equal to $G_{b1}+G_{b2}$. It is worth noting that one of the heat fluxes G_{b1} and G_{a2} must be zero when there is no other path between R_{b1} and R_{a2}. The hot spot is located in the element in which the two heat fluxes generated by this element are all positive. This can be explained that the heat fluxes are always flowing from the high-temperature object to low-temperature objects. In addition, since the maximum temperature of the element with negative flux is located at the interface face. The corresponding compensation thermal voltage is related to the interface temperature. Thus, for the general cases, V_c can be derived as (6.26). The results of this case between the FEM (Fig. 6.15) the proposed LPTM (Fig. 6.11(c)) are summarized in Table 6.1. It can be seen that the critical results which are marked with "*" have good agreement with FEM.

$$V_c = \begin{cases} G_a R_a \left(1 - \dfrac{R_a + R_b}{2R_a} \dfrac{G_a}{G}\right) \cdots\cdots\cdots G_a G_b > 0 \\ -R_a G_a \cdots\cdots\cdots\cdots\cdots\cdots G_a < 0 \\ -R_b G_b \cdots\cdots\cdots\cdots\cdots\cdots G_b < 0 \end{cases} \tag{6.29}$$

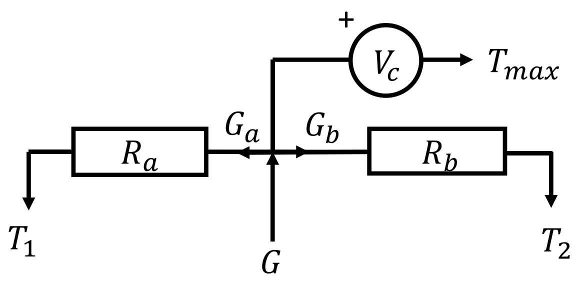

(a) Proposed LPTM of a single element with internal heat

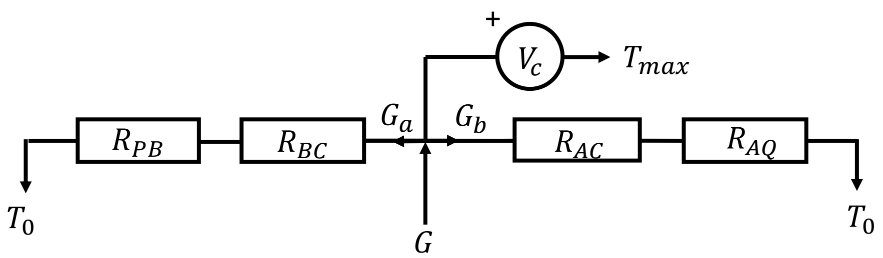

(b) Proposed LPTM with side elements (Fig. 6.12)

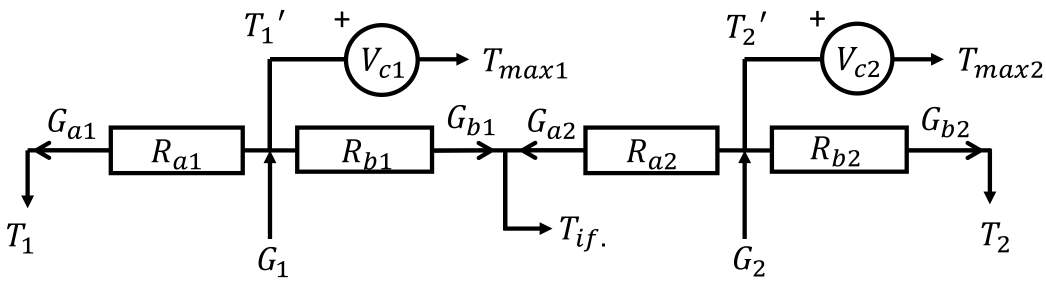

(c) Proposed LPTM of two elements both with internal heat (Fig. 6.15)

Fig. 6.11. Proposed LPTM models of different cases.

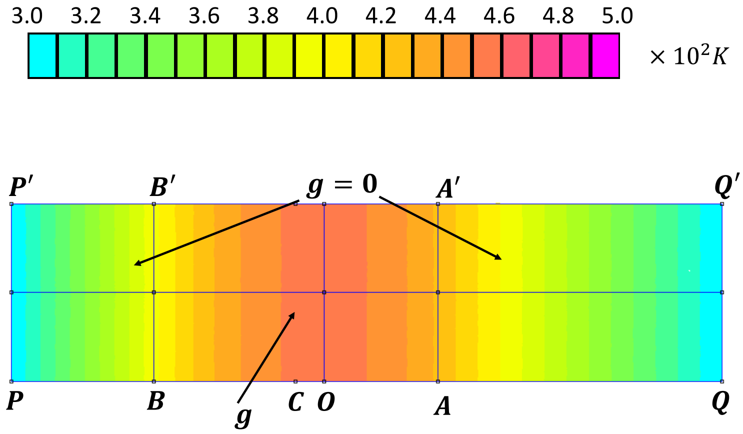

(a) Distributed loss model

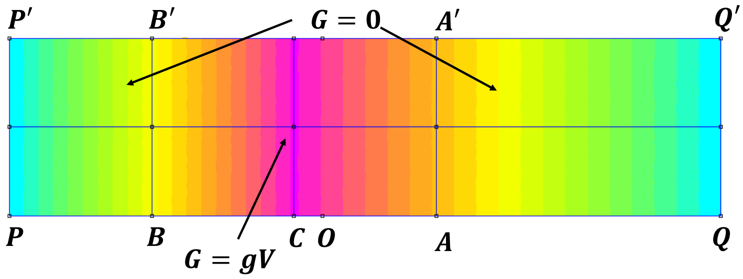

(b) Concentrated loss model

Fig. 6.12. Comparison of distribution loss model and concentrated loss model of a sandwich model in the Cartesian coordinate.

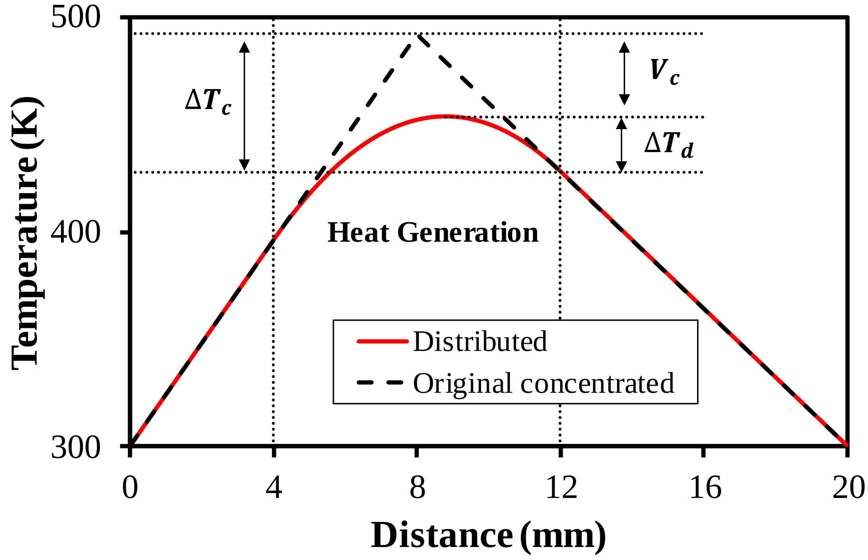

Fig. 6.13. Comparison of horizontal temperature profiles of the sandwich model in the Cartesian coordinate.

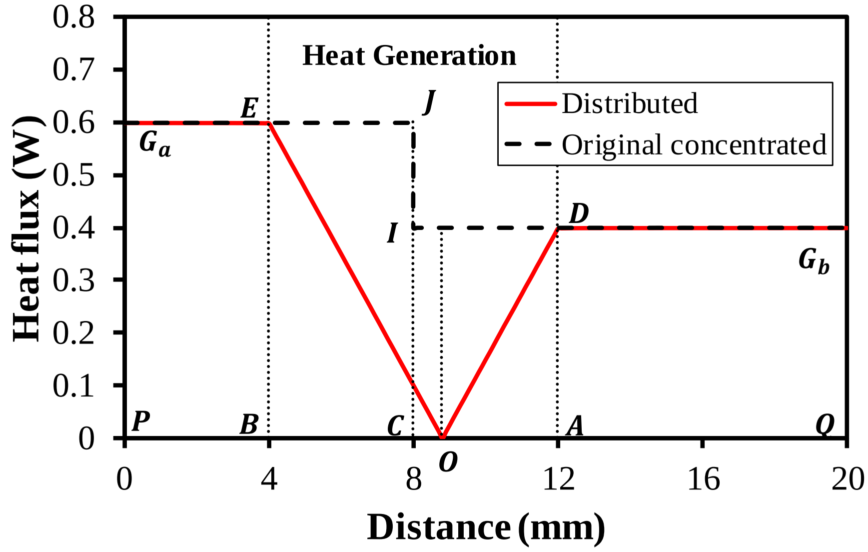

Fig. 6.14. Comparison of horizontal heat flux profiles of the sandwich model in the Cartesian coordinate.

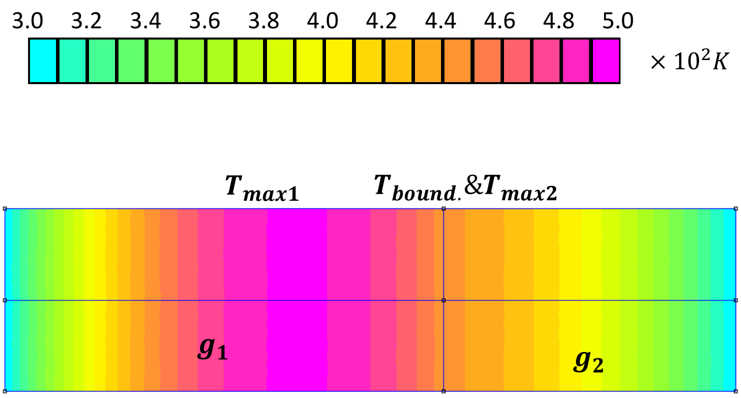

(a) Temperature distribution

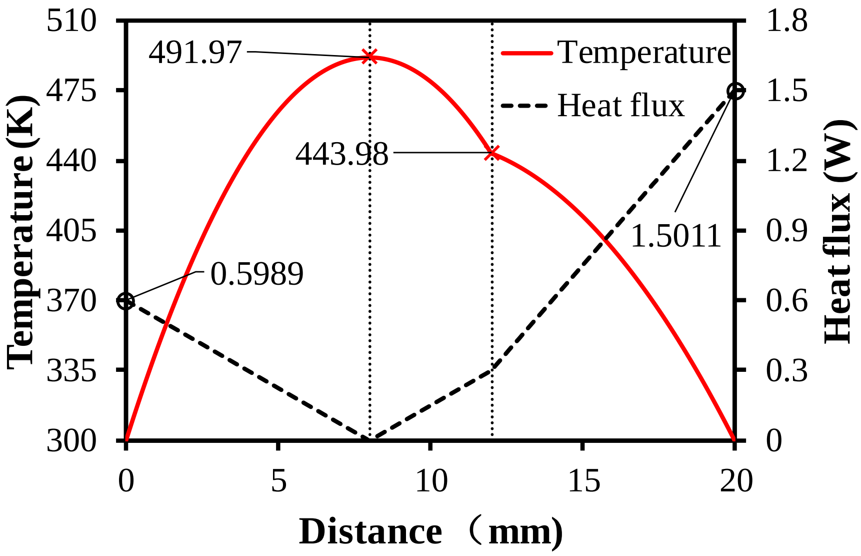

(b) Temperature and heat flux profiles

Fig. 6.15. The FEM temperature distribution and corresponding temperature and flux profiles of two-loss models.

Table 6.1. Comparison of the results between FEM and LPTM of two elements both with an internal heat source.

Name	Proposed LPTM (Concentrated loss)	FEM (Distributed loss)
T_1' (K)	588	
V_{c1}(K)	96	491.97
T_{max1}(K) *	492	
T_2' (K)	420	
V_{c2}(K)	-24	443.98
T_{max2} (K) *	444	
$T_{if.}$ (K) *	444	443.98
G_{a1} (W) *	0.6	0.5989
G_{b1} (W)	0.3	
G_{a2} (W)	-0.3	
G_{b2} (W) *	1.5	1.5011

6.4. Comparison of Existing LPTMs and Proposed LPTM

As mentioned previously, the temperature difference between the distributed loss model and the concentrated loss model can be eliminated by different methods:

- introducing an extra resistance
- reducing the power loss
- modifying the thermal conductivity
- introducing the compensated thermal voltage source on the main load or sub-load

Since the model with extra resistance gives the mean temperature and others are aiming for the hot spot temperature. The following comparison is focused on the latter three models.

In this case, two rings are connected in the radial direction. The original ring, which from r_1 to r_2, has heat generation with uniform density g, is set as the lamination material. The outer ring has zero loss generation and can be regarded as the housing of the machine, as shown in Fig. 6.16(a). For the same reason, when the LPTM is used to analyze, the power loss is usually applied to the middle of the element, i.e. the equivalent loss applied to the mean radius r_m shown in Fig. 6.16(b). The comparison of radial temperature profiles and heat flux profiles from r_1 to r_3 between different models are shown in Fig. 6.17 and Fig. 6.18 respectively. It shows that the temperature of the element with internal heat generation is higher than the distribution loss model.

To eliminate this difference, both the loss value and the thermal conductivity can be modified and they have the same effect in one element. However, if the loss value is modified to half, only half of the loss can flow into the adjacent elements. The temperature of this element will be lower than the actual value. It can be easy to see the difference between point A and point B, as shown in Fig. 6.17 and Fig. 6.18. By modifying the thermal conductivity of the material with internal loss, the fluxes deviation ratio is changed due to the thermal resistance ratio of two flowing paths is changed. It can be seen in Fig. 6.18 that the flux profile of the doubled conductivity model (C) is different from the original concentrated model and distributed model (A), and results in the temperature difference shown in Fig. 6.17. It should be noted that the original thermal conductivity of the element with internal heat at the center is much lower than the side elements. It can be seen that the received heats at point A and point D are the same, while the gradient of temperature at point D is much larger than that at point A. For the same reason, the gradient of temperature at point E is also larger than that at point B. Since in the double conductivity model, the thermal resistance of the material with internal loss is modified to half. The temperature gradient difference between point F and point C is smaller. It is worth noting that it is meaningless to calculate the temperature profiles of the model with compensated thermal voltage source analytically or in FEM. Thus, the expressions of the parallel path ratio and hot spot temperature are compared in (6.30) and (6.31) respectively.

The LPTMs of two elements case are shown in Fig. 6.14. It can be seen that the parallel path ratio of the doubled conductivity model and the Gerling's compensated model are different from the proposed model and the half loss model. It can be explained as that the main branch has been modified in the first two models. The primary results of the LPTMs are compared with FEM in Table 6.2. It can be seen that the proposed model has the highest accuracy compared with FEM results.

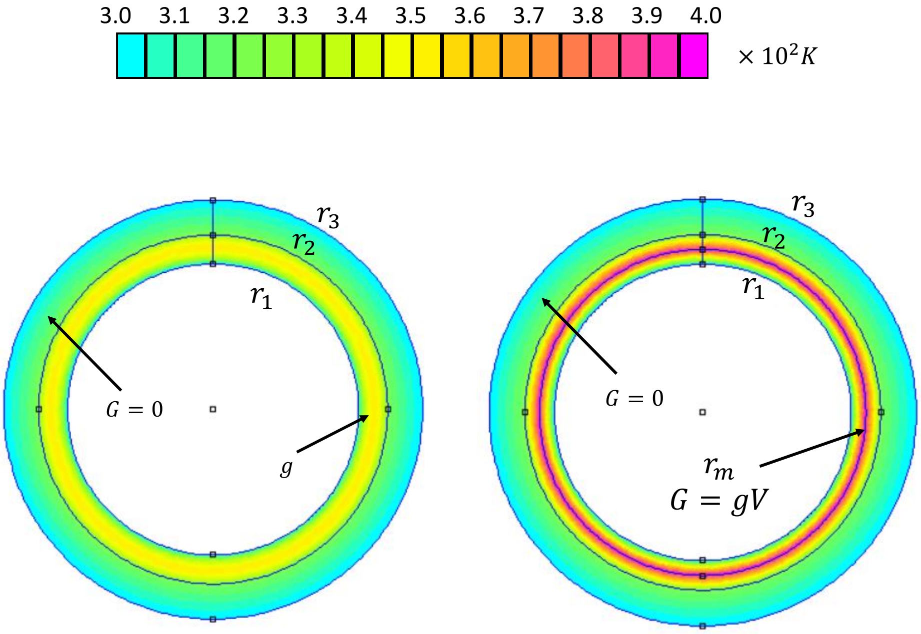

(a) Distributed loss mode **(b)** Concentrated loss model

Fig. 6.16. Comparison of distribution loss model and concentrated loss model of two-element case in polar coordinate.

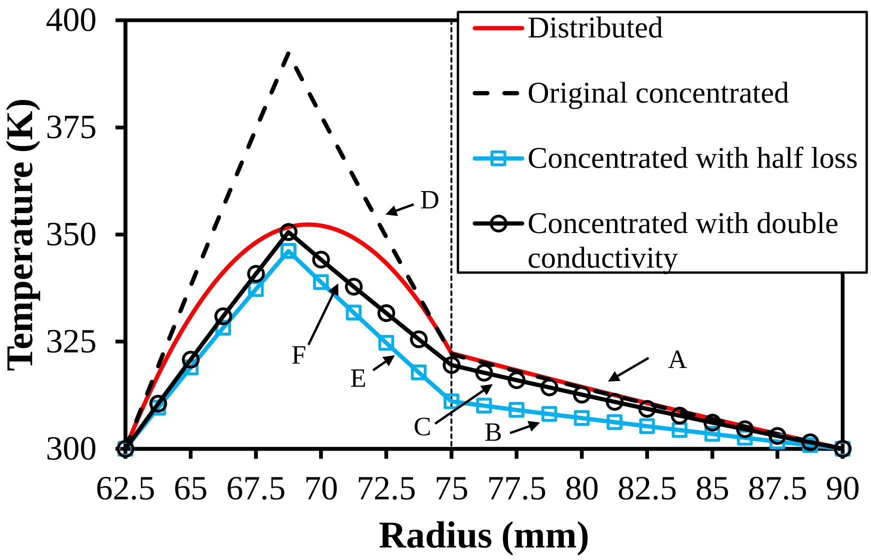

Fig. 6.17. Comparison of radial temperature profiles of two-elements case calculated in FEM.

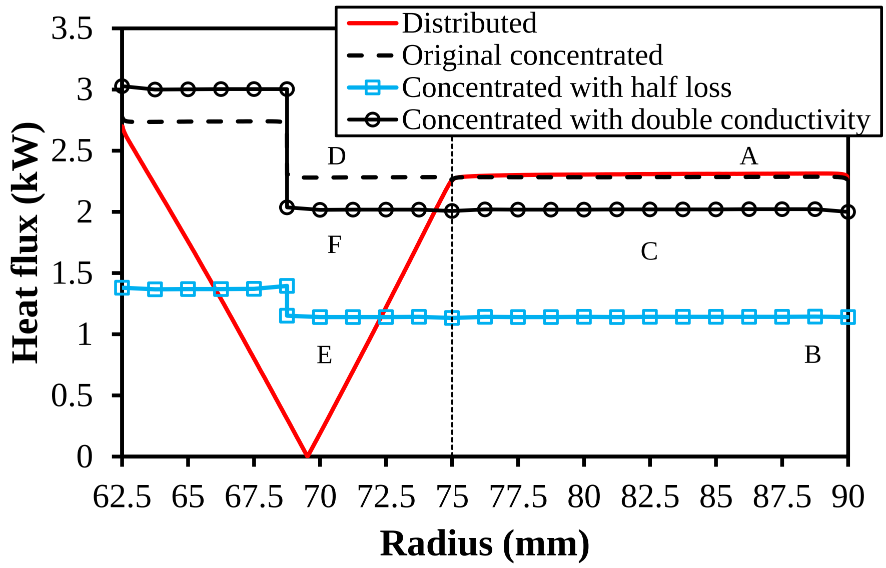

Fig. 6.18. Comparison of radial heat flux profiles of two-elements case.

$$
\left.\begin{aligned}
&\text{Proposed} && \frac{G_{2a}}{G_{2b}} = \frac{(R_{2b}+R_3)}{R_{2a}} \\
&\text{Half loss} && \frac{G_{2a}}{G_{2b}} = \frac{(R_{2b}+R_3)}{R_{2a}} \\
&\text{Double conductivity:} && \frac{G_{2a}}{G_{2b}} = \frac{(R_{2b}+2R_3)}{R_{2a}} \\
&\text{Compensated voltage:} && \frac{G_{2a}}{G_{2b}} = \frac{(R_{2b}+2R_3)}{R_{2a}}
\end{aligned}\right\} \tag{6.30}
$$

$$
\left.\begin{aligned}
&\text{Proposed} && T_{max} = G\frac{R_{2a}(R_{2b}+R_3)}{R_{2a}+R_{2b}+R_3} - V_c \\
&\text{Half loss:} && T_{max} = \frac{G}{2}\frac{R_{2a}(R_{2b}+R_3)}{R_{2a}+R_{2b}+R_3} \\
&\text{Double conductivity:} && T_{max} = \frac{G}{2}\frac{R_{2a}(R_{2b}+2R_3)}{R_{2a}+R_{2b}+2R_3} \\
&\text{Compensated voltage:} && T_{max} = \frac{G}{2}\frac{R_{2a}(R_{2b}+2R_3)}{R_{2a}+R_{2b}+2R_3}
\end{aligned}\right\} \tag{6.31}
$$

where R_3 is the thermal resistance of the outer element in Fig. 6.16.

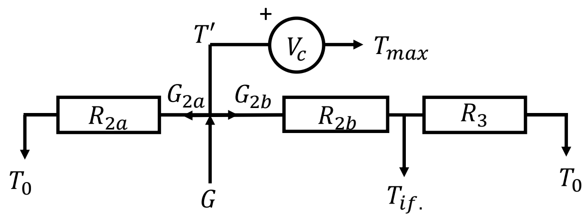

(a) Proposed model

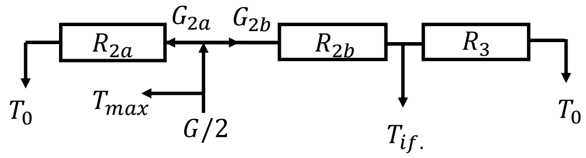

(b) Half loss model

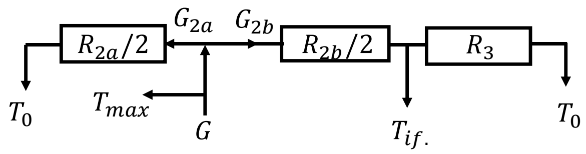

(c) Doubled conductivity model

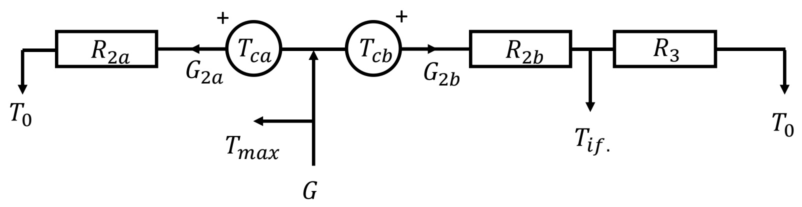

(d) Compensation thermal voltage model (Gerling)

Fig. 6.19. LPTM models of two elements with one internal loss.

Table 6.2. Comparison of the results between FEM and LPTMs of two elements with one heat source.

Name	FEM	(a)	(b)	(c)	(d)
T_{max} (K)	352.3	352.7	346.2	350.6	351.2
$T_{if.}$ (K)	322.3	322.1	311	319.5	320.6
G_{2b} (kW)	2.72	2.74	1.37	3	2.89
G_{2b} (kW)	2.3	2.28	1.14	2.02	2.13

6.5. Conclusion

In this chapter, a novel LPTM model is proposed to solve the difference in temperature rise between the distributed loss model and the concentrated loss model. The concentrated loss model is commonly employed in LPTM, and it assumes that all the losses are generated at one location. While the distributed loss model is more suitable for FEM, the loss is generated uniformly inside the element and it is more close to the real case. The temperature rise is caused by the received loss of the elements and their thermal resistance. In the proposed method, the element with internal heat generation is relatively isolated from other elements. Comparing with the existing models, it utilizes full loss and full resistance, which maintains the same parallel flux divide ratio comparing with the distribution model. It should be noted that the model with half loss as input and the model with compensation thermal voltages on the main load are available for a single element with internal heat generation. While when there exist other elements, the parallel path ratio will be changed and results in different parallel flux divide ratios. It should be noted that both the proposed model and Gerling's model introduce the compensated thermal voltage. Since the thermal voltage source is located in the main load in Gerling's model, the values of the thermal voltage sources and the currents are interrupted. In the proposed model, the thermal voltage source is located in the sub-load and ideally isolated with the main load currents. Mellor's model is appropriate for more general cases while the network is more complicated and it aims for mean temperatures. Thus, the proposed model is ideal for the thermal analysis to predict the hot spot temperature of electrical machines.

CHAPTER 7

General Conclusion and Future Work

In this thesis, AC copper loss and its influence on the electromagnetic and thermal performance of IPM machines for low voltage and high-speed operation are investigated. AC copper losses for two types of rectangular conductors, i.e. solid and hollow rectangular conductors, are firstly studied. It has shown that AC copper loss accounts for a major part of the total loss in the electrical machines with hair-pin windings. The thermal performance and electromagnetic performance are significantly affected by AC copper loss. It has also shown that there is a tradeoff between high maximum torque capability and low AC copper loss at high-speed operation. Thus, it is essential to consider AC copper loss in the calculation of torque-speed and power-speed characteristics for the electrical machines employing hair-pin windings with the requirement for high-speed operation. Further, a hybrid analytical and FE model is proposed for calculating AC copper loss, accounting for the influences of temperature, frequency, current angle, and saturation. In addition, a novel 1-dimensional lumped parameter thermal model has been proposed based on heat transfer physics.

7.1. Influence of Design Parameters on AC Copper Loss of IPM Machines

7.1.1. With Solid Rectangular Conductors

Generally, the overall AC copper loss is related with the leakage fluxes inside the slot and decreases with a lower packing factor. It is shown that the relative ratio between the slot size and the conductor size impacts AC copper loss strongly. The larger the slot size, the lower the AC copper loss.

In addition, AC copper loss can be affected by the relative position between the slot and the conductors. When the conductors are located near the slot opening region, the generated AC copper losses are relatively higher than those located at the slot bottom region.

Moreover, it is shown that the tendencies of AC copper loss are opposite between different orientations of conductors in the slot due to different directions of the dominating flux leakages. When the slot aspect ratio is small, the vertical leakage fluxes are dominating and perpendicular to the long side of the horizontal conductor. Thus, for the horizontal conductor, AC copper loss is high at a small aspect ratio. For the same reason, the vertical conductor has high AC copper loss at a large aspect ratio.

Furthermore, the lowest AC copper loss occurs when the slot opening is zero and the tooth-tip has a certain height. When the conductors are located in the closed slot with a thick tooth tip, the majority of the flux lines flow through the lamination materials. Thus, the introduced AC copper loss is minimized.

Besides, it shows that the conductor aspect ratio also has dominated AC copper loss. It has been shown that AC copper loss of the conductor in the airgap is identical for the conductors with reciprocal aspect ratio. The highest AC copper loss can be found when the aspect ratio equals to 1. For the conductors located in the slot with semi-open slot opening, the overall introduced AC copper loss is much higher. While the minimum AC copper loss can be found when the aspect ratio equals to 1. It has been shown that the influence of conductor shape is more dominated than the slot aspect ratio. However, AC copper loss can be reduced significantly when the conductor shape and the slot shape vary together.

More importantly, in the electrical machine with a fixed outer diameter, more space for the slot means that less space for lamination materials such as stator teeth. It should be noted that when the input current is zero, i.e. on open circuit, AC copper loss introduced by PM is not significant.

Thus, it is necessary to calculate the torque/power-speed characteristics and the corresponding temperatures for different design parameters. It has been shown that the low-speed torque decreases due to the thinner stator tooth but the high-speed performance improves significantly, especially the maximum output power and the machine efficiency.

7.1.2. With Hollow Rectangular Conductors

Generally, when hollow rectangular conductors are employed, the introduced AC copper loss is higher than the solid conductor with the same conducting area. The relationships between the conductors and the slots are similar to the case of solid conductors. In addition, the hollow regions also affect AC copper losses. It has been shown that the minimum AC copper loss occurs when the hollow region towards the slot bottom. When two conductors are connected in series in the slot, the transposition at the end winding may cause extra loss. It is due to the fact that when there is a transposition at the end winding, the hollow regions of the conductors may toward different directions and only one of them can achieve the minimum AC copper loss.

Furthermore, the influences of the hollow shape on AC copper loss and the thermal dissipation capability are analyzed. It has been noted that the minimum AC copper loss occurs when the conductor is the shortest (just like the solid one). However, these conductors generating lower AC copper loss could have worse thermal dissipation capability since the hollow region is very small. It has been shown that the convection coefficient and the thermal resistance are affected by the hollow shape considerably. It is worth noting that the condition for the lower thermal resistance is opposite to the condition for the lower AC copper loss. When the overall temperature is considered, the thermal dissipation capability is more dominated when the hollow aspect ratio is relatively high.

In the conventional analysis of the convection coefficient, the flow rate is usually set as constant. However, it has been shown that better overall performance can be obtained by considering the variable flow rate.

7.1.3. Comparison of Solid and Hollow Rectangular Conductors

The comparison of using solid and hollow rectangular conductors is listed in Table 7.1.

Table 7.1. Comparison of solid and hollow rectangular conductors.

	Solid conductor	Hollow conductors
Influential factors on AC copper loss	• Relative position and size between the slot and the conductor • Slot opening width and tooth-tip height • Different orientations of the conductor • Aspect ratios of slot and conductors	• Relative position and size between the slot and the conductor • Slot opening width and tooth-tip height • Different orientations of the conductor • Aspect ratios of conductor, slot, and hollow region • Relative locations between the conductor and the hollow region • Relative location of the hollow region • Transposition at the end winding
Influential factors on thermal dissipation capability	• Insulation materials	• Aspect ratio of the hollow region • Flow rate of the coolant
Comparison	• Lower AC copper loss • Less influential factors • Poor thermal dissipation capability • AC copper loss is more dominated	• Higher AC coper loss • More influential factors • Good thermal dissipation capability • Thermal dissipation capability is more dominated

7.2. AC Copper Loss and Thermal Modelling

7.2.1. One-Dimensional Lumped Parameter Thermal Model of Electrical Machines

A novel LPTM model is proposed to solve the difference in temperature rise between the distributed loss model and the concentrated loss model. The distributed loss model is defined as that with the loss generated uniformly inside the element, which is usually used in FEM. The concentrated loss model assumes that all the heat is generated at one face inside the element which is usually used in LPTM models. When only one element exists, the difference between the distributed and concentrated loss models can be eliminated by other methods such as the half loss model [Ger06a] and the doubled conductivity model [Ger06a]. However, when other elements are located adjacently, these methods may not give correct results. The temperature rise in the adjacent element is lower than the expected one when the half loss model is used. The flux deviation ratio is changed when the doubled conductivity model is employed.

The proposed method is based on the heat transfer physics, the element with internal heat generation is relatively isolated from other elements to prevent over-prediction. Comparing with the existing models, it utilizes full loss and full resistance, which maintains the same parallel flux divide ratio comparing with the distribution loss model. In Gerling's model [Ger06b], the compensated thermal voltage is located in the main branch, the values of the thermal voltage sources and the currents are interrupted. While in the proposed model, the thermal voltage source is located in the sub-load and ideally isolated from the main load currents. Thus, the proposed model is ideal for the thermal analysis to predict the hot spot temperature of electrical machines.

7.2.2. Hybrid Analytical and Finite Element AC Copper Loss Model

An efficient and accurate hybrid method is proposed to predict AC copper loss of the rectangle conductors at different temperatures. It is a faster method comparing with the pure FE method, and it can also consider the effects which are not considered in existing analytical models. With the help of FE method, the saturation effect due to different d- and q-axis currents and geometry effect (i.e. tooth tips and slot opening) can be considered.

It has been shown that the predicted AC copper losses by the proposed model are more accurate than the original analytical method at different temperatures and frequencies. In addition, it is also shown by the proposed method that the current and current angle will affect AC copper loss due to the flux density distribution in the conductors. However, these effects are not considered in the existing analytical models.

Furthermore, the proposed method is more convenient to couple with the thermal model to consider the temperature effect compared with FE.

7.2.3. Thermal and Electromagnetic Performance of PM Machines Accounting for AC Copper Losses

AC copper loss could be one of the major total losses in the electrical machines especially with large solid conductors and at high-speed operation. High AC copper loss and equivalent resistance limit the machine output power. However, it is simply considered as a product of DC copper loss and coefficient during the conventional machine design. It has been shown that the performance may be over-estimated when AC effects are not considered, especially in high-speed operation regions. It has been shown that the efficiency maps with and without considering AC effect are significantly different. The high-efficiency region (>80%) almost covers the whole operation regions when AC effects are not accounted for. However, the high-efficiency region shrinks to the low-speed region (<5krpm) when AC effects are considered. The difference between the efficiency maps is mainly due to the copper loss with and without considering AC effects. It is shown that the difference between the copper loss is remarkable, especially at high-speed.

The temperature prediction is obtained by lumped parameter thermal model accounting AC copper loss. It is a simple model and the majority of thermal coefficients are obtained by material properties including the coolant liquid and the water jacket. Some critical parameters are obtained by a DC test with different current levels. It has been shown that the temperatures of the winding and the stator back-iron predicted by the developed LPTM have good agreement with measured results.

In addition, the thermal performance of the prototype machine with different sizes of conductors are compared under two operating conditions. It has been shown that the machine employing the smaller conductors has better performance at high-speed due to lower AC copper loss. It improves the temperature of winding by a maximum of 60 degrees in the high-speed region. However, the machine performance at low-speed is sacrificed due to higher DC copper loss, and the temperature increases by 20 degrees by employing the smaller conductors. The optimal conductor size can be identified according to the overall loss and temperature limitations.

7.3. Future Work

Based on the above analyses and conclusions, some future work is summarized as follows:

(1) Experimental validation of thermal and electromagnetic performance on the prototype machine which has been affected by COVID-19.

(2) Investigation of AC copper loss model and LPTM for PM machines with other PM rotor topologies.

(3) Investigation of AC copper loss model and LPTM for other types of electrical machines such as stator PM machines, stator wound field machines, and switch reluctance machines.

(4) Investigation and improvement of AC copper loss model and LPTM for different driving cycles.

(5) Investigation of LPTM considering PM eddy current losses and air turbulence.

(6) Simplification of AC copper loss model and LPTM for fast predictions during the initial design process.

It is worth noting that the above proposed future work is currently being conducted by a PhD student in the Electrical Machines and Drives Group at the University of Sheffield.

REFERENCE

[Aoy18] M. Aoyama, J. Deng, Y. Sunayama and M. Miwa, “Large-scale electromagnetic field analysis on conductor eddy current loss in bar-wound coil type permanent magnet synchronous motor for automotive applications,” *Proc. 2018 IEEE Energy Conversion Congr. and Expo. (ECCE)*, pp. 248-254, 2018.

[Ata00] K. Atallah, D. Howe, P. Mellor, and D. Stone, “Rotor loss in permanent-magnet brushless AC machines,” *IEEE Transactions on Industry Applications*, vol. 36, no. 6, pp. 1612–1618, Nov. 2000.

[Ata92] K. Atallah, Z. Q. Zhu, D. Howe, “An improved method for predicting iron losses in brushless permanent-magnet DC drives”, *IEEE Trans. Magn.*, 1992, 28, (5), pp. 2997–2999

[Aza10] Z. Azar, L. J. Wu, D. Evans, Z. Q. Zhu, "Influence of rotor configuration on iron and magnet losses of fractional-slot IPM machines", *5th IET International Conference on Power Electronics, Machines and Drives (PEMD2010)*, pp.1-5, 2010.

[Bar18] C. Du-Bar, and O. Wallmark, “Eddy current losses in a hairpin winding for an automotive application,” *Proc. 2018 IEEE International Conference on Electrical Machines (ICEM)*, pp. 710-716, 2018.

[Bec62] K.-M. Becker and J. Kaye, “Measurement of adiabatic and diabatic fluid flow in an annulus with an inner rotating cylinder,” *J. Heat Transfer*, vol. 84, pp. 97–105, 1962.

[Ber85] G. Bertotti, “Physical interpretation of eddy current losses in ferromagnetic materials, I. theoretical considerations”, *J. Appl. Phys.*, 1985, 57, (6), pp. 2110–2117

[Bim18] F. Bimkammmer, J. Mayer, D. Gerling, “Calibration of the state space thermal model of a directly cooled permanent magnet synchronous machine”. *Proc. Int. Conf. on Electrical Machines and Systems (ICEMS)*, pp. 16-20, 2018.

[Bog03a] A. Boglietti, A. Cavagnino, M. Lazzari, et al., “Predicting iron losses in soft magnetic materials with arbitrary voltage supply: an engineering approach”, *IEEE Trans. Magn.*, 2003, vol. 39, no. 2, pp. 981–989

[Bog03b] A. Boglietti, A. Cavagnino, M. Lazzari, and M. Pastorelli, “A simplified thermal model for variable-speed self-cooled industrial induction motor,” *IEEE Trans. Ind. Appl.*, vol. 39, no. 4, pp. 945–952, July/Aug. 2003.

[Bog06] A. Boglietti, A. Cavagnino, M. Parvis and A. Vallan, "Evaluation of radiation thermal resistances in industrial motors," *IEEE Trans. Ind. Appl.*, vol. 42, no. 3, pp. 688-693, May-June 2006

[Bog08a] A. Boglietti, A. Cavagnino, D. Staton, "Determination of critical parameters in electrical machine thermal models," Industry Applications, *IEEE Transactions on*, vol.44, no.4, pp.1150-1159, July-Aug. 2008

[Bog08b] A. Boglietti, A. Cavagnino, D. A. Staton, “End space heat transfer coefficient determination for different induction motor enclosure types”, *Proc. Conf. Rec. 43rd IEEE IAS Annu. Meeting*, Oct. 2008, pp. 1–8.

[Bog09] A. Boglietti, A. Cavagnino, D. Staton, M. Shanel, M. Mueller, C. Mejuto, "Evolution and modern approaches for thermal analysis of electrical machines", *IEEE Trans. Ind. Electron.*, vol. 56, no. 3, pp. 871-882, Mar. 2009.

[Bol02] I. Boldea, S. A. Nasar, “Skin and on-load saturation effects” in *the induction machine handbook*, Boca Raton: CRC Press, 2002, pp 249-294

[Bou97] A. Bousbaine, M. McCormick, and W. F. Low, “Thermal modelling of permanent-split-capacitor single-phase induction motors based on accurate loss density measurement,” in *Proc. IEE EMD Conf.*, 1997, pp. 175–179.

[Che15a] X. Chen, J. Wang, and G. Antonio, “A high-fidelity and computationally efficient electro-thermally coupled model for interior permanent-magnet machines in electric vehicle traction applications,” *IEEE Transactions on Transportation Electrification*, vol.1, no. 4, pp. 336-347, Dec. 2015.

[Che15b] J. Chen, D. Wang, S. Cheng, et al., “Modeling of temperature effects on magnetic property of non-oriented silicon steel lamination”, *IEEE Trans. Magn*, 2015, 51, (11), pp. 1–4

[Che15c] X. Chen, J. Wang, B. Sen, P. Lazari, and T. Sun, “A high-fidelity, computationally efficient model for interior permanent magnet machines considering the magnetic saturation, spatial harmonics and iron loss effect,” *IEEE Trans. Ind. Electron.*, vol. 62, no. 7, pp. 4044–4055, July 2015.

[Che19] X. Chen, J. Wang, A. Griffo, and A. Spagnolo, “Thermal modelling of hollow conductors for direct cooling of electrical machines,” *IEEE Transactions on Industrial Electronics*, vol. 67, pp. 895-905, Feb. 2019.

[Cro77] D. R. Croft, *Heat Transfer Calculation Using Finite Difference Equations*, London, UK: Applied Science Publishers, 1977.

[Dem13] Y. Demir, O. Ocak, and M. Aydin, “Design, optimization and manufacturing of a spoke type interior permanent magnet synchronous motor for low voltage-high current servo applications,” in *Proc. IEEE Int. Elect. Mach. Drive Conf.*, Chicago, IL, USA, May 2013, pp. 9–14.

[Dow66] P.L. Dowell, “Effects of eddy currents in transformer windings”, *Proceedings of the IEEE*, vol. 113, no. 8, pp. 1387-1394, Aug. 1966.

[Ede67] A. J. Ede, *An Introduction to Heat Transfer Principles and Calculations*, 1st ed., Oxford, UK: Pergamon Press Ltd. 1967.

[Fai96] A. Faiz, C. S. Weaver, M. P. Walsh, *Air Pollution from Motor Vehicles*. World Bank Publications, 1996.

[Fan18] X. Fan, D. Li, R. Qu, C. Wang and J. Li, "Hybrid rectangular bar wave windings to minimize winding losses of permanent magnet machines for EV/HEVs over a driving cycle.," *2018 IEEE International Magnetic Conference (INTERMAG)*, Singapore, 2018, pp. 1-2.

[Fer94] J. A. Ferreira, “Improved analytical modelling of conductive losses in magnetic components”, *IEEE Transactions on Power Electronics,* vol. 9, no. 1, pp. 127-131, Jan. 1994.

[Fou22] J. B. Fourier, *Théorie analytique de la chaleur*, Paris, 1822. Translated by A. Freeman, Dover Publication, New York, 1955.

[Ge16] X. Ge, Z. Q. Zhu, J. Li and J. Chen, "A spoke-type IPM machine with novel alternate airspace barriers and reduction of unipolar leakage flux by step-staggered rotor," in *IEEE Transactions on Industry Applications*, vol. 52, no. 6, pp. 4789-4797, Nov.-Dec. 2016

[Ger04] M. Gerber, J. A. Ferreira, I.W. Hofsajer, and N. Seliger, “A high-density heat-sink-mounted inductor for automotive applications,” *IEEE Trans. Ind. Appl.*, vol. 40, no. 4, pp. 1031–1038, June/July 2004.

[Ger06a] D. Gerling, G. Dajak, “Thermal calculation of systems with distributed heat generation’. *Thermal and Thermomechanical Proceedings 10th Intersociety Conference on Phenomena in Electronics Systems, 2006. ITHERM* 2006.

[Ger06b] D. Gerling, G. Dajak, “Novel lumped parameter thermal model for electrical systems”. *Proc. EPE Power Electronics and Applications Conf.*, 2006, pp. 1-10.

[Han07a] S.-H. Han, T. M. Jahns, and W. L. Soong, “Torque ripple reduction in interior permanent magnet synchronous machines using the principle of mutual harmonics exclusion,” in *Proc. 2007 IEEE Ind. Appl. Soc. Annu. Meet*, pp. 558–565.

[Han07b] S.-H. Han, W. L. Soong, and T. M. Jahns, “An analytical design approach for reducing stator iron losses in interior PM synchronous machines during flux-weakening operation,” in *Conf. Rec. IEEE IAS Annu. Meeting*, New Orleans, LA, USA, Sept. 2007, pp. 103–110.

[Han08] S. H. Han, T. M. Jahns, and Z. Q. Zhu, “Analysis of rotor core eddy-current losses in interior permanent magnet synchronous machines,” in *Proc. IEEE Ind. Appl. Soc. Annu. Meeting*, 2008.

[Han10] S.-H. Han, W. L. Soong, and T. M. Jahns, “Reducing harmonic eddy-current losses in the stator teeth of interior permanent magnet synchronous machines during flux weakening,” *IEEE Trans. Energy Convers.*, vol. 25, no. 2, pp. 441–449, June 2010.

[Ion07] D. M. Ionel, M. Popescu, M. I. McGilp, et al., “Computation of core losses in electrical machines using improved models for laminated steel”, *IEEE Trans. Ind. Appl.*, 2007, 43, (6), pp. 1554–1564

[Ish06] D. Ishak, Z. Q. Zhu and D. Howe, "Comparison of PM brushless motors, having either all teeth or alternate teeth wound," in *IEEE Transactions on Energy Conversion*, vol. 21, no. 1, pp. 95-103, Mar. 2006.

[Ish15] T. Ishigami, Y. Tanaka and H. Homma, "Motor stator with thick rectangular wire lap winding for HEVs," in *IEEE Transactions on Industry Applications*, vol. 51, no. 4, pp. 2917-2923, July-Aug. 2015.

[Iwa09] S. Iwasaki, R. P. Deodhar, Y. Liu, A. Pride, Z. Q. Zhu and J. J. Bremner, "Influence of PWM on the proximity loss in permanent magnet brushless ac machines," *IEEE Trans. on Ind. Appl.*, vol. 45, No. 4, 2009, pp. 1359 - 1367.

[Jah86] T. M. Jahns, G. B. Kliman, and T. W. Neumann, "Interior permanent magnet synchronous motors for adjustable-speed drives," *IEEE Trans. Ind. Appl.*, vol. IA-22, pp. 738-747, July/Aug. 1986.

[Jah96] T. M. Jahns and W. L. Soong, "Pulsating torque minimization techniques for permanent magnet AC motor drives—A review," *IEEE Trans. Ind. Electron.*, vol. 43, no. 2, pp. 321–330, Apr. 1996.

[Joo11] D. Joo, J. H. Cho, K. Woo, B. T. Kim, and D. K. Kim, "Electromagnetic field and thermal linked analysis of interior permanent-magnet synchronous motor for agricultural electric vehicle," *IEEE Trans. Magn.*, vol. 47, no. 10, pp. 4242–4245, Oct. 2011.

[Jun12] D. Jung, Y. Kim U. Lee, and H. Lee, "Optimum design of the electric vehicle traction motor using the hairpin winding", *Vehicular Technology Conference (VTC Spring)*, 2012 IEEE 75th, pp. 1-4, May, 2012.

[Kaw09] Y. Kawase, T. Yamaguchi, Z. Tu, M. Mizuno, N. Minoshima, and M. Watanabe," Electrical loss and temperature analysis of interior permanent magnet motor with divided magnets", *Electrical Machines and Systems, 2009. ICEMS 2009. International Conference on*, Nov. 2009.

[Kla06] M. Klauz and D. G. Dorrell, “Eddy current effects in a switched reluctance motor”, *IEEE Trans. Magn.*, vol. 42, no. 10, pp. 3437 - 3439, 2006.

[Kra08] C. Kral, A. Haumer, and T. Bauml, "Thermal model and behavior of a totally-enclosed-water-cooled squirrel-cage induction machine for traction applications," *IEEE Transactions on Industrial Electronics*, vol. 55, pp. 3555-3565, 2008.

[Kyl95] G. Kylander, “Thermal modelling of small cage induction motors,” Ph.D. dissertation, Dept. of Electric Power Eng., Chalmers Univ. Technol., Göteborg, Sweden, 1995 [Online]. Avail- able: http:// http://webfiles.portal.chalmers.se/et/PhD/KylanderGunnarPhD.pdf

[Lee12] B.-H. Lee, K.-S. Kim, J.-W. Jung, J.-P. Hong, and Y.-K. Kim, "Temperature estimation of IPMSM using thermal equivalent circuit," *IEEE Trans. Magn.*, vol. 48, pp. 2949-2952, 2012.

[Lew96] R. W. Lewis, K. Morgan, H. R. Thomas, and K. N. Seetharamu, *The Finite Element Method in Heat Transfer Analysis*, 1st ed., Chichester ,UK: Wiley, 1996.

[Li11] G. Li, J. Ojeda, E. Hoang, M. Lecrivain, and M. Gabsi, “Comparative studies between classical and mutually coupled switched reluctance motors using thermal-electromagnetic analysis for driving cycles,” *IEEE Trans. Magn.*, vol. 47, no. 4, pp. 839–847, Apr. 2011.

[Li12] G. Li, J. Ojeda, E. Hoang, M. Gabsi and M. Lecrivain, "Thermal–electromagnetic analysis for driving cycles of embedded flux-switching permanent-magnet motors," *IEEE Transactions on Vehicular Technology*, vol. 61, no. 1, pp. 140-151, Jan. 2012

[Li14] G. J. Li, Z. Q. Zhu, M. Foster and D. Stone, “Comparative studies of modular and unequal tooth PM machines either with or without tooth tips,” *IEEE Trans. Magn.*, vol. 50, no. 7, 2014.

[Li16] S. Li, B. Sarlioglu, S. Jurkovic, N. Patel, and P. Savagian, “Analysis of temperature effects on performance of interior permanent magnet machines,” *Energy Conversion Congress and Exposition (ECCE)*, 2016 IEEE, Sept. 2016

[Li18] S. Li, J. R. Mayor, R. G. Harley, and T. G. Habetler, “Efficient calculation of the strand eddy current loss distributions in the end stepped-stator region of large synchronous generators,” *Proc. 2018 IEEE Energy Conversion Congr. and Expo. (ECCE)*, pp. 1783-1783, 2018.

[Liu93a] Z. J. Liu, D. Howe, P. H. Mellor, and M. K. Jenkins, "Coupled thermal and electromagnetic analysis of a permanent magnet brushless DC servo motor," in *Electrical Machines and Drives, 1993. Sixth International Conference* on (Conf. Publ. No. 376), 1993, pp. 631-635.

[Liu93b] Z. J. Liu, D. Howe, P. H. Mellor and M. K. Jenkins, “Thermal analysis of permanent magnet machines,” *ICEM 1993*, pp. 359-364.

[Ma16] X. Y. Ma, G. J. Li, G. W. Jewell, Z. Q. Zhu, and H. L. Zhan, “Performance comparison of doubly salient reluctance machine topologies supplied by sinewave currents,” *IEEE Trans. Ind. Electron.*, vol. 63, no. 7, pp. 4086–4096, July 2016.

[McA54] W. H. McAdams, *Heat transmission*, 3rd ed., New York, USA: McGRAW-Hill, 1954.

[Mcc89] J. McCabe and M. Young, “Beating the heat: temperature control of a high-performance spindle," *The Technical Writer’s Handbook*, Mill Valley, CA: University Science, 1989.

[Mel06] P. H. Mellor, R. Wrobel, N. McNeill, “Investigation of proximity losses in a high speed brushless permanent magnet motor,” *IEEE Industry Applications Conference – 41st IAS Annual Meeting*, pp. 1514 – 1518, Oct. 2006.

[Mel11] P. Mellor, R. Wrobel, A. Mlot, T. Horseman, and D. Staton, “Influence of winding design on losses in brushless AC IPM propulsion motors,” in *Energy Conversion Congress and Exposition (ECCE)*, 2011 IEEE. IEEE, 2011, pp. 2782–2789.

[Mel88] P. Mellor, and D. Turner, “Real time prediction of temperature in an induction motor using microprocessor,” *Elect. Mach. Power Syst.*, vol. N.15, pp. 333–352, 1988.

[Mel91] P. Mellor, D. Roberts, and D. Turner, “Lumped parameter thermal model for electrical machines of TEFC design,” *Proc. Inst. Elect. Eng.*, vol. 138, no. 5, pp. 205–218, Sept. 1991.

[Mom19] F. Momen, K. Rahman and Y. Son, "Electrical propulsion system design of Chevrolet bolt battery electric vehicle," in *IEEE Transactions on Industry Applications*, vol. 55, no. 1, pp. 376-384, Jan.-Feb. 2019.

[Nan03] X. Nan and C. R. Sullivan, "An improved calculation of proximity effect loss in high-frequency windings of round conductors," *IEEE Power Electronics specialists Conf.*, June 2003, pp. 853-860.

[Nan04] X. Nan and C. R. Sullivan, "Simplified high-accuracy calculation of eddy-current losses in round-wire windings," *IEEE Power Electronics specialists Conf.*, June 2004, pp. 873-879.

[Nel09] G. Nellis and S. Klein, *Heat Transfer*: Cambridge University Press, 2009.

[Ner08] J. Nerg, M. Rilla, and J. Pyrhönen, “Thermal analysis of radial-flux electrical machines with a high power density,” *IEEE Trans. Ind. Electron.*, vol. 55, no. 10, pp. 3543–3554, Oct. 2008

[Par14] D. Park, S. Seo, Y. Kim, and S. Jung, “Comparison of loss and thermal analysis according to square conductor division considering skin effect,” *17th International Conference on Electrical Machines and Systems (ICEMS)*, 2014.

[Phu07] A.T. Phung, G. Meunier, O. Chadebec, X. Margueron, and J.-P. Keradec, "High-frequency proximity losses determination for rectangular cross-section conductors," *IEEE Trans. on Magn.*, Vol. 43, No. 4, 2007, pp. 1213-1216

[Pop13] M. Popescu and D. G. Dorrell, “Skin effect and proximity losses in high speed brushless permanent magnet motors,” *in Proc. IEEE ECCE*, 2013, pp. 3521–3527.

[Pop18] M. Popescu, J. Goss, D. A. Staton, D. Hawkins, Y. C. Chong and A. Boglietti, "Electrical vehicles—practical solutions for power traction motor systems," in *IEEE Transactions on Industry Applications*, vol. 54, no. 3, pp. 2751-2762, May-June 2018.

[Qi09] G. Qi, J. T. Chen, Z. Q. Zhu, D. Howe, L. Zhou, and C. L. Gu, "Influence of skew and cross-coupling on flux-weakening performance of permanent-magnet brushless AC machines," *IEEE Trans. Magn.*, vol. 45, no. 5, pp. 2110-2117, May. 2009.

[Rah12] K. Rahman, S. Jurkovic, C. Stancu, J. Morgante, and P. Savagian, "Design and performance of electrical propulsion system of extended range electric vehicle (EREV) Chevrolet Voltec", *Proc. 2012 IEEE Energy Conversion Congr. and Expo. (ECCE)*, pp. 4152-4159.

[Red08] P. B. Reddy, Z. Q. Zhu, Seok-Hee Han and T. M. Jahns, "Strand-level proximity losses in PM machines designed for high-speed operation," *Int. Conf. on Elec. Machines (ICEM)*, 2008, pp. 1-6.

[Red10] P. B. Reddy, T. M. Jahns and T. P. Bohn, “Modelling and analysis of proximity losses in high-speed surface permanent magnet machines with concentrated windings,” *IEEE Energy Conversion Congress and Exposition*, ECCE, 2010, pp. 996 – 1003.

[Red11] P. B. Reddy and T. M. Jahns, “Scalability investigation of proximity losses in fractional-slot concentrated winding surface PM machines during high-speed operation," *IEEE Energy Conversion Congress and Exposition, ECCE*, 2011, pp. 1670 – 1675.

[Ref04] A. M. EL-Refaie, N. C. Harris, T. M. Jahns, and K. M. Rahman, "Thermal analysis of multibarrier interior PM synchronous machine using lumped parameter model," *IEEE Trans. Energy Convers*., vol. 19, no. 2, pp. 303–309, June 2004.

[Ref06] A. M. EL-Refaie, T.M. Jahns, D.W. Novotny, "Analysis of surface permanent magnet machines with fractional-slot concentrated windings", *IEEE Transaction on Energy Conversion*, Vol. 21, Issue I, pp. 34-43, Mar. 2006.

[Rob86] D. Roberts, "The application of an induction motor thermal model to motor protection and other functions," PhD thesis, the University of Liverpool, Step. 1986.

[Sch89] R. Schifer and T. A. Lipo, "Core loss in buried magnet permanent magnet synchronous motors," *IEEE Trans. Energy Conversion*, vol. 4, no. 2, pp. 279-284, June 1989.

[Seb95] T. Sebastian, "Temperature effects on torque production and efficiency of PM motors using NdFeB magnets," *IEEE Trans. Ind. Appl.*, vol. 31, no. 2, pp. 353–357, Mar./Apr. 1995.

[Sim14] N. Simpson, R. Wrobel, P. H. Mellor, "A General Arc-Segment Element for Three-Dimensional Thermal Modeling," *IEEE Trans. Magn.*, 2014, vol. 50, no. 2, pp. 265-268.

[Sim18] N. Simpson, and P. H. Mellor, "Additive manufacturing of shaped profile windings for minimal AC loss in electrical machines," *Proc. 2018 IEEE Energy Conversion Congr. and Expo. (ECCE)*, pp. 5765-5772, 2018.

[Sim75] J. R. Simonson, "One-dimensional steady state conduction," in *Engineering heat transfer,* The Mcamillan Press LTD, 1975.

[Sim88] J. R. Simonson, *Engineering Heat Transfer*, 2nd ed. London, UK: The MACMILLAN Press Ltd. 1988.

[Sta05] D. Staton, A. Boglietti, and A. Cavagnino, "Solving the more difficult aspects of electric motor thermal analysis in small and medium size industrial induction motors," Energy Conversion, *IEEE Transaction on*, vol. 20, pp. 620-628, 2005.

[Sta06] D. Staton, and A. Cavagnino, “Convection heat transfer and flow calculations suitable for analytical modelling of electric machines,” in *Proc. IEEE IECON, Paris*, France, Nov. 6–10, 2006, pp. 4841–4846.

[Ste92] C. P. Steinmetz, “On the law of hysteresis”, *Trans. Am. Inst. Electr. Eng.*, 1892, 9, (1), pp. 3–64

[Sug70] G. B. Sugden, "Oil-cooled a.c. generators for aircraft -- present trends," *Students' Quarterly Journal*, vol. 40, pp. 128-133, 1970.

[Sul01] C. R. Sullivan, "Computationally efficient winding loss calculation with multiple windings, arbitrary waveforms, and two-dimensional or three-dimensional field geometry," *IEEE Trans. on Power Electronics*, Vol. 16, No. 1, 2001, pp. 142-150.

[Sul99a] C.R. Sullivan, "Optimal choice for number of strands in a litz-wire transformer winding," *IEEE Trans. on Power Electr.*, vol. 14, no. 2, 1999, pp. 283 - 291.

[Sul99b] C. R. Sullivan, " Winding loss calculation with multiple windings, arbitrary waveforms and two-dimensional field geometry," *IEEE Ind. Appl. Soc. Annual Meeting*, Oct. 1999, pp. 2093-2099

[Sun12] X. Sun, M. Cheng, S. Zhu, and J. Zhang, “Coupled electromagnetic-thermal-mechanical analysis for accurate prediction of dual-mechanical-port machine performance,” *IEEE Trans. Ind. Appl.*, vol. 48, no. 6, pp. 2240–2248, Nov./Dec. 2012.

[Tan15] D. Tanguy, S. Harmand, J. Pelle, and R. Yu, "Experimental study of oil cooling systems for electric motors," *Applied Thermal Engineering*, vol. 71, p. 607, Jan. 2015.

[Tho09] A. S. Thomas, Z. Q. Zhu and G. W. Jewell, " Proximity loss study in high speed flux-switching permanent magnet machine," *IEEE Trans. on Magn.*, Vol. 45, No. 10, 2009, pp. 4748-4751.

[Tod04] H. Toda, Z. Xia, J. Wang, K. Atallah, and D. Howe, "Rotor eddy-current loss in permanent magnet brushless machines," *IEEE Trans. Magn.*, vol. 40, no. 4, pp. 2104–2106, July 2004

[Tri06] J. F. Trigeol, Y. Bertin, and P. Lagonotte, "Thermal modeling of an induction machine through the association of two numerical approaches," *IEEE Trans. Energy Convers*., vol. 21, no. 2, pp. 314–323, Jun. 2006

[Vet15] M. Vetuschi and F. Cupertino, "Minimization of proximity losses in electrical machines with tooth-wound coils," in *IEEE Transactions on Industry Applications*, vol. 51, no. 4, pp. 3068-3076, July-Aug. 2015.

[Vol18] G. Volpe, M. Popescu, F. Marignetti, and J. Goss, "Modelling AC winding losses in a pmsm with high frequency and torque density," *Proc. 2018 IEEE Energy Conversion Congr. and Expo. (ECCE)*, pp. 2300-2305, 2018.

[Vol19] G. Volpe, M. Popescu, F. Marignetti, and J. Goss," AC winding losses in automotive traction e-machines: a new hybrid calculation method," *Proc. 2019 IEEE International Electric Machines & Drives Conference (IEMDC)*, 2019.

[Wan10] J. Wang, K. Atallah, R. Chin, W. M. Arshad, and H. Lendenmann, "Rotor eddy current loss in permanent magnet brushless AC machines," *IEEE Trans. Magn.*, vol. 46, no. 7, pp. 2701–2707, Jul. 2010.

[Wib66] P. Wibulswas, "Laminar Flow Heat Transfer in Non-Circular Ducts," Ph.D. Thesis, University of London, London, 1966.

[Woj13] R. P. Wojda and M. K. Kazimierczuk, “Analytical optimization of solid–round-wire windings,” *IEEE Trans, on Ind. Electr.*, vol. 60, no. 3, 2013, pp. 1033 – 1041.

[Wro10a] R. Wrobel, A. Mlot and P. H. Mellor, "Investigation of end-winding proximity losses in electromagnetic devices," *XIX Int. Conf. on Elect. Machines (ICEM)*, Rome, 2010, pp. 1-6.

[Wro10b] R. Wrobel, N. McNeill, and P. H.Mellor, “Performance analysis and thermal modeling of high-energy-density prebiased inductor,” *IEEE Trans. Ind. Electron.*, vol. 57, no. 1, pp. 201–208, Jan. 2010.

[Wro12] R. Wrobel, A. Mlot and P. H. Mellor, “Contribution of end-winding proximity losses to temperature variation in electromagnetic devices,” *IEEE Trans. on Ind. Electr*., vol. 59, no. 2, 2012, pp. 848 – 857.

[Xue16] S. Xue, W. Q. Chu, Z. Q. Zhu, J. Peng, S. Guo, and J. Feng, “Iron loss calculation considering temperature influence in non-oriented steel laminations”, *IET Sci. Meas. Technol.*, vol. 10, 2016, pp. 846-854.

[Yah14] K. Yahia, D. Matos, J. O. Estima, and A. J. M. Cardoso, “Modeling synchronous reluctance motors including saturation, iron losses and mechanical losses,” *2014 International Symposium on Power Electronics, Electrical Drives, Automation and Motion*, SPEEDAM 2014, pp. 601–606, 2014.

[Yu10] Q. Yu, C. Laudensack, D. Gerling, “Improved lumped parameter thermal model and sensitivity analysis for SR drives” *Proc. Int. Conf. on Electrical Machines and Systems (ICEMS)*, 2010.

[Yun11] Yunus A. Cengel, Afshin J. Ghajar, *Heat and Mass Transfer: Fundamentals & Applications*, Fourth Edition, McGraw-Hill, 2011.

[Zha19] Y. Zhao, D. Li, T. Pei, R. Qu, "Overview of the rectangular wire windings AC electrical machine," *CES Transactions on electrical machines and systems*, vol. 3, no. 2, June 2019

[Zhu00] Z. Q. Zhu and D. Howe, "Influence of design parameters on cogging torque in permanent magnet machines," *IEEE Trans. Energy Conversion*, vol.15, pp. 407-412, Dec. 2000

[Zhu02] Z. Q. Zhu, Y. S. Chen, and D. Howe, "Iron loss in permanent magnet brushless AC machines under maximum torque per ampere and flux weakening control," *IEEE Trans. on Magnetics*, vol. 38, no. 5, pp. 3285-3287, Sep 2002.

[Zhu07] Z. Q. Zhu and D. Howe, "Electrical machines and drives for electric, hybrid, and fuel cell vehicles," in *Proceedings of the IEEE*, vol. 95, no. 4, pp. 746-765, Apr. 2007.

[Zhu14] Z. Q. Zhu, "Permanent magnet machines for traction applications", *Encyclopaedia of Automotive Engineering*, pp. 1-20, 2014

[Zhu15] S. Zhu, M. Cheng, X. Cai, "A coupled field-circuit method for thermal modeling of electrical machine". *Proc. Energy Conversion Congress and Exposition (ECCE)*, 2015, pp. 805-812.

APPENDIX

Prototype machine

The cross-section of the prototype IPM machine under investigation is shown in Fig. A.1. Its main parameters are listed in Table A.1. It is a 12 kW PMSM with 72 slots and 12 poles designed for hybrid electric vehicles. A spoke type IPM rotor with ferrite magnets is employed. The rotor magnet slot opening is the opening width above the spoke magnet, and the magnet slot tip height is the distance from the rotor surface to the top above the spoke magnet. The stator is equipped with a dual-three phase winding with a 30-degree phase shift and the coil pitch is 6 slot pitches to maximize the distribution and pitch factors. The conductors employed in this machine are rectangular conductors with 2 mm width and 5 mm height. Two conductors located in the same slot are connected in series to the same phase winding shown in Fig. A.2. The parallel slots are chosen instead of parallel teeth for higher packing factor and higher heat dispassion capability. However, these large conductors employed in the prototype machine generate a large AC copper loss at high speed as investigated in the thesis.

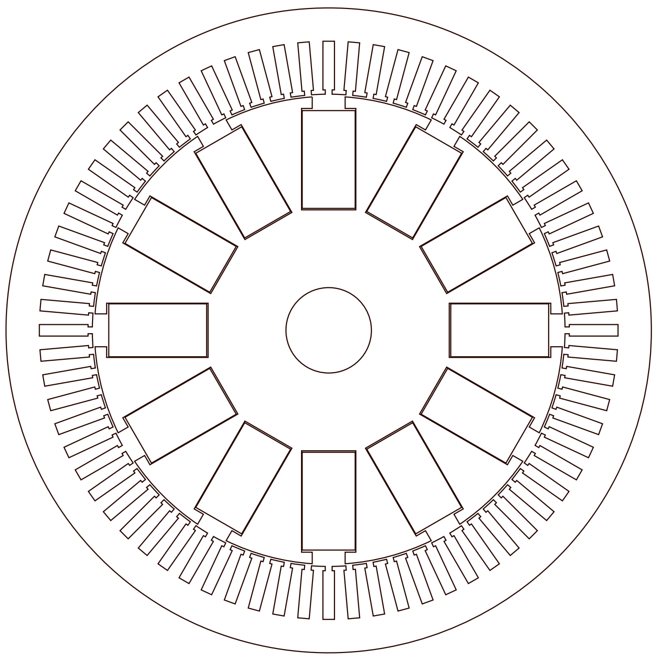

Fig. A.1. Cross-section of the prototype machine with a spoke IPM rotor.

TABLE A.1. Major Parameters of Prototype IPM Machine

Parameter	Value	Parameter	Value
Stator outer diameter	151 mm	Numbers of slots and poles	72/12
Stator inner diameter	110.6 mm	Axial length	67 mm
Slot depth	11.4 mm	Rotor outer diameter	109.6 mm
Slot width	2.7 mm	Magnet thickness	12.4 mm
Slot opening width	1.6 mm	Magnet height	24 mm
Slot tooth tip height	1 mm	Magnet slot opening	7.7 mm
Magnet remanence at 70 °C	0.39 T	Magnet permeability	1.1

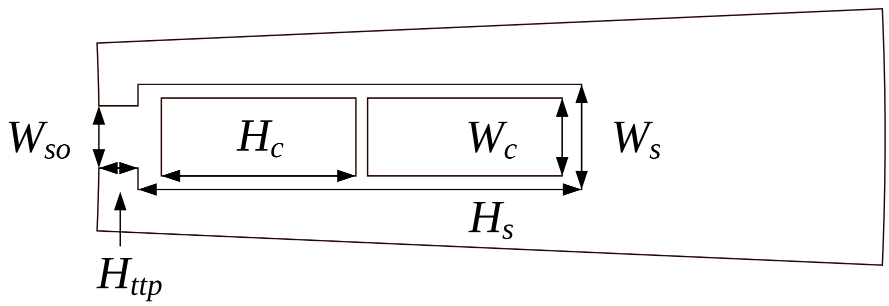

Fig. A.2. Geometry of the stator.

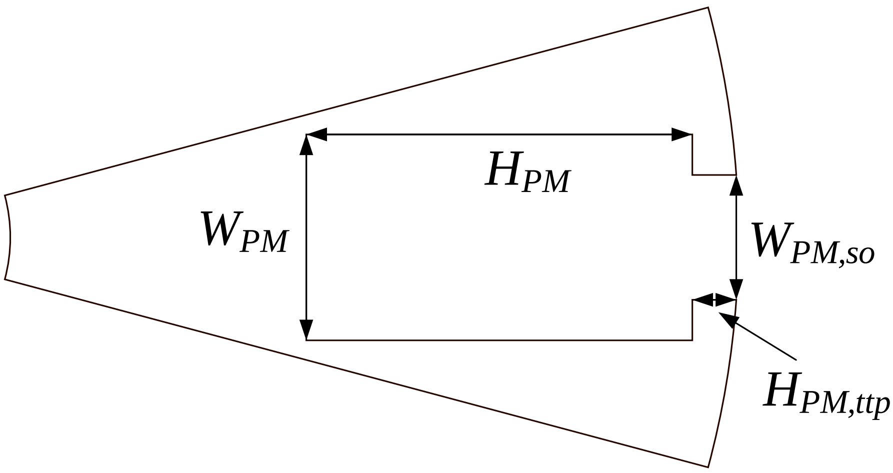

Fig. A.3. Geometry of the rotor.

It should be noted that W_{so} is the width of slot opening, H_{ttp} is the slot tooth tip height, H_c, W_c, H_s, and W_s are the height and width of conductor and slot, respectively, shown in Fig. A.2. In Fig. A.3, $W_{PM,so}$ represents the magnet slot opening, $H_{PM,ttp}$ is the height of magnet slot tip, H_{PM}, and W_{PM} are the height and width of conductor and slot, respectively.

To validate the FE model of the prototype machine, the back-EMF is tested. Fig. A.3 compares the tested and FE calculated phase back-EMF waveforms. It can be seen that the FE calculated back-EMF has good agreement with the measured one. The photos of the laminations and the assembled machine are shown in Figs. A.4. and A.5.

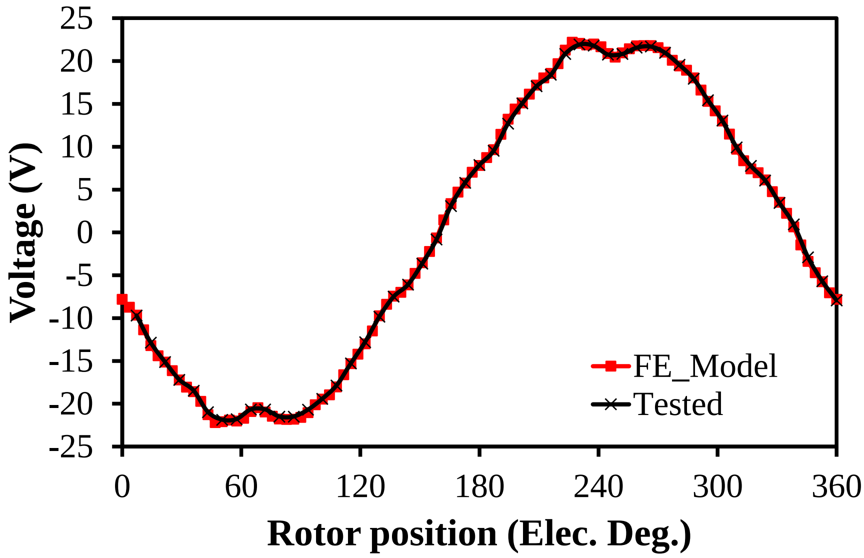

Fig. A.4. Measured and FE calculated back-EMF waveforms at 2000rpm.

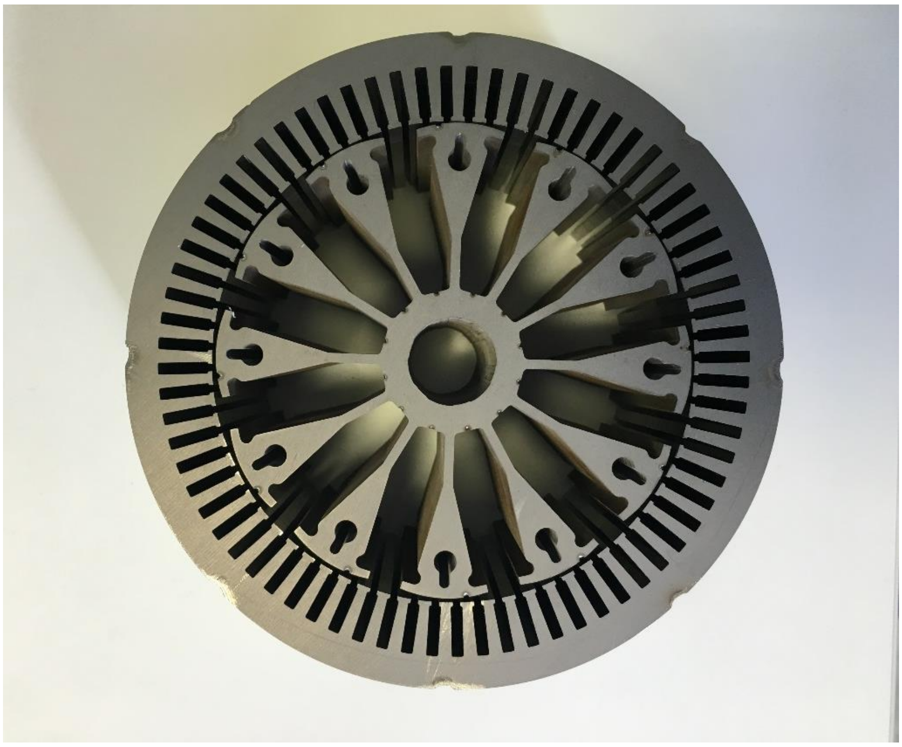

Fig. A.5. Photo of the stacked laminations.

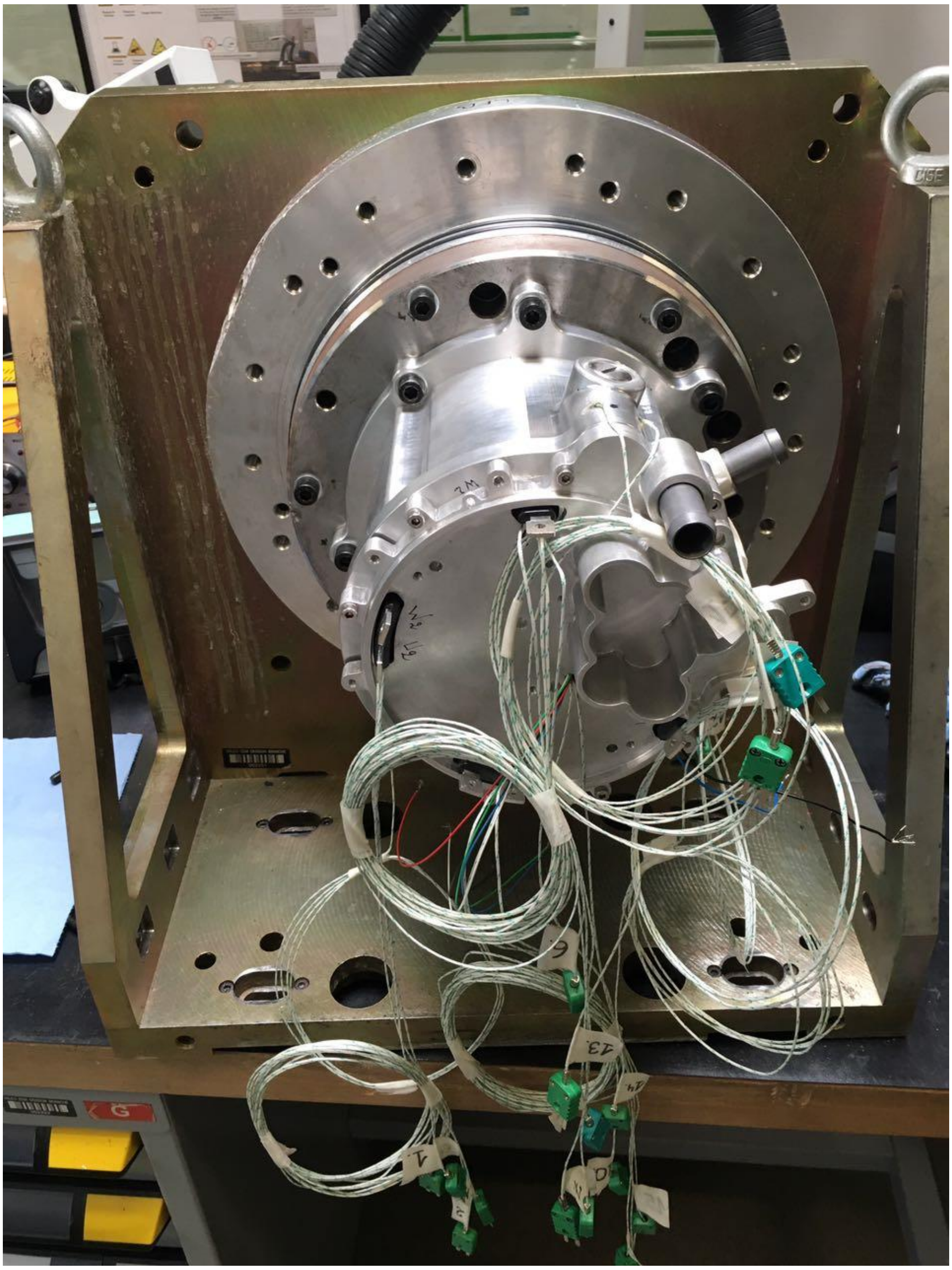

Fig. A.6. Photo of assembled prototype IPM machine.